University of Alberta

Synthesis of Copper and Silver Nanowires in Porous Aluminum Oxide Templates and Preparation of Polymer Nanocomposites

by

Genaro Alberto Gelves Canas ©

A thesis submitted to the Faculty of Graduate Studies and Research
in partial fulfillment of the requirements for the degree of

Doctor of Philosophy

Department of Chemistry

Edmonton, Alberta
Spring 2007

Library and
Archives Canada

Published Heritage
Branch

395 Wellington Street
Ottawa ON K1A 0N4
Canada

Bibliothèque et
Archives Canada

Direction du
Patrimoine de l'édition

395, rue Wellington
Ottawa ON K1A 0N4
Canada

Your file Votre référence
ISBN: 978-0-494-29677-6
Our file Notre référence
ISBN: 978-0-494-29677-6

NOTICE:
The author has granted a non-exclusive license allowing Library and Archives Canada to reproduce, publish, archive, preserve, conserve, communicate to the public by telecommunication or on the Internet, loan, distribute and sell theses worldwide, for commercial or non-commercial purposes, in microform, paper, electronic and/or any other formats.

The author retains copyright ownership and moral rights in this thesis. Neither the thesis nor substantial extracts from it may be printed or otherwise reproduced without the author's permission.

AVIS:
L'auteur a accordé une licence non exclusive permettant à la Bibliothèque et Archives Canada de reproduire, publier, archiver, sauvegarder, conserver, transmettre au public par télécommunication ou par l'Internet, prêter, distribuer et vendre des thèses partout dans le monde, à des fins commerciales ou autres, sur support microforme, papier, électronique et/ou autres formats.

L'auteur conserve la propriété du droit d'auteur et des droits moraux qui protège cette thèse. Ni la thèse ni des extraits substantiels de celle-ci ne doivent être imprimés ou autrement reproduits sans son autorisation.

In compliance with the Canadian Privacy Act some supporting forms may have been removed from this thesis.

While these forms may be included in the document page count, their removal does not represent any loss of content from the thesis.

Conformément à la loi canadienne sur la protection de la vie privée, quelques formulaires secondaires ont été enlevés de cette thèse.

Bien que ces formulaires aient inclus dans la pagination, il n'y aura aucun contenu manquant.

Canada

Para mi amada Laura Isabel

Abstract

High-aspect ratio metal nanowires may be an alternative to carbon nanotubes in the preparation of electrically conductive polymer nanocomposites. Metal nanowire/polymer nanocomposites are promising materials for applications such as electrostatic dissipation, electromagnetic interference, and electromagnetic shielding.

This thesis presents the synthesis of copper and silver nanowires on a large scale using template-directed synthesis in porous aluminum oxide (PAO) templates. The nanowires were synthesized by AC electrodeposition through the barrier layer at the bottom of the pores in PAO. Copper nanowires were electrodeposited using continuous sine waves and silver nanowires were electrodeposited using pulsed AC square waves. The nanowires are harvested by dissolution of the PAO template in NaOH(aq) solutions and dispersion in methanol using ultrasound. Liberation using acidic solutions affects the diameter and dispersion of the nanowires. The methodology is amenable to adaptation for the synthesis of other metals and compound nanowires in gram quantities. The process yields Cu and Ag nanowires 25 nm in diameter and average aspect ratios (*l/d*) between 50 and 70. The nanowires were characterized by SEM, TEM, XRD, XPS, and TGA. Metal nanowires produced by AC electrodeposition were polycrystalline. Some surface oxidation was observed in Cu nanowires, and Ag nanowires were oxide-free. The nanowires were used for the preparation and study of electrical and rheological properties of polymer nanocomposites.

Metal nanowire/polystyrene nanocomposites were prepared using two methods: solution mixing and melt-mixing. The morphology of the nanowire/polymer nanocomposites were characterized by SEM and TEM. The effects of the mixing method, the concentration, and surface functionalization of Cu and Ag nanowires with alkanethiols on the dispersion, and electrical and rheological properties of polystyrene nanocomposites were studied. Low electrical percolation thresholds of 0.46 vol. % Cu and 0.51 vol. % Ag were obtained by solution mixing. Surface functionalization of the nanowires with alkanethiols significantly improved the dispersion of the nanowires in the nanocomposites. Percolated nanocomposites showed changes of 10 and 11 orders of magnitude in the electrical resistivity relative to the pristine polymer. The electrical resistivities of percolated (Cu or Ag) nanowire/nanocomposites indicate their potential application in electrostatic dissipation.

Acknowledgements

I will always remember that morning of January 2003, when I step for the first time in Edmonton on a white blanket of snow at -10 °C. I must confess that it was hard, especially, after being more than two decades of my life used to the tropical weather. Although the snow-covered city looked beautiful that morning, -10 °C were too cold for me. A few days later, the winter temperature in Edmonton gradually decreased even more, while I gradually warmed up for my graduate student life at the University of Alberta. It was an excellent experience.

I want to thank the Department of Chemistry at U of A for giving me the opportunity of coming here and for providing such a good environment for developing research and pursuing graduate studies. My very special acknowledgements to professors Joel Haber and Uttandaraman Sundararaj for all their encouragement, contributions, understanding, support, advice and friendship during these years. Discussions were always challenging and fruitful and this work had not been possible without all their support. I learned a lot and enjoyed working with them during these years, that was a big part of the process of shaping myself into a good scientist.

I want to thank all the people that contributed to the development of this work. Thanks to Mr. Matthieu Versavel for the training and cooperation with X-ray Diffraction Analysis, but most importantly for his friendship. I thank Mr. George

Braybrook for all his experience and input during the characterization by Scanning Electron Microscopy (SEM). I also appreciate the good conversations that we had in the dark room during the collection of SEM images on Monday mornings, it was a good way to start the week. Special thanks to Dr. Bin Lin from the Chemical and Materials Engineering department for her cooperation with the rheological characterization of polymer nanocomposites. I want to thank Mr. Daniel Salamon for SEM characterization and Dr. Dimitre Karpusov for the data collection by X-ray Photoelectron Spectroscopy (XPS). I acknowledge Dr. Guy Bernard in Dr. Wasylishen group for data collection by Solid State Nuclear Magnetic Resonance (^{13}C CPMAS NMR). I also want to thank the National Research Council-National Institute of Nanotechnology (NRC-NINT) for the facilities of XRD and SEM, Alberta Center for Surface Engineering and Science (ACSES) at the University of Alberta for XPS facilities, the Glass and Electronic Shops for their contribution to the set-up necessary for the synthesis of nanowires, and the Microanalytical Laboratory at the Department of Chemistry for the data collection by Elemental, Thermogravimetric (TGA) and Differential Scanning Calorimetry (DSC) Analyses. The economic support of the Natural Sciences and Engineering Research Council of Canada (NSERC) is highly appreciated. Thanks to all of you for your valuable contributions.

Finally, my special thanks to my dear and lovely Laura Isabel, who has been my strength in this journey. Thanks for all your love and patience, thanks for sharing the difficult and good times of this stage of my life. Thanks for being there for me.

Table of Contents

Chapter 1. Introduction

1.1 Synthesis and applications of metal nanowires 1

1.1.1 Hard template assisted synthesis of metal nanowires 3

1.1.1.1 DC electrodeposition 4

1.1.1.2 AC electrodeposition 7

1.1.2 Soft template assisted synthesis of metal nanowires 11

1.1.3 Other syntheses of metal nanowires 13

1.1.4 Surface functionalization of metal nanowires 13

1.1.4.1 The structure of SAMs of alkanethiols on Cu and Ag 15

1.1.4.2 The effect of surface oxidation on self-assembly of alkanethiols 16

1.1.5 Applications and challenges of metal nanowires 17

1.2 Porous aluminum oxide (PAO) templates 19

1.2.1 Structure of PAO templates 20

1.2.2 Mechanism of pore growth and self-ordering of PAO templates 21

1.3 Metal/polymer nanocomposites 23

1.3.1 Rheology of polymer nanocomposites 24

1.3.2 Rheological and electrical percolation 28

1.4 Motivation and overview of the thesis 31

1.5 References 33

Chapter 2. Multigram synthesis of Cu and Ag nanowires using AC electrodeposition into porous aluminum oxide templates

2.1 Introduction 44

2.2 Experimental 45

2.2.1 Development of porous aluminium oxide templates (PAO) for multigram synthesis of nanowires 45

2.2.1.1 Smaller-scale process for preparation of PAO templates 46

2.2.1.2 Larger-scale process for preparation of PAO templates 48

2.2.2 Electrodeposition of CuNWs 50

2.2.3 Electrodeposition of AgNWs 51

2.2.4 Liberation of nanowires from PAO templates 53

2.2.5 Length distribution of NaOH-liberated nanowires 54

2.2.6 Preparation of nanowire samples for XPS, XRD and TGA analysis 54

2.2.7 Depth profiling of pore-filling 55

2.2.8 Instrumentation 55

2.3 Results 56

2.3.1 Template directed-synthesis of CuNWs 56

2.3.1.1 Micrometer-size edge cracks 56

2.3.1.2 Effect of counter electrode on electrolyte stability and electrodeposition time 58

2.3.1.3 Effect of pore depth on yield 61

2.3.1.4 Electrode size and yield 63

2.3.2 Dissolution of PAO templates and CuNW liberation 64

2.3.2.1 Effect of liberation process on morphology and dispersion of CuNWs 65

2.3.2.2 Effect of liberation process on surface chemistry of CuNWs 68

2.3.2.3 Length distribution of CuNWs 71

2.3.2.4 Transmission electron microscopy and thermogravimetric analysis of CuNWs 71

2.3.3 Template directed-synthesis of AgNWs 74

2.3.3.1 Effect of AC signal on Ag electrodeposition into PAO templates 74

2.3.3.2 Effect of liberation process on morphology of AgNWs 75

2.3.3.3 Characterization of AgNWs 77

2.4 Discussion 82

2.5 Conclusions 90
2.6 References 91

Chapter 3. Surface functionalization of Cu and Ag nanowires using alkanethiols

3.1 Introduction 96
3.2 Experimental 97
  3.2.1 Materials 97
  3.2.2 Synthesis and surface functionalization of Cu and Ag nanowires 98
  3.2.3 Characterization 99
3.3 Results 100
  3.3.1 Surface functionalization of CuNWs using alkanethiols 100
    3.3.1.1 Thermogravimetric and elemental analysis 100
    3.3.1.2 X-ray photoelectron spectroscopy 108
    3.3.1.3 X-ray diffraction 113
    3.3.1.4 Differential scanning calorimetry 116
    3.3.1.5 Solid state CPMAS ^{13}C NMR 118
  3.3.2 Surface functionalization of AgNWs using 1-octanethiol 121
3.4 Discussion 123
3.5 Conclusions 129
3.6 References 130

Chapter 4. Cu and Ag nanowire/Polystyrene nanocomposites produced by solution processing

4.1 Introduction 133
4.2 Experimental 135
  4.2.1 Preparation of polystyrene nanocomposites by solution processing 135
  4.2.2 SEM and TEM of nanocomposites 135
  4.2.3 Measurement of electrical resistivity of nanocomposites 136
  4.2.4 Rheological characterization 138
4.3 Results 139
  4.3.1 Dispersion and electrical percolation of metal nanowires in PS 139

nanocomposites
4.3.1.1 Dispersion and electrical resistivity of CuNW/PS nanocomposites - Initial experiments 139
4.3.1.2 Electrical percolation of CuNWs and AgNWs in PS 145
4.3.2 The effect of surface functionalization on dispersion and electrical percolation 157
4.3.2.1 Dispersion of $C_8H_{17}S$-CuNWs 157
4.3.2.2 Electrical percolation of $C_8H_{17}S$-CuNWs 161
4.3.2.3 Fragmentation of $C_8H_{17}S$-AgNWs 164
4.3.3 Rheological percolation of metal nanowire/PS nanocomposites 168
4.3.3.1 Viscoelastic properties of CuNW/PS nanocomposites 170
4.3.3.2 Viscoelastic properties of $C_8H_{17}S$-CuNW/PS nanocomposites 176
4.3.3.3 Viscoelastic properties of AgNW/PS nanocomposites 183
4.4 Discussion 187
4.5 Conclusions 194
4.6 References 196

Chapter 5. Copper nanowire/Polystyrene nanocomposites prepared by melt mixing: Surface functionalization, dispersion, and electrical-rheological percolation

5.1 Introduction 201
5.2 Experimental 203
5.2.1 Synthesis and chemical modification of CuNWs 203
5.2.2 Preparation of polymer nanocomposites by melt mixing 204
5.2.3 Morphology characterization 205
5.2.4 Rheological characterization 205
5.2.5 Electrical resistivity measurements 206
5.2.6 Glass transition temperature by Differential Scanning Calorimetry 206
5.3 Results 206

5.3.1 Dispersion of as-liberated and chemically modified CuNWs in PS prepared by melt mixing 206

5.3.2 Rheological behavior of melt-mixed CuNW/PS nanocomposites 208

5.3.3 Electrical resistivity of melt-mixed CuNW/PS nanocomposites 220

5.4 Discussion 221

5.4.1 Effect of surface functionalization of CuNWs on dispersion 222

5.4.2 Effect of surface functionalization of CuNWs on rheology of melt-mixed CuNW/PS nanocomposites 222

5.4.3 Effect of surface functionalization of CuNWs on electrical percolation of melt-mixed CuNW/PS nanocomposites 226

5.4.4 Rheological and electrical percolation of melt-mixed CuNW/PS nanocomposites 229

5.5 Conclusions 231

5.6 References 232

Chapter 6. Concluding remarks and future work

6.1 General conclusions 236

6.2 Future work 242

6.2.1 Synthesis of nanowires in PAO templates 242

6.2.2 Dispersion of metal nanowires in polymer nanocomposites 243

6.2.3 Electrical percolation threshold 245

6.3 References 247

Appendix A. Surface functionalization of CuNWs using benzenethiol and characterization of C_6H_5S-CuNW/PS nanocomposites

A.1 Introduction 249

A.2 Surface functionalization of CuNWs using benzenethiol 249

A.3 C_6H_5S-CuNW/PS nanocomposites - dispersion and electrical resistivity 250

A.4 Conclusion 251

List of Tables

Table 1.1. Typical dimensions of pores under conditions yielding self-ordered PAO templates.[96] 23

Table 2.1. Representation of electrochemical cells and half reactions for AC electrodeposition of copper into PAO templates. 59

Table 2.2. Influence of counter electrode on time required for copper electrodeposition and the final pH of the electrodeposition solution containing 0.5 M $CuSO_4$ and 0.285 M H_3BO_3. (Aluminum electrodes used were 11 × 5 cm^2 and the deposition conditions were 10 Vrms and 200 Hz continuous sine waves). 60

Table 2.3. Measured d-spacings and corresponding planes from electron diffraction pattern for Cu nanowires (Length of camera = 100 cm, 200 kV). 73

Table 2.4. Measured d-spacings and corresponding planes from electron diffraction pattern for Ag nanowires (Camera length = 100 cm, 200 kV) 80

Table 3.1. Weight loss percentage from TGA and elemental analysis of copper nanowires functionalized using different concentrations of $C_8H_{17}SH$. 102

Table 3.2. Percentage of weight loss and temperature of desorption for unfunctionalized CuNWs and CuNWs functionalized using 5.0 mM thiol solutions. 107

Table 3.3. Elemental analysis of copper nanowires functionalized with different alkanethiols. 107

Table 3.4. Electron binding energies for copper oxides and hydroxides[14,15] 110

Table 3.5. d-spacings for the reflections from alkanethiol-functionalized CuNWs at small angles. 114

Table 3.6. Melting points and enthalpies of copper nanowires functionalized with different alkanethiols (a) C_4H_9SH (b) $C_8H_{17}SH$ (c) $C_{18}H_{37}SH$. 118

Table 3.7. Chemical shifts for CuNWs functionalized with different alkanethiols and typical chemical shifts for the corresponding alkanethiols in solution.[29,30] 120

Table 3.8. Weight loss percentage from TGA and results of elemental analysis of silver nanowires functionalized using 5.0 M solution of $C_8H_{17}SH$. 123

Table 4.1. Specifications of the Model 8009 Keithley resistivity test fixture. 138

Table 4.2. Average volume electrical resistivity and standard deviations calculated for Cu nanowire/PS nanocomposites with different concentrations of Cu nanowires (prepared in 16 μm thick PAO templates using the smaller-scale process, average length = 1.78 ± 1.37 μm). 141

Table 4.3. Average volume electrical resistivity and standard deviations calculated for spherical micron-sized Cu particle/PS nanocomposites at different concentrations of copper. 142

Table 4.4. Average volume electrical resistivity and standard deviations calculated for $C_{18}H_{37}S$-CuNW/PS nanocomposites for different concentrations of copper. 145

Table 4.5. Average volume electrical resistivity and standard deviations calculated for Cu nanowire/polystyrene nanocomposites with different concentrations of Cu. 153

Table 4.6. Average volume electrical resistivity and standard deviations calculated for Ag nanowire/polystyrene nanocomposites with different concentrations of Ag. 153

Table 4.7. Volume electrical resistivity of 1.0 vol. % CuNW/polystyrene nanocomposites containing unfunctionalized copper nanowires and copper nanowires chemically functionalized in different concentrations of 1-octanethiol (mM = 0.1, 1.0, 2.5 and 5.0) 158

Table 4.8. Average volume electrical resistivity and standard deviations calculated for $C_8H_{17}S$-CuNW/polystyrene nanocomposites at different concentrations of Cu. 163

Table 4.9. Volume electrical resistivity of $C_8H_{17}S$-AgNW/PS nanocomposites containing 1.0 vol. % Ag and prepared by different methods. 165

Table 4.10. Electrical and rheological percolation thresholds for metal nanowire/PS nanocomposites. 188

Table 5.1. Specifications of the Alberta Polymer Asymmetric Minimixer (APAM)[13] 204

Table 5.2. Slopes of Log G' and Log G" versus Log ω at frequencies between 0.1 and 1.0 rad/s for CuNW/PS nanocomposites prepared by melt mixing. 211

Table 5.3. Slopes of Log G' and Log G" versus Log ω at frequencies between 0.1 and 1.0 rad/s for $C_8H_{17}S$-CuNW/PS nanocomposites prepared by melt mixing. 215

Table 5.4. Slopes of Log G' and Log G" versus Log ω at frequencies between 0.1 and 1.0 rad/s for C_4H_9S-CuNW/PS nanocomposites prepared by melt mixing. 218

Table 5.5. Glass transition temperature (T_g) of pure PS, PS processed by melt mixing, and PS nanocomposites containing 1 vol. % Cu of unfunctionalized and functionalized nanowires. 225

List of Figures

Figure 1.1. Different approaches utilized for the growth of 1D nanostructures reproduced from Xia et al.[1] (a) Anisotropic growth, (b) confinement by a liquid droplet (c) template-directed synthesis (d) surfactant-assisted kinetic control (e) self-assembly of 0D nanostructures, and (f) size reduction of a 1D microstructure. 2

Figure 1.2 Schematic representation of the synthesis of nanowires in PAO templates using DC electrodeposition. 6

Figure 1.3 Schematic representation of the synthesis of nanowires in PAO templates using AC electrodeposition. 9

Figure 1.4. (a) Illustration of a fully extended structure of a chemisorbed alkanethiol and the coordinates typically used to define the orientations of the chain, (b) illustration of the surface structures formed by chemisorption of alkanethiols on Ag and Cu surfaces. Reprinted with permission from *J. Am. Chem. Soc.*, 1991, 113, 19, 7152-7167. Copyright 1991, American Chemical Society. 16

Figure 1.5. Structure of an ideal nanostructure of porous alumina template. Reproduced with permission from *J. Electrochem. Soc.* 2001, 148, 4, B152-B156. Copyright 2001, The Electrochemical Society. 20

Figure 1.6. SEM image of a PAO surface obtained in sulfuric acid solution at 25 V, 12.5 h, and 10 °C. Reproduced with permission from *J. Electrochem. Soc.* 1997, 144, 5, L127-L130. Copyright 1997, The Electrochemical Society. 21

Figure 1.7. Illustration of polymer-polymer, nanofiller-polymer, and nanofiller-nanofiller networks of polymer nanocomposites with the increase in concentration of nanofiller. Reprinted with permission from *Macromolecules*, 2004, 37, 24, 9048-9055. Copyright 2004, American Chemical Society. 29

Figure 2.1. Photograph of a double-walled 3 liter anodization bath containing five Al electrodes 5 cm wide × 11 cm high × 1 mm thick interdigitated with stainless steel counter electrodes (Smaller-scale process). 48

Figure 2.2. Photograph of a chilled 30 liter anodization bath containing ten Al electrodes 10 cm wide × 25 cm high × 1 mm thick interdigitated with graphite electrodes (Larger-scale process). 50

Figure 2.3. Continuous sine sequence used for the AC electrodeposition of copper into PAO templates. 51

Figure 2.4. Pulsed squared-wave sequence used for the AC electrodeposition of silver into PAO templates. 52

Figure 2.5. SEM of (a) micron-size crack that forms on 90 degree edges and (b) bulk deposition of Cu that occurs at the crack if it is not coated before AC electrodeposition. 57

Figure 2.6. SEM images of cross sections of PAO templates prepared in 0.3 M H_2SO_4(aq) solutions for different anodization times: (a) 4 h (b) 6 h and (c) 8 h. The arrows indicate the thickness of the PAO templates: (a) 18 μm, (b) 27 μm, and (c) 36 μm. 62

Figure 2.7. Yield of Cu nanowires from PAO templates prepared by anodization for different times in 0.3M H_2SO_4 solutions (4, 6, or 8 hours corresponding to 62

18, 27 or 36 μm thick PAO templates, respectively). The line corresponds to the linear least-square fit of the average yields. The standard deviations were calculated from five replicates.

Figure 2.8. SEM images of top surfaces of ion-milled Cu-filled PAO templates (5 cm × 11 cm electrodes) to show degree of pore-filling as a function of depth: (a) 0.5 μm and (b) 10 μm removed from the top of 36 μm deep-pores. 63

Figure 2.9. SEM images of porous alumina template surfaces (a) after CuNW electrodeposition and (b) after CuNW electrodeposition and surface wiping. The images show the removal of bulk overgrowth before CuNW liberation. 65

Figure 2.10. SEM of (a) and (b) 0.6 M H_3PO_4-liberated CuNWs and (c) and (d) 1.0 M NaOH-liberated CuNWs. 66

Figure 2.11. Copper nanowires after dissolution of the PAO template in 0.6 M H_3PO_4(aq) solution at 60 °C. The images indicate that coarsening of the nanowires occurred during the 30 minute dissolution of the PAO template. The tips of the nanowires are more exposed to the H_3PO_4(aq) solution and become thicker than the bottoms. 67

Figure 2.12. X-ray difractograms of Cu nanowires (a) liberated in 1 M NaOH solutions, and (b) liberated in 0.6M H_3PO_4 solutions. Standard powder patterns for (c) Cu (JCPDS 4-836), (d) Cu_2O (JCPDS 77-199), and (e) CuO (JCPDS 78-428). The nanowires were exposed to air for less than 30 minutes before the analysis. 69

Figure 2.13. X-ray photoelectron spectra of Cu foil and CuNWs. (a) Surveys, (b) high resolution XP spectra of Cu(2p) peak, and (c) high resolution XP spectra of Cu($L_3M_{4.5}M_{4.5}$) Auger peak. The spectra correspond to (A) sputter- 70 cleaned Cu foil, (B, C) NaOH-liberated CuNWs exposed to air for (B) <30 min. and (C) 3 days, and (D, E) H_3PO_4-liberated CuNWs exposed to air for (D) <30 min. and (E) 3 days. Satellite peaks on Cu(2p) spectra labeled with an * indicate the presence of Cu(II) species, such as CuO. Dashed lines indicate the shift of the most intense component of the $Cu(L_3M_{4.5}M_{4.5})$ peak from Cu(0) to Cu(I) and Cu(II).

Figure 2.14. SEM images and length distribution of copper nanowires grown in PAO templates anodized for 8 hours and liberated using 1.0 M NaOH(aq) produced using (a,b) smaller-scale process (1.78 ± 1.37 μm) and (c,d) larger-scale process (1.29 ± 0.83 μm). Lines are guides to the eye. 72

Figure 2.15. (a) Low magnification and (b) high magnification TEM images of copper nanowires liberated from PAO templates using 1.0 M NaOH(aq). The inset corresponds to SAED of the nanowire in (b). 73

Figure 2.16. Thermogravimetric analysis of NaOH-liberated CuNWs heated to 550 °C under nitrogen at 10 °C/minute. 74

Figure 2.17. SEM images of AgNWs liberated using 1.0 M NaOH(aq) (a) low magnification (b) high magnification. 76

Figure 2.18. SEM image of Ag nanostructure resulting from the liberation of AgNWs from PAO templates using 0.6 M H_3PO_4 at 60 °C. 77

Figure 2.19. (a) X-ray diffractogram of Ag nanowires after liberation from the PAO template using 1.0 M NaOH(aq) and (b) Standard powder pattern for fcc silver (JCPDS 04-0783). 78

Figure 2.20. X-ray photoelectron spectra of AgNWs liberated in 1.0 M 79

NaOH(aq), (a) Survey, (b) Ag(3d) peak, and (c) Ag(MNN) Auger peak. The spectra show that AgNWs do not have silver oxides at the surface.

Figure 2.21. (a) Low magnification and (b) high magnification TEM images of AgNWs liberated from PAO templates using NaOH (aq). The inset corresponds to SAED of the nanowire in (b). 80

Figure 2.22. (a) Typical SEM image of AgNWs dispersed on a glass surface used to measure their length distribution, and (b) length distribution of AgNWs. AgNWs were prepared in PAO templates anodized for 8 hours and liberated using 1.0 M NaOH(aq). Average length = 1.37 ± 0.76 μm. Line is a guide to the eye. 81

Figure 2.23. Schematic diagram comparing the surface chemistry and coarsening process for the Cu nanowires during liberation in 0.6 M H_3PO_4(aq) and 1.0 M NaOH(aq). 86

Figure 2.24. Overview of the synthesis of metal nanowires and preparation of polymer nanocomposites. 91

Figure 3.1. Alkanethiols utilized for surface modification of CuNWs. 98

Figure 3.2.Thermogravimetric analysis of (a) NaOH-liberated CuNWs and functionalized CuNWs using different concentrations of $C_8H_{17}SH$: (b) 0.1 mM, (c) 1.0 mM, (d) 2.5 mM, (e) 5 mM, and (f) 10 mM. 101

Figure 3.3. Variation of % weight loss and the sulfur content of copper nanowires exposed to different concentrations of $C_8H_{17}SH$. Lines are guides to the eye. 103

Figure 3.4. Cu to S ratio of CuNWs surface functionalized in different concentrations of $C_8H_{17}SH$. Line is a guide to the eye. 103

Figure 3.5. Thermogravimetric analysis of (a) NaOH-liberated CuNWs and CuNWs functionalized with 5 mM solutions of (b) C_4H_9SH (c) $C_8H_{17}SH$, and (d) $C_{18}H_{37}SH$. 106

Figure 3.6. First derivative of thermogravimetric analyses for (a) NaOH-liberated CuNWs and Cu nanowires functionalized with 5 mM solutions of (b) C_4H_9SH (c) $C_8H_{17}SH$, and (d) $C_{18}H_{37}SH$. 106

Figure 3.7. X-ray photoelectron survey of (a) NaOH-liberated CuNWs, and CuNWs functionalized with (b) C_4H_9SH (c) $C_8H_{17}SH$, and (d) $C_{18}H_{37}SH$. 109

Figure 3.8. High resolution X-ray photoelectron spectra of (a) Cu 2p peak, (b) Cu $L_3M_{4.5}M_{4.5}$ Auger peak, (c) O(1s) peak, and (d) S(2p) peak for (A) NaOH-liberated CuNWs, and CuNWs functionalized with (B) C_4H_9SH (C) $C_8H_{17}SH$ (D), and $C_{18}H_{37}SH$. Dotted lines indicate the binding energies according to literature.[14,15] 111

Figure 3.9. XRD of CuNWs functionalized with (a) C_4H_9SH (b) $C_8H_{17}SH$, and (c) $C_{18}H_{37}SH$. Standard powder patterns of (d) Cu (e) Cu_2O (f) CuO. 114

Figure 3.10. DSC of CuNWs functionalized with (a) C_4H_9SH (b) $C_8H_{17}SH$, and (c) $C_{18}H_{37}SH$. 117

Figure 3.11. CPMAS ^{13}C NMR spectra for CuNWs functionalized using (a) C_4H_9SH (b) $C_8H_{17}SH$, and (c) $C_{18}H_{37}SH$. 119

Figure 3.12. Thermogravimetric analysis of (a) NaOH-liberated AgNWs and (b) 122

AgNWs surface functionalized with $C_8H_{17}SH$.

Figure 3.13. X-ray photoelectron spectra of AgNWs functionalized with $C_8H_{17}SH$. (a) Survey, and high resolution spectra of (b) Ag(3d) peak, (c) Ag(MNN) Auger, and (d) S(2p) peak. Dashed lines indicate the binding energies of Ag, Ag_2O, and AgO according to literature.[10] 124

Figure 3.14. Schematic representation of possible self-assembled structures formed on CuNWs after surface modification with alkanethiols. (a) monolayer on the nanowire surface and (b) self-assembled alkanethiolate copper complexes that may be present in the multilayer.[24-27] 129

Figure 4.1. Photographs of the two different probes used for measurement of volume electrical resistivity of polymer nanocomposites. (a) Electrical resistivity probe ETS-804B used along with a Keithley Electrometer 617; the reflected image on the copper plate shows the inner disk and the ring of the probe, (b) 6517A Keithley electrometer and 8009 Keithley resistivity test fixture. 137

Figure 4.2. Backscattered SEM images for a freeze-fractured sample of a CuNW/PS nanocomposite containing 4 vol. % CuNWs: (a) low magnification image of a cross section showing agglomerates of unfunctionalized CuNWs and (b) high magnification image of a cross section showing the presence of dispersed nanowires in the polymer between the agglomerates. 140

Figure 4.3. Backscattered SEM images for a freeze-fractured sample of $C_{18}H_{37}S$-CuNW/PS nanocomposite containing 4 vol. % CuNWs: (a) low magnification image showing absence of CuNW agglomerates and (b) high magnification image of a cross section showing good dispersion of functionalized nanowires. 144

Figure 4.4. Low magnification secondary (left) and backscattered (right) SEM images of freeze-fractured samples of solution-processed CuNW/PS nanocomposites containing different concentrations of CuNWs. The distribution of CuNWs is shown across the thickness of the samples. 147

Figure 4.5. High magnification secondary (left) and backscattered (right) SEM images of freeze-fractured samples of solution-processed CuNW/PS nanocomposites containing different concentrations of CuNWs. The dispersion of individual nanowires increases with Cu concentration. Surface features on secondary images (left) are due to polymer fracture. 148

Figure 4.6. TEM images of CuNW/PS nanocomposite containing 1.0 vol. % CuNWs. 149

Figure 4.7. Low magnification secondary and backscattered SEM images of freeze-fractured samples of solution-processed AgNW/PS nanocomposites containing different concentrations of AgNWs. The distribution of the nanowires is shown across the thickness of the samples. 150

Figure 4.8. High magnification secondary and backscattered SEM images of freeze-fractured samples of solution-processed AgNW/PS nanocomposites containing different concentrations of AgNWs. Surface features on secondary images (left) are due to polymer fracture. 151

Figure 4.9. TEM images of AgNW/PS nanocomposite containing 1.0 vol. % AgNWs. 151

Figure 4.10. Volume electrical resistivity of polystyrene nanocomposites for different concentrations of Cu and Ag nanowires. (a) CuNW/PS and (b) AgNW/PS. Lines connect the average ρ_v. 152

Figure 4.11. (a) Electrical conductivity of CuNW/PS nanocomposites above the electrical percolation threshold of copper nanowires, and (b) log-log plot of the electrical conductivity as a function of ($V - Vc$), where, Vc is the percolation threshold = 0.46 vol. %. Critical exponent $t = 3.34$. Line in (a) is a guide to the eye and line in (b) corresponds to the linear least-square fit of the data. 154

Figure 4.12. (a) Electrical conductivity of Ag NW/PS nanocomposites above the electrical percolation threshold of silver nanowires, and (b) log-log plot of the electrical conductivity as a function of ($V - Vc$), where, Vc is the percolation threshold = 0.51 vol. %. Critical exponent $t = 1.16$. Line in (a) is a guide to the eye and line in (b) corresponds to the linear least-square fit of the data. 155

Figure 4.13. Low magnification backscattered SEM images of solution processed PS nanocomposites containing $C_8H_{17}S$-CuNWs functionalized with different concentrations of $C_8H_{17}SH$: (a) 0.1 mM, (b) 1.0 mM, (c) 2.5 mM, and (d) 5.0 mM. Bright domains indicate agglomerated copper nanowires. 160

Figure 4.14. High magnification backscattered SEM images of solution processed PS nanocomposites containing $C_8H_{17}S$-CuNWs functionalized with different concentrations of $C_8H_{17}SH$: (a) 0.1 mM, (b) 1.0 mM, (c) 2.5 mM, and (d) 5.0 mM. Bright domains indicate individual copper nanowires. 161

Figure 4.15. Volume electrical resistivity of polystyrene nanocomposites for different concentrations of (a) copper nanowires surface functionalized with $C_8H_{17}SH$ (b) unfunctionalized copper nanowires. Lines connect the average ρ_v at each concentration. 162

Figure 4.16. SEM images of $C_8H_{17}S$-AgNW/PS nanocomposites prepared by solution casting-hot molding show the break up of silver nanowires into nanospheres. 166

Figure 4.17. Backscattered SEM images of $C_8H_{17}S$-AgNW/PS nanocomposites. (a) PS nanocomposite film obtained after solution casting and solvent evaporation, showing no fragmentation of $C_8H_{17}S$-AgNWs and (b) PS Nanocomposite after hot molding showing the break-up of $C_8H_{17}S$-AgNWs after hot molding. 167

Figure 4.18. Backscattered SEM images of freeze-fractured samples of $C_8H_{17}S$-AgNW/PS nanocomposites prepared by solution casting-melt mixing showing silver nanowires and silver nanospheres formed from fragmentation of $C_8H_{17}S$-AgNWs. 168

Figure 4.19.Several magnification SEM images of a freeze-fractured sample of $C_8H_{17}S$-AgNW/PS nanocomposite (1.0 vol. % Ag) prepared by solution casting-melt mixing-hot molding showing dispersion and significant break-up of silver nanowires. (a, c, e) Secondary electron SEM images, (b, d, f) Backscattered electron SEM images. 169

Figure 4.20. Rheological characterization of solution-processed CuNW/PS nanocomposites at 200 °C. Complex viscosity ($|\eta^*|$), storage modulus (G'), and loss modulus (G") as a function of: (a,c,e) frequency and (b,d,f) concentration of CuNWs, at several frequencies. Lines are guides to the eye. 171

Figure 4.21. Storage modulus (G') as a function of the loss modulus (G") of solution-processed CuNW/PS nanocomposites. (a) Low concentrations of CuNWs (0.25-1.0 vol. %) and (b) high concentrations of CuNWs (2.0-4.0 vol. %). The change in G' vs G" curve between 0.5 and 1.0 vol. % indicates the formation of a polymer-nanowire network. Lines are guides to the eye. 174

Figure 4.22. Phase angle (δ) as a function of the absolute value of the complex modulus (van Gurp-Palmen Plot) of solution-processed CuNW/PS 175 nanocomposites. Lines are guides to the eye.

Figure 4.23. Storage modulus (G') of CuNW/PS nanocomposites over G' of pure PS at 0.1 rad/s as a function of the CuNW concentration up to 2.0 vol. %. The change in $G'_{CuNW/PS}/G'_{PS}$ observed for concentrations of 0.5 - 1.0 vol. % Cu indicates formation of a polymer-nanowire network. Line is a guide to the eye. 175

Figure 4.24. Rheological characterization of solution-processed $C_8H_{17}S$-CuNW/PS nanocomposites at 200 °C. Complex viscosity ($|\eta^*|$), storage modulus (G'), and loss modulus (G") as a function of: (a,c,e) frequency and (b,d,f) concentration of $C_8H_{17}S$-CuNWs, at several frequencies. Lines are guides to the eye. 177

Figure 4.25. Storage modulus (G') as a function of the loss modulus (G") of solution-processed $C_8H_{17}S$-CuNW/PS nanocomposites. (a) Low concentrations of $C_8H_{17}S$-CuNWs (0.1 - 0.5 vol. %) and (b) high concentrations of $C_8H_{17}S$-CuNWs (1.0 - 4.0 vol. %). Lines are guides to the eye. 180

Figure 4.26. Phase angle as a function of the absolute value of the complex modulus (van Gurp-Palmen Plot) of solution-processed $C_8H_{17}S$-CuNW/PS nanocomposites. Lines are guides to the eye. 181

Figure 4.27. Storage modulus (G') of $C_8H_{17}S$-CuNW/PS nanocomposites over G' of pure PS at 0.1 rad/s as a function of the $C_8H_{17}S$-CuNW concentration up to 2.0 vol. %. The change in $G'_{C8H17\text{-}SCuNW/PS}/G'_{PS}$ observed for concentrations of 1.0 – 2.0 vol. % Cu indicates formation of a polymer-nanowire network. The data of CuNW/PS is included for comparison purposes. Lines are guides to the eye. 181

Figure 4.28. Rheological characterization of solution-processed AgNW/PS nanocomposites at 200 °C. Complex viscosity ($|\eta^*|$), storage modulus (G'), and loss modulus (G") as a function of: (a,c,e) frequency and (b,d,f) concentration of AgNW, at several frequencies. Lines are guides to the eye. 184

Figure 4.29 .Phase angle as a function of the absolute value of the complex modulus (van Gurp-Palmen Plot) of solution-processed AgNW/PS nanocomposites. Lines are guides to the eye. 185

Figure 4.30. Storage modulus (G') as a function of the loss modulus (G") of solution-processed AgNW/PS nanocomposites. (a) Low concentrations of AgNWs (0.25-0.75 vol. %) and (b) high concentrations of AgNWs (1.0-4.0 vol. %). The change in G' vs G" curve between 1.0 and 2.0 vol. % indicates the formation of a polymer-nanowire network. Lines are guides to the eye. 186

Figure 4.31. Storage modulus (G') of AgNW/PS nanocomposites over G' of pure PS at 0.1 rad/s as a function of the AgNW concentration up to 2.0 vol. %. The change in $G'_{AgNW/PS}/G'_{PS}$ observed for concentrations of 1.0 – 2.0 vol. % AgNW indicates the formation of a polymer-nanowire network. The data of CuNW/PS is included for comparison purposes. Lines are guides to the eye. 186

Figure 4.32. Schematic representation of the microstructure of metal nanowire/polymer nanocomposites containing individual and agglomerate nanowires. (a) At the electrical percolation threshold, electrically conductive networks of nanowires are established, but polymer chains between agglomerates dominate the rheological behavior. (b) At the rheological percolation threshold, the mechanical behavior of the polymer chains is restricted by the nanowires. 190

Figure 5.1. Photograph of the Alberta Polymer Asymmetric Minimixer (APAM).[13] 205

Figure 5.2. Backscattered electron SEM images of polystyrene nanocomposites containing 4 vol. % CuNW. Bright domains correspond to copper nanowires dispersed in the polymer matrix. PS nanocomposites containing (a,b) unfunctionalized nanowires, (c,d) $C_8H_{17}S$-CuNW, and (e,f) C_4H_9S-CuNW. The images show the enhancement of dispersion of copper nanowires using surface modification with $C_8H_{17}SH$ and C_4H_9SH. 208

Figure 5.3. Complex viscosity ($|\eta^*|$), storage modulus (G') and loss modulus (G") of CuNW/polystyrene nanocomposites prepared by melt mixing in an APAM as a function of (a, c, e) frequency and (b, d, f) concentration of unfunctionalized Cu nanowires. Lines are guides to the eye. 210

Figure 5.4. Complex viscosity ($|\eta^*|$), storage modulus (*G'*) and loss modulus of $C_8H_{17}S$-CuNW/polystyrene nanocomposites prepared by melt mixing in an APAM as a function of (a, c, e) frequency and (b, d, f) concentration of copper nanowires. Lines are guides to the eye. 212

Figure 5.5. Complex viscosity ($|\eta^*|$), storage modulus (*G'*) and loss modulus of C_4H_9S-CuNW/polystyrene nanocomposites prepared by melt mixing in an APAM as a function of (a,c,e) frequency and (b,d,f) concentration of copper nanowires. Lines are guides to the eye. 216

Figure 5.6. Storage modulus (*G'*) versus loss modulus (*G"*) and phase angle versus complex modulus for PS nanocomposites prepared by melt mixing in an APAM (a, b) using unfunctionalized CuNW, (c, d) $C_8H_{17}S$-CuNW, and (e, f) C_4H_9S-CuNW. Lines are guides to the eye. 219

Figure 5.7. Volume electrical resistivity of polystyrene nanocomposites prepared by melt mixing using different concentrations of (a) unfunctionalized copper nanowires and copper nanowires functionalized with (b) C_4H_9SH, and (c) $C_8H_{17}SH$. Lines are guides to the eye.

List of Abbreviations and Symbols

Abbreviations

AC	Alternate current
AFM	Atomic force microscopy
BE	Binding energy, eV
CP	Cross polarization
DC	Direct current
DSC	Differential scanning calorimetry
ESD	Electrostatic dissipation
EMI	Electromagnetic interference
fcc	Faced-centered cubic lattice
HRTEM	High resolution transmission electron microscopy
MAS	Magic angle spinning
MI	Melt index
MIM	Metal-insulator-metal junction
MWNT	Multi-walled carbon nanotube
NMR	Nuclear magnetic resonance
NW	Nanowire
o.d.	Outer diameter
i.d.	Inner diameter
PAO	Porous aluminum oxide
PS	Polystyrene

SAM	Self-assembled monolayer
SAED	Selected-area electron diffraction
SEM	Scanning electron microscopy
SERS	Surface enhanced Raman spectroscopy
STM	Scanning tunneling microscopy
SWNT	Single-walled carbon nanotube
TEM	Transmission electron microscopy
TGA	Thermogravimetric analysis
XPS	X-ray photoelectron spectroscopy
XRD	X-ray diffraction

Symbols

G^*	Complex dynamic modulus, Pa
G'	Storage modulus, Pa
G''	Loss modulus, Pa
I_{rms}	Root mean square current
M_w	Average molecular weight, g/mol
R_v	Volume resistance, Ω
t	Average thickness of specimens
t	Critical exponent of percolation theory
t_{bl}	Barrier layer thickness, nm
T_g	Glass transition temperature, °C

V_a	Anodization voltage
V_{DC}	Direct current voltage
V_c	Percolation threshold, vol. %
V_f	Volume fraction of filler
V_p	Peak voltage
V_{rms}	Root mean square voltage

Greek letters

δ	Phase angle, °
η^*	Complex viscosity, Pa·s
η'	Dynamic viscosity, Pa·s
η''	Out-of-phase viscosity, Pa·s
γ^*	Complex strain
ρ_v	Volume electrical resistivity, Ω·cm
σ_c	Volume electrical conductivity, S·cm^{-1}
τ^*	Complex stress, Pa
ω	Angular frequency, s^{-1}

Chapter 1

Introduction

In this dissertation, the synthesis of metal nanowires by AC electrodeposition in porous alumina templates, and the study of the electrical and rheological properties of metal nanowire/polymer nanocomposites are presented. This chapter provides an overview to the diverse background related to the development of this work; specifically, the synthesis and applications of metal nanowires, porous alumina templates, and metal/polymer nanocomposites. The motivation for this work and the organization of the thesis are presented at the end of the chapter.

1.1 Synthesis and applications of metal nanowires

Since the development of microscopy techniques such as electron microscopy (SEM and TEM), and, more recently, atomic force microscopy (AFM), and scanning tunneling microscopy (STM), the knowledge of the morphology, structure, and properties of nanostructures or nanostructure-based systems has evolved steadily. New and controllable properties of matter with at least one dimension in the 1-100 nm regime, as well as more efficient processes and materials with outstanding properties provided by the nanostructures are expected to revolutionize sectors such as electronics, biotechnology, chemicals, medicine and therapy, energy, and polymer science. This section presents an overview of the synthesis of 1D metal nanostructures, with emphasis on Cu and Ag nanowires.

The synthesis and characterization of nanowires, nanorods, nanobelts, and nanotubes have been reported over the last three decades. Xia et al. provided an extensive review of the synthesis, characterization, and applications of 1D-nanostructures.[1] Figure 1.1 shows schematic illustrations of the different strategies that have been developed for the growth of these nanostructures.[1] These methods can be divided into three categories: (1) anisotropic growth dictated by the crystallographic structure of material, (2) template-directed synthesis, and (3) kinetically-controlled growth mechanism by supersaturation or use of capping reagents.

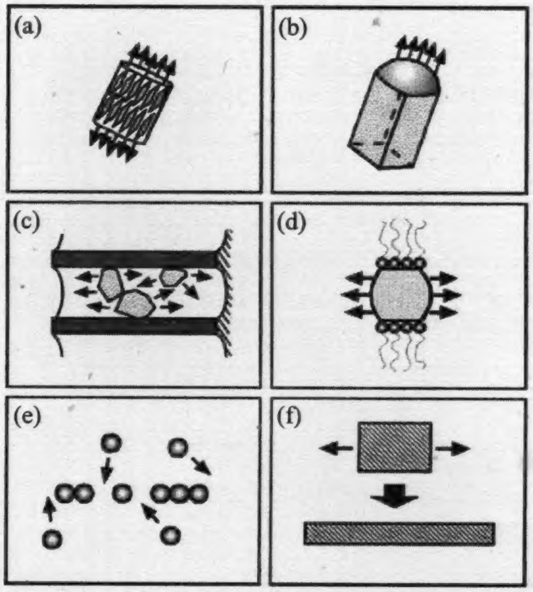

Figure 1.1. Different approaches utilized for the growth of 1D nanostructures reproduced from Xia et al.[1] (a) Anisotropic growth, (b) confinement by a liquid droplet (c) template-directed synthesis (d) surfactant-assisted kinetic control (e) self-assembly of 0D nanostructures, and (f) size reduction of a 1D microstructure. Reproduced with permission from *Adv. Mater.* 2003, 15, 5, 353-389, Copyright 2003, Wiley-VCH.

In particular, syntheses of metal 1D-nanostructures have been developed using two approaches: hard-template assisted synthesis, and soft-template assisted synthesis (and its variations).[2,3] In the hard-template method, the growth of the metal nanostructure is confined between the walls of pores with diameters in the nano-regime (Figure 1.1c). In the soft-template method, the growth of the metal nanostructure may occur through chemical reduction from solution, usually in the presence of surfactants or other substances that either inhibit the growth of certain crystalline facets or alter transport of metal and reagents to certain crystalline facets, favoring the preferential growth in one direction (Figure 1.1d).

1.1.1 Hard-template assisted synthesis of metal nanowires

Template-directed syntheses in the pores of porous aluminum oxide (PAO) or track-etched polymer membranes have been widely used to produce uniformly sized 1D-nanostructures of many materials and composite structures. The first work in this area was reported by Possin in 1970.[4] Nanowires of Sn, In, and Zn, 40 - 70 nm in diameter and up to 15 μm in length, were produced by DC electrodeposition into pores of mica membranes that were previously coated on one side with a metallic contact. The membranes were produced by acid etching of tracks produced in mica by highly charged nuclear particles using the method reported by Price and Walker in 1962 at General Electric.[5,6] Other pioneering efforts in this area were developed by the groups of Giordano and Martin since 1984. Giordano and co-workers refined the method of Possin to synthesize Au wires as small as 8 nm in diameter using track-etched mica membranes.[7] Martin and co-workers reported the use of track-etched polymeric membranes first,[8] and later the use of porous aluminum oxide templates for the synthesis of different kinds of 1D nanostructures such as conductive polymers, metals and semiconductors.[9] Moskovits and collaborators contributed to these developments with works that were initially related to the coloration of Al,[10] and later evolved to the synthesis of metal nanostructures by AC electrodeposition in PAO templates.[11]

The DC and AC electrodeposition of metals into PAO templates have been investigated for decades. Liberation of the metal nanoparticles by dissolution of the alumina has been used to produce small quantities ($\leq$1 mg) of metal nanoparticles or metal nanowires whose fundamental properties and applications have been investigated, notably by Gösele, Mallouk, Martin, Masuda, and Moskovits.

1.1.1.1 DC electrodeposition

The well-developed approach of DC electrodeposition of metals in polymer or PAO template membranes affords control over the crystallinity of nanowires[12-16] and enables precise modulation of the composition along the length of the nanowire.[17-23] Several steps are required to enable DC electrodeposition in polymer or alumina membranes. First, one side of the membrane is coated with an electrical contact by evaporation of a metal, usually Au or Ag (Ag is preferable), then a metal contact is electrodeposited to facilitate contact to and manipulation of the electrode, and finally, the electrode is immersed in an electrolyte and DC electrodeposition is applied. The liberation of the nanostructures require the dissolution of Ag and alumina in solutions of HNO_3(aq) and NaOH(aq), respectively, and subsequent rinsing and purification.[9,24]

Several of the studies of DC electrodeposition have been developed using alumina membranes that are commercially available for filtration applications.[13-15] The membranes contain poorly ordered pores and the pore diameters vary as a consequence of the low ordering; therefore, a wide distribution of nanowire diameters can be obtained. The use of self-ordered PAO templates for DC electrodeposition is enables production of monodisperse nanostructures. However, DC electrodeposition in PAO templates attached to the Al substrate is prevented by the capacitance of the so-called alumina barrier layer that separates the Al and the bottom of the pores (the structure and growth of the PAO templates are presented in section 1.2). High voltages are required for tunneling of the electrons through the barrier layer and uniform deposition cannot be obtained.[25] Thus, if nanowires are to be synthesized by DC electrodeposition into ordered PAO templates instead of using the commercially available membranes, two additional steps are required. The membrane must be removed from the Al substrate by dissolution in $HgCl_2$(aq) or CuCl(aq) solutions and the pores opened by removal of the barrier layer by etching in H_3PO_4(aq).[26,27] Subsequently, the electrically conductive contact of Au or Ag must be sputtered and/or electrodeposited on one side of the membrane to enable DC electrodeposition. A schematic representation of the steps involved in the synthesis of nanowires by DC electrodeposition into PAO templates is presented in Figure 1.2.

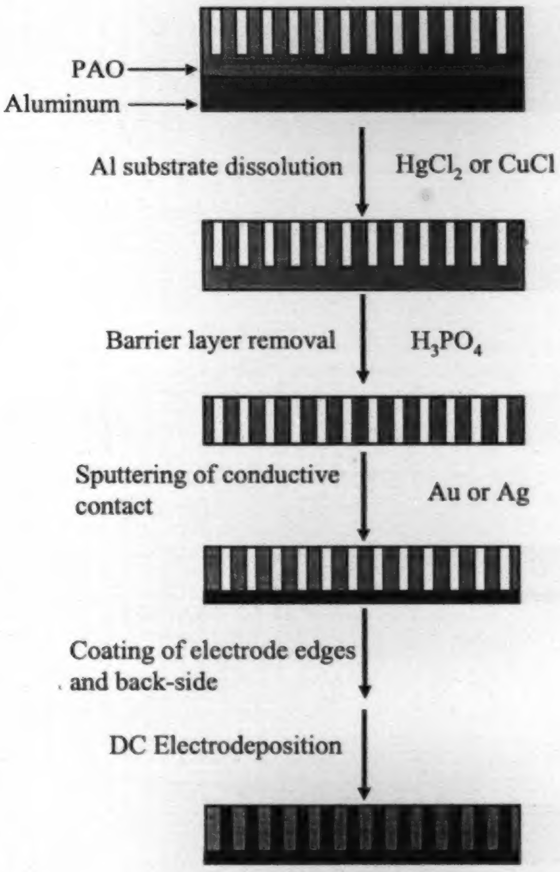

Figure 1.2. Schematic representation of the synthesis of nanowires in PAO templates using DC electrodeposition.

Other strategies have been tested to enable DC electrodeposition into PAO templates. For example, Gösele and co-workers reported the synthesis of Ag nanowires in 30 μm deep templates by DC electrodeposition after thinning of the barrier layer to ~ 1 nm by slowly reducing the anodization voltage to 1 V.[28] However, the barrier layer thinning is time-consuming and uniform barrier layers over large Al areas might be difficult to obtain. For instance, when the barrier layer is too thin, large portions of the alumina membrane can peel off of the Al after applying the voltage for DC electrodeposition of the nanostructures.[29] In another approach to enable DC electrodeposition, Stacy and collaborators produced Ag/Al electrodes by mechanical polishing of Al foils, chemical treatment of the thermal oxide, and sputtering of Ag in one side of the foil to enable electrical contact.[30] The uncoated side of the Al electrode is then mechanically polished and anodized to produce the PAO template. The barrier layer is removed by soaking the electrode for 1 to 2 hours in 1M HNO_3 facilitating contact to the Ag and enabling DC electrodeposition.[30] In this approach, several steps are required for the preparation of adequate electrodes. In addition, uniform anodization of the Al foil until it reaches the Ag contact may be difficult to attain in electrodes with areas on the order of several m^2. In summary, the multiple processing steps required to produce the rather fragile free-standing PAO membranes and then to prepare electrodes suitable for DC electrodeposition may prevent this method from being used to produce metal nanowires in sufficient quantity for many potential applications.

1.1.1.2 AC electrodeposition

Although the high resistance of the barrier layer at the bottom of the pores of PAO templates attached to the Al substrate prevents DC electrodeposition, the rectification properties of the barrier layer enable the electrodeposition of nanostructures using AC signals (voltage or current).[25,29,31-40] This is because Al is a valve metal and its oxide conducts current preferentially in the cathodic direction. This characteristic of the barrier layer enables the reduction of the metals at the bottom of the pores of the PAO/Al electrode when it is biased as the cathode during the negative pulse of the AC signal, without allowing the oxidation (i.e. redissolution) of the metal when it is biased as the anode during the positive pulse of the AC signal. The thickness of the barrier layer in PAO templates is dependent on the anodization voltage at which Al is anodized, V_a ($t_{bl} = 1.2$ nm/V × V_a),[41] and high AC voltages might be required for tunneling of the electrons through the thick barrier layer under AC electrodeposition conditions. This is particularly important for PAO templates produced by anodization of Al in oxalic and phosphoric acid solutions (e.g. anodizations typically require 40 V_{DC} or 195 V_{DC}, respectively).[42] However, the voltage dependence of the barrier layer thickness facilitates the thinning of the barrier layer to thicknesses that are suitable for AC electrodeposition, by turning down the voltage at the end of the anodization. As mentioned previously, prolonged thinning of the barrier layer may cause the PAO to peel off of the Al substrate. Typically, the final voltage after barrier layer thinning is turned down to 6 V_{DC} to prevent damage of the templates during the electrodeposition.[29] Figure 1.3 shows a schematic representation of the steps involved in the preparation of the PAO templates for AC electrodeposition. The use of AC electrodeposition enables use of both faces of the Al electrodes for electrodeposition and more efficient use of the Al. In addition, the mechanical strength of thick Al plates facilitates handling of large area electrodes between the different baths required for anodization, electrodeposition and liberation of the nanostructures. The preparation of PAO templates for AC electrodeposition is simpler and less infrastructure intensive than that required for DC electrodeposition.

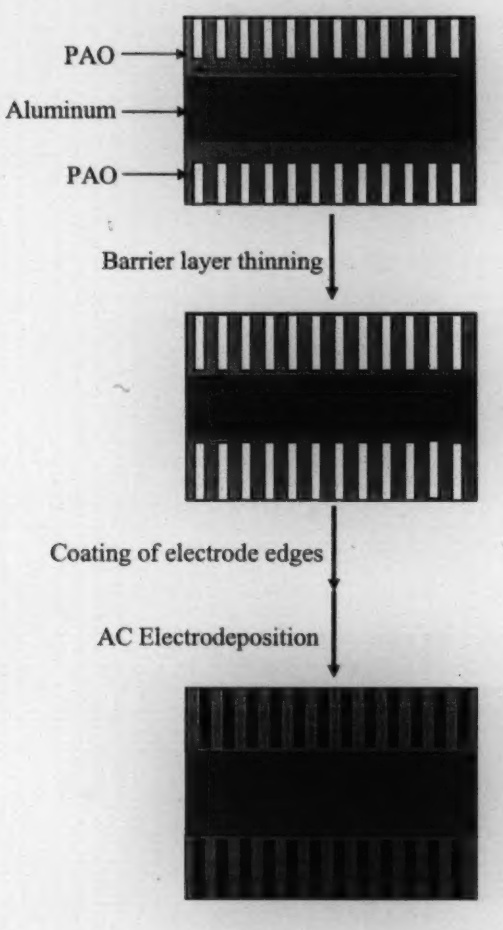

Figure 1.3. Schematic representation of the synthesis of nanowires in PAO templates using AC electrodeposition.

The less developed approach of AC electrodeposition into PAO templates through the resistive, rectifying barrier layer, without separation from the Al substrate affords good quality filling of the pores with single metals, if optimized electrodeposition conditions are used. [25,29,31-40]Typical variables that influence the efficiency of AC electrodeposition are: voltage, frequency, AC waveform, composition of the electrolyte (solvent, concentrations, pH), and temperature.[25,29,31-40] Different AC waves (voltage or current controlled), more particularly sinusoidal and square waves in continuous or pulsed forms have demonstrated efficient pore filling.[25,28,29] High uniformity of deposition has been demonstrated by using current-controlled deposition sequences.[25,29] For instance, Gösele and collaborators proposed the concept of pulsed electrodeposition as a means of compensation for the slow thermal diffusion of the ions in the pores of PAO templates and minimization of hydrogen evolution. The electrochemical evolution of hydrogen gas may become dominant when the concentration of ions at the bottom of the pores is significantly reduced by every cathodic pulse of the AC wave. In pulsed AC electrodeposition, an appropriate delay time between pulses is introduced in order to maintain high concentrations of ions at the bottom of the pores during the electrodeposition, leading to uniform nanowire growth.[25]

It is technically feasible to produce kg quantities of metal nanowires using the AC electrodeposition process, as the anodization and electrodeposition processes are fundamentally similar to the Anolok® process (a trademark of Alcan International Ltd.) that is used to anodize and then colorize, by metal deposition, large Al pieces (7 m × 1.8 m) for architectural applications (http://www.hmfltd.co.uk). However, large scale production of nanowires using template-directed synthesis has not been demonstrated, until the development of the present work.

Copper nanowires (CuNWs) and silver nanowires (AgNWs) have been synthesized in hard templates such as track etched polycarbonate (PC) or porous aluminum oxide (PAO) using electroless deposition,[43] DC electrodeposition,[14,44-47] and AC electrodeposition.[28,29] Poly- or single crystalline nanowires result from tuning of the electrodeposition potential.[3] However, single crystal Cu and Ag nanowires can be grown only when the pore diameter of the templates is less than 70 nm.[3] TEM characterization of nanowires showed that single crystal CuNWs and AgNWs grow epitaxially, preferentially along the [111] direction by a 2D nucleation growth mechanism.[14] In regard to aspect ratios, nanowires embedded in track etched PC and PAO have been produced with diameters from 40 to 500 nm, with aspect ratios of up to 500, which are determined by the dimensions of the template.[28,46] However, it is expected that during the release process from the templates, the aspect ratio of the nanowires may be reduced.

It is worth noting that one of the main advantages of template-directed synthesis over other methods developed, including soft templates, is the possibility of growing heterostructure nanowires. Two strategies can be used to produce heterostructures using templates: alternately placing the electrode in different electrolytes, and the use of different potentials for the preferential deposition of different metals using a single electrolyte. These approaches have been demonstrated for Au-Sn-Au nanowires and Au-Pd nanorods by Mallouk and co-workers.[3,23,24]

1.1.2 Soft-template assisted synthesis of metal nanowires

An overview of methods developed for the synthesis of copper and silver nanowires using the soft-template method or variations of this method is presented below.

CuNWs have been produced by direct reduction of copper ions from aqueous solutions.[48,49] Recently, single crystalline CuNWs several tens of micrometers in length and 90 - 120 nm in diameter were obtained by reduction of Cu^{2+}(aq) ions in a basic solution containing hydrazine (N_2H_4) and ethylenediamine (EDA, $C_2H_8N_2$).[48] CuNWs of similar dimensions were obtained by reduction of the complex Cu^{II}-glycerol ($Cu(C_3H_6O_3)$) in a basic solution, with the assistance of surfactant sodium dodecyl benzenesulfonate (SDBS). However, the mechanisms of CuNW growth, and the role of EDA and SDBS are still unclear, but it is believed that they direct the nanowire growth by preferential adsorption on certain crystallographic facets, and by preventing agglomeration of the nanoparticles during the initial stages of nanowire formation. It is worth noting that the presence of a 1-2 nm copper oxide layer was evident from HRTEM analysis of individual nanowires produced by this route.[49]

AgNWs have been produced from different methods of synthesis in solution; for example, reduction of $AgNO_3$ in ethylene glycol solutions containing poly(vinyl pyrrolidone),[50-54] synthesis in aqueous solutions in the presence or absence of seeds and surfactants,[55-58] hydrothermal synthesis using glucose as the reducing agent,[59] and microwave assisted synthesis.[60] The nanowires usually have to be separated from nanoparticles that remain after reaction. In regard to AgNW monodispersity and aspect ratios, AgNWs produced by the polyol process were 30 - 40 nm in diameter and 1 - 50 μm in length (25 - 1666 aspect ratios).[53,54] Recently, Murphy and collaborators have obtained Ag nanowires 35 nm in diameter and up to 12 μm in length.[2] In addition, AgNWs produced from solution methods were reported as single and twinned crystals. Progress in elucidating the growth mechanisms of silver nanowires and nanorods has recently been made.[54] For instance, the growth of AgNWs by the polyol process occurs through an initial step of homogeneous (i.e. from solution) and heterogeneous (i.e. onto Pt or Ag seeds) reduction of Ag, producing a bimodal distribution of nanoparticles, and a second step in which the larger particles grow at the expense of the smaller ones through the Ostwald ripening process. However, greater understanding is still required to rationally design syntheses of other nanostructures through templateless and seedless solution growth processes.

1.1.3 Other syntheses of metal nanowires

Other alternatives have been developed for the synthesis of metal nanowires, including vacuum deposition,[50] chemical vapor deposition,[61] and vapor-solid reaction growth.[62] Although important for fundamental studies, these alternatives do not seem to be promising for large-scale production of metal nanowires compared to the less expensive and less infrastructure intensive template-directed syntheses using hard or soft templates.

1.1.4 Surface functionalization of metal nanowires

To fully exploit the properties of nanostructures in different applications, control of their surface chemistry is required. Therefore, studies related to applications of nanoparticles are usually accompanied by surface modification steps that enable enhanced interaction of their surfaces with their environment or vice versa (i.e. a decrease or increase in the interfacial tension). The spontaneous chemisorption of organic molecules by specific interaction of a functional group (i.e. head group) with surficial atoms on metal, metal oxide, and semiconductor surfaces results in the formation of self-assembled monolayers (SAMs).[63,64] SAMs facilitate tailoring the interaction of surfaces with their environment, enabling control of wetting, reactivity, aggregation, and dispersion. The current development and understanding of SAMs on 2D-surfaces may be applied to the surface modification of metal nanowires. In the particular case of metal and metal oxides, there is a plethora of studies related to the chemical modification of their surfaces by SAMs of different chemical entities such as thiols, disulfides, dialkyl disulfides, carboxylic acids, nitriles, and ammines (see review by Love et al.).[64] However, SAMs of alkanethiols have been more widely studied given the high affinity of the S atoms for metals such as Au, Ag, and Cu.[65]

The pioneering work of Allara and Nuzzo on chemisorption of bifunctional organic disulfides on gold gave rise to a worldwide interest on the self-assembly of organic compounds containing sulfur in the headgroup.[63] The self-assembly of alkanethiols and their derivatives on metal surfaces was reviewed by Whitesides and co-workers.[64] It is clear that although alkanethiol SAMs have been studied for more than two decades, challenges still remain to fully understand the thermodynamic and kinetic aspects of their formation, as well as for the development of new applications.

The structure and rate of formation of thiolate SAMs are mainly affected by the following: solvent, temperature, concentration of adsorbate, immersion time, purity of the adsorbate, presence of oxygen at the surface or in solution, cleanliness of the substrate, and structure of the adsorbate.[64] For fundamental studies, the reproducibility of the SAM structure is very important and the parameters for its formation must be carefully considered. Due to its strong resistance to oxidation, Au has been the preferred substrate for the study of the self-assembly of alkanethiols; fewer efforts have been devoted to self-assembly on Ag and Cu surfaces. The next sections present an overview to the studies of self-assembly of alkanethiols on these metals.

1.1.4.1 The structure of SAMs of alkanethiols on Cu and Ag

The structures of self-assembled monolayers of alkanethiols on Cu and Ag were studied by Laibinis et al.[66] The self-assembly of alkanethiol monolayers on Cu is more complex and sensitive to sample preparation than on Au or Ag; however, alkanethiols may form densely packed SAMs on Cu if careful experimental conditions are utilized.[66,67] The structures of SAMs of alkanethiols on Ag and Cu differ from those that form on Au. Figure 1.4 shows an illustration of the structures of alkanethiols chemisorbed on 2D-surfaces of Ag and Cu that result when high quality SAMs on Cu and Ag are obtained.[66] The alkyl chains adopt a semicrystalline structure in which the chains are fully extended in the trans conformation. The tilt angle (α, relative to the plane perpendicular to the surface) of the chains is ~ 12 °, and the twist angle (β) that describes the chain/plane rotation is 45 °, which compares with $\alpha = 28$ ° and $\beta = 53$ °, for alkanethiol chains on Au (111) surfaces. Another significant difference from SAMs on Au is that α is positive for an even number of methylene groups and is negative for an odd number of methylene groups of the alkanethiol adsorbed on Cu or Ag.

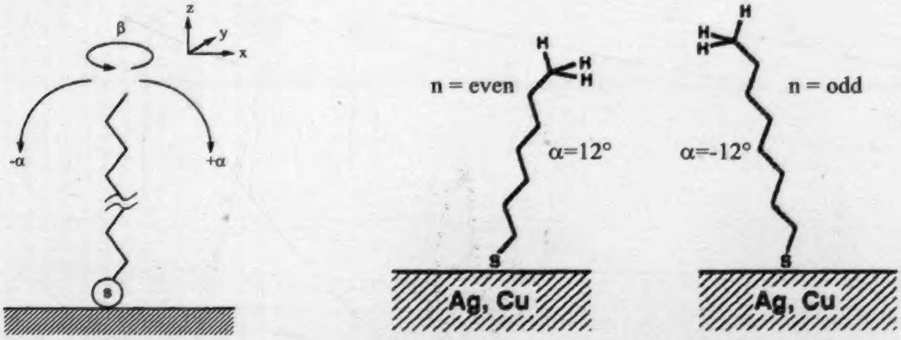

(a) (b)

Figure 1.4. (a) Illustration of a fully extended structure of a chemisorbed alkanethiol and the coordinates typically used to define the orientations of the chain. (b) Illustration of the surface structures formed by chemisorption of alkanethiols on Ag and Cu surfaces. Reprinted with permission from *J. Am. Chem. Soc.*, 1991, 113, 19, 7152-7167. Copyright 1991, American Chemical Society.

1.1.4.2 The effect of surface oxidation on self-assembly of alkanethiols

Unlike Au surfaces, copper oxides are usually present on the surface of the Cu substrates, affecting the self-assembly and structure of the thiol monolayers. Rubinstein and co-workers demonstrated that high quality $C_{18}H_{37}SH$-SAMs on copper can be fabricated on sputter deposited and annealed Cu surfaces.[68,69] The surface roughness, the presence of oxides, and the solvent (ethanol or toluene) significantly affected the quality of the SAMs formed on copper. These studies indicate that the presence of oxides is detrimental to the formation of high quality SAMs on copper.

Keller et al. discussed the formation of self-assembled multilayers that resulted from the reaction of oxidized copper surfaces with alkanethiols, and promoted the build-up of self-assembled copper thiolate complexes (CuSR), which crystallize at the surface.[70] Their results agree with previous experimental observations that indicated poor reproducibility of SAMs on copper due to surface oxidation.[66] Indeed, it is recognized that the structures of thiolates on copper remain incompletely elucidated.[64] Studies of self-assembly of alkanethiols on pre-oxidized Au surfaces have also demonstrated the effect of oxygen on the quality of the monolayers and the possibility of formation of multilayers.[69,71,72] Unfortunately, to date these types of structures are not completely understood, but their formation may be of more importance to the surface functionalization of 1D metal nanostructures, which are more likely to suffer surface oxidation.

1.1.5 Applications and challenges of metal nanowires

1D metal nanostructures display a plethora of electrical, optical, chemical, and magnetic properties with diverse applications.[17-20,23,73-77] The phenomenon of electromagnetic field enhancement at the tip of metal nanowires suggest their application for chemical sensing as in Surface Enhanced Raman Spectroscopy (SERS).[78] For instance, rod-gap-rod nanostructures provided strong electric fields to molecules localized in the gap, facilitating their detection by SERS. The response of the resistivity of Au, Ag, and Pt nanowires to chemical species was used for the development of sensors for ammonia,[79] amines,[80] and hydrogen,[81] respectively. Metal nanowires are being considered for plasmonics applications.[82] Some other potential applications of metal nanowires are in catalysis and surface enhanced fluorescence; however, literature related to these applications is scarce. Biological applications of metal nanowires have also been considered. For instance, gene delivery was demonstrated with Ni-Au nanorods 100 nm in diameter that were internalized into cells to deliver the gene directly to their nucleus.[76] In other studies, the strong absorption of near-infrared radiation by Au nanorods caused a local increase in temperature, which was utilized to killed cancer cells in cell cultures.[83] It is believed that high aspect ratio metal nanowires may be used to form electrically conductive networks at low concentrations in polymeric nanocomposites, which can be utilized in electrostatic dissipation, electromagnetic shielding, and electromagnetic interference applications.[84,85]

Although numerous efforts have been devoted to the synthesis and characterization of nanowires, it is rare to find yields of metal nanowires in the literature. This might be due to the general interest in discovering new strategies for their synthesis and developing fundamental studies related to the properties of these nanostructures, but it may also be due to the small amounts and perhaps low yields that have been obtained to date. Thus, one of the challenges is the synthesis of 1D nanostructures is to demonstrate the scalability of the synthetic methods, opening the door to the development of new studies that require grams or even kilograms of material to be realized. Studies oriented in this direction will be well received by the scientific and industrial communities in the coming years. This dissertation is a contribution to that challenge.

Some other challenges for future applications of 1D nanostructures are the control of their chemical, thermal, and mechanical stability.[1] For instance, Rayleigh instability (fragmentation) of CuNWs has been reported at lower temperatures than the melting temperature of copper.[86] Another challenge is their self-assembly into complex structures or devices that may find application in photonics. Similarly, the impact of nanostructures on environment and health deserves further scrutiny and research.

1.2 Porous aluminum oxide (PAO) templates

Porous aluminum oxide templates have been studied for decades.[41,87] Initially, work using disordered porous alumina was motivated by its importance for strengthening and protection of Al surfaces against corrosion and for decoration of Al surfaces. More recently, there has been growing interest in porous alumina, primarily due to the development of membranes for filtration, sensing, magnetic, electronic, and optoelectronic devices, and the synthesis of 1D nanostructures that can either be left embedded in the template or released from the template for subsequent use.[26] This section presents an overview of the structure and recent developments in the understanding and preparation of self-ordered porous aluminum oxide templates.

1.2.1 Structure of PAO templates

The structure of an ideal ordered porous aluminum oxide template is presented in Figure 1.5. The anodization of aluminum in acidic solutions under specific conditions results in a close-packed array of hexagonal cells containing nanopores parallel to each other and oriented perpendicularly to the Al surface. An alumina barrier layer of a certain thickness is located adjacent to the Al surface. The cell interspacing, pore diameters, and the barrier layer thickness are all proportional to the anodization voltage.[41] The diameters of the PAO pores are tunable from 4 to 400 nm depending on the anodization conditions, electrolyte, and post-growth etching. The depth of the pores is dependent on the anodization time, and PAO with pore depths as small as hundreds of nanometers and as great as hundred of micrometers may be prepared.

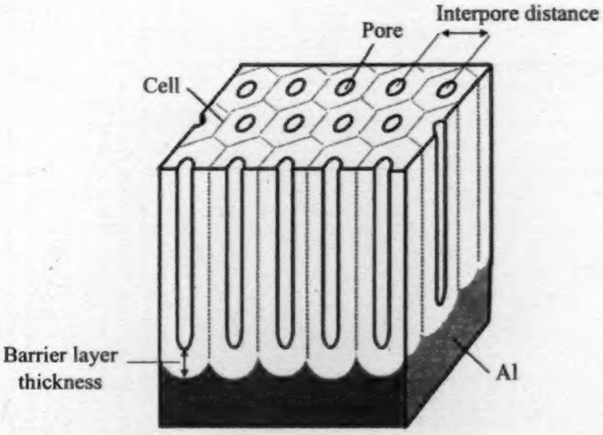

Figure 1.5. Structure of an ideal nanostructure of porous alumina template. Reproduced with permission from *J. Electrochem. Soc.* 2001, 148, 4, B152-B156. Copyright 2001, The Electrochemical Society.

The hexagonally ordered array of nanopores was first reported by Masuda.[89-91] In a study of anodization of Al in oxalic acid solutions, Masuda et al. found that self-ordering of the pores could be accomplished under specific conditions using long anodization times (i.e. 40 V_{DC}, 160 h, 0 °C). The technique was then extended to anodization in sulfuric acid solutions, for which the nanostructure ordering required a lower voltage (25 V) than in oxalic acid solution.[90] A two-step anodization process was suggested by Masuda and collaborators, indicating that selective removal of porous alumina formed after one step anodization provided a structured Al surface that favored the formation of ordered pores during a second anodization step.[92] Some additional studies of this aspect were later developed by Gösele and collaborators.[93,94] Depending on the anodization conditions, the pore density can range from 6×10^8 to 5×10^{10} pores cm^{-2}. Figure 1.6 shows a SEM image of a self-ordered PAO template grown in sulfuric acid solution.

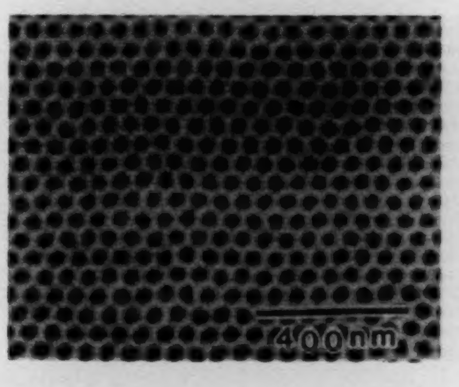

Figure 1.6. SEM image of a PAO surface obtained in sulfuric acid solution at 25 V, 12.5 h, and 10 °C. Reproduced with permission from *J. Electrochem. Soc.* 1997, 144, 5, L127-L130. Copyright 1997, The Electrochemical Society.

1.2.2 Mechanism of pore growth and self-ordering of PAO templates

Several models have been developed to explain the mechanism of growth and formation of porous alumina templates.[41,87,95,96] The most widely accepted model is that of O'Sullivan, in which the growth of the pores is determined by the equilibria of (1) oxide growth at the Al oxide/Al interface, and (2) the electrical field-enhanced oxide dissolution at the oxide/electrolyte interface.[41] This implies the diffusion of O^{2-} ions to the metal surface for the oxidation of Al, as well as the diffusion of Al^{3+} ions through the barrier layer to the oxide/electrolyte interface and diffusion into the acidic solution. The electric field assisted dissolution proceeds at a much faster rate than the chemical dissolution of the oxide at the surface leading to the growth of the pores. In addition, Joule heating of the solution at the bottom of the pores may also increase the dissolution rate of the oxide at the bottom of the pores relative to the dissolution of the film surface as a whole.

The model described by O'Sullivan[41] does not explain the self-organization of pores attained using specific anodization conditions, as reported by Masuda. A contribution of Gösele and co-workers proposed that the mechanical stress, associated with a moderate volume expansion upon conversion of Al into Al_2O_3, causes repulsive forces between neighboring pores, which leads to self-ordering of the pores in hexagonal arrays. Given that pore growth rates change for different acidic solutions, a moderate volume expansion requires specific voltages for different electrolytes.[93] In a subsequent work, it was demonstrated that self-ordering of PAO templates requires a porosity of 10 %, which corresponds to a volume expansion ($V_{Al\ oxide} / V_{Al}$) of 1.2.[42] Table 1.1 presents typical dimensions of pores and the porosity of the templates when self-ordering of porous alumina is attained.

Table 1.1. Typical dimensions of pores under conditions yielding self-ordered PAO templates.[42]

Electrolyte	Pore diameter (nm)	Inner wall thickness (nm)	Interpore distance (nm)	Porosity (%)
H_2SO_4, 25 V, 0.3 M	24	7.2	66.3	12
$(COOH)_2$, 40 V, 0.3 M	31	9.1	105	8
H_3PO_4,195 V, 0.1 M	158.4	54	501	9

1.3 Metal/Polymer nanocomposites

The synthesis and characterization of polymer nanocomposites has recently received significant attention due to the new and improved properties of these materials in a wide range of potential applications (i.e. aerospace, catalysis, sensors, and optical devices),[97-99] produced by the synergy between macromolecules and inorganic particles with at least one dimension in the nanometer regime.

Intense effort has been devoted to the study of physical blending of polymers and nanofillers such as layered inorganic clays,[100-102] carbon black,[103] vapour grown carbon fibers (VGCF),[104,105] and fullerene nanotubes.[106-111] In particular, significant effort has been devoted to the study of electrical and mechanical properties of polymer-matrix composites containing low volume fractions (0.1 - 5 vol. %) of multi- and single-walled fullerene nanotubes (MWNT and SWNT, respectively). This is due to the ability of high aspect-ratio conductive fillers to produce a percolated, conducting network at much lower volume fractions than spherical carbon black or metal nanoparticles, which enables the production of highly conductive or electrostatically dissipative composites without reduction of polymer processibility or degradation of polymer properties.

Polymer nanocomposites containing high aspect-ratio conductive metal nanoparticles may be considered alternatives to carbon nanotube composites for use in electrostatic dissipation (ESD), electromagnetic interference (EMI), electromagnetic shielding, and other electronic applications, such as heat sinks requiring the good thermal conductivity of metals.[112,113] For example, a few studies have been dedicated to the preparation and characterization of the properties of epoxy filled with spherical silver nanoparticles for applications such as embedded capacitors,[114-116] and electromagnetic shielding.[117] Promising results have been demonstrated. Nonetheless, polymer nanocomposites containing metal nanowires have not been studied, likely due to the unavailability of these nanoparticles in gram quantities.

1.3.1 Rheology of polymer nanocomposites

The knowledge of the viscoelastic properties of polymers are important to determine their behavior under conditions of stress that are typically used by the polymer industry. This section provides the reader a basic understanding of the rheological parameters and rheological characterization of polymers, particularly those concerning polymers containing fillers and their relation to the analysis of the dispersion and the microstructure of polymer composites. For a complete review of the fundamentals of rheology of filled polymers, the work by Shenoy is recommended.[118]

Rheology is the study of the response of materials to mechanical force. The response may be irreversible flow, reversible elastic deformation or a combination of both. Polymers are viscoelastic materials in the sense that they may show viscous or elastic behavior in response to applied stress. Thus, both types of deformation must be considered to explain their behavior. A viscous liquid is one in which an irreversible deformation occurs after stress is applied. In this case, the energy is dissipated as heat. An elastic solid is a solid for which a reversible deformation occurs after stress is applied; in this case energy is stored and is recoverable.

As the rheological behavior of viscoelastic materials is hard to visualize, several mechanical models have been employed to understand it. For instance, a Newtonian fluid (one for which the viscosity is independent of the shear rate, i.e. rate of deformation) can be represented by a dashpot, which is a piston operating on a cylinder containing the fluid. The dashpot represents the dissipation of energy as heat, which occurs in viscous liquids. Similarly, a Hookean solid is represented by a spring that represents the energy storage ability of elastic materials. Mechanical models made by a combination of dashpots and springs have been proposed for the study, modeling and understanding of the response of viscoelastic materials to applied stress. However, it is worth noting that none of these models can represent the dynamic behavior of polymers in a full range of conditions, given that a viscoelastic material may behave as a viscous liquid or an elastic solid, depending on the time required for the system to respond to a certain stress or deformation used during the rheological measurement.

In the dynamic rheological analysis of a polymer, a cyclic stress is applied and the response of the system is studied. The dynamic behavior of a viscoelastic material is analyzed by complex variables that represent stress and strain. The variables are vectors in the complex planes:[119,120]

$$\tau^* = \tau_0 e^{i\omega t} \tag{1.1}$$

$$\gamma^* = \gamma_0 e^{i(\omega t-\delta)} \tag{1.2}$$

where, τ^* is the complex stress, γ^* is the complex strain, ω is the angular frequency ($\omega=2\pi f$), δ is the phase angle, and $i=\sqrt{-1}$. The complex stress and strain can be written into real and imaginary components.

$$\tau^* = \tau' + i\tau'' \tag{1.3}$$

$$\gamma^* = \gamma' + i\gamma'' \tag{1.4}$$

The shear modulus (ratio of stress to strain), can be also represented by a complex variable, G^*, known as the dynamic modulus:

$$G^* = \tau^* / \gamma^* \tag{1.5}$$

or, written in real and imaginary components:

$$G^* = G' + iG'' \tag{1.6}$$

where the magnitude is:

$$|G^*| = \sqrt{(G')^2 + (G'')^2} \tag{1.7}$$

and,

$$G' = |G^*| \cos\delta \tag{1.8}$$

$$G'' = |G^*| \sin\delta \tag{1.9}$$

G' is the storage modulus, and it is a measure of the elasticity. Thus, it is associated with the energy stored in the material by elastic deformation. G' is in phase with the real components of τ^* and γ^*. On a macromolecular basis, G' depends on the contour arrangements that can occur within the time frame of the oscillatory deformation. G'' is the loss modulus, and it is a measure of the viscous energy dissipation. On a macromolecular basis, G'' depends on the molecular arrangements capable of dissipating energy within the time frame of the oscillatory deformation.

In addition, the analysis of the dynamic response of a viscoelastic material leads to the complex dynamic viscosity, η^*:

$$\eta^* = \eta' + i\eta'' \tag{1.10}$$

η^* is related to the complex modulus as shown below:

$$\eta^* = \frac{G^*}{i\omega} \tag{1.11}$$

The dynamic response of polymers can be obtained by using a rotational viscometer with a parallel disc configuration. The sample (e.g. polymer nanocomposite) is located between two discs, the system is held at a temperature above the flow temperature of the polymer, and the stress is applied in a time-dependent manner. The oscillatory rheometer registers the response of the specimen to the applied stress and the frequency dependence of the viscoelastic properties (G', G'', η^*, and $tan\delta$) can be characterized.

1.3.2 Rheological and electrical percolation

In the particular case of filled polymers, rheological characterization has been used to demonstrate different degrees of dispersion and orientation of the nanofiller.[109,121-123] For constant processing variables, the rheological response of a composite depends on factors such as the characteristics of the filler (size, aspect ratio, and orientation), filler loading, polymer molecular weight, and the surface tension between the polymer and filler.[118] The rheology of a filled polymer at different filler concentrations shows a transition from a rheological state dominated by a polymer-polymer entangled network with liquid-like behavior ($G' \propto \omega^2$) to a combined polymer-polymer and nanofiller-polymer network with solid-like behavior ($G' \propto \omega$); the concentration at which this transition occurs is known as the rheological percolation threshold.[109,110,118,121] If electrically conductive nanofillers are utilized, further increase in the concentration (i.e. beyond the rheological percolation threshold) results in the formation of a nanofiller network that enhances the electrical conductivity of the nanocomposite. The concentration at which the electrical properties of the nanocomposite change from insulating to conductive is known as the electrical percolation threshold. Figure 1.7 shows illustrations of polymer nanocomposites with increasing concentrations of high-aspect ratio nanofiller (i.e.

carbon nanotubes), and its relation to the rheological and electrical percolation thresholds.[109,110,121]

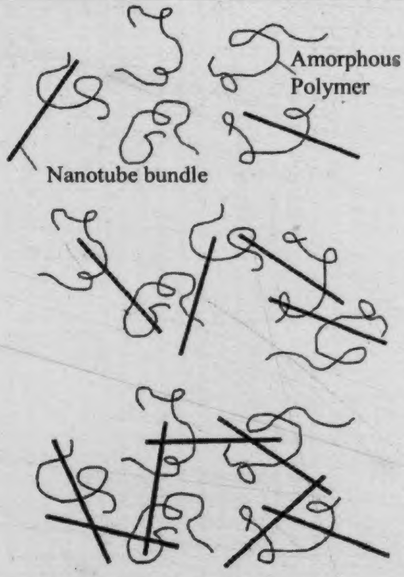

Low nanotube concentration. The rheological behavior is dominated by the polymer-polymer networks. Electrical resistivity is close to that of the polymer.

The nanotube concentration reaches rheological percolation (onset of solid-like behavior) threshold. The rheological behavior is dominated by the polymer-polymer and polymer-nanofiller networks.

The nanotube concentration reaches the electrical percolation threshold. The rheological behavior shows solid-like behavior, and the small distance between the nanofiller particles induces electrical conductivity.

Figure 1.7. Illustration of polymer-polymer, nanofiller-polymer, and nanofiller-nanofiller networks of polymer nanocomposites with the increase in concentration of nanofiller. Reprinted with permission from *Macromolecules*, 2004, 37, 24, 9048-9055. Copyright 2004, American Chemical Society.

The response of the complex viscosity (η^*) and modulus (G' and G'') as a function of the frequency of applied stress of polymer nanocomposites provide useful information about the internal structure. For instance, it is recognized that poor dispersion of the nanofiller leads to rheological behavior similar to that of the pristine polymer,[108,121] and enhanced dispersion can be identified from the slope or the value of the storage modulus at low frequencies.[121] Indeed, the rheological aspects of nanocomposites continue to be an important and active area of research, given that new phenomena are expected from changing the size, distribution, aspect ratio and surface chemistry of nanofillers dispersed into polymer matrixes.

Although several models have been developed for predicting and modeling the behavior of physical properties of polymer composites, the percolation theory continues being the preferred model.[124,125] Thus, it has been used for predicting percolation thresholds and modeling percolation behavior of properties such as electrical conductivity and viscoelasticity of polymer composites beyond a critical value of filler concentration.[126] Based on the percolation theory, the electrical percolation threshold in polymer composites is generally determined assuming a power law dependence of the conductivity relative to the concentration of the filler determined by (1.12):

$$\sigma_c = \sigma_m (V_f - V_c)^t \tag{1.12}$$

where, σ_c is the conductivity of the composite, σ_m is the conductivity of the filler, V_f is the volume fraction of the filler, V_c is the percolation threshold, and t is the critical exponent, which is dependent on the dimensions of the lattice (1.6 for three dimensional lattices).[124] Equation 1.12 is valid only at concentrations above the percolation threshold. The value of the percolation threshold can be between some value close to 0 and that corresponding to a close packed arrangement of the filler particles. In addition, the percolation threshold can be affected by variables such as the filler size, aspect ratio, degree of dispersion, orientation (i.e. alignment), and surface modification, and by the polymer viscosity and crystallinity, and by processing conditions. The interaction of these parameters makes the preparation of polymer nanocomposites for specific applications a challenging task.

1.4 Motivation and overview of the thesis

Potential applications of 1D-nanostructures are still to be realized. One of the main challenges is the synthesis of these nanoparticles on a large scale. An example of the importance of the development of large-scale syntheses of nanoparticles is the synthesis of carbon nanotubes. Large scale syntheses of these 1D-nanostructures have been developed since the discovery of these materials by Iijima.[127] Currently, carbon nanotubes are available in kilogram quantities dispersed into polymeric materials, such as those produced and distributed by Hyperion Catalyst (www.fibrils.com). These nanocomposites find use in applications such as electrostatic painting and electrostatic dissipation. The synthesis of metal 1D-nanostructures on a large scale is still in its infancy, but progress in this area may be expected over the next years. The scale-up of synthetic strategies is not a trivial task, and, as for any process, it requires the ongoing involvement of the scientific and engineering community. Template directed-synthesis provides a versatile route to the synthesis of 1D-nanostructures, such as metals, semiconductors, and conductive polymers with exceptionally small diameters and high aspect ratios. In addition, the use of templates and electrodeposition enables the synthesis of heterostructures and alloys, which can be difficult to attain by other strategies. Despite this versatility and the large number of reports on template-directed synthesis of nanostructures, to our knowledge, no previous work has reported synthesis on a large scale. In fact, the yields and quality of metal 1D-nanostructures are still generally not reported.

High aspect-ratio metal nanowires may enable the preparation of electrically conductive polymer nanocomposites with low concentrations of the nanofiller. The use of low concentrations of filler is beneficial by maintaining the processibility of the polymer, while enhancing the electrical properties. Metal nanowires may be an alternative to conventional fillers such as carbon black, or metal fibers and flakes, as well as more modern nanofillers such as carbon nanofibers and carbon nanotubes. One of the major potential applications of novel polymer nanocomposites is as electrically conductive or dissipative packaging materials, for protecting electronic devices from electrostatic discharge. Nonetheless, the application of metal nanowires in the preparation of polymer nanocomposites has scarcely been studied, compared to carbon nanotube- and carbon nanofiber-based composites. This work is a contribution to the development of novel materials based on metal nanowire/polymer nanocomposites, a challenging process that requires the synergy of materials science and engineering.

The organization of this thesis is as follows: The second chapter presents the synthesis of metal nanowires using AC electrodeposition into PAO templates. Gram amounts of nanowires were produced after scaling up the synthesis using PAO templates from 1 cm^2 to a set of electrodes with 4500 cm^2 of total Al surface. The third chapter reports the surface modification of copper and silver nanowires prepared by AC electrodeposition. Alkanethiols were used for the chemical modification of the nanowires, given their high affinity for Cu and Ag surfaces. The objective was to decrease the aggregation of the nanowires after liberation from PAO templates, as well as to enhance their dispersion in polymer nanocomposites. The fourth chapter presents the results of the preparation and characterization of polymer nanocomposites containing metal nanowires using solution processing. The dispersion of the nanowires, and the electrical and rheological percolation of the composites were studied. The fifth chapter presents the results of melt mixing of Cu nanowire/polymer nanocomposites using an asymmetric minimixer. Although melt mixing is the most widely utilized process for the polymer industry, obtaining good dispersion of nanoparticles in a molten polymer is challenging. Polymer nanocomposites were prepared with copper nanowires, with and without chemical modification, and their dispersion and properties were compared to those of nanocomposites produced by the solution method. The sixth chapter highlights the conclusions and future work.

1.5 References

1. Xia, Y. N.; Yang, P. D.; Sun, Y. G.; Wu, Y. Y.; Mayers, B.; Gates, B.; Yin, Y. D.; Kim, F.; Yan, Y. Q., *Adv. Mater.* **2003,** 15, (5), 353-389.
2. Murphy, C. J.; Gole, A. M.; Hunyadi, S. E.; Orendorff, C. J., *Inorg. Chem.* **2006,** 45, (19), 7544-7554.
3. Kline, T. R.; Tian, M. L.; Wang, J. G.; Sen, A.; Chan, M. W. H.; Mallouk, T. E., *Inorg. Chem.* **2006,** 45, (19), 7555-7565.

4. Possin, G. E., *Rev. Sci. Instrum.* **1970,** 41, (5), 772-774.

5. Price, P. B.; Walker, R. M., *J. Appl. Phys.* **1962,** 33, (12), 3407-3412.

6. Fleischer, R. L.; Price, P. B.; Walker, R. M., *Rev. Sci. Instrum.* **1963,** 34, (5), 510-512.

7. Williams, W. D.; Giordano, N., *Rev. Sci. Instrum.* **1984,** 55, (3), 410-412.

8. Penner, R. M.; Martin, C. R., *J. Electrochem. Soc* **1986,** 133, (10), 2206-2207.

9. Martin, C. R., *Science* **1994,** 266, (5193), 1961-1966.

10. Goad, D. G. W.; Moskovits, M., *J. Appl. Phys.* **1978,** 49, (5), 2929-2934.

11. Pontifex, G. H.; Zhang, P.; Wang, Z.; Haslett, T. L.; Almawlawi, D.; Moskovits, M., *J. Phys. Chem.* **1991,** 95, (24), 9989-9993.

12. Pan, H.; Liu, B. H.; Yi, J. B.; Poh, C.; Lim, S.; Ding, J.; Feng, Y. P.; Huan, C. H. A.; Lin, J. Y., *J. Phys. Chem. B* **2005,** 109, (8), 3094-3098.

13. Tian, M. L.; Wang, J. G.; Snyder, J.; Kurtz, J.; Liu, Y.; Schiffer, P.; Mallouk, T. E.; Chan, M. H. W., *Appl. Phys. Lett.* **2003,** 83, (8), 1620-1622.

14. Tian, M. L.; Wang, J. U.; Kurtz, J.; Mallouk, T. E.; Chan, M. H. W., *Nano Lett.* **2003,** 3, (7), 919-923.

15. Wang, J. G.; Tian, M. L.; Mallouk, T. E.; Chan, M. H. W., *J. Phys. Chem. B* **2004,** 108, (3), 841-845.

16. Yi, G.; Schwarzacher, W., *Appl. Phys. Lett.* **1999,** 74, (12), 1746-1748.

17. de Horne, F. D.; Piraux, L.; Michotte, S., *Appl. Phys. Lett.* **2005,** 86, (15), 152510.

18. Gravier, L.; Serrano-Guisan, S.; Ansermet, J. P., *J. Appl. Phys.* **2005,** 97, (10), 10C501.

19. Keating, C. D.; Natan, M. J., *Adv. Mater.* **2003,** 15, (5), 451-454.

20. Nicewarner-Pena, S. R.; Freeman, R. G.; Reiss, B. D.; He, L.; Pena, D. J.; Walton, I. D.; Cromer, R.; Keating, C. D.; Natan, M. J., *Science* **2001,** 294, (5540), 137-141.

21. Salem, A. K.; Chao, J.; Leong, K. W.; Searson, P. C., *Adv. Mater.* **2004,** 16, (3), 268-271.

22. Salem, A. K.; Chen, M.; Hayden, J.; Leong, K. W.; Searson, P. C., *Nano Lett.* **2004,** 4, (6), 1163-1165.

23. Wang, J. G.; Tian, M. L.; Mallouk, T. E.; Chan, M. H. W., *Nano Lett.* **2004,** 4, (7), 1313-1318.

24. Martin, B. R.; Dermody, D. J.; Reiss, B. D.; Fang, M. M.; Lyon, L. A.; Natan, M. J.; Mallouk, T. E., *Adv. Mater.* **1999,** 11, (12), 1021-1025.

25. Nielsch, K.; Muller, F.; Li, A.-P.; Gosele, U., *Adv. Mater.* **2000,** 12, (8), 582-586.

26. Shingubara, S., *J. Nanopart. Res.* **2003,** 5, (1-2), 17-30.

27. Zhang, X. Y.; Zhang, L. D.; Lei, Y.; Zhao, L. X.; Mao, Y. Q., *J. Mater. Chem.* **2001,** 11, 1732-1734.

28. Choi, J.; Sauer, G.; Nielsch, K.; Wehrspohn, R. B.; Gosele, U., *Chem. Mater.* **2003,** 15, (3), 776-779.

29. Sauer, G.; Brehm, G.; Schneider, S.; Nielsch, K.; Wehrspohn, R. B.; Choi, J.; Hofmeister, H.; Gosele, U., *J. Appl. Phys.* **2002,** 91, (5), 3243-3247.

30. Sander, M. S.; Prieto, A. L.; Gronsky, R.; Sands, T.; Stacy, A. M., *Adv. Mater.* **2002,** 14, (9), 665-667.

31. AlMawlawi, D.; Coombs, N.; Moskovits, M., *J. Appl. Phys.* **1991,** 70, (8), 4421-4425.

32. AlMawlawi, D.; Liu, C. Z.; Moskovits, M., *J. Mater. Res.* **1994,** 9, (4), 1014-1018.

33. Davydov, D. N.; Haruyama, J.; Routkevitch, D.; Statt, B. W.; Ellis, D.; Moskovits, M.; Xu, J. M., *Phys. Rev. B* **1998,** 57, (21), 13550-13553.

34. Davydov, D. N.; Sattari, P. A.; AlMawlawi, D.; Osika, A.; Haslett, T. L.; Moskovits, M., *J. Appl. Phys.* **1999,** 86, (7), 3983-3987.

35. Li, F.; Zhang, L.; Metzger, R. M., *Chem. Mater.* **1998,** 10, 2470-2480.

36. Preston, C.; Moskovits, M., *J. Phys. Chem.* **1993,** 97, 8495-8503.

37. Routkevitch, D.; Tager, A. A.; Haruyama, J.; Almawlawi, D.; Moskovits, M.; Xu, J., *IEEE Trans. Electr. Dev.* **1996,** 43, (10), 1646-1658.

38. Sun, M.; Zangari, G.; Metzger, R. M., *IEEE Trans. Magn.* **2000,** 36, (5), 3005-3008.

39. Sun, M.; Zangari, G.; Shamsuzzoha, M.; Metzger, R. M., *Appl. Phys. Lett.* **2001,** 78, (19), 2964-2966.

40. Yin, A. J.; Li, J.; Jian, W.; Bennett, A. J.; Xu, J. M., *Appl. Phys. Lett.* **2001,** 79, (7), 1039-1041.

41. O'Sullivan, J. P.; Wood, G. C., *Proc. R. Soc. London, Ser. A* **1970,** 317, (1531), 511-543.

42. Nielsch, K.; Choi, J.; Schwirn, K.; Wehrspohn, R. B.; Gosele, U., *Nano Lett.* **2002,** 2, (27), 677-680.

43. Zhang, S. H.; Xie, Z. X.; Jiang, Z. Y.; Xu, X.; Xiang, J.; Huang, R. B.; Zheng, L. S., *Chem. Commun.* **2004,** (9), 1106-1107.

44. Barbic, M.; Mock, J. J.; Smith, D. R.; Schultz, S., *J. Appl. Phys.* **2002,** 91, (11), 9341-9345.

45. Gao, T.; Meng, G.; Wang, Y.; Sun, S.; Zhang, L., *J. Phys.: Condens. Matter* **2002,** 14, 355-363.

46. Molares, M. E. T.; Buschmann, V.; Dobrev, D.; Neumann, R.; Scholz, R.; Schuchert, I. U.; Vetter, J., *Adv. Mater.* **2001,** 13, (1), 62-65.

47. Schuchert, I. U.; Toimil-Molares, M. E.; Dobrev, D.; Vetter, J.; Neumann, R.; Martin, M., *J. Electrochem. Soc* **2003,** 150, (4), C189-C194.

48. Chang, Y.; Lye, M. L.; Zeng, H. C., *Langmuir* **2005,** 21, (9), 3746-3748.

49. Liu, Z. P.; Yang, Y.; Liang, J. B.; Hu, Z. K.; Li, S.; Peng, S.; Qian, Y. T., *J. Phys. Chem. B* **2003,** 107, (46), 12658-12661.

50. Gao, Y.; Jiang, P.; Liu, D. F.; Yuan, H. J.; Yan, X. Q.; Zhou, Z. P.; Wang, J. X.; Song, L.; Liu, L. F.; Zhou, W. Y.; Wang, G.; Wang, C. Y.; Xie, S. S., *Chem. Phys. Lett.* **2003,** 380, (1-2), 146-149.

51. Gao, Y.; Jiang, P.; Liu, D. F.; Yuan, H. J.; Yan, X. Q.; Zhou, Z. P.; Wang, J. X.; Song, L.; Liu, L. F.; Zhou, W. Y.; Wang, G.; Wang, C. Y.; Xie, S. S.; Zhang, J. M.; Shen, A. Y., *J. Phys. Chem. B* **2004,** 108, (34), 12877-12881.

52. Murphy, C. J.; San, T. K.; Gole, A. M.; Orendorff, C. J.; Gao, J. X.; Gou, L.; Hunyadi, S. E.; Li, T., *J. Phys. Chem. B* **2005,** 109, (29), 13857-13870.

53. Sun, Y. G.; Gates, B.; Mayers, B.; Xia, Y. N., *Nano Lett.* **2002,** 2, (2), 165-168.

54. Sun, Y. G.; Mayers, B.; Herricks, T.; Xia, Y. N., *Nano Lett.* **2003,** 3, (7), 955-960.

55. Caswell, K. K.; Bender, C. M.; Murphy, C. J., *Nano Lett.* **2003,** 3, (5), 667-669.

56. Hu, J. Q.; Chen, Q.; Xie, Z. X.; Han, G. B.; Wang, R. H.; Ren, B.; Zhang, Y.; Yang, Z. L.; Tan, Z. Q., *Adv. Funct. Mater.* **2004,** 14, (2), 183-189.

57. Jana, N. R.; Gearheart, L.; Murphy, C. J., *Chem. Commun.* **2001**, (7), 617-618.

58. Zhang, S. H.; Jiang, Z. Y.; Xie, Z. X.; Xu, X.; Huang, R. B.; Zheng, L. S., *J. Phys. Chem. B* **2005,** 109, (19), 9416-9421.

59. Wang, Z. H.; Liu, J. W.; Chen, X. Y.; Wan, J. X.; Qian, Y. T., *Chem. --Eur. J.* **2005,** 11, (1), 160-163.

60. Liu, F. K.; Huang, P. W.; Chang, Y. C.; Ko, F. H.; Chu, T. C., *J. Mater. Res.* **2004,** 19, (2), 469-473.

61. Choi, H.; Park, S. H., *J. Am. Chem. Soc.* **2004,** 126, (20), 6248-6249.

62. Yen, M. Y.; Chiu, C. W.; Hsia, C. H.; Chen, R.; Kai, J. J.; Lee, C. Y.; Chiu, H. T., *Adv. Mater.* **2003,** 15, (3), 235-237.

63. Nuzzo, R. G.; Allara, D. L., *J. Am. Chem. Soc.* **1983,** 105, (13), 4481-4483.

64. Love, J. C.; Estroff, L. A.; Kriebel, J. K.; Nuzzo, R. G.; Whitesides, G. M., *Chem. Rev.* **2005,** 105, (4), 1103-1169.

65. Ulman, A., *Chem. Rev.* **1996,** 96, (4), 1533-1554.

66. Laibinis, P. E.; Whitesides, G. M.; Allara, D. L.; Tao, Y. T.; Parikh, A. N.; Nuzzo, R. G., *J. Am. Chem. Soc.* **1991,** 113, (19), 7152-7167.

67. Laibinis, P. E.; Whitesides, G. M., *J. Am. Chem. Soc.* **1992,** 114, (23), 9022-9028.

68. Ron, H.; Cohen, H.; Matlis, S.; Rappaport, M.; Rubinstein, I., *J. Phys. Chem. B* **1998,** 102, (49), 9861-9869.

69. Ron, H.; Rubinstein, I., *Lagmuir* **1994,** 10, (12), 4566-4573.

70. Keller, H.; Simak, P.; Schrepp, W.; Dembowski, J., *Thin Solid Films* **1994,** 244, (1-2), 799-805.

71. Woodward, J. T.; Walker, M. L.; Meuse, C. W.; Vanderah, D. J.; Poirier, G. E.; Plant, A. L., *Langmuir* **2000,** 16, (12), 5347-5353.

72. Yan, C.; Golzhauser, A.; Grunze, M.; Woll, C., *Langmuir* **1999,** 15, (7), 2414-2419.

73. Paxton, W. E.; Sen, A.; Mallouk, T. E., *Chem. --Eur. J.* **2005,** 11, (22), 6462-6470.

74. Paxton, W. F.; Kistler, K. C.; Olmeda, C. C.; Sen, A.; St Angelo, S. K.; Cao, Y. Y.; Mallouk, T. E.; Lammert, P. E.; Crespi, V. H., *J. Am. Chem. Soc.* **2004,** 126, (41), 13424-13431.

75. Salem, A. K.; Hung, C. F.; Kim, T. W.; Wu, T. C.; Searson, P. C.; Leong, K. W., *Nanotechnology* **2005,** 16, (4), 484-487.

76. Salem, A. K.; Searson, P. C.; Leong, K. W., *Nat. Mater.* **2003,** 2, (10), 668-671.

77. Wang, J. G.; Tian, M. L.; Kumar, N.; Mallouk, T. E., *Nano Lett.* **2005,** 5, (7), 1247-1253.

78. Jeong, D. H.; Zhang, Y. X.; Moskovits, M., *J. Phys. Chem. B* **2004,** 108, (34), 12724-12728.

79. Li, C. Z.; He, H. X.; Bogozi, A.; Bunch, J. S.; Tao, N. J., *Appl. Phys. Lett.* **2000,** 76, (10), 1333-1335.

80. Murray, B. J.; Newberg, J. T.; Walter, E. C.; Li, Q.; Hemminger, J. C.; Penner, R. M., *Anal. Chem.* **2005,** 77, (16), 5205-5214.

81. Favier, F.; Walter, E. C.; Zach, M. P.; Benter, T.; Penner, R. M., *Science* **2001,** 293, (5538), 2227-2231.

82. Maier, S. A.; Atwater, H. A., *J. Appl. Phys.* **2005,** 98, (1).

83. Huang, X. H.; El-Sayed, I. H.; Qian, W.; El-Sayed, M. A., *J. Am. Chem. Soc.* **2006,** 128, (6), 2115-2120.

84. Gelves, G. A.; Lin B.; Sundararaj, U.; Haber, J. A., *Adv. Funct. Mater.* **2006,** 16, 2423-2430.

85. Gelves, G. A.; Sundararaj, U.; Haber, J. A., *Macromol. Rap. Comm.* **2005,** 26, (21), 1677-1681.

86. Toimil-Molares, M. E.; Balogh, A. G.; Cornelius, T. W.; Neumann, R.; Trautmann, C., *Appl. Phys. Lett.* **2004,** 85, (22), 5337-5339.

87. Diggle, J. W.; Downie, T. C.; Goulding, C. W., *Chem. Rev.* **1969,** 69, (3), 365-405.

88. Asoh, H.; Nishio, K.; Nakao, M.; Tamamura, T.; Masuda, H., *J. Electrochem. Soc.* **2001,** 148, (4), B152-B156.

89. Masuda, H.; Fukuda, K., *Science* **1995,** 268, (5216), 1466-1468.

90. Masuda, H.; Hasegwa, F.; Ono, S., *J. Electrochem. Soc.* **1997,** 144, (5), L127-L130.

91. Masuda, H.; Yada, K.; Osaka, A., *Jpn. J. Appl. Phys., Part 2* **1998,** 37, (11A), L1340-L1342.

92. Masuda, H.; Yada, K.; Osaka, A., *Jpn. J. Appl. Phys., Part 2* **1998,** 37, L1340-L1342.

93. Jessensky, O.; Muller, F.; Gosele, U., *Appl. Phys. Lett.* **1998,** 72, (10), 1173-1175.

94. Jessensky, O.; Muller, F.; Gosele, U., *J. Electrochem. Soc.* **1998,** 145, (11), 3735-3740.

95. Keller, F.; Hunter, M. S.; Robinson, D. L., *J. Electrochem. Soc* **1953,** 100, (9), 411-419.

96. Hoar, T. P.; Mott, N. F., *J. Phys. Chem. Solids* **1959,** 9, (2), 97-99.

97. Njuguna, B.; Pielichowski, K., *Adv. Eng. Mater.* **2003,** 5, (11), 769-778.

98. Caseri, W., *Macromol. Rap. Comm.* **2000,** 21, (11), 705-722.

99. Sanchez, C.; Julian, B.; Belleville, P.; Popall, M., *J. Mater. Chem.* **2005,** 15, (35-36), 3559-3592.

100. LeBaron, P. C.; Wang, Z.; Pinnavaia, T. J., *Appl. Clay Sci.* **1999,** 15, (1-2), 11-29.

101. Ray, S. S.; Okamoto, M., *Prog. Polym. Sci.* **2003,** 28, (11), 1539-1641.

102. Alexandre, M.; Dubois, P., *Mater. Sci. Eng. R* **2000,** 28, (1-2), 1-63.

103. Schueler, R.; Petermann, J.; Schulte, K.; Wentzel, H. P., *J. Appl. Polym. Sci.* **1997,** 63, (13), 1741-1746.

104. Finegan, I. C.; Tibbetts, G. G., *J. Mater. Res.* **2001,** 16, (6), 1668-1674.

105. Zhang, C.; Yi, X. S.; Yui, H.; Asai, S.; Sumita, M., *J. Appl. Pol. Sci.* **1998,** 69, (9), 1813-1819.

106. Baughman, R. H.; Zakhidov, A. A.; de Heer, W. A., *Science* **2002,** 297, (5582), 787-792.

107. Haggenmueller, R.; Gommans, H. H.; Rinzler, A. G.; Fischer, J. E.; Winey, K. I., *Chem. Phys. Lett.* **2000,** 330, (3-4), 219-225.

108. Mitchell, C. A.; Bahr, J. L.; Arepalli, S.; Tour, J. M.; Krishnamoorti, R., *Macromolecules* **2002,** 35, (23), 8825-8830.

109. Pötschke, P.; Abdel-Goad, M.; Alig, I.; Dudkin, S.; Lellinger, D., *Polymer* **2004,** 45, (26), 8863-8870.

110. Pötschke, P.; Fornes, T. D.; Paul, D. R., *Polymer* **2002,** 43, (11), 3247-3255.

111. Sandler, J. K. W.; Kirk, J. E.; Kinloch, I. A.; Shaffer, M. S. P.; Windle, A. H., *Polymer* **2003,** 44, (19), 5893-5899.

112. Chung, D. D. L., *J. Mater. Sci.* **2004,** 39, (8), 2645-2661.

113. Huang, J. C., *Adv. Polym. Technol.* **1995,** 14, (2), 137-150.

114. Gonon, P.; Boudefel, A., *J. Appl. Phys.* **2006,** 99, (2), 024308.

115. Qi, L.; Lee, B. I.; Chen, S. H.; Samuels, W. D.; Exarhos, G. J., *Adv. Mater.* **2005,** 17, (14), 1777-1779.

116. Pothukuchi, S.; Li, Y.; Wong, C. P., *J. Appl. Polym. Sci.* **2004,** 93, (4), 1531-1538.

117. Jung, W. K.; Ahn, S. H.; Won, M. S., *J. Compos. Mater.* **2006,** 40, (2), 175-188.

118. Shenoy, A. V., *Rheology of filled polymer systems*. Kluwer Academy Publishers: Dordrecht, 1999.

119. Mark, H. F.; Kroschwitz, J. I., *Encyclopedia of Polymer Science and Technology*. 2nd ed.; John Wiley & Sons, Inc.: New York, 1988; Vol. 14.

120. Ferry, J. D., *Viscoelastic Properties of Polymers*. 3rd ed.; John Wiley & Sons, Inc.: New York, 1980.

121. Du, F. M.; Scogna, R. C.; Zhou, W.; Brand, S.; Fischer, J. E.; Winey, K. I., *Macromolecules* **2004,** 37, (24), 9048-9055.

122. Pötschke, P.; Bhattacharyya, A. R.; Janke, A., *Polymer* **2003,** 44, (26), 8061-8069.

123. Potschke, P.; Bhattacharyya, A. R.; Janke, A., *Eur. Polym. J.* **2004,** 40, (1), 137-148.

124. Kirkpatrick, S., *Rev. Mod. Phys.* **1973,** 45, (4), 574-588.

125. Lux, F., *J. Mater. Sci.* **1993,** 28, (2), 285-301.

126. Moniruzzaman, M.; Winey, K. I., *Macromolecules* **2006,** 39, (16), 5194-5205.

127. Iijima, S., *Nature* **1991,** 354, (6348), 56-58.

Chapter 2

Multigram synthesis of copper and silver nanowires using AC electrodeposition into porous aluminum oxide templates

2.1 Introduction

As mentioned previously in Chapter 1, template-directed synthesis using AC electrodeposition through the barrier layer of porous aluminum oxide templates might enable the synthesis of different 1D-nanostructures on a large scale. The use of AC electrodeposition for the synthesis of metal nanowires in PAO templates has been reported previously.[1-6] The process of AC electrodeposition has been mainly developed on an experimental basis, and it is known to be influenced by the interaction of the electrolyte composition, temperature, and parameters of the AC wave such as voltage (or current), frequency, and shape (continuous, pulsed, sinusoidal, square, and triangular). However, to date the complex interactions between the electrodeposition parameters, the structure of the barrier layer, and the electrical behaviour of the aluminum-alumina-metal junctions during AC electrodeposition is not completely understood. In an effort to optimize the AC electrodeposition of metals, the Haber group studied how to increase the efficiency of the pore-filling on the small scale using different electrodeposition conditions.[7,8] This work is aimed to extend those efforts to the synthesis and liberation of metal nanowires from PAO templates on a large scale.

In this chapter, the development of a scalable, versatile, bench-top electrosynthesis of gram quantities of high-aspect ratio Cu nanowires is presented. The nanowires are produced by AC electrodeposition into porous alumina templates. Different procedures for liberation of the nanowires were studied, resulting in nanostructures with different morphology and surface chemistry. With appropriate modification of the electrodeposition conditions, the process described here might be applied to the multigram synthesis of other nanostructures. Following this approach, synthesis of silver nanowires using PAO templates was studied.

2.2 Experimental

2.2.1 Development of porous aluminum oxide templates (PAO) for multigram synthesis of nanowires

In this section, the development of PAO templates for the synthesis of copper nanowires is described. Initially, two different Al electrodes were prepared using Al foils (100 μm) and Al plates (1 mm thick). The experiments with Al foils aimed to anodize the Al all the way through until reaching a Ag back contact that would enable DC electrodeposition into PAO templates.[9] However, experiments realized with 1 cm^2 Al electrodes proved this route to be difficult to reproduce. In addition, construction of the PAO electrode required several steps, such as the deposition of a back contact of Ag and attaching the Al/Ag electrode to an inert substrate for support. Furthermore, scale-up of the template-directed synthesis of nanowires would require increasing the electrode area to the point that handling the PAO/Ag electrodes would be impractical, given the brittle nature of the PAO structures.

A second alternative for PAO template preparation using thicker Al electrodes combined with AC electrodeposition was identified as more suitable for scaling-up the synthesis of copper and other nanowire structures. By this route, Al electrodes require fewer preparation steps than those reported in previous works using DC electrodeposition.[9-12] In addition, anodization of both sides of the Al foils would be possible, and the rugged thick Al plates would require only simple handling through the processing steps. Slightly different processing conditions were developed for 1 mm thick Al electrodes of different sizes, in order to demonstrate and facilitate the synthesis of nanowires in gram quantities using porous aluminum oxide templates.

2.2.1.1 Smaller-scale process for preparation of PAO templates

For the smaller-scale process, aluminum electrodes were prepared by cutting Al plates (99.99+%, Alfa Aesar, 1 mm thick) into 5 cm × 11 cm pieces, which were annealed at 500 °C in air for 24 h. The electrodes were etched in 60 °C, 1.0 M NaOH (aq) for 2 min, and both faces immediately electropolished in a 1 °C double walled, cooled cylindrical bath containing 500 mL of solution consisting of a mixture of 115 mL of 70% perchloric acid, 90 mL of 2-butoxyethanol, 600 mL of ethanol and 150 mL of water. Graphite foil (99%, Alfa

Aesar, 1 mm thick) was used for the counter electrodes (one on each side of the Al, 2 cm from and parallel to the Al face), with electrical contacts made using copper alligator clips. Three pulses with a current density of 280 mA/cm^2 and 15 s duration were applied with a 5 min period between pulses to allow the bath to cool to 1 °C.

The electropolished electrodes were anodized following the two-step process of Masuda.[13] Five electrodes were anodized in parallel by immersing them to a depth of 9.5 cm in 3.0 L of 0.3 M H_2SO_4 (aq) at 2 °C in a double walled, chilled cylindrical bath, as shown in Figure 2.1. Each Al electrode was separated by a counter electrode (6 counter electrodes in total) 1.5 cm from the face of each Al plate. Materials used for counter electrodes were either 304 stainless steel gauze (150 mesh, 0.066 mm dia., Fe:Cr:Ni; 70:19:11 wt. %) or 316 stainless steel plates (1 mm thickness, Fe:Cr:Ni:Mo; 69:18:10:3 wt. %). Electrical contact was again made by attaching an alligator clip to the top of each plate connected in parallel to the positive terminal, while the 6 counter electrodes were connected in parallel to the negative terminal of a Hewlett Packard 6024A DC power supply (0-70 V and 0-12 A). The electrodes were first anodized at 25.0 V (producing a current of 1.5 A) for 2 h, removed from the anodizing bath and the alumina film removed by etching for 30 min in a 60 °C mixture of 0.20 M H_2CrO_4 and 0.60 M H_3PO_4, followed by reanodization in the H_2SO_4 electrolyte for 4, 6, or 8 h, producing pores ~ 25 nm in diameter and 18, 27, or 36 μm deep, respectively. At the completion of the second anodization the barrier layer thickness was reduced by decreasing the voltage in 2 V increments every 2 min until 15 V was reached, then in 1 V increments every 1 min until 9 V was reached, which potential was held for 5 min and then the power supply was turned off. The electrodes were soaked in deionized water for 5 min and then dried with compressed air.

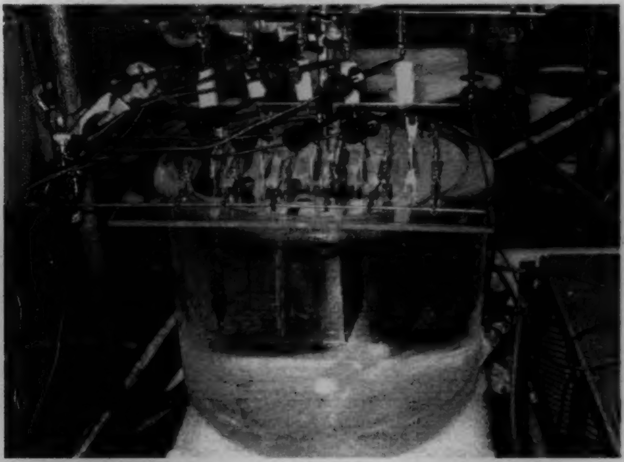

Figure 2.1. Photograph of a double-walled 3 liter anodization bath containing five Al electrodes 5 cm wide × 11 cm high × 1 mm thick interdigitated with stainless steel counter electrodes (Smaller-scale process).

2.2.1.2 Larger-scale process for preparation of PAO templates

For the larger-scale process, electrodes were prepared by cutting Al plate (99.99+%, Alfa Aesar, 1 mm thick) into 10 cm × 25 cm pieces, which were neither annealed nor electropolished, but instead chemically polished before their first use. To chemically polish the electrodes, they were individually immersed for 3 min in a bath at 80-85 °C consisting of 4 L of a mixture in the ratio of 784 ml of 85% H_3PO_4, 98 mL of HNO_3 conc., 40 g of $NaNO_3$, and 118 mL of H_2O (caution:

this bath evolves NO_x).[14] They were anodized following a two-step process similar to that described above, in an anodization tank composed of 0.75 inch thick plexiglass walls, containing 30 L of 0.30 M H_2SO_4 (Fig. 2.2). Each Al electrode was separated by graphite foil (1 mm thick, Alfa Aesar, 97%) or 316 stainless steel counter electrodes (10.6 cm × 25 cm, 11 counter electrodes in total) 2.0 cm from the face of each Al plate. Electrical contact was again made by attaching an alligator clip to the top of each plate connected in parallel to the positive terminal, while the 11 counter electrodes were connected in parallel to the negative terminal, of a Lambda LK-351-FM power supply (0-40 V and 0-30 A). The two-step anodization process at 25.0 V and barrier layer thinning procedure described for the smaller-scale process was used.

The temperature was controlled by a combination of circulating the acid mixture through a heat-exchange coil immersed in a cooling bath using a peristaltic pump and by circulating cooling fluid through glass radiators immersed on both sides of the anodizing tank. Maintaining the bath at 0-4 °C is critical to maintaining a constant anodization current. If the bath heats up to above 4 °C the chemical etch rate at the pore bottom increases, reducing the barrier layer thickness, enabling the anodization current to increase and producing a run-away feedback loop, until the current limit of the power supply is reached. At this point the voltage decreases and moves away from the conditions that enable attainment of good pore-ordering. Additional circulation of the anodizing solution was provided by two mechanical stirrers in addition to the circulation of the solution with the peristaltic pump.

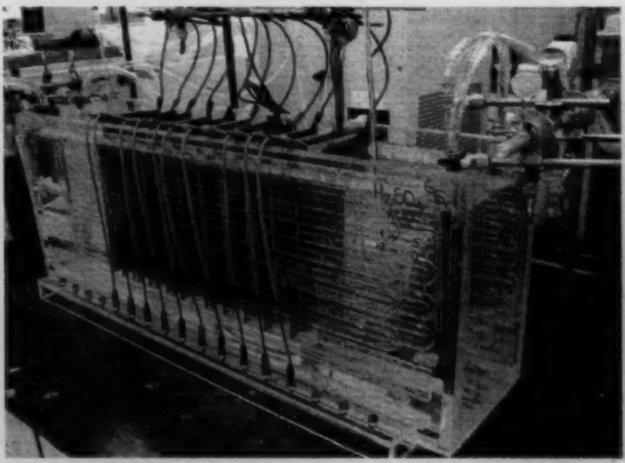

Figure 2.2. Photograph of a chilled 30 liter anodization bath containing ten Al electrodes 10 cm wide × 25 cm high × 1 mm thick interdigitated with graphite electrodes (Larger-scale process).

2.2.2 Electrodeposition of CuNWs

The pores of the alumina films were filled with Cu using AC electrodeposition. The edges of the anodized electrodes were coated with nail polish. This is necessary because micrometer sized cracks at all 90° edges provide a low resistance deposition pathway that prevents electrodeposition into the 25 nm diameter pores. Although, ultrasound was used in previous works to improve wetting of the pores prior to electrodeposition;[8,15] this step was eliminated because it damaged the surface of the electrodes and reduced the ability to reuse the Al plates. Electrodes were wet with distilled water and then individually immersed for 5 min in the deposition solution consisting of 600 mL (for 5 cm × 11 cm electrodes) or 4 L (for 10 cm × 25 cm electrodes) of 0.50 M $CuSO_4$/0.285 M H_3BO_3(aq). Each electrode was filled by applying a continuous 200 Hz sine wave at 10 V_{rms} (Fig. 2.3) for 10-15 min between the anodized Al and Cu plate (99.999%, Alfa Aesar) counter electrodes 2 cm from both faces of the Al electrode. The deposition signal was generated using a Tabor Electronics 8023 function generator, the output of which was amplified with a 1600 W Pyramid PB1281X car stereo amplifier powered with a LOKO 45 A, 16 V DC power supply or a car battery. The nail polish was removed from the edges of the electrodes with acetone. Bulk Cu deposition was removed by immersing the electrode in 60 °C, 0.6 M H_3PO_4 for 1 min, followed by cleaning the surface with a Kimwipe.

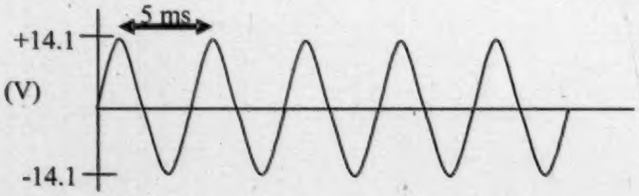

Figure 2.3. Continuous 200 Hz sine sequence used for the AC electrodeposition of copper into PAO templates.

2.2.3 Electrodeposition of AgNWs

Preliminary deposition experiments were performed on 10 cm^2 PAO electrodes to determine electrodeposition conditions that would yield good quality pore-filling. Conditions evaluated included: continuous sinusoidal AC voltage (9.0 to 10.0 V_{rms}, 200 Hz), pulsed sinusoidal (8.0 to 9.5 V_{rms}, 100 Hz triggered at 400 ms), pulsed AC square waves (7.5 to 9.0 V_p, 100 Hz, triggered at 400 ms intervals), and pulse polarities (negative followed by positive, and positive followed by negative). The Ag electrodeposition conditions used for synthesis of gram quantities of Ag nanowires were selected based on the degree of pore-filling observed by SEM analysis of top surfaces of electrodes after deposition, electrode coloration, and the appearance of gas evolution and bulk deposition. Electrodeposition of silver into the pores of 90 cm^2 PAO electrodes was accomplished by (1) coating the edges of the electrodes with nail polish, (2) individually immersing them for 5 min in the deposition solution consisting of an electrolyte of silver sulphate (Ag_2SO_4, 8.5 g/L), diammonium hydrogen citrate ($(NH_4)_2HC_6H_5O_7$, 200 g/L) and potassium thiocyanate (KSCN, 105 g/L), and (3) applying 100 Hz square wave pulses (± 8.0 V_p triggered at 400 ms intervals with the reductive followed by oxidative pulse polarity, Fig. 2.4) for 90 min between the anodized Al and Ag foil (Alfa Aesar, 0.127 mm thick, 99.9%) counter electrodes positioned 2 cm from both faces of the Al electrode. A power amplifier was built by the Electronics Shop at the department of Chemistry in order to carry out pulsed square AC depositions of silver in 90 cm^2 electrodes.

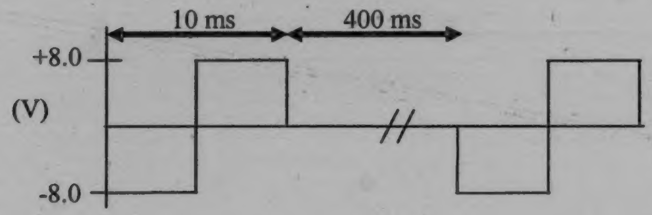

Figure 2.4. Pulsed squared-sequence used for the AC electrodeposition of silver into PAO templates.

2.2.4 Liberation of nanowires from PAO templates

Two methods for dissolving the PAO template to liberate Cu nanowires were used. The first method attempted was dissolution of the alumina at 60 °C, in 0.6 M H_3PO_4(aq). This process took around 30 min and the nanowires needed to be harvested by filtration. The second method consisted of dissolving the alumina at 40 °C in 1.0 M NaOH(aq). This process took 3 min and the nanowires were released as a large mass from each electrode, and could be harvested from the surface of the basic solution by using a spatula. The aqueous NaOH treatment was preferred, for reasons that will be discussed in the results section. The NaOH-liberated nanowires were cleaned for 10 min in a 1:1 mixture of 0.10 M NaOH(aq) and methanol (CH_3OH), filtered using filter paper (Whatman, < 1μm pore size), rinsed with CH_3OH, and transferred to 100 ml or 250 ml of CH_3OH. The nanowires were then sonicated for a period of 1 h in a sonication bath of 135 W average power and 38.5-40.5 kHz frequency by applying the ultrasound for 5 min with a 5 min rest period between sonications. After sonication, dispersed copper nanowires were collected by filtration on Osmonics Inc. nylon membranes (0.45 μm pore size) and dried under reduced pressure. The yields were: 0.867 mg/cm^2 (390 ± 22.5 mg per batch of 5 electrodes) for the 4 h anodized (18 μm deep pores) and 1.68 mg/cm^2 (756 ± 58.5 mg per batch of 5 electrodes) for the 8 h anodized (36 μm deep pores) 5 cm × 11 cm electrodes, and 0.786 mg/cm^2 (3,459 ± 270 mg per batch of 10 electrodes) for the 10 cm × 25 cm electrodes anodized for 8 h (36 μm deep pores).

Silver nanowires were liberated in $H_3PO_4(aq)$ and NaOH(aq) solutions using procedures similar to those used for the liberation of copper nanowires. The average yield of NaOH-liberated Ag nanowires was 0.900 mg Ag/cm^2 (405 ± 33.0 mg per batch of 5 electrodes) from electrodes 5 cm × 11 cm anodized for 8 h (36 μm deep pores).

2.2.5 Length distribution of NaOH-liberated nanowires

Copper and silver nanowires were grown in pores anodized for 8 h using 5 cm × 11 cm electrodes, and liberated using 1.0 M NaOH(aq). The nanowires were cleaned and sonicated as described above. The resultant suspension of nanowires in CH_3OH was spin cast at 3000 rpm on 2.5 cm × 2.5 cm glass slides. SEM images were collected of the well-dispersed nanowires and the lengths of more than 1000 individual CuNWs and > 500 AgNWs were measured using the Image J image analysis software program (Wayne Rasband, National Institutes of Health, USA, http://rsb.info.nih.gov/ij/).

2.2.6 Preparation of nanowire samples for XPS, XRD and TGA analysis

Suspensions of metal nanowires in CH_3OH obtained from the liberation process were dried under reduced pressure in glass vials containing 1 cm × 1 cm silicon wafers on the bottom. The nanowires were sedimented and dried onto the Si slide. The X-ray Photoelectron Spectra (XPS) and X-ray diffraction (XRD) patterns were immediately collected, limiting air exposure to less than 30 min.

The diffraction peak of the silicon wafer was removed by excluding the diffraction spot arising from the single crystal silicon from the integration of the 2D image of XRD to produce the 2θ plot. For TGA analysis, samples of nanowires were dried under reduced pressure, introduced into the TG analyzer and heated from room temperature to 550 °C at 10 °C/min under nitrogen.

2.2.7 Depth profiling of pore-filling

Following electrodeposition into 5 cm × 11 cm electrodes the surfaces were cleaned (0.5 μm removed from the surface) or ion-milled (10 μm removed from the surface) using an Oxford Ion Fab 300+ ion mill. The surfaces were characterized by SEM, and the percentage of pores filled to the top of the new surface was determined using the cell counter plugin developed for ImageJ 1.35j image analysis software (Wayne Rasband, National Institutes of Health, USA, http://rsb.info.nih.gov/ij/).

2.2.8 Instrumentation

Characterization of the nanowires was accomplished by scanning electron microscopy (SEM) using a JEOL 6301F FESEM equipped with an energy dispersive X-ray spectrometer (EDX), X-ray diffraction (XRD) using a Bruker AXS D8 Discover with GADDS detector, X-ray photoelectron spectroscopy (XPS) with a Kratos Axis Ultra or Kratos Axis 165 spectrometer, transmission electron microscopy (TEM) using a JEOL 2010 equipped with a CCD camera and EDX spectrometer, and thermogravimetric analysis using a Perkin Elmer Thermogravimetric Analyzer (Pyris 1 TGA).

2.3 Results

2.3.1 Template directed-synthesis of CuNWs

CuNWs are produced by AC electrodeposition into PAO templates followed by dissolution of the alumina in acidic (H_3PO_4) or basic (NaOH) aqueous solutions. This section deals with the development of, and results obtained for, AC electrodeposition of CuNWs.

2.3.1.1 Micrometer-sized edge cracks

Anodization of both faces of bare Al plate resulted in the formation of ~ 10 micrometer sized cracks on all 90° edges as a consequence of the volume expansion accompanying conversion of Al to Al_2O_3 that leads to mechanical stress at the electrode edge (Fig. 2.5a). When these edge-cracks were not coated before electrodeposition under continuous AC conditions, most Cu was deposited in them, because the diffusion limitation into the ~ 10 micrometer cracks is far less than the diffusion limitation into the ~ 20 nm diameter, 18, 27, and 36 μm deep pores (Fig. 2.5b). Pulsed electrodeposition conditions might be used to minimize the effect of this parasitic pathway by introducing a "hold-time" between deposition pulses to allow diffusion of $Cu^{2+}(aq)$ into the pores, but at the expense of greatly increasing the time required for the electrodeposition to be completed. It was more efficient to coat the edges of the electrodes with nail polish to prevent electrodeposition in the cracks and enable continuous AC conditions to be used. The coating is removed with acetone after the electrodeposition, facilitating the reutilization of the aluminum after harvesting the nanowires.

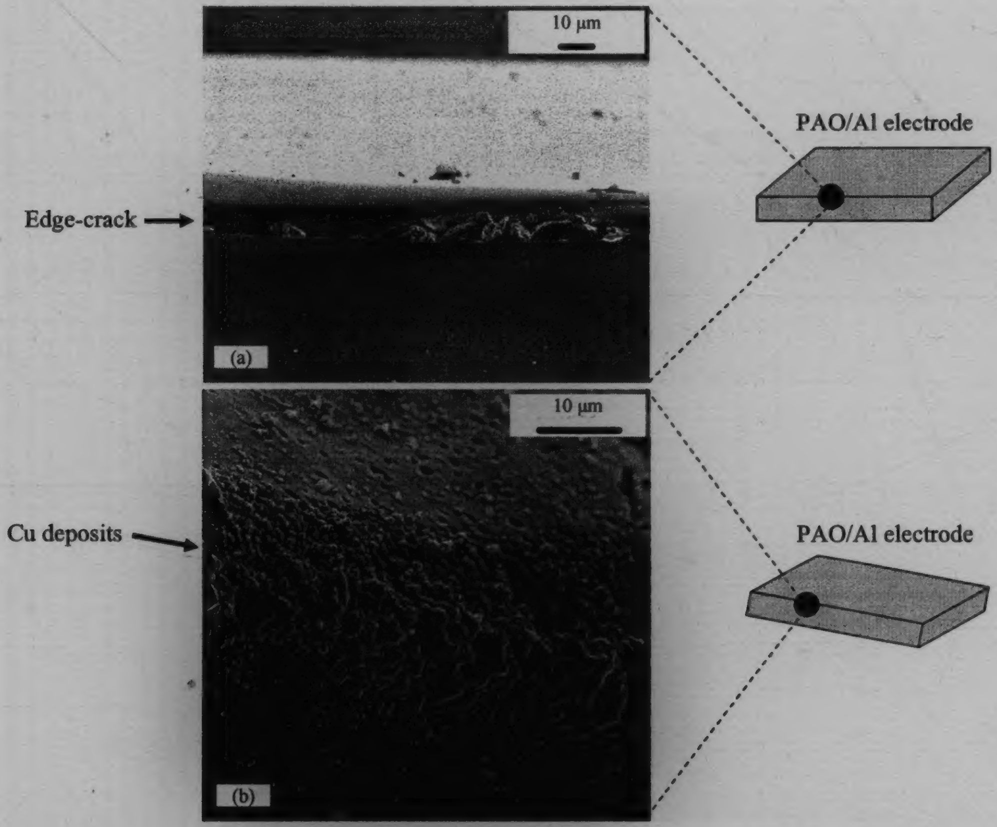

Figure 2.5. SEM of (a) micron-size crack that forms on 90 degree edges and (b) bulk deposition of Cu that occurs at the crack if it is not coated before AC electrodeposition.

2.3.1.2 Effect of counter electrode on electrolyte stability and electrodeposition time

In prior work with small-area electrodes (1.5 cm^2 Al), platinum or stainless steel counter-electrodes were used for Cu electrodeposition utilizing a $CuSO_4$ (aq) solution.[8] With large area aluminum electrodes, Pt counter electrodes are not recommended as they are very expensive. For 90 cm^2 Al electrodes in this work, electrodeposition using 304 stainless steel counter electrode, demonstrated that the electrolyte solution could only be used twice before deposition quality was adversely affected and the yield of Cu nanowires decreased substantially. The pH of the electrolyte decreased with each electrode into which Cu was electrodeposited.

Table 2.1 shows the electrochemical cells and possible half reactions during the negative pulse of the AC voltage that leads to copper electrodeposition in the PAO templates. The primary electrochemically active species considered are Cu^{2+}(aq), H^+(aq) and H_2O. As the barrier layer at the bottom of the pores passes current preferentially in the cathodic direction, copper electrodeposition occurs in the PAO during the negative pulse. Simultaneously, an anodic reaction occurs at the counter electrode to allow current flow and maintain electroneutrality. Table 2.1 indicates that the decrease in pH might have been due to the evolution of O_2(aq) and H^+(aq) ions from the anodic reaction of water at the stainless steel counter electrodes.

Table 2.1. Representation of electrochemical cells and half reactions for AC electrodeposition of copper into PAO templates (Standard electrode potentials at 25 °C vs NHE in aqueous solutions).

1. Stainless steel | Cu^{2+} (0.5M), H_3BO_3 (0.285 M) | PAO
2. Cu | Cu^{2+} (0.5M), H_3BO_3 (0.285 M) | PAO

Anodic reactions		Cathodic reactions	
$2H_2O \rightarrow O_2 + 4H^+ + 4e$	$E^0 = -1.23$ V	$Cu^{2+} + 2e \rightarrow Cu$	$E^0 = +0.34$ V
$Cu \rightarrow Cu^{2+} + 2e$	$E^0 = -0.34$ V	$2H_2O + 2e \rightarrow H_2 + 2OH^-$	$E^0 = +0.83$ V

Given the decrease of pH observed with stainless steel electrodes, copper plates were introduced as counter electrode for electrodeposition. It is worth mentioning that a pH < 3 can decrease the stability of the porous aluminum oxide.[16] Table 2.2 shows the effect of changing from stainless steel to copper counter electrodes on the time required to fill 36 μm deep PAO templates, as well as on the pH of the electrolyte after only one electrodeposition. Using stainless steel, the pH decreased to 2.75 after only one electrodeposition which took 40 minutes to complete. By contrast, a less significant pH change occurred when using Cu as the counter electrode and the pH was relatively stable for deposition into tens of electrodes; for instance, it took 50 electrodepositions using the same electrolyte for the pH to decrease to the same degree observed after only one electrodeposition using stainless steel counter electrodes. By using copper as the counter electrodes, the dissolution of Cu is the most favorable anodic reaction accompanying the cathodic reaction of Cu in the PAO template, which replenishes the Cu^{2+}(aq) ions in the electrolyte. A small decrease in the pH of the electrolyte using Cu as the counter electrodes indicates that the AC voltage applied might still supply the overpotential required for the electrochemical oxidation of water at the Cu counter electrode.

Table 2.2. Influence of counter electrode on time required for copper electrodeposition and the final pH of the electrodeposition solution containing 0.5 M $CuSO_4$ and 0.285 M H_3BO_3. (Aluminum electrodes used were 11 × 5 cm^2 and the deposition conditions were 10 Vrms and 200 Hz continuous sine waves).

Counter electrode	Initial pH	Electrodeposition time (min)	Final pH of solution
Stainless steel	3.40	40	2.75
Copper	3.40	15	3.22

In summary, using copper instead of stainless steel as the counter electrodes enabled less significant changes in pH during electrodeposition, shorter times for electrodeposition, and more consistent results for tens of electrodepositions. The enhancement in the kinetics of Cu electrodeposition may be the result of changes in the overpotential required for the electrochemical reactions using different counter electrodes. The complexity of AC electrodeposition on PAO templates would require a thorough study of the electrochemical process not only involving heterogeneous reactions occurring in electrodes acting as cathode and anode sequentially, but also reactions involving the solid state equilibria of the barrier layer at the bottom of the PAO templates. These studies may be the subject of future work.

2.3.1.3 Effect of pore depth on yield

Figure 2.6 shows cross sections of PAO templates prepared in H_2SO_4 acid solutions for which the second anodization step was held for 4, 6 and 8 hours. The thickness of the PAO templates were 18, 27, and 36 μm, giving an average PAO thickness growth rate of 4.5 μm/h, including the barrier layer thinning step. Figure 2.7 shows that the mass of nanowires produced per cm^2 of electrode area increases approximately linearly with pore depth, over the range of anodization times investigated (4 h, 6 h, and 8 h).

Figure 2.8 shows SEM images of top surfaces of a 36 μm thick PAO template filled with Cu and then ion milled to show the degree of pore-filling at 0.5 and 10 μm below the initial surface. Pores filled with Cu appear as bright spots. The fraction of pores filled to a level 0.5 μm below the surface of 36 μm deep pores is ~ 20% (Fig 2.8a), while the fraction filled to a level 10 μm below the initial surface is 60% (Fig 2.8b). The fraction of pores filled as a function of depth beneath the initial electrode surface is comparable to that reported previously for small-area electrodes (1 cm × 1.5 cm) filled using pulsed sine wave electrodeposition conditions,[8] except that the pores utilized in this work were deeper and deposition required only 1/3 to 1/4 as long.

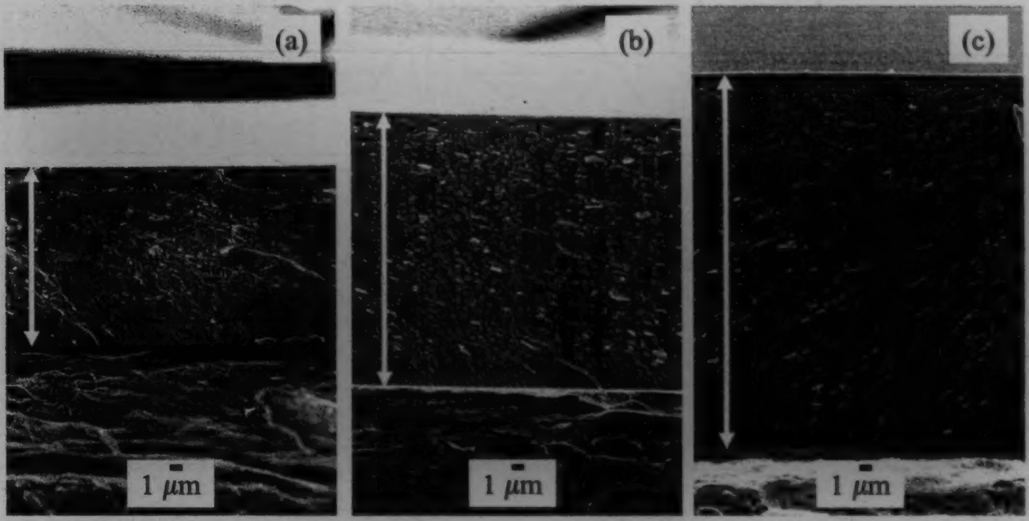

Figure 2.6. SEM images of cross sections of PAO templates prepared in 0.3 M H_2SO_4(aq) solutions for different anodization times: (a) 4 h, (b) 6 h, and (c) 8 h. The arrows indicate the thickness of the PAO templates: (a) 18 μm, (b) 27 μm, and (c) 36 μm.

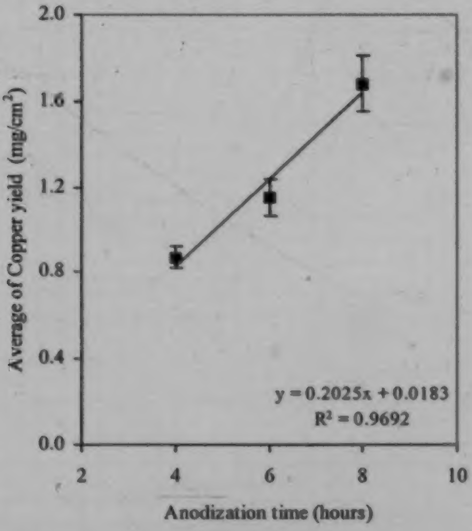

Figure 2.7. Yield of Cu nanowires from PAO templates prepared by anodization for different times in 0.3M H_2SO_4 solutions (4, 6, or 8 hours corresponding to 18, 27 or 36 μm thick PAO templates, respectively). The line corresponds to the linear least-square fit of the average yields. The standard deviations were calculated from five replicates.

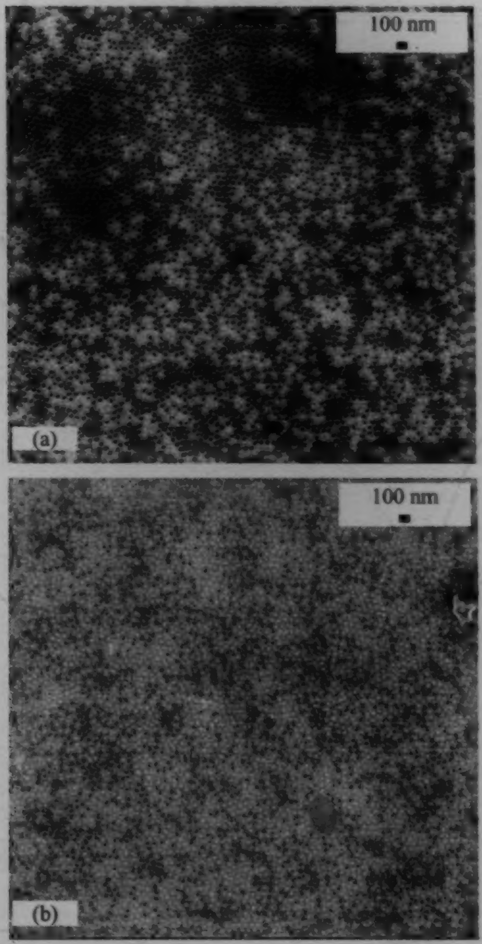

Figure 2.8. SEM images of top surfaces of ion-milled Cu-filled PAO templates (5 cm × 11 cm electrodes) to show degree of pore-filling as a function of depth: (a) 0.5 μm and (b) 10 μm removed from the top of 36 μm deep-pores.

2.3.1.4 Electrode size and yield

One of the limitations encountered in the scale-up of the process was the ability to supply sufficient current during each deposition pulse. In particular, during the first seconds of electrodeposition a much higher current is required, because the bulk concentration of Cu^{2+} (i.e. the concentration of Cu^{2+} in the electrolyte) is present at the pore bottoms. As the deposition continues, the Cu^{2+} concentration depletes to a steady-state value and a lower current is required. However, it appears that this initial, high-current period is critical to nucleating and depositing Cu in all of the pore bottoms. The amplifier used was limited to I_{rms} 30 A peak current (before it goes into protection mode). The smaller 5 cm × 11 cm electrodes initially require I_{rms} 15 A current which declines to a steady-state I_{rms} 5 A current after 60 seconds. The larger 10 cm × 25 cm electrodes required $I_{rms} > 30$ A current initially, and declined to a steady-state current of I_{rms} 15-20 A after 60 seconds. A higher yield of copper nanowires per unit electrode area was obtained from the 5 cm × 11 cm electrodes (1.68 mg/cm^2, 756 ± 58.5 mg per batch) than from the larger 10 cm × 25 cm electrodes (0.786 mg/cm^2, 3,459 ± 270 mg per batch). The yield per cm^2 for the 10 cm × 25 cm electrodes was ~ 50 % of the yield obtained for the smaller electrodes.

2.3.2 Dissolution of PAO templates and CuNW liberation

Two different solutions of H_3PO_4(aq) and NaOH(aq) were used to dissolve the alumina and release the nanowires electrodeposited into the pores. Acidic or basic conditions were expected to produce different surface chemistry on the liberated nanowires. The results obtained with different liberation procedures are described as follows.

2.3.2.1 Effect of liberation process on morphology and dispersion of CuNWs

A first step in the liberation consisted of removing the bulk overgrowth that occurs due to the differences in the growth rate of nanowires from pore to pore. Typical copper deposits at the surface of the filled PAO templates are shown in Figure 2.9a. This bulk overgrowth was removed by immersing the electrode for 1 minute in a solution of 0.6 M H_3PO_4 at 60 °C. The slow etching of the alumina surface in the acidic solution exposed the tips of the nanowires and enabled us to wipe away the copper deposits at the surface of the electrode (Fig. 2.9b) leaving the pores with copper nanowires free of mushroom-shaped tips.

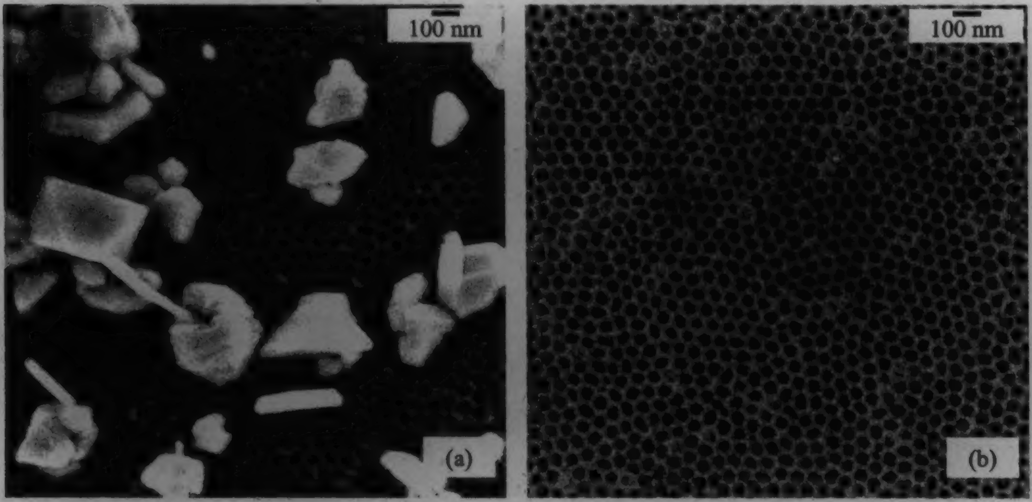

Figure 2.9. SEM images of porous alumina template surfaces (a) after CuNW electrodeposition and (b) after CuNW electrodeposition and surface wiping. The images show the removal of bulk overgrowth before CuNW liberation.

Scanning electron microscopy images indicate that the nanowires liberated by dissolving the PAO template in 0.6 M H_3PO_4 (Figure 2.10a and b) are significantly less dispersed than those liberated by dissolving the PAO template in 1.0 M NaOH (aq) (Figure 2.10 c and d). In addition, the morphology of copper nanowires liberated using H_3PO_4 does not replicate that of the PAO templates. An average diameter of 69 ± 19 nm for H_3PO_4-liberated nanowires shows a significant increase in diameter (coarsening) when compared to the average diameter of 25 ± 4 nm for nanowires liberated in NaOH. In addition, the H_3PO_4-liberated nanowires display noticeable oscillations in diameter along their length.

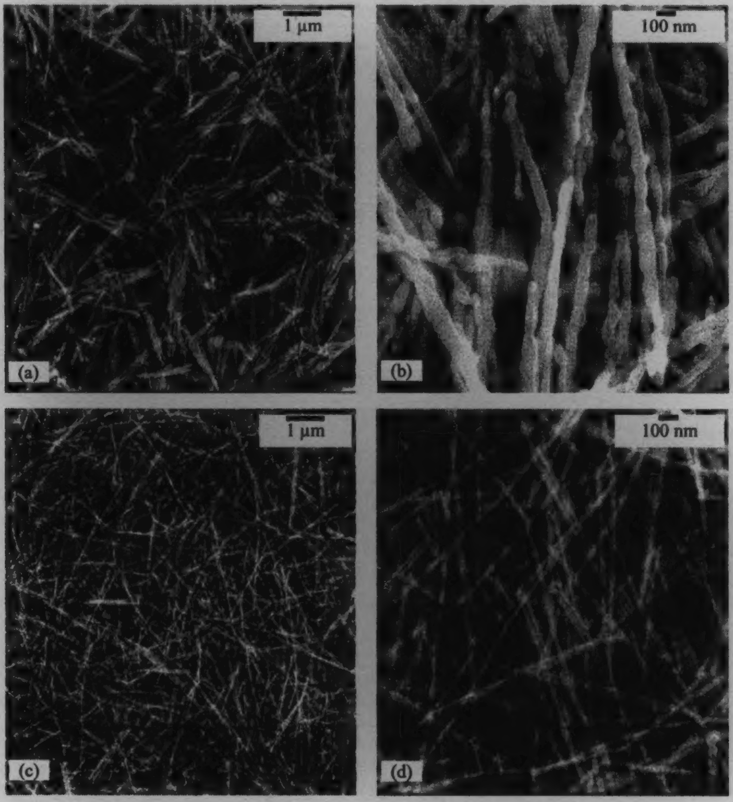

Figure 2.10. SEM of (a) and (b) 0.6 M H_3PO_4-liberated CuNWs and (c) and (d) 1.0 M NaOH-liberated CuNWs.

Figure 2.11 shows SEM images of copper nanowires liberated using H_3PO_4 right after the step of alumina dissolution without application of ultrasound. The nanowires coarsened during the 30 minute process of alumina dissolution.

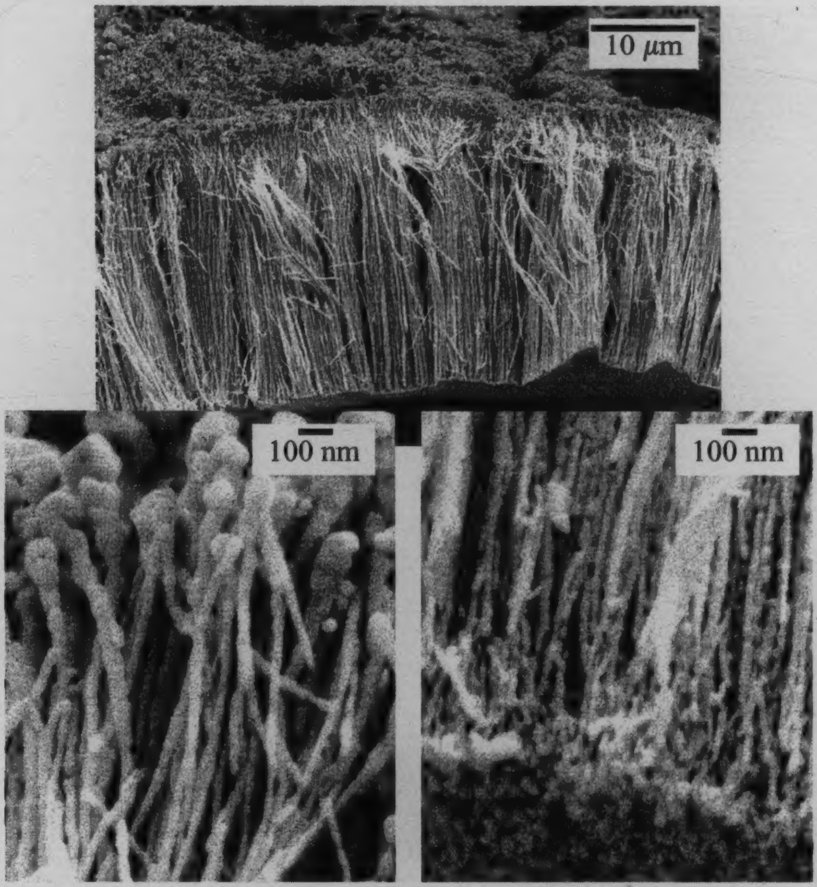

Figure 2.11. Copper nanowires after dissolution of the PAO template in 0.6 M H_3PO_4(aq) solution at 60 °C. The images indicate that coarsening of the nanowires occurred during the 30 minute dissolution of the PAO template. The tips of the nanowires are more exposed to the H_3PO_4(aq) solution and become thicker than the bottoms.

2.3.2.2 Effect of liberation process on surface chemistry of CuNWs

Figure 2.12 shows the XRD patterns for CuNWs liberated in H_3PO_4(aq) and NaOH(aq) solutions. The origin of small peaks at low angles in Fig. 2.12.a was not identified. XRD patterns collected from NWs after liberation (< 30 min of air exposure) show no evidence of crystalline oxides (CuO or Cu_2O). The diffraction peaks were assigned to the fcc lattice of Cu. The intensity ratios of (111) to (200) and (111) to (220) were 3.2 and 7.7 for H_3PO_4-liberated CuNWs, and 4.4 and 8.8 for NaOH-liberated CuNWs, which when compared to the intensity ratios from the standard powder pattern JCPDS 4-836 (2.2 and 5.0) indicate that the CuNWs have a slightly preferred orientation along the (111) planes. The difference between the intensity ratios of H_3PO_4(aq) and NaOH(aq) liberated NWs may be related to the coarsening phenomenon in acidic solution.

Figure 2.13 show the XPS survey spectra and high resolution XP spectra of Cu(2p) and Cu($L_3M_{4.5}M_{4.5}$) Auger peaks for CuNWs liberated in acidic and basic solutions. The XP spectra of a sputtered copper foil was also obtained using similar conditions in order to compare the XP spectra of the nanowires to that of elemental copper. The survey spectra of liberated nanowires showed good purity of the nanowires with no presence of residual Al from the PAO dissolution, but some P and Na impurities from the acidic and basic solutions (Fig. 2.13a). The presence of surface oxide (CuO) is evidenced from the satellite peaks indicated by stars in the Cu2p spectra (Fig. 2.13b). XPS collected immediately after liberation

(<30 minutes air exposure) indicates little surface oxidation of the nanowires liberated by either method (Fig. 2.13b). After exposure of the liberated copper nanowires to atmosphere for 3 days, the satellite peaks are more prominent, indicating surface oxidation of CuNWs. This is corroborated by the increase in intensity of the O1s peak observed from the XPS survey of nanowires exposed to air for < 30 min versus exposure for 3 days. To elucidate if a different degree of oxidation is obtained in acidic or basic solutions, the Cu Auger peak was used. The $Cu(L_3M_{4.5}M_{4.5})$ Auger spectra in Figure 2.13c for nanowires exposed to air for <30 min or 3 days clearly show that the NaOH-liberated nanowires have a larger fraction of oxidized Cu(I) on their surface than do the H_3PO_4-liberated nanowires.[17,18]

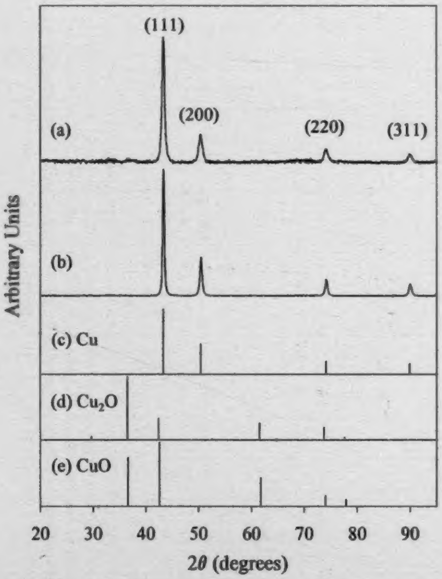

Figure 2.12. X-ray diffractograms of Cu nanowires (a) liberated in 1 M NaOH solutions, and (b) liberated in 0.6M H_3PO_4 solutions. Standard powder patterns for (c) Cu (JCPDS 4-836), (d) Cu_2O (JCPDS 77-199), and (e) CuO (JCPDS 78-428). The nanowires were exposed to air for less than 30 minutes before the analysis.

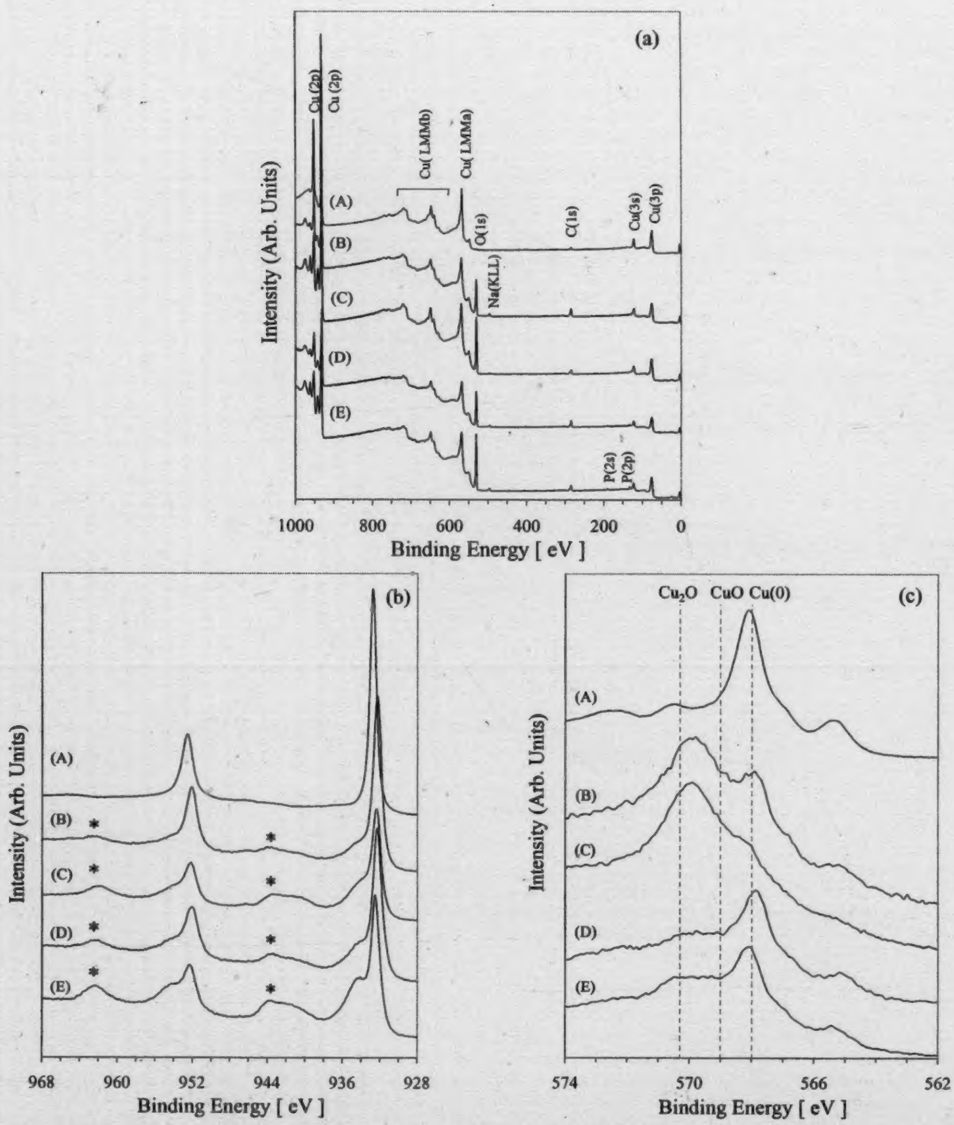

Figure 2.13. X-ray photoelectron spectra of Cu foil and CuNWs. (a) Surveys, (b) high resolution XP spectra of Cu(2p) peak, and (c) high resolution XP spectra of Cu(L$_3$M$_{4.5}$M$_{4.5}$) Auger peak. The spectra correspond to (A) sputter-cleaned Cu foil, (B, C) NaOH-liberated CuNWs exposed to air for (B) <30 min. and (C) 3 days, and (D, E) H$_3$PO$_4$-liberated CuNWs exposed to air for (D) <30 min. and (E) 3 days. Satellite peaks on Cu(2p) spectra labeled with an * indicate the presence of Cu(II) species, such as CuO. Dashed lines indicate the shift of the most intense component of the Cu(L$_3$M$_{4.5}$M$_{4.5}$) peak from Cu(0) to Cu(I) and Cu(II).

2.3.2.3 Length distribution of CuNWs

Although the pores of the PAO template are quite well filled to depths of 30 μm, the length of the liberated nanowires is significantly less. Figure 2.14 presents SEM images obtained for the measurement of the length distribution of NaOH-liberated CuNWs. An average length of 1.78 ± 1.37 *μm* was obtained for nanowires from the smaller-scale process, while the average length was 1.29 ± 0.83 *μm* for the nanowires obtained from the larger-scale process. Even when grown in pores 36 μm deep, after fragmentation during the liberation process, 86 % of CuNWs obtained from the smaller-scale process and 95 % of CuNWs obtained from the larger-scale process are < 3 μm in length (Figure 2.14). For these 25 nm diameter nanowires, however, this still translates into high average aspect ratios of 71 and 52.

2.3.2.4 Transmission electron microscopy and thermogravimetric analysis of CuNWs

Figure 2.15 shows TEM images of copper nanowires liberated in NaOH(aq). Polycrystalline grains are observed from the TEM images. Figure 2.15b shows a typical TEM image of a small segment of a copper nanowire and the corresponding selected area electron diffraction pattern (SAED). The diffraction pattern shows the polycrystalline nature of the copper nanowires produced by the AC electrodeposition conditions used in this study. Table 2.3 shows the d-spacings measured from the diffraction pattern and the corresponding planes for Cu nanowires. In the case of single-crystal Cu nanowires, works by Mallouk and co-workers using DC electrodeposition have demonstrated that nanowires grow primarily along the [111] direction.[10,19] In this case, AC electrodeposition may have introduced more defects and produced smaller crystallite sizes during the growth of nanowires, given the changing characteristic of the sinusoidal wave compared to the uniform conditions provided by DC electrodeposition conditions used in prior work.[10,19]

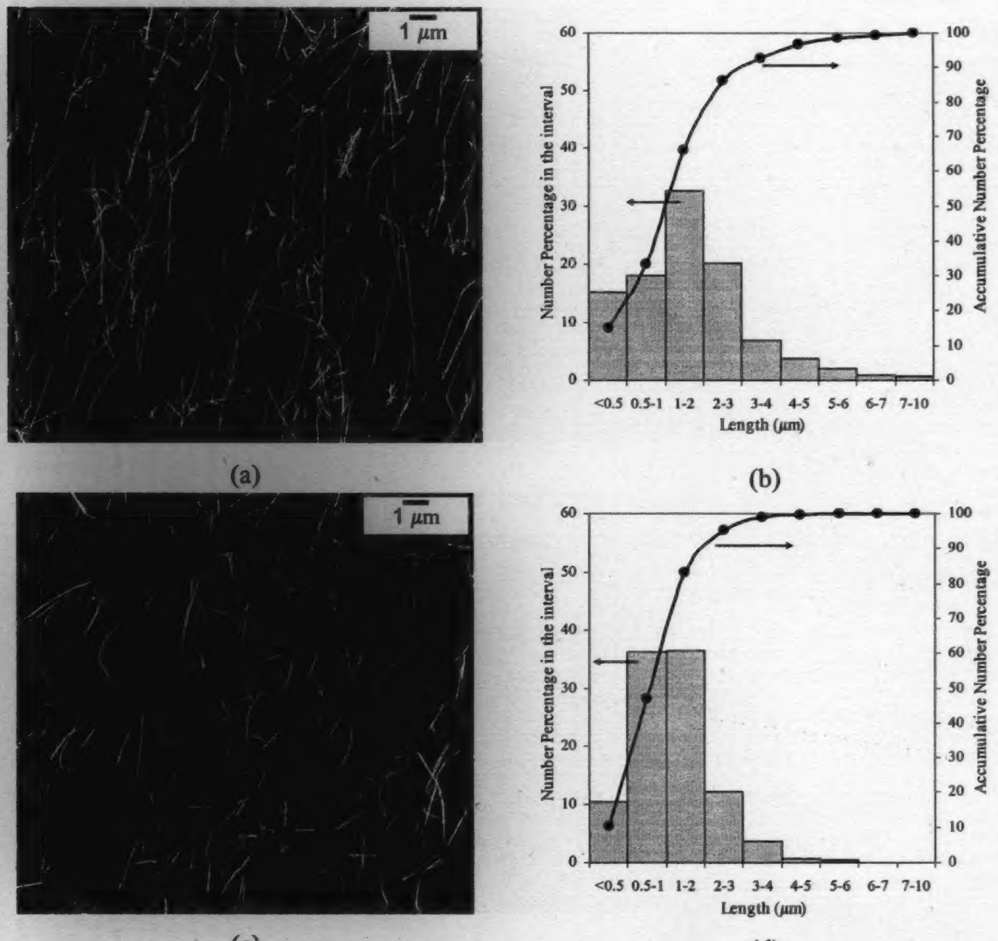

(c) (d)

Figure 2.14. SEM images and length distribution of copper nanowires grown in PAO templates anodized for 8 hours and liberated using 1.0 M NaOH(aq) produced using (a,b) smaller-scale process (1.78 ± 1.37 μm) and (c,d) larger-scale process (1.29 ± 0.83 μm). Lines are guides to the eye.

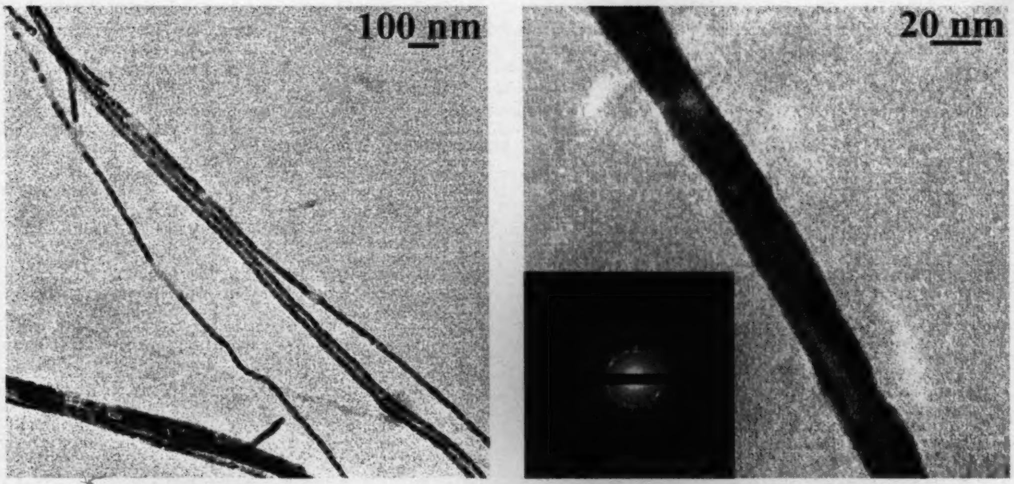

(a) (b)

Figure 2.15. (a) Low magnification and (b) high magnification TEM images of copper nanowires liberated from PAO templates using 1.0 M NaOH(aq). The inset corresponds to SAED of the nanowire in (b).

Table 2.3. Measured d-spacings and corresponding planes from electron diffraction pattern for Cu nanowires (Length of camera = 100 cm, 200 kV).

(hkl)	d (Å)
(111)	2.0880
(200)	1.8080
(220)	1.2780
(311)	1.0900

The result of thermogravimetric analysis of NaOH-liberated CuNWs when heated up to 550 °C is shown in Figure 2.16. A mass loss of 4.0 % was registered at ~ 120 °C. This mass decrease is consistent with desorption of methoxy adsorbates from the CuNW surfaces.[20]

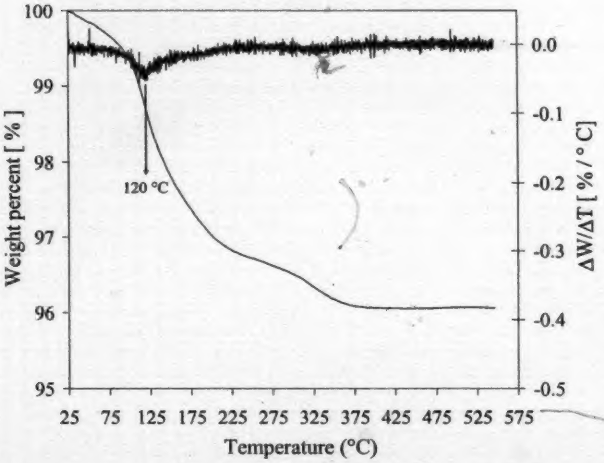

Figure 2.16. Thermogravimetric analysis of NaOH-liberated CuNWs heated to 550 °C under nitrogen at 10 °C/minute.

2.3.3 Template directed-synthesis of AgNWs

In an effort to demonstrate the applicability of the synthesis of nanowires using AC electrodeposition into PAO templates as described in the previous section, and considering the good electrical conductivity of silver for the purpose of preparation of metal nanowire/polymer nanocomposites, silver nanowires were synthesized into PAO templates. The results of AC electrodeposition of silver and the characterization of Ag nanowires are described below.

2.3.3.1 Effect of AC signal on Ag electrodeposition into PAO templates

The AC electrodeposition of nanomaterials into PAO templates with good pore-filling is a challenging process. For instance, silver electrodeposition into PAO templates could not be achieved using the continuous sine waves (9.0 to 10.0 V_{rms}, 200 Hz) successfully utilized for the synthesis of copper nanowires.[21] The rectification provided by the alumina barrier layer quickly disappeared. Silver deposition initially occurred, but the metal deposited in the pores during the first seconds of the electrodeposition was completely reoxidized after 30 to 60 seconds, as evidenced by the coloration and subsequent decoloration of the electrode. In addition, gas evolution was significant, indicating the presence of side reactions at the PAO electrode. Electrodeposition using AC conditions cannot be realized without the rectification provided by the barrier layer. Thus, continuous sine waves could not be used for the synthesis of silver nanowires, instead pulsed AC signals were utilized.[22] The electrodeposition conditions for synthesis of Ag nanowires on 90 cm^2 electrodes were selected based on the results of preliminary experiments utilizing 10 cm^2 Al electrodes using pulsed sinusoidal (8.0 to 9.5 V_{rms}) and pulsed square waves (7.5 to 9.0 V_p), with different pulse polarities (negative followed by positive, and positive followed by negative). Electrodeposition of silver into 90 cm^2 electrodes using pulsed voltage square waves of 8.0 V_p, 10 ms pulse width, pulsed every 400 ms, and the reductive followed by oxidative pulse polarity (Figure 2.4) for 90 min had an average yield of ~ 0.9 mg/cm^2 (405 mg/batch).

2.3.3.2 Effect of liberation process on morphology of AgNWs

Electron microscopy images show that NaOH-liberated AgNWs were well dispersed (Fig. 2.17). A diameter of 25 nm measured on individual silver nanowires from SEM and TEM images corresponded well to the pore diameter of the PAO templates used in this study. By contrast, scanning electron microscopy images indicate that Ag nanowires had a significant change in morphology when liberated in 60 °C, 0.6 M H_3PO_4 (Fig. 2.18). Individual and long silver nanowires as those observed from liberation in NaOH were not observed, instead an intricate silver nanostructure was formed. The reasons for the transformation of silver nanowires during the PAO dissolution in phosphoric acid solution are not clear; however, the change in the morphology of the nanowires compared to the NaOH-liberated AgNWs as well as CuNWs implies that 25 nm nanowires presented significant instability in H_3PO_4 solutions and indicates that acidic solutions are not recommended for the liberation of base metal nanowires such as Cu and Ag.

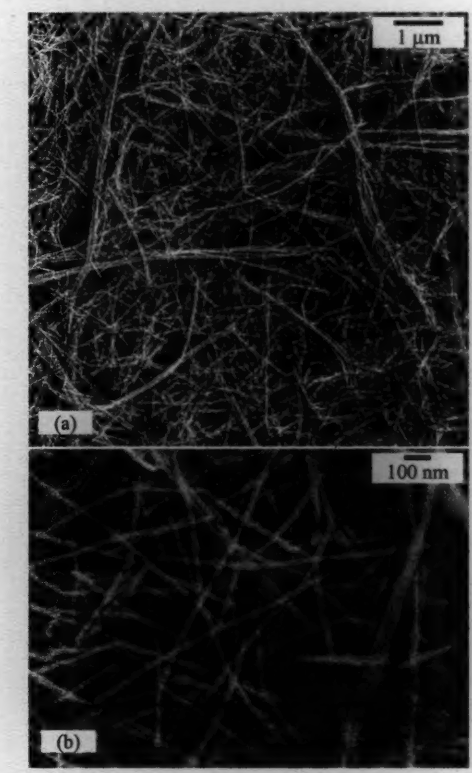

Figure 2.17. SEM images of AgNWs liberated using 1.0 M NaOH(aq) (a) low magnification (b) high magnification.

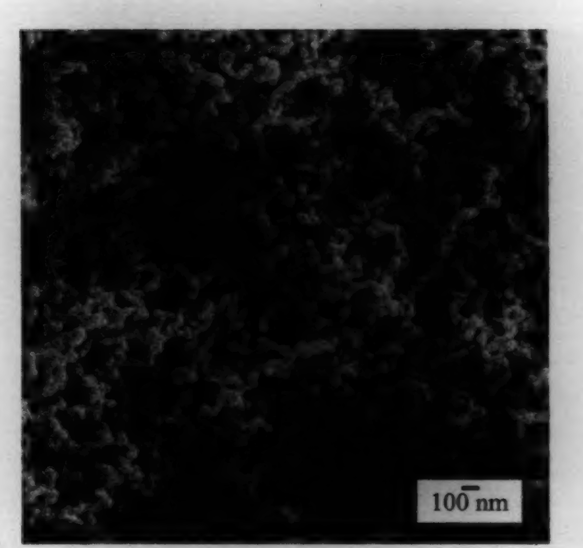

Figure 2.18. SEM image of Ag nanostructure resulting from the liberation of AgNWs from PAO templates using 0.6 M H_3PO_4 at 60 °C.

2.3.3.3 Characterization of AgNWs

Silver nanowires were liberated by dissolving the PAO template in 1.0 M NaOH (aq) and dispersed in methanol using ultrasound. Thermal gravimetric analysis (TGA) of silver nanowires indicated a weight loss of only 0.64 wt % when heated to 550 °C under N_2. The XRD pattern of silver nanowires after liberation from the PAO template is shown in Figure 2.19. The diffraction peaks were assigned to the fcc structure of silver. The intensity ratios of (111) to (200) and (111) to (220) were 2.3 and 5.1 respectively, which when compared to the intensity ratios from the standard powder pattern JCPDS (2.1 and 4.0) indicate that the silver nanowires may have a slightly preferred orientation along the (111) planes. No evidence of crystalline silver oxides was found by XRD. XP Spectra of liberated silver nanowires are shown in Figure 2.20. The Ag 3d doublet identified at 374.2 (Ag $3d_{3/2}$) and 368.2 eV (Ag $3d_{5/2}$) as well as the shape and position of the Auger peaks (Ag MNN) corresponded well to silver metal,[23,24] corroborating that oxide-free silver nanowires were produced by the synthesis and liberation method developed in this work. This also indicates that the presence of O(1s) XP peaks in the survey spectrum might have been due to the presence of atmospheric contaminants after a short exposure of the sample to room conditions before the analysis. In contrast to Ag nanowires, XPS indicated surface oxidation of Cu nanowires after liberation from the PAO templates.[21]

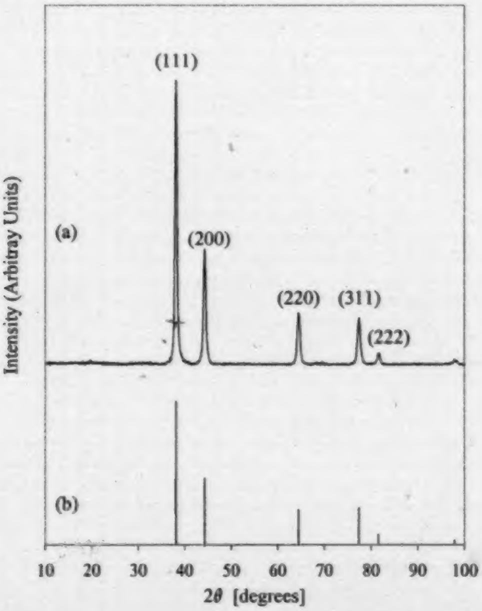

Figure 2.19. (a) X-ray diffractogram of Ag nanowires after liberation from the PAO template using 1.0 M NaOH(aq) and (b) Standard powder pattern for fcc silver (JCPDS 04-0783).

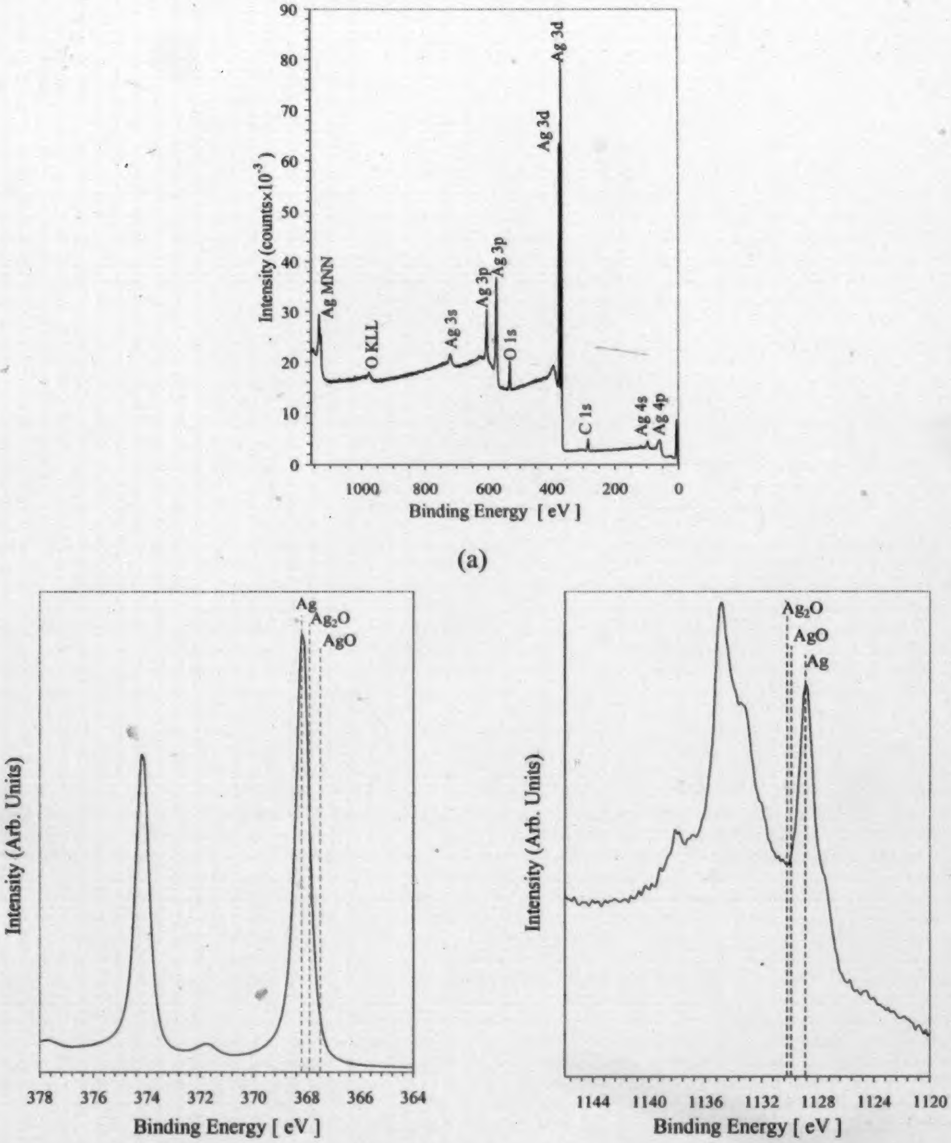

(a)

(b)

(c)

Figure 2.20 X-ray photoelectron spectra of AgNWs liberated in 1.0 M NaOH(aq), (a) Survey, (b) Ag(3d) peak, and (c) Ag(MNN) Auger peak. The spectra show that AgNWs do not have silver oxides at the surface.

Figure 2.21 shows TEM images of Ag nanowires liberated in NaOH, as well as electron diffraction pattern. Table 2.4 shows the d-spacings measured from the rings and the corresponding planes. Ag nanowires deposited by AC electrodeposition are polycrystalline as were the copper nanowires.

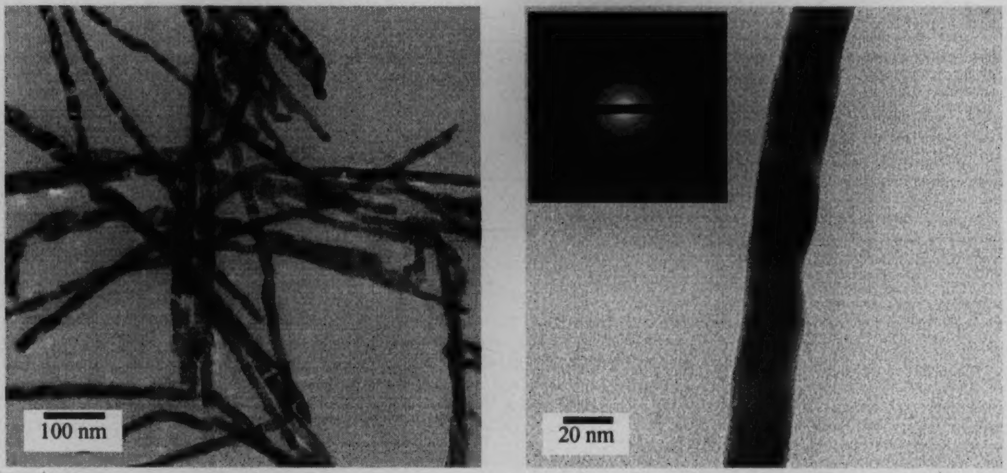

(a) (b)

Figure 2.21. (a) Low magnification and (b) high magnification TEM images of AgNWs liberated from PAO templates using NaOH (aq). The inset corresponds to SAED of the nanowire in (b).

Table 2.4. Measured d-spacings and corresponding planes from electron diffraction pattern for Ag nanowires (Camera length = 100 cm, 200 kV)

(hkl)	d (Å)
(111)	2.3590
(200)	2.0440
(220)	1.4450
(311)	1.2310

Assuming the 25 nm × 36 μm pores were completely filled with Ag, an aspect ratio of 1440 would be expected for the silver nanowires. However, the length distribution of the nanowires shown in Figure 2.22 demonstrates that ~ 97 % of the liberated Ag nanowires have lengths < 3.0 μm. An average length of 1.37 ± 0.76 μm was obtained. The liberation process and the necessary dispersion using ultrasound lead to nanowire fragmentation and a decrease in the length distribution. Although liberated nanowires showed lower aspect ratios (average *l/d* = 55) than expected (maximum *l/d* = 1,440 for nanowires that fill pores 25 nm in diameter and 36 *μ*m deep), these aspect ratios are still appropriate to obtain low percolation thresholds in metal/polymer nanocomposites.

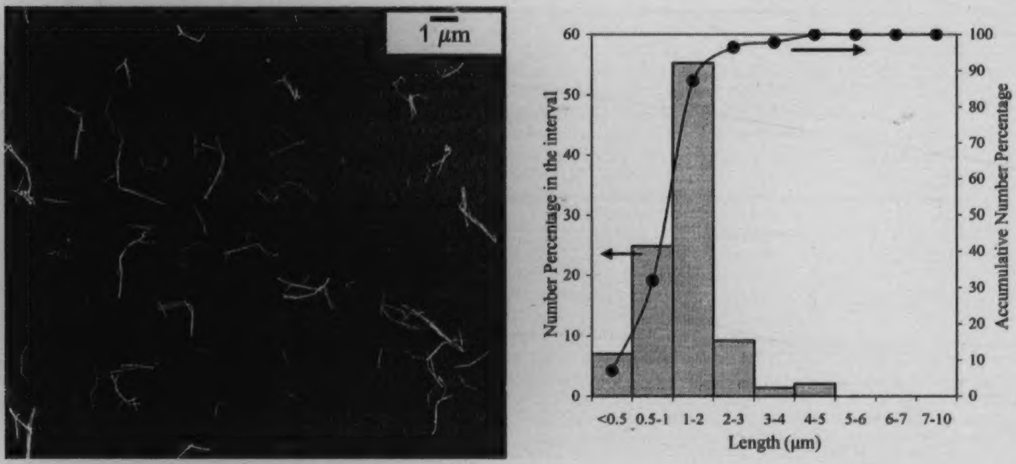

(a)

(b)

Figure 2.22. (a) Typical SEM image of AgNWs dispersed on a glass surface used to measure their length distribution, and (b) length distribution of AgNWs. AgNWs were prepared in PAO templates anodized for 8 hours and liberated using 1.0 M NaOH(aq). Average length = 1.37 ± 0.76 *μ*m. Line is a guide to the eye.

2.4 Discussion

PAO templates used in this study have been produced by a two-step anodization method.[13] The capacitance of the electrically insulating alumina barrier layer at the base of the pores (between the Al metal and the solution) prevents electrodeposition of materials using DC voltage or current signals. Nonetheless, AC signals can be utilized for electrodeposition, because Al is a valve metal and this barrier layer displays rectification by preferentially passing current in the cathodic direction. In this work, the barrier layer is thinned by slowly reducing the anodizing voltage from 25 to 9 V at the end of the 8 hour anodization process, so that AC signals can be used for electrosynthesis of metal nanowires without removing the alumina film from the aluminum electrode.

One of the advantages of the AC deposition technique over the DC deposition technique is the lower consumption of high-purity Al. As mentioned in Chapter 1, to perform DC electrodeposition into PAO templates grown on Al substrates, several processing steps are required before deposition: (1) the Al substrate is dissolved using $HgCl_2$ or CuCl(aq), (2) the barrier layer at the base of the pores is removed by dissolution in H_3PO_4(aq) (the pores are also widened), and (3) a metallic contact is deposited on one side of the membrane. Although DC electrodeposition enables greater control over the crystallinity and structure of the deposited nanowires, it is not easily scalable to produce grams of nanomaterials. In contrast, AC electrodeposition requires no additional processing steps, but finding conditions enabling uniform pore-filling and efficient utilization of the template is challenging. Most importantly, with AC deposition (once efficient voltage controlled deposition conditions are developed) scale-up to the multi-gram scale is possible. Besides, with AC electrodeposition, the Al substrate is not sacrificed. Once the nanowires are liberated by dissolution of the PAO template, the Al substrate can be re-anodized. Starting with 1 mm thick plate, each electrode was recycled 12 times before it was completely consumed.

Copper electrodeposition into PAO templates can be carried out using continuous or pulsed AC signals. In a related work developed in the Haber Group, on the effect of electrodeposition parameters upon the uniformity of pore-filling of PAO templates with Cu, it was noted that continuous AC deposition conditions produced significant damage in the PAO templates[8] and pulsed AC electrodeposition yielded less damage and uniform pore-filling. In this work, the voltage used for copper electrodeposition was 10 V_{rms} rather than the 14 V_{rms} used previously,[8] and evidence of damage to the PAO templates using these deposition conditions was not observed. Continuous sine waves for the electrodeposition of Cu were selected because it requires a fraction of the time to complete compared to pulsed depositions and produced similarly uniform pore-filling. In addition, the introduction of copper as a counter electrode favoured the kinetics of the electrodeposition process and provided enhanced control over the stability of the electrolyte, so that it could be reused for tens of electrodes without replenishment or pH regulation.

Based on the Pourbaix diagram of copper in an aqueous environment,[25] Cu nanowire surfaces are expected to be less susceptible to oxide formation during the H_3PO_4-liberation process than during the NaOH-liberation.[25] From studies of anodic oxidation of copper in aqueous solutions, it is widely accepted that a duplex film forms, composed of a bottom layer of Cu_2O formed during the initial stage of oxidation, and a top layer of $Cu(OH)_2$ or CuO formed primarily at the expense of the Cu_2O layer. The composition of the top layer is dependent on the conditions of the oxidation treatment and the composition of the aqueous electrolyte.[26,27] Copper surfaces exposed to acidic and basic solutions have shown different mechanisms of oxidation.[28] Acidic conditions resulted in Cu_2O-rich oxide layers, whereas strongly basic conditions (pH 13) resulted in a CuO-rich layer after 24 hours exposure. The presence of CuO is observed from the weak signals obtained for the satellite peaks in the Cu(2p) XP spectra of both NaOH- and H_3PO_4-liberated nanowires (Fig. 2.13b).[17] However, the $Cu(L_3M_{4,5}M_{4,5})$ Auger spectrum of NaOH-liberated nanowires has an intense signal corresponding to Cu_2O (at BE 569.8 eV) along with a less intense signal corresponding to Cu(0) at BE 567.9 eV.[18] In contrast, a signal corresponding primarily to Cu(0) was obtained for H_3PO_4-liberated nanowires indicating less surface oxidation (Fig. 2.13c). In conclusion, surface oxidation of copper nanowires occurred to some degree after liberation, but the kinetics of oxide formation is much slower when H_3PO_4 solutions were used. Unfortunately, surface quantification of Cu (I), Cu (II) and Cu (0) species is not possible from XPS and Auger peaks.[29,30]

It is believed that because the nanowires are held parallel to each other by the PAO and collapse together as a result of van der Waals forces,[31] the metallic surfaces exposed during H_3PO_4 liberation come in contact and irreversibly cold-weld,[32] such that each apparent nanowire may be actually a fused bundle of several nanowires. In contrast, liberation in NaOH solution produces a surface oxide or hydroxide layer[33,34] that inhibits the fusing process, ultimately yielding a finer nanowire dispersion (Fig. 2.23). The coarsening phenomenon and the diameter fluctuations observed for H_3PO_4-liberated nanowires might be related to instability of these high aspect ratio nanoparticles.[35] For example, Rayleigh instability of other types of nanowires has generally been observed after annealing of the nanoparticles at high temperatures.[35,36] The morphology variation in the Cu and Ag nanowires liberated in H_3PO_4(aq) was evident following the etching step at 60°C. The reason CuNWs with modulated diameters are obtained from H_3PO_4-liberation and not from NaOH-liberation is not clear, but it is believed that the phenomenon could be caused by enhanced diffusion of metal atoms promoted by factors such as surface chemistry, surface tension, pH, and temperature during the liberation process.

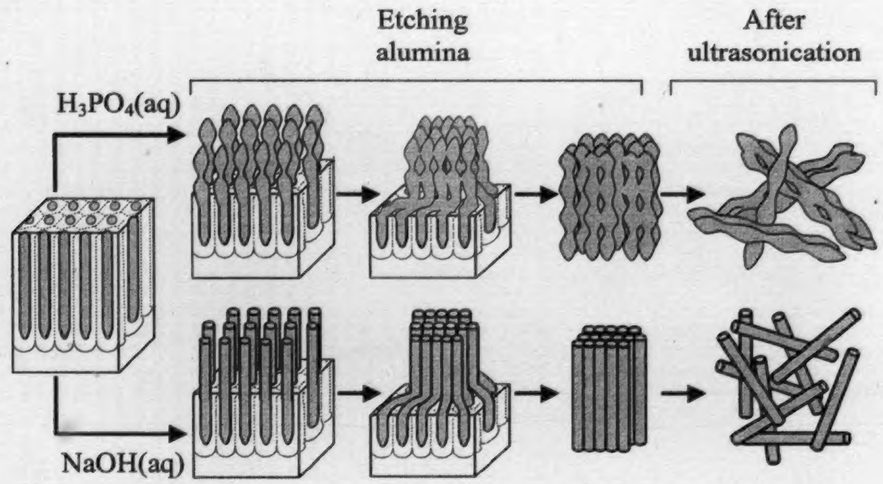

Figure 2.23. Schematic diagram comparing the surface chemistry and coarsening process for the Cu nanowires during liberation in 0.6 M H_3PO_4(aq) and 1.0 M NaOH(aq).

For AC electrodeposition of Ag nanowires into PAO templates, a pulsed AC signal was required. Experimental observations indicated that the barrier layer at the bottom of the pores lost rectification after a short time of applying a continuous sine wave. This result may be related to the electrical breakdown of the metal/insulator/metal junction (MIM). After deposition of a small amount of Ag into the PAO template (a few nanometers) an Al/Al-oxide/Ag system at the bottom of the pores must be considered. The electrical breakdown of valve-metal/valve-metal-oxide/silver tunnel junctions containing anodic oxides was reported by Hassel and Diesing.[37] The thickness of the anodic oxides studied was in the range of 2 - 15 nm, which compares well to the range of the barrier layer thickness expected for the PAO templates produced in this work. The main factor contributing to electrical breakdown of the junctions is the mobilization of ionic defects in the anodic film.[37] This process is activated when the voltage applied to the junction exceeds that utilized for anodization of the valve metal. The mobilization of ionic defects increases the current flow in the junction through resonant tunneling, causing local heating and activating a higher concentration of defects. This process results in distortion of the tunneling barrier leading to electrical breakdown.[38] The activation of defects increases with the voltage, temperature and time of polarization. Electrical breakdown in the Al/PAO/Ag junctions in the current work may have occurred by a similar process to that described by Hassel and Diesing. Thus, continuous sine waves (9-10 V_{rms}, 200 Hz) might have caused enhancement of mobilization of defects and local heating in the Al/PAO/Ag junction that resulted in the lost of rectification after a short period of electrodeposition. The use of pulsed AC electrodeposition with a delay time between pulses of 400 ms and lower voltage (8.0 V) than the final anodization voltage (9.0 V after barrier layer thinning) might have not only prevented local heating and electrical breakdown, but also contributed to the diffusion of silver ions from the bulk to the pore bottoms for the growth of Ag nanowires. The rectifying properties of the barrier layer were mantained by applying pulsed AC signals, providing succesful conditions for Ag electrodeposition at the expense of a significant increase in the time required for electrodeposition.

In the current work, electrical breakdown was not observed during Cu electrodeposition using continuous sinusoidal waves. However, studies in the Haber group related to the growth of Cu nanowires into different PAO templates indicated that migration of defects in the barrier layer during the electrodeposition may affect the efficiency of pore-filling.[8] The results obtained with continuous sinusoidal waves for Cu and Ag electrodeposition indicate the significant effect that the second metal may have on the electrical breakdown of the Al/PAO/metal junction and the loss of rectification that precludes the AC electrodeposition process. It is expected that different metals may lead to different trapezoidal potential barriers and different tunneling probability through the junction. Efforts towards the understanding of the AC electrodeposition process of different metals in PAO templates will require the characterization of the trapezoidal potential barriers in the Al/PAO/M junctions formed with different metals, more specifically, the determination of the energy levels (i.e. the differences between the Fermi levels of the second metal and the conduction band of the aluminum oxide and between Al and conduction band of aluminum oxide) and their relation to the tunnel current through the junction. One may expect that an increase in the tunnel current results in increased defect migration in the barrier layer, leading to localized heating and potentially to electrical breakdown.[37] Hence, finding conditions for high yield synthesis of nanowires of metals, compounds, or heterostructures in PAO templates is challenging, given the interplay of parameters such as those involved in the preparation of the PAO templates (anodization voltage, voltage after barrier layer thinning, temperature, acid and concentration), the Fermi levels of the metals or compounds that will form the junction, and electrodeposition conditions such as temperature and AC wave parameters: voltage, frequency, sinusoidal waves, square waves, triangular waves, continuous AC waves, pulsed AC waves, and pulse delay. Syntheses of copper and silver nanowires were successfully obtained in this work; however, there is plenty of room for further optimization and understanding of the AC electrodeposition process into PAO templates.

Silver nanowires synthesized as described in this study are oxide free, as demonstrated by XPS and XRD. As the nanowires have not been surface functionalized, only a weak physisorption of methanol is expected to result from the dispersion process. Indeed, TGA results showed an ~ 0.6 % weight loss upon heating the silver nanowires up to 550 °C, demonstrating that AgNWs are almost free of volatile surface adsorbed species. In the case of CuNWs, TGA showed 4 % weight decrease at a desorption temperature of 120 °C, which indicated chemisorption of methanol on CuNWs. Silver nanowires produced by this method are much cleaner than silver nanowires produced by the polyol process, from which purified Ag nanowires display a loss of 9 wt. % during heating to 500 °C, due to adsorption of ethylene glycol and PVP utilized in the synthesis.[39] However, AgNWs can be surface contaminated by adsorption and reaction during prolonged exposure to atmospheric gases, and they are transferred and stored under nitrogen atmosphere immediately after synthesis. For example, a recent study demonstrates that a silver sulfide shell and silver sulfide nanocrystal are likely to occur on the surface of silver nanowires synthesized by the polyol process when exposed to air under room conditions.[40] Traces of sulphur in the atmosphere such as CS_2 and H_2S could initiate the degradation and surface contamination of the nanowires given the high reactivity between silver and gaseous sulphur compounds, as well as the large surface area of the nanowires. Similarly, copper nanowires are prone to oxidation.[41-44] Hence, exposure of the metal nanowires to air after liberation from the PAO templates was minimized before their use in the preparation of metal nanowire/polymer nanocomposites.

2.5 Conclusions

Copper and silver nanowires have been synthesized by AC electrodeposition in PAO templates through the barrier layer of aluminum oxide located at the pore bottoms. The nanowires are harvested by dissolution of the template in basic aqueous solution and dispersion in methanol using ultrasound. NaOH-liberated copper and silver nanowires were characterized by SEM, TEM, XPS, and TGA. Good purity polycrystalline copper nanowires with little surface oxidation, as well as polycrystalline oxide-free silver nanowires were produced with average aspect-ratios ranging between 50 and 70, which are adequate for their use as electrically conductive nanofillers in polymer nanocomposites. The process allows production of gram quantities of nanowires and is amenable to adaptation for the synthesis of other metal or compound nanowires. In addition, the process facilitates reusing the aluminum for continuous preparation of nanowires and avoids intricated processing steps that otherwise would be required for large scale syntheses by DC electrodeposition in PAO templates. Figure 2.24 shows the scheme of the synthesis of nanowires in PAO templates coupled to the preparation of polymer nanocomposites.

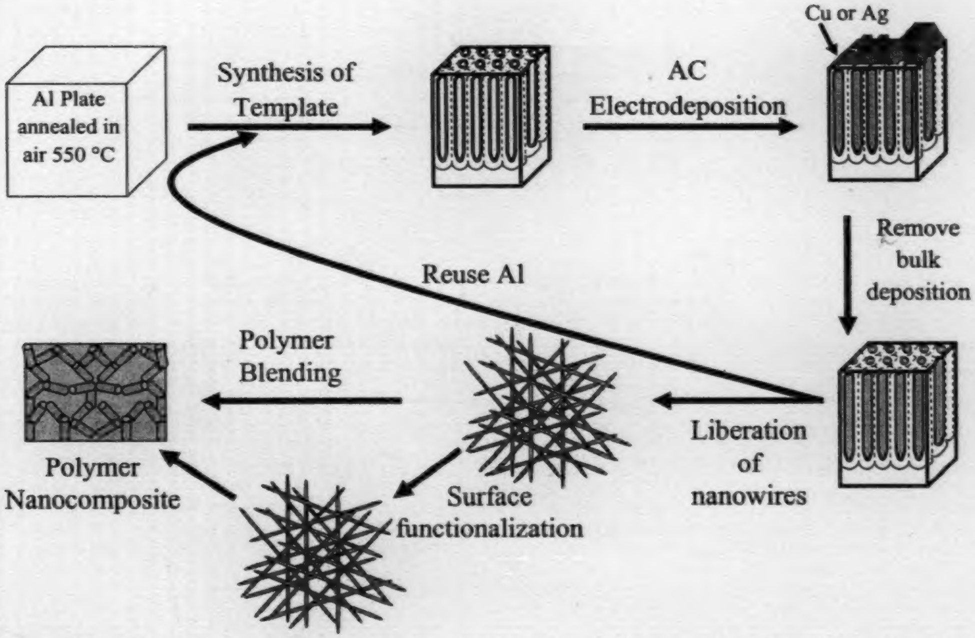

Figure 2.24. Overview of the synthesis of metal nanowires and preparation of polymer nanocomposites.

2.6 References

1. AlMawlawi, D.; Liu, C. Z.; Moskovits, M., *J. Mater. Res.* **1994,** 9, (4), 1014-1018.
2. Preston, C.; Moskovits, M., *J. Phys. Chem.* **1993,** 97, 8495-8503.
3. Davydov, D. N.; Sattari, P. A.; AlMawlawi, D.; Osika, A.; Haslett, T. L.; Moskovits, M., *J. Appl. Phys.* **1999,** 86, (7), 3983-3987.
4. Sun, M.; Zangari, G.; Metzger, R. M., *IEEE Trans. Magn.* **2000,** 36, (5), 3005-3008.
5. Sun, M.; Zangari, G.; Shamsuzzoha, M.; Metzger, R. M., *Appl. Phys. Lett.* **2001,** 78, (19), 2964-2966.

6. Nielsch, K.; Muller, F.; Li, A.-P.; Gosele, U., *Adv. Mater.* **2000,** 12, (8), 582-586.

7. Krantz, M. J.; Gelves, G. A.; Sundararaj, U.; Haber, J. A., *Mater. Res. Soc. Symp. Proc.* **2005,** 879E, Z7.20.1-6.

8. Gerein, N. J.; Haber, J. A., *J. Phys. Chem. B* **2005,** 109, (37), 17372-17385.

9. Sander, M. S.; Prieto, A. L.; Gronsky, R.; Sands, T.; Stacy, A. M., *Adv. Mater.* **2002,** 14, (9), 665-667.

10. Tian, M. L.; Wang, J. U.; Kurtz, J.; Mallouk, T. E.; Chan, M. H. W., *Nano Lett.* **2003,** 3, (7), 919-923.

11. Wang, J. G.; Tian, M. L.; Mallouk, T. E.; Chan, M. H. W., *Nano Lett.* **2004,** 4, (7), 1313-1318.

12. Nicewarner-Pena, S. R.; Freeman, R. G.; Reiss, B. D.; He, L.; Pena, D. J.; Walton, I. D.; Cromer, R.; Keating, C. D.; Natan, M. J., *Science* **2001,** 294, (5540), 137-141.

13. Masuda, H.; Fukuda, K., *Science* **1995,** 268, (5216), 1466-1468.

14. Said, M.I., *Eur. Appl. Pat.* 325097A1, 1989.

15. Martin, B. R.; Dermody, D. J.; Reiss, B. D.; Fang, M. M.; Lyon, L. A.; Natan, M. J.; Mallouk, T. E., *Adv. Mater.* **1999,** 11, (12), 1021-1025.

16. Bard, A. J., *Encyclopedia of electrochemistry of the elements*. Marcel Dekker: New York, 1973; Vol. VI.

17. Larson, P. E., *J. Electron Spectrosc. Relat. Phenom.* **1974,** 4, (3), 213-218.

18. McIntyre, N. S.; Cook, M. G., *Anal. Chem.* **1975,** 47, (13), 2208-2213.

19. Wang, J. G.; Tian, M. L.; Mallouk, T. E.; Chan, M. H. W., *J. Phys. Chem. B* **2004,** 108, (3), 841-845.

20. Sexton, B. A., *Surf. Sci.* **1979,** 88, (2-3), 299-318.

21. Gelves, G. A.; Murakami, Z. T. M.; Krantz, M. J.; Haber, J. A., *J. Mater. Chem.* **2006,** 16, (30), 3075-3083.

22. Sauer, G.; Brehm, G.; Schneider, S.; Nielsch, K.; Wehrspohn, R. B.; Choi, J.; Hofmeister, H.; Gosele, U., *J. Appl. Phys.* **2002,** 91, (5), 3243-3247.

23. Kaushik, V. K., *J. Electron Spectrosc. Relat. Phenom.* **1991,** 56, (3), 273-277.

24. Schon, G., *Acta Chem. Scand.* **1973,** 27, (7), 2623-2633.

25. Pourbaix, M., In *Atlas of electrochemical equilibria in aqueous solutions*, Pergamon: London, England, 1966; pp 384-392.

26. Kautek, W.; Gordon, J. G., *J. Electrochem. Soc* **1990,** 137, (9), 2672-2677.

27. Strehblow, H. H.; Titze, B., *Electrochim. Acta* **1980,** 25, (6), 839-850.

28. Feng, Y.; Siow, K. S.; Teo, W. K.; Tan, K. L.; Hsieh, A. K., *Corrosion* **1997,** 53, (5), 389-398.

29. Laibinis, P. E.; Whitesides, G. M., *J. Am. Chem. Soc.* **1992,** 114, (23), 9022-9028.

30. Speckmann, H. D.; Haupt, S.; Strehblow, H. H., *Surf. Interf. Anal.* **1988,** 11, (3), 148-155.

31. Lee, S. J.; Morrill, A. R.; Moskovits, M., *J. Am. Chem. Soc.* **2006,** 128, (7), 2200-2201.

32. Ferguson, G. S.; Chaudhury, M. K.; Sigal, G. B.; Whitesides, G. M., *Science* **1991,** 253, (5021), 776-778.

33. Pan, H.; Liu, B. H.; Yi, J. B.; Poh, C.; Lim, S.; Ding, J.; Feng, Y. P.; Huan, C. H. A.; Lin, J. Y., *J. Phys. Chem. B* **2005,** 109, (8), 3094-3098.

34. Choi, J.; Sauer, G.; Nielsch, K.; Wherspohn, R. B.; Gosele, U., *Chem. Mater.* **2003,** 15, 776-779.

35. Toimil-Molares, M. E.; Balogh, A. G.; Cornelius, T. W.; Neumann, R.; Trautmann, C., *Appl. Phys. Lett.* **2004,** 85, (22), 5337-5339.

36. Fukunaga, A.; Chu, S. Y.; McHenry, M. E., *J. Mater. Res.* **1998,** 13, (9), 2465-2471.

37. Hassel, A. W.; Diesing, D., *Thin Solid Films* **2002,** 414, 296-303.

38. Schmidlin, F. W., *J. Appl. Phys.* **1966,** 37, (7), 2823-2832.

39. Sun, Y. G.; Yin, Y. D.; Mayers, B. T.; Herricks, T.; Xia, Y. N., *Chem. Mater.* **2002,** 14, (11), 4736-4745.

40. Elechiguerra, J. L.; Larios-Lopez, L.; Liu, C.; Garcia-Gutierrez, D.; Camacho-Bragado, A.; Yacaman, M. J., *Chem. Mater.* **2005,** 17, (24), 6042-6052.

41. Gao, T.; Meng, G.; Wang, Y.; Sun, S.; Zhang, L., *J. Phys.: Condens. Matter* **2002,** 14, 355-363.

42. Molares, M. E. T.; Buschmann, V.; Dobrev, D.; Neumann, R.; Scholz, R.; Schuchert, I. U.; Vetter, J., *Adv. Mater.* **2001,** 13, (1), 62-65.

43. Chang, Y.; Lye, M. L.; Zeng, H. C., *Langmuir* **2005,** 21, (9), 3746-3748.

44. Toimil-Molares, M. E.; Hohberger, E. M.; Schaeflein, C.; Blick, R. H.; Neumann, R.; Trautmann, C., *Appl. Phys. Lett.* **2003,** 82, (13), 2139-2141.

Chapter 3

Surface functionalization of Cu and Ag nanowires using alkanethiols

3.1 Introduction

The use of inorganic nanofillers in the preparation of polymer composites requires a good interaction between the polymer chains and nanoparticle surfaces to reduce the strong agglomeration forces of the particles and promote homogeneous distribution in the polymer matrix. In particular, the agglomeration of carbon nanotubes is considered to be a serious impediment to harnessing their potential in nanocomposites and substantial effort has been directed towards enhancing their dispersion via surface modification and/or different methods of composite preparation.[1,2]

In this work, strong agglomeration of metal nanowires was observed after removal of the solvent (CH_3OH) used for dispersion after CuNW liberation from PAO templates (Chapter 2).[3] This agglomeration prevented their complete dispersion in polymer solutions (Chapter 4). Thus, surface functionalization was required to avoid direct surface interaction between the nanowires after solvent evaporation or filtration, facilitating their re-dispersion in other solvents and/or polymers. This can be realized through self-assembly of alkanethiols on the metal nanowire surface. The self-assembly of these organic compounds will create a new interface between the conductive particles in the nanocomposite, affecting their electrical percolation in the polymer matrix. Nonetheless, little is known about the extent to which the electrical and rheological properties of the polymer nanocomposites will be affected by the surface chemistry of metal nanowires.

In this chapter, metal nanowires produced from AC electrodeposition into PAO templates and liberated in NaOH(aq) solutions are surface functionalized with different alkanethiols. Surface functionalized CuNWs were characterized by thermogravimetric analysis (TGA), elemental analysis, X-ray photoelectron spectroscopy (XPS), X-ray diffraction (XRD), differential scanning calorimetry (DSC), and nuclear magnetic resonance (^{13}C NMR) to provide insight into the surficial organic layer formed. The characterization of CuNWs indicate that multilayers of RS-Cu complexes form on the surface of the CuNWs. The formation of multilayers is influenced by surficial copper oxides on the CuNW surface.

3.2 Experimental

3.2.1 Materials

1-butanethiol (C_4H_9SH, 99 %), 1-octanethiol ($C_8H_{17}SH$, 98.5 %), and 1-octadecanethiol ($C_{18}H_{37}SH$, 98 %) were obtained from Sigma-Aldrich. Methanol (CH_3OH, 99.8 %) and methylene chloride (CH_2Cl_2, 99.5 %) were from Fisher Scientific. All reagents and solvents were used as received. The alkanethiol compounds used are shown schematically in Figure 3.1. (*Caution:* alkanethiols should be handled in a fume hood, C_4H_9SH is flammable and toxic, $C_8H_{17}SH$ and $C_{18}H_{37}SH$ are irritant; many thiols produce stench).

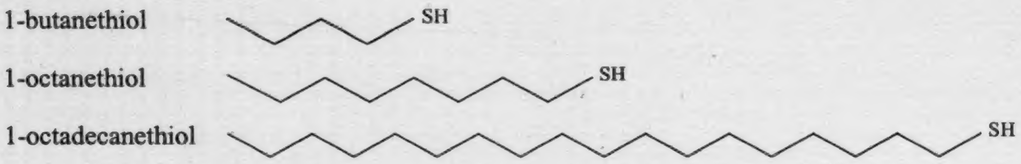

Figure 3.1. Alkanethiols utilized for surface modification of CuNWs

3.2.2 Synthesis and surface functionalization of Cu and Ag nanowires

Copper nanowires were produced using AC electrodeposition into porous aluminum oxide templates fabricated by the two-step anodization in H_2SO_4 of 5 cm × 11 cm aluminum (Al) electrodes. The synthesis and liberation of CuNWs were described in Chapter 2.[3] In the final step of the liberation, CuNWs were dispersed in methanol (CH_3OH). Measured volumes of 1-butanethiol (C_4H_9SH) and 1-octanethiol ($C_8H_{17}SH$) were added from a micropipette to methanolic suspensions of CuNWs containing ~ 1.6 mg Cu / ml CH_3OH. Surface functionalization with 1-octadecanethiol ($C_{18}H_{37}SH$) was obtained by adding a known volume of a 50 mM solution of the thiol in methylene chloride (CH_2Cl_2) to the CuNW suspension. The mixtures of CuNW suspensions and alkanethiols were sonicated for 5 minutes and then stirred with a magnetic stir bar for 1 hour, collected by filtration on Osmonics Inc. nylon membranes (0.45 μm pore size), and rinsed vigorously with CH_2Cl_2. To ensure complete removal of by-products from the reactions of Cu with the thiols, nanowires were re-suspended in CH_2Cl_2 using ultrasound for 10 minutes, collected by filtration on nylon membranes, rinsed vigorously with CH_2Cl_2, collected, dried under vacuum for 24 hours, and transferred into a nitrogen-filled glove box.

3.2.3 Characterization

Elemental analyses were performed by combustion at 1000 °C in O_2 using a Carlo Erba CHNS-O EA1108 Elemental Analyzer. Thermogravimetric analyses (TGA) were performed using a Perkin Elmer Thermogravimetric Analyzer (Pyris 1 TGA) under nitrogen and heated from room temperature to 550 °C at 10 °C/min. Differential scanning calorimetry (DSC) was performed with a Perkin Elmer Pyris 1 DSC under nitrogen at a heating rate of 10 °C/min.

For X-ray photoelectron spectroscopy (XPS) and X-ray diffraction (XRD) analysis, suspensions of alkanethiol functionalized Cu or Ag nanowires in CH_2Cl_2 were dried under reduced pressure in glass vials containing 1 cm × 1 cm silicon wafers on the bottom. The nanowires sedimented and dried onto the Si slide. The XPS spectra and XRD pattern were immediately collected, limiting air exposure to <30 min. XPS spectra were collected with a Kratos Axis 165 X-ray photoelectron spectrometer using Al Kα X-rays (1486.6 eV) from a source operating at 15 kV and 14 mA, the base pressure of the instrument was about 3×10^{-10} mbar (1 mbar = 100 Pa). XRD patterns were collected using a Bruker AXS D8 Discover with GADDS detector equipped with a Cu K_α source (λ = 1.5418 Å) collimated with a 0.5 mm pinhole collimator. The diffraction peak of the silicon wafer was removed by excluding the diffraction spot arising from the single crystal silicon from the integration of the 2D diffraction image of XRD to produce the 2θ plot.

^{13}C NMR spectra were recorded with a Bruker Avance 300. Samples were packed in 4 mm o.d. MAS rotors, spectra were acquired with ^{13}C Cross polarization coupled with magic angle spinning (CPMAS), MAS Spinning frequency 4 or 5 kHz, H-1 90 degrees, pulse length of 4 μs, contact time from 1.5 to 2.0 ms. All spectra were referenced such that the peak for TMS would be at 0.0 ppm by setting the isotropic high frequency peak of adamantane to 38.56 ppm.

3.3 Results

3.3.1 Surface functionalization of CuNWs using alkanethiols

CuNWs were modified with different alkanethiols. The results of surface functionalization of CuNWs after dissolution of PAO templates in NaOH(aq) and suspension in methanol is described as follows.

3.3.1.1 Thermogravimetric and elemental analysis

Surface modification of CuNWs using $C_8H_{17}SH$. Figure 3.2 shows the results of thermogravimetric analysis of copper nanowires functionalized with different concentrations of $C_8H_{17}SH$. Liberated (unfunctionalized) CuNWs show ~ 4.0 % weight loss (Fig. 3.2, curve a). The total percent weight loss of the functionalized copper nanowires at 550 °C increases with the thiol concentration from 6.1 % (at 0.1 mM) to 13.7 % (at 10 mM), indicating that the chemisorption of $C_8H_{17}SH$ on CuNWs is dependent on the thiol concentration.

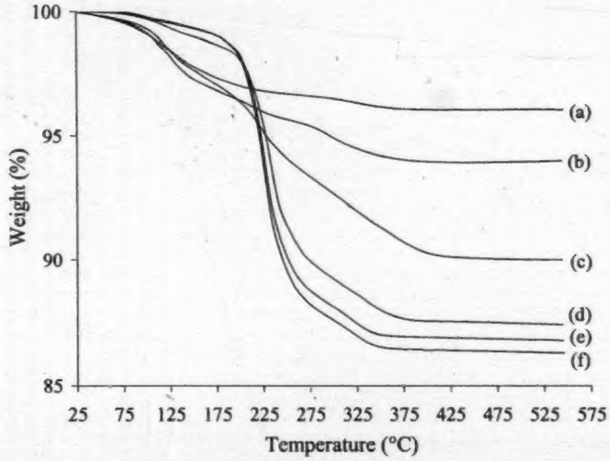

Figure 3.2. Thermogravimetric analysis of (a) NaOH-liberated CuNWs and functionalized CuNWs using different concentrations of $C_8H_{17}SH$: (b) 0.1 mM, (c) 1.0 mM, (d) 2.5 mM, (e) 5 mM, and (f) 10 mM.

The weight of unfunctionalized CuNWs as a function of temperature showed a mass decrease at ~ 120 °C, which corresponds to desorption of methoxy species from copper, as mentioned in Chapter 2.[4] The thermograms of $C_8H_{17}S$-CuNW resulting from exposure of the nanowires to 0.1 and 1.0 mM solutions of $C_8H_{17}SH$ (Fig. 3.2, curves b and c), show significant mass losses at two temperatures ~ 120 °C and ~ 228 °C, which indicates the presence of adsorbed species from both CH_3OH and $C_8H_{17}SH$. This might occur as a result of a partial displacement of methoxy adsorbates by thiolates, and, therefore, suggests incomplete coverage of the nanowire surface with the thiol. The thermograms of $C_8H_{17}S$-CuNW resulting from exposure to more concentrated solutions of thiol (5.0 and 10.0 mM, Fig. 3.2 curves e and f) show a sharp mass loss primarily at ~ 228 °C, which indicates a more complete coverage of the nanowires by the thiol at these concentrations.

Results of TGA and elemental analysis (Table 3.1) indicate that the weight loss percent as well as S content of the CuNWs showed a continuous increase at low thiol concentrations, but reached saturation above 2.5 mM concentrations (Figure 3.3). The C/S and H/C ratios obtained from elemental analysis for copper nanowires prepared using 5 and 10 mM solutions of $C_8H_{17}SH$ agree well with the molar ratios C/S = 8 and H/C of 2.1 of the $C_8H_{17}S$- bound to the copper nanowire surface (Table 3.1). In addition, Table 3.1 indicates that the surface properties of the nanowires changed significantly above 2.5 mM concentration, above which agglomeration and sedimentation of the alkanethiol-functionalized CuNWs in methanol during surface modification was observed.

Table 3.1. Weight loss percentage from TGA and elemental analysis of copper nanowires functionalized using different concentrations of $C_8H_{17}SH$.

Conc. $C_8H_{17}SH$ (mM)	Weight Loss (%)	S (%)	C (%)	H (%)	C+S+H (%)	C/S	H/C	Cu/S	Agglomeration
0	3.99	0	0.48	0.40	0.88	-	9.9	-	No
0.1	6.09	0.16	0.78	0.48	1.42	13.0	7.3	310.9	No
1.0	10.05	1.07	3.62	0.89	5.58	9.0	2.9	44.5	No
2.5	12.58	2.64	7.85	1.53	12.02	7.9	2.3	16.8	Yes
5.0	13.23	3.11	9.22	1.63	13.96	7.9	2.1	13.9	Yes
10.0	13.68	3.30	9.69	1.72	14.71	7.8	2.1	13.0	Yes

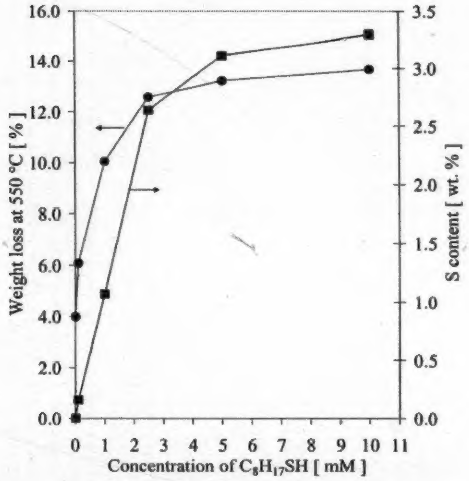

Figure 3.3. Variation of % weight loss and the sulfur content of copper nanowires exposed to different concentrations of $C_8H_{17}SH$. Lines are guides to the eye.

Figure 3.4 shows the Cu to S ratio of the functionalized CuNWs calculated using the elemental analysis of the samples, which indicates that the ratio reached saturation at a value of Cu/S ~ 13 above 2.5 mM $C_8H_{17}SH$ concentrations.

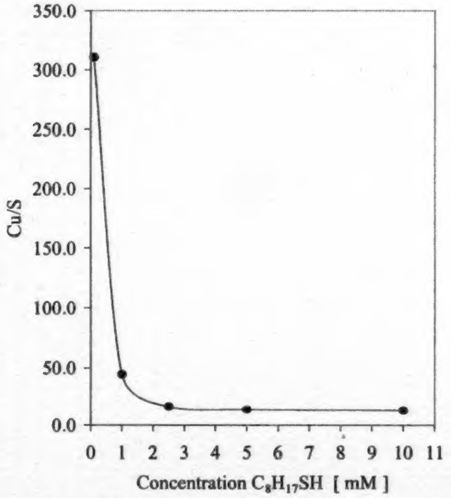

Figure 3.4. Cu to S ratio of CuNWs surface functionalized in different concentrations of $C_8H_{17}SH$. Line is a guide to the eye.

For the purpose of preparation of polymer nanocomposites containing CuNWs, it was interesting to determine how the surface modification of the $C_8H_{17}S$-CuNWs in solutions of thiol of different concentration would affect the dispersion of the particles in the polymer. As will be discussed further in Chapter 4, when copper nanowires were functionalized in ≥5.0 mM concentrations of $C_8H_{17}SH$, the density of CuNW agglomerates in the polymer decreased significantly, i.e., the dispersion of the CuNWs was enhanced.

A concentration of $C_8H_{17}SH$ of 5.0 mM was utilized for surface modification of CuNWs and the study of dispersion and properties of CuNW/PS nanocomposites, as will be presented in Chapter 4. This concentration was selected because a change in the surface chemistry of the CuNWs and more complete coverage of the CuNWs by $C_8H_{17}SH$ was produced at 5 mM as evidenced by: (1) the agglomeration of the functionalized CuNWs in CH_3OH, (2) the plateau of the Cu/S ratio versus $C_8H_{17}SH$ concentration, (3) the atomic Cu/S and H/C ratios that agree with the elemental composition of $C_8H_{17}S$-, and (4) enhanced dispersion of CuNWs in a polymer matrix.

Surface modification of CuNWs using C_4H_9SH and $C_{18}H_{37}SH$. Surface functionalization was carried out using thiol concentrations of 5 mM, because of the results obtained for $C_8H_{17}SH$. CuNWs surface functionalized in 5 mM solutions of C_4H_9SH and $C_{18}H_{37}SH$ showed Cu/S and H/C ratios that agreed with the elemental composition of 1-butanethiol and 1-octadecanethiol, and presented agglomeration and sedimentation in CH_3OH, which demonstrated that good surface coverage was obtained. CuNWs were also functionalized in 5 mM solutions of C_4H_9SH and $C_{18}H_{37}SH$ for subsequent preparation of polymer nanocomposites. Results of TGA and elemental analyses of CuNWs functionalized using different thiols are presented below.

The percent weight loss and the first derivative of percent weight loss obtained from thermogravimetric analysis of CuNWs functionalized with different thiols after chemical modification using 5 mM thiol solutions are shown in Figures 3.5 and 3.6. The samples were heated to 550 °C under nitrogen at 10 °C per min. For comparison purposes, the TGA for unfunctionalized CuNWs is also shown in Figures 3.5 and 3.6. Table 3.2 presents the weight loss percentages of the samples recorded from the thermograms, as well as the temperatures of desorption obtained from the first derivative plots. The percent weight loss increases with the length of the alkyl chain of the alkanethiols. However, the percent weight loss for C_4H_9S-CuNWs is significantly higher than expected, considering the molecular weight of this thiol relative to $C_8H_{17}SH$ and $C_{18}H_{37}SH$. From the first derivative plot, one may see that thermal desorption of thiolates does not occur in a single step for the longer alkyl thiols, as can be inferred from the shoulders of the desorption peaks. In addition, thermal desorption of the different chemisorbed thiols occurs at different temperatures (Table 3.2). Interestingly, C_4H_9S-CuNWs showed thermal desorption at a higher temperature than longer chain alkanethiol-functionalized CuNWs.

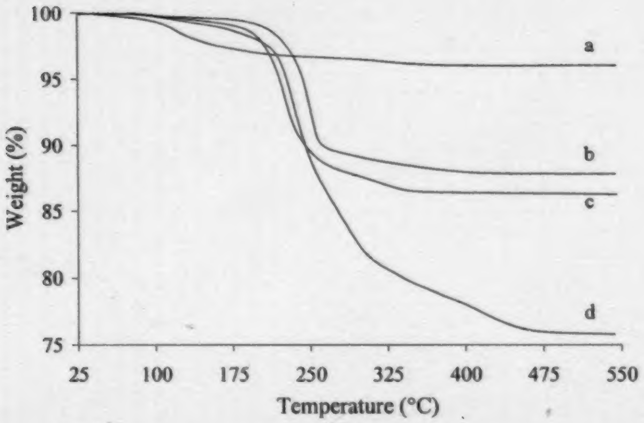

Figure 3.5. Thermogravimetric analysis of (a) NaOH-liberated CuNWs and CuNWs functionalized with 5 mM solutions of (b) C_4H_9SH (c) $C_8H_{17}SH$, and (d) $C_{18}H_{37}SH$.

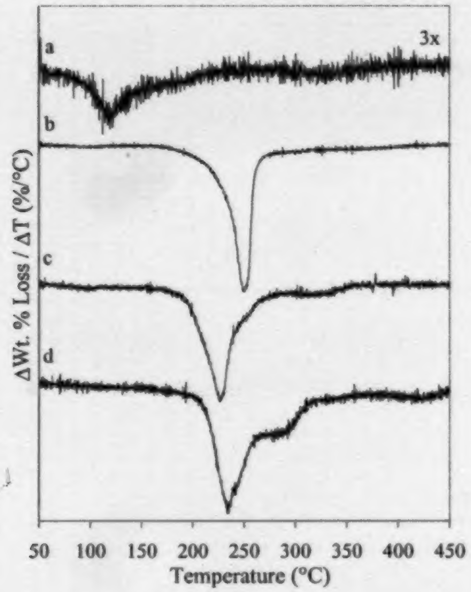

Figure 3.6. First derivative of thermogravimetric analyses for (a) NaOH-liberated CuNWs and Cu nanowires functionalized with 5 mM solutions of (b) C_4H_9SH (c) $C_8H_{17}SH$, and (d) $C_{18}H_{37}SH$.

Table 3.2. Percentage of weight loss and temperature of desorption for unfunctionalized CuNWs and CuNWs functionalized using 5.0 mM thiol solutions.

RS-CuNW	Weight Loss Percent (%)	Temperature of desorption (°C)
CuNW	4.0	121*
C_4H_9S-CuNW	12.2	252
$C_8H_{17}S$-CuNW	13.2	228
$C_{18}H_{37}S$-CuNW	24.2	237

* Thermal desorption of methoxy adsorbates.

Table 3.3 shows the results of elemental analyses obtained for CuNWs that were surface functionalized in thiol solutions of 5.0 mM concentration. The C/S and H/C ratios agreed well with the atomic ratios of the alkanethiols. In addition, the Cu/S ratios of the CuNWs indicate significant adsorption of thiol on the CuNWs. More adsorption was observed for C_4H_9SH (Cu/S ~ 8) than that for longer alkanethiols ($C_8H_{17}SH$ and $C_{18}H_{37}SH$, Cu/S of ~14 and ~13 respectively). The results of TGA and elemental analysis can be rationalized by considering the formation of multilayers, for which further evidence and discussion is presented in the next sections.[5-7]

Table 3.3. Elemental analysis of copper nanowires functionalized with different alkanethiols.

RS-CuNW	S (%)	C (%)	H (%)	C+S+H (%)	C/S	H/C	Cu/S
C_4H_9S-CuNW	5.20	7.74	1.46	14.40	4.0	2.2	8.31
$C_8H_{17}S$-CuNW	3.11	9.22	1.63	13.96	7.9	2.1	14.0
$C_{18}H_{37}S$-CuNW	2.96	19.03	3.31	25.30	17.2	2.1	12.7

3.3.1.2 X-ray photoelectron spectroscopy

XPS was utilized for the characterization of surface functionalized CuNWs in order to: (1) determine the type of bonding of the alkanethiols to the copper surface, (2) elucidate the presence of unbound thiols (RSH) or unbound dialkyl disulfides $(RS)_2$ in the multilayer that can be produced during the surface reaction of alkanethiols with Cu surfaces containing oxides,[5,8,9] and (3) find evidence for the degree of Cu reduction and O removal from the CuNW surface, given that alkanethiols have the capability of removing oxygen at copper surfaces, reduce Cu(II) species, and protect copper surfaces from oxidation.[10,11]

Figure 3.7 shows the survey X-ray photoelectron spectra of unfunctionalized CuNWs and CuNWs functionalized with the different alkanethiols. The C(1s) peaks at BE of 284.8 eV were used to normalize the BE scale. The surveys were normalized relative to the intensity of the $Cu(2p_{3/2})$ peak, in order to compare the intensities of the copper peaks to those of oxygen, sulfur, and carbon. A higher intensity of the C(1s) peak of thiol-functionalized CuNWs (Fig. 3.7 b-d) relative to the unfunctionalized CuNWs (Fig. 3.7a) corroborates the presence of alkanethiols. The intensity of the $C(1s)/Cu(2p_{3/2})$ peak ratio is in the order: $C_{18}H_{37}S$-CuNWs > C_4H_9S-CuNWs > $C_8H_{17}S$-CuNWs, indicating a larger than anticipated adsorption of C_4H_9SH. The O(1s) peak decreases when CuNWs are surface functionalized. Indeed, it is known that alkanethiols may act as reducing agents for copper oxides present at Cu surfaces or inhibit oxidation of the Cu surfaces.[5,10,12]

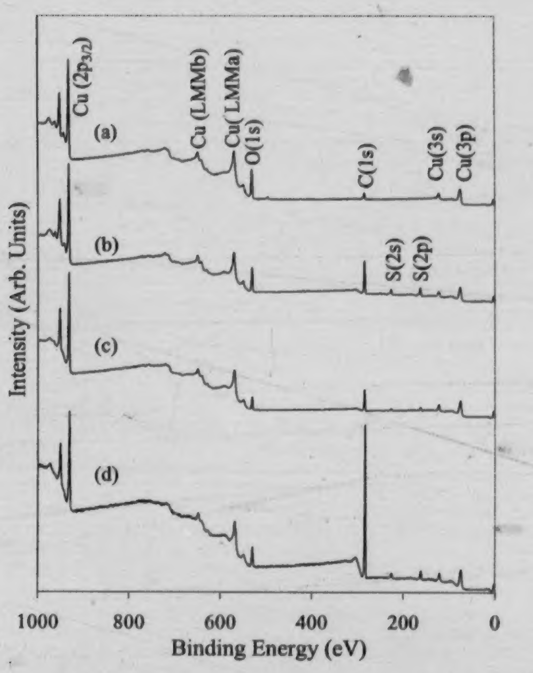

Figure 3.7. X-ray photoelectron survey of (a) NaOH-liberated CuNWs, and CuNWs functionalized with (b) C_4H_9SH (c) $C_8H_{17}SH$, and (d) $C_{18}H_{37}SH$.

It is worth mentioning that C and O peaks will be observed in XPS, due to contamination produced by exposure of samples to atmosphere before being introduced into the vacuum chamber. However, because the samples were all prepared and exposed simultaneously to air before analysis (<30 min), the differences in C and O peak intensities between alkanethiol-functionalized CuNWs observed from the spectra are related to the formation of multilayers by the different thiols.

Figure 3.8a presents the high resolution XP spectra for the Cu(2p) peak for unfunctionalized CuNWs and CuNWs functionalized with alkanethiols. The presence of Cu(II) species, such as CuO at the surface of unfunctionalized Cu nanowires, is evident from the satellite peaks indicated with stars in the Cu(2p) spectra.[11,13] These satellite peaks are still observed for C_4H_9S-CuNW, while they are not observed (i.e. are below the detection limit of the XP spectrometer, 0.1 at. %) for $C_8H_{17}S$-CuNW and $C_{18}H_{37}S$-CuNW. This indicates that longer chain alkyl thiols prevent oxidation of the CuNWs more effectively.[11]

Given that the binding energies of the Cu($2p_{3/2}$) peaks for Cu(0) and Cu(I) species are indistinguishable, their presence has to be elucidated using the Cu($L_3M_{4.5}M_{4.5}$) peak (Table 3.4).[10,14,15] The spectra of the Cu($L_3M_{4.5}M_{4.5}$) Auger peak of unfunctionalized CuNWs in Figure 3.8b indicates the presence of elemental copper (BE 567.9 eV) and surficial copper oxides (predominantly Cu_2O at BE 569.8 eV). The Cu($L_3M_{4.5}M_{4.5}$) Auger spectrum for C_4H_9S-CuNW indicates more surface oxidation (Cu(I)) of CuNW relative to unfunctionalized CuNWs, while for $C_8H_{17}S$-CuNW and $C_{18}H_{37}S$-CuNW, the Auger spectra are similar to that of unfunctionalized CuNW indicating that 1-octanethiol and 1-octadecanethiol provided better protection against oxidation than 1-butanethiol.

Table 3.4. Electron binding energies for copper oxides and hydroxides[14,15]

Copper compound	Binding Energies (eV)		
	Cu($2p_{3/2}$)	Cu($L_3M_{4.5}M_{4.5}$)	O(1s)
Cu	932.5	568.0	-
Cu_2O	932.5	570.3	530.5
CuO	933.8	569.0	529.6
$Cu(OH)_2$	934.4	570.3	530.9

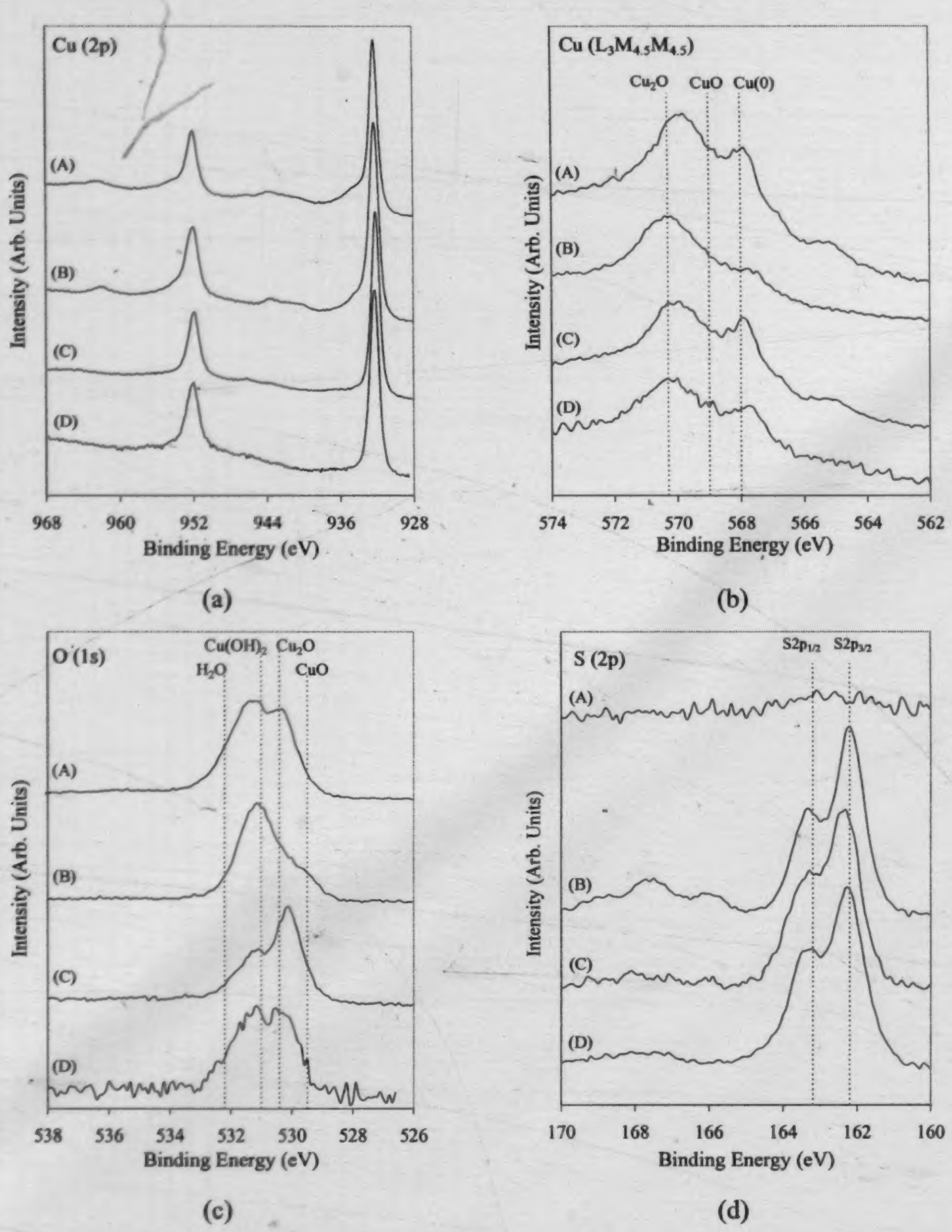

Figure 3.8. High resolution X-ray photoelectron spectra of (a) Cu(2p) peak, (b) Cu($L_3M_{4.5}M_{4.5}$) Auger peak, (c) O(1s) peak, and (d) S(2p) peak for (A) NaOH-liberated CuNWs, and CuNWs functionalized with (B) C_4H_9SH (C) $C_8H_{17}SH$ (D), and $C_{18}H_{37}SH$. Dotted lines indicate the binding energies according to literature.[14,15]

The XP spectra of O(1s) shown in Figure 3.8c, indicates that oxygen at the surface of functionalized CuNWs is associated primarily with Cu_2O (BE 530.5 eV) and to a small degree with CuO (BE 529.6 eV), which agrees with the $Cu(L_3M_{4.5}M_{4.5})$ spectra. A signal of O(1s) at BE 531 eV might indicate possible association of Cu(II) species to $Cu(OH)_2$; however, the presence of oxygen as $Cu(OH)_2$ is ruled out because the $Cu(L_3M_{4.5}M_{4.5})$ shows that Cu_2O is predominant. According to previous studies, the O(1s) peak corresponding to methoxy species chemisorbed at the surface of Cu is detected at BE 530.1 eV,[16,17] which is only 0.3 eV from that of Cu_2O. If methoxy species are not completely displaced from the copper surface by the alkanethiols, this peak could be a small fraction of the O(1s) peak observed for functionalized CuNWs. Thus, the O(1s) peaks are consistent with the Cu(2p) and Cu $(L_3M_{4.5}M_{4.5})$ peaks, indicating that of the copper oxides, Cu_2O is more abundant than CuO. In addition, the O(1s) peaks indicate (1) that oxygen at the surface of CuNWs is only partially displaced by the action of the alkanethiolates and (2) the coexistence of copper oxides (primarily Cu_2O) and thiolates in the multilayer at the surface of the CuNWs is likely.

Figure 3.8d shows the XP spectra for the S(2p) peak of unfunctionalized and surface functionalized CuNWs. The doublet of the $S(2p_{3/2})$ peak at 162.2 eV corresponds very well to that of thiolate (R-S-Cu).[10,18] The S doublet ($S2p_{1/2}$ and $S2p_{3/2}$) fits well to a separation of 1.2 eV, indicating the presence of only one S species. The $S(2p_{3/2})$ peaks of free thiol or disulfide formed as the by-product of the surface functionalization process should appear between 163-164 eV.[10,19] No evidence of unbound thiols or unbound disulfides is observed. In addition, weak signals observed from BE 166 to 169 eV for C_4H_9S-CuNW indicates little oxidation of the thiolate to sulfonate (RSO_3).[10,11,20]

3.3.1.3 X-ray diffraction

One may wonder if the alkanethiols chemisorbed on CuNWs are ordered in a way that can be detected by XRD. In addition, as alkanethiol functionalized CuNWs showed the presence of surficial oxides (as determined by XPS), one may ask if the oxides are present as crystalline species. Figure 3.9 shows the XRD patterns recorded for CuNWs functionalized with C_4H_9SH, $C_8H_{17}SH$, and $C_{18}H_{37}SH$. Clear evidence of crystalline copper oxides, CuO or Cu_2O, is not observed. The diffraction peaks were assigned to the fcc lattice of copper. The intensity ratios of the (111) relative to (220) and (200) were similar to those of CuNWs (Chapter 2) without functionalization, showing a slightly preferred orientation along the (111) planes.

Interestingly, diffraction peaks are observed at small angles (4 - 25°) in Figure 3.9, indicating that alkanethiolates chemisorbed on CuNWs present some degree of conformational ordering (or crystallization). The number of diffraction peaks decreased with increasing alkyl chain length of the alkanethiol-functionalized CuNWs. For $C_{18}H_{37}S$-CuNWs, only two broad peaks were observed. Table 3.5 shows the d-spacings corresponding to the diffraction peaks observed for functionalized CuNWs calculated using Bragg's law ($\lambda = 2d \sin\theta$) in order to show the distances between the planes that lead to X-ray diffraction from the functionalized CuNWs.

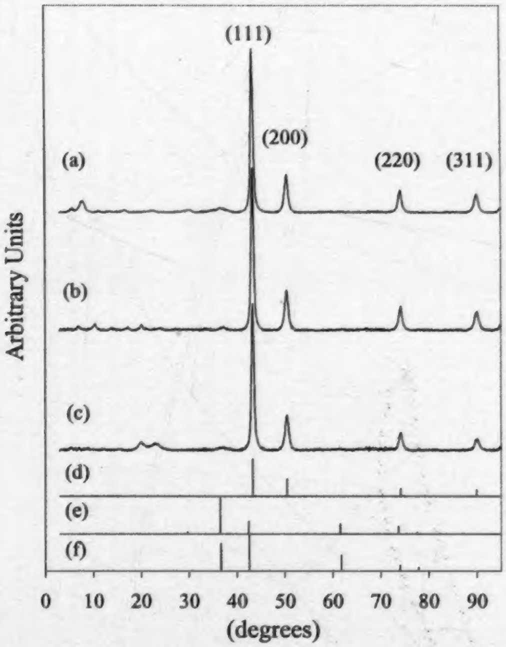

Figure 3.9. XRD of CuNWs functionalized with (a) C_4H_9SH (b) $C_8H_{17}SH$, and (c) $C_{18}H_{37}SH$. Standard powder patterns of (d) Cu (e) Cu_2O (f) CuO.

Table 3.5. d-spacings for the reflections from alkanethiol-functionalized CuNWs at small angles

C_4H_9S-CuNW 2*θ* (deg)	d (Å)	$C_8H_{17}S$-CuNW 2*θ* (deg)	D (Å)	$C_{18}H_{37}S$-CuNW 2*θ* (deg)	d (Å)
5.7	15.5	7.1	12.5	20.1	4.4
7.9	11.2	10.5	8.5	23.1	3.9
11.2	7.9	13.9	6.4		
13.5	6.5	17.3	5.1		
16.7	5.3	20.2	4.4		
22.4	4.0				

The diffraction peaks of surface-modified CuNWs produced in this work might have resulted from (1) interdigitation between alkyl thiols on adjacent CuNWs or (2) a multilayer of RS-Cu complexes self-assembled on the surface of the CuNWs.

Interdigitation has been reported from studies related to the self-assembly of alkanethiol-functionalized Ag and Cu nanoclusters and the formation of superlattices.[21-23] However, in this work, the number of diffraction peaks at small angles decreases with the length of the alkanethiol, which indicates that shorter chain alkanethiols might have produced more crystalline multilayers than long chain alkanethiols. Therefore, interdigitation might not be the reason for diffraction peaks from the functionalized CuNWs.[24-27] Previous studies have reported the formation of layered metal thiolate structures by self-assembly of alkanethiols. In these structures, sulfur atoms from the alkanethiols are attached to metal atoms arranged in a plane.[24-27] For instance, for layered copper thiolates, XRD studies have demonstrated that interdigitation does not occur (i.e. the interlayer spacing corresponded to twice the length of the alkanethiols).[27] It is known that self-assembly of alkanethiols into these structures occurred under special conditions; previous studies discussed the difficulty of obtaining crystallites for XRD studies.[25,28]

The formation of the multilayers on the CuNW surfaces might be related to the formation of RS-Cu complexes that self-assemble at the surface of the CuNWs. XRD patterns indicate that C_4H_9SH produces more crystallization than long alkanethiols, which indicates that the mechanism of self-assembly of these complexes is favoured by using short alkyl chains under the conditions of nanowire functionalization. Further studies would be required to elucidate the crystalline structure of the multilayer. For the purpose of this work, XRD characterization provided a good indication that multilayers of RS-Cu complexes on the CuNWs may present some degree of ordering in the solid state.

3.3.1.4 Differential scanning calorimetry

DSC analysis of functionalized CuNWs indicated the presence of endothermic peaks below the temperature of desorption of the alkanethiols (see Table 3.2). Considering the presence of diffraction peaks obtained from XRD analyses of functionalized CuNWs, the endothermic peaks observed from DSC analysis must correspond to the melting process of the multilayer at the CuNW surfaces. Endothermic processes have been reported for Cu and Ag nanoclusters functionalized with alkanethiols,[21-23] as well as for layered metal thiolates.[27]

Figure 3.10 shows the results of differential scanning calorimetry analyses of functionalized copper nanowires; endothermic peaks corresponding to the melting process of the multilayers are observed between 145 and 174 °C. The melting points are in the order C_4H_9S-CuNWs > $C_8H_{17}S$-CuNWs > $C_{18}H_{37}S$-CuNWs. Interestingly, the melting point for C_4H_9S-CuNWs was higher than those obtained for longer chain alkylthiols. In addition, C_4H_9S-CuNWs showed an exothermic peak at a temperature of ~ 120 °C. Self-assembled monolayers of short alkanethiols are expected to show little conformational ordering, because of lower van der Waals interactions between the short alkyl chains. The exothermic and endothermic changes for C_4H_9S-CuNWs suggest that during heating, a crystallization process occurred first, promoted by thermal motion and organization of the RS-Cu complexes. This leads to a different crystalline phase that melts at higher temperatures than that observed for longer alkanethiols. The XRD pattern of C_4H_9S-CuNWs agrees with the DSC results, indicating more crystallinity of the multilayer formed by short alkanethiols.

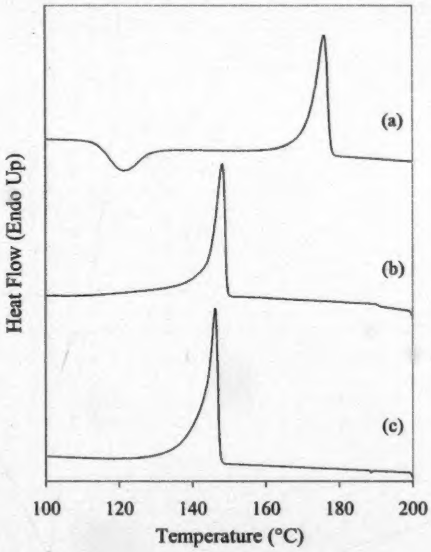

Figure 3.10. DSC of CuNWs functionalized with (a) C_4H_9SH (b) $C_8H_{17}SH$, and (c) $C_{18}H_{37}SH$.

Table 3.6 shows the melting temperature and melting enthalpies for alkanethiol-functionalized CuNWs. It can be inferred from Table 3.6 that the melting enthalpy increases with the chain length of the thiol. The decrease of the melting point with the alkyl chain length does not agree with the possibility of interdigitation of alkyl chains between adjacent nanowires. However, a similar trend was reported in a study of the melting behavior of copper alkanethiolates to mesogenic phases by Espinet et al.[25] They found that the melting points of the layered structures decrease with increasing alkyl chain length (172.6 °C, 136.4 °C and 140.6 °C for $n = 4$, 8 and 18, respectively, where n is the number of carbons of the alkanethiol). Although strictly similar structures are not expected for the multilayer on CuNW surfaces, the similarity to the results in this work is intriguing and points to the possibility of self-assembled RS-Cu complexes on the CuNW surfaces.

Table 3.6. Melting points and enthalpies of copper nanowires functionalized with different alkanethiols (a) C_4H_9SH (b) $C_8H_{17}SH$ (c) $C_{18}H_{37}SH$

RS-CuNW	Melting Point (°C)	Melting Enthalpy (J/g)
C_4H_9S-CuNW	174	29.1
$C_8H_{17}S$-CuNW	147	30.1
$C_{18}H_{37}S$-CuNW	145	35.2

3.3.1.5 Solid state CPMAS ^{13}C NMR

Solid state NMR provided more supporting evidence for the formation of thiolate bonds in functionalized nanowires. The CPMAS ^{13}C NMR spectra for CuNWs functionalized with different alkanethiols are presented in Figure 3.11. The assignment of the chemical shifts to the C atoms of each alkylthiol has been performed by comparison to the shifts of pure alkanethiols as well as those reported in the literature for self-assembled monolayers of thiols on Cu and Au nanoclusters.[21,29] C atoms are numbered starting from C1 for the C atom bound to S to the last C in the alkyl chain (Figure 3.11 and Table 3.7).

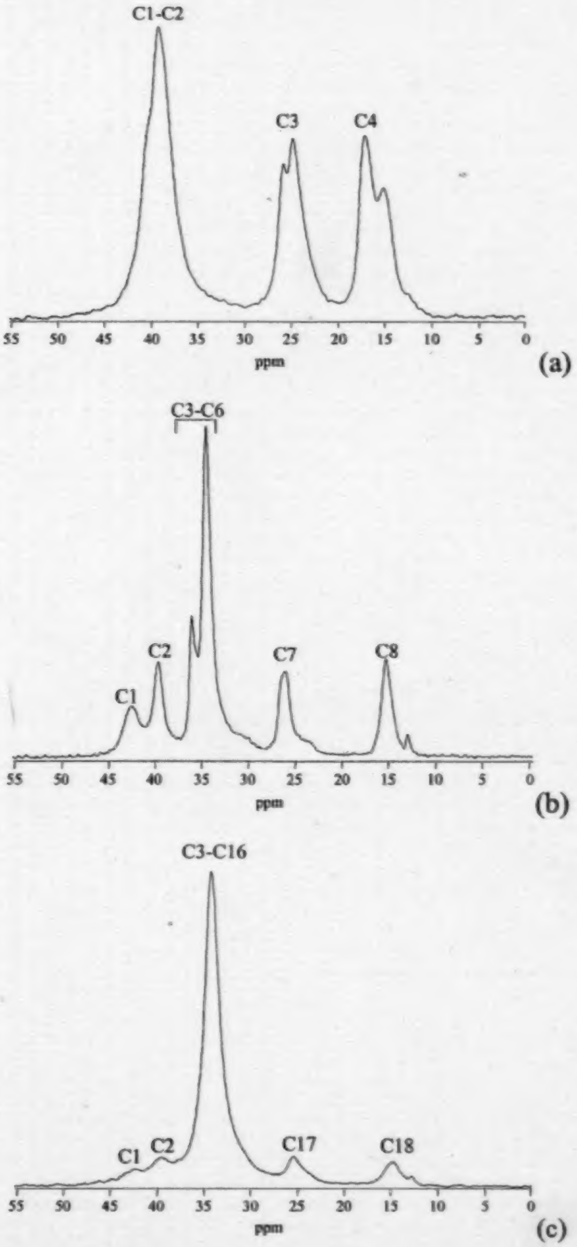

Figure 3.11. CPMAS ^{13}C NMR spectra for CuNWs functionalized using (a) C_4H_9SH (b) $C_8H_{17}SH$, and (c) $C_{18}H_{37}SH$.

Table 3.7. Chemical shifts for CuNWs functionalized with different alkanethiols and typical chemical shifts for the corresponding alkanethiols in solution.[29,30]

C_4H_9S-CuNW		C_4H_9SH	
C	δ (ppm)	C	δ (ppm)
1-2	39.1	1	24.1
3	25.7 - 24.7	2	35.9
4	17.1 - 15.1	3	21.3
		4	13.3
$C_8H_{17}S$-CuNW		$C_8H_{17}SH$	
C	δ (ppm)	C	δ (ppm)
1	42.6	1	24.5
2	39.7	2	33.9
3-6	34.5 - 36.1	3	28.2
7	26.0	4, 5	28.9 - 29.0
8	15.3	6	31.6
		7	22.5
		8	13.9
$C_{18}H_{37}S$-CuNW		$C_{18}H_{37}SH$	
C	δ (ppm)	C	δ (ppm)
1	42.4	1	24.5
2	39.6	2	33.9
3-16	34.2	3	28.2
17	25.4	4-15	28.9 - 29.6
18	14.7	16	31.8
		17	22.5
		18	13.9

There is a significant downfield shift for the alkanethiol-functionalized CuNWs relative to the chemical shift of the alkanethiols in solution. It is worth noting that C_4H_9SH and $C_8H_{17}SH$ are liquids at room temperature, while $C_{18}H_{37}SH$ is a solid with a melting point of ~ 30 °C. The most significant shift occurs for the C1 atoms, similar to what has been reported for alkanethiols on Cu and Au nanoclusters in previous studies.[21,29] In the case of Cu nanowires, the C1 shift is ~ 15 ppm for C_4H_9S-CuNWs and ~ 18 ppm for $C_8H_{17}S$- and $C_{18}H_{37}S$-CuNWs. The shift of Cs along the alkyl chain decreases gradually. The downfield shift obtained in the ^{13}C NMR spectra of the functionalized CuNWs confirmed the presence of a Cu-thiolate bond. In addition, the significant downfield chemical shift of C1 indicates the absence of unbound alkanethiols or weakly adsorbed species of organosulfur compounds.[29]

3.3.2 Surface functionalization of AgNWs using 1-octanethiol

In the previous section, CuNWs with little surface oxidation presented significant chemisorption of alkanethiols. The chemisorption of alkanethiols on copper surfaces leading to the formation of multilayers is significantly enhanced by the presence of copper oxides at the surface of CuNWs produced by AC electrodeposition into and liberation from PAO templates. The self-assembly of multilayers at metal surfaces has been reported for Au and Cu oxidized surfaces.[5,7] The presence of oxygen at metal surfaces has been considered to be critical to the formation of multilayers. AgNWs produced by AC electrodeposition and liberation from PAO templates showed much less O at the surface than CuNWs, as discussed in Chapter 2. In an effort to elucidate the different degrees of thiol adsorption on Ag and CuNWs produced by AC electrodeposition, the surface functionalization of AgNWs with $C_8H_{17}SH$ was studied.

AgNWs were prepared by AC electrodeposition into PAO templates, as described in Chapter 2.[31] AgNWs were surface functionalized with $C_8H_{17}SH$ using a similar procedure to that utilized for surface modification of CuNWs. Suspensions of AgNWs in methanol after liberation from PAO templates were treated with solutions of different concentrations of $C_8H_{17}SH$. Interestingly, TGA results indicated an ~ 2 %

weight loss of AgNWs functionalized in solutions with concentrations of 1.0, 2.5, 5.0 and 10.0 mM (average weight loss = 2.25 ± 0.17 %). Unlike $C_8H_{17}S$-CuNWs, the weight loss on $C_8H_{17}S$-AgNWs did not show any dependence on the concentration of $C_8H_{17}SH$, which is likely due to the self-assembly of monolayers of $C_8H_{17}SH$ on the oxide-free AgNW surface. Figure 3.12 shows a typical TGA of $C_8H_{17}S$-AgNWs relative to unfunctionalized AgNWs. The desorption temperature of $C_8H_{17}S$- determined from the first derivative of the thermogram was 170 °C.

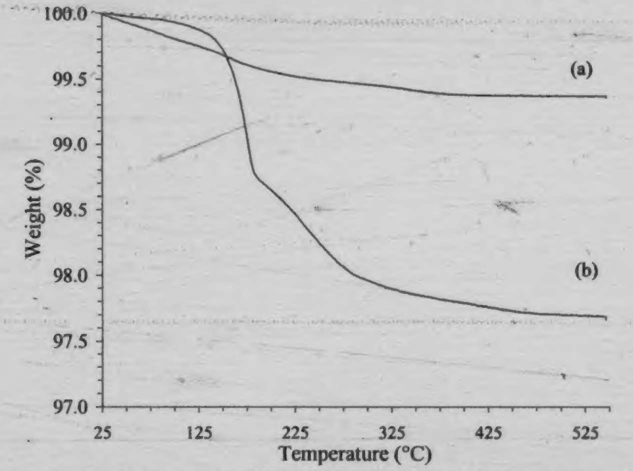

Figure 3.12. Thermogravimetric analysis of (a) NaOH-liberated AgNWs and (b) AgNWs surface functionalized with $C_8H_{17}SH$.

Table 3.8 shows results of weight loss percent and elemental analysis of a typical sample of AgNWs surface functionalized using 5.0 mM solution of $C_8H_{17}SH$. The C/S and H/C ratios obtained from elemental analysis of functionalized AgNWs agree well with the molar ratios of $C_8H_{17}S$- (C/S = 8.0 and H/C = 2.1) bound to the AgNW surface. The Ag/S ratio shows a value of ~ 72, which is 5 times higher than that obtained for $C_8H_{17}S$-CuNWs (Cu/S ~ 14, Table 3.1), and indicates significantly less adsorption of the 1-octanethiol on Ag than on Cu nanowires. It is worth mentioning that DSC analysis of AgNWs did not provide evidence of melting processes as obtained for functionalized CuNWs.

Table 3.8. Weight loss percentage from TGA and results of elemental analysis of silver nanowires functionalized using 5.0 M solution of $C_8H_{17}SH$.

Conc. $C_8H_{17}SH$ (mM)	Weight Loss (%)	S (%)	C (%)	H (%)	C+S+H (%)	C/S	H/C	Ag/S	Agglomeration
5.0	2.44	0.41	1.25	0.27	1.93	8.2	2.6	71.6	Yes

Figure 3.13 shows the XP survey and high resolution XP spectra of the Ag(3d), Ag(MNN) Auger, and S(2p) peaks for $C_8H_{17}S$-AgNWs. The presence of the thiolate bond (RS-Ag) on the AgNW surface is evidenced by the $S(2p_{3/2})$ peak at 161.8 eV (Fig. 3.13d),[10] The characterization of $C_8H_{17}S$-AgNWs by TGA, elemental analysis, and XPS suggest the formation of self-assembled monolayers on AgNWs.

3.4 Discussion

In this work, surface functionalization of CuNWs with alkanethiols has resulted in multilayers on the surface of the nanowires. The formation of a multilayer on CuNWs after surface functionalization with alkanethiols is inferred from the following reasons: (1) the ratios of Cu to S of functionalized CuNWs from elemental analysis were ~ 8 for C_4H_9S-CuNWs and ~ 13 for $C_8H_{17}S$-CuNWs and $C_{18}H_{37}S$-CuNWs, indicating significant adsorption of alkanethiols. An approximate calculation

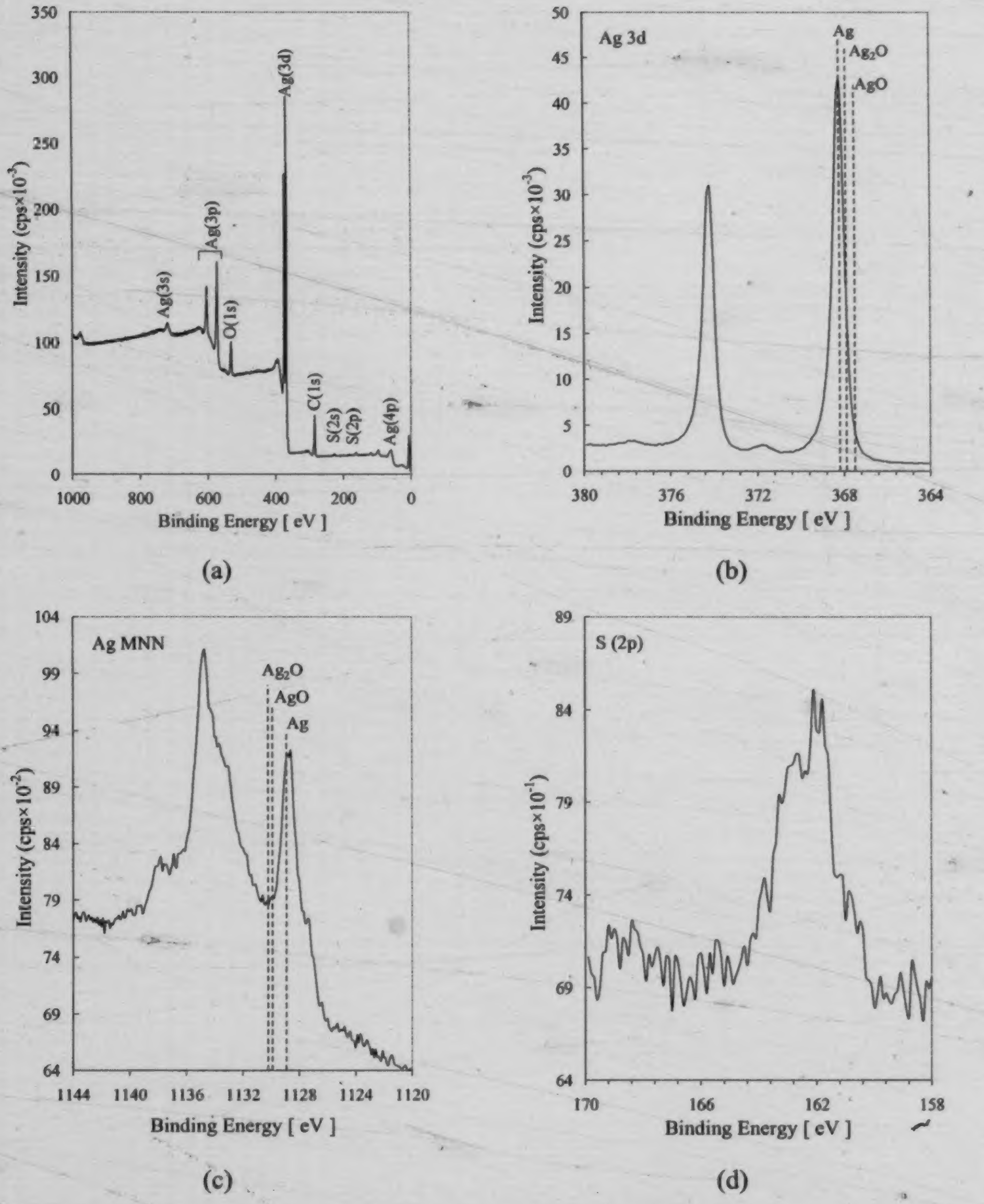

(a) (b)

(c) (d)

Figure 3.13. X-ray photoelectron spectra of AgNWs functionalized with $C_8H_{17}SH$. (a) Survey, and high resolution spectra of (b) Ag(3d) peak, (c) Ag(MNN) Auger, and (d) S(2p) peak. Dashed lines indicate the binding energies of Ag, Ag_2O, and AgO according to literature.[10]

of Cu atoms at the surface of CuNWs, assuming the nanowires are 1 μm in length and 25 nm in diameter, indicates that ~ 3.6 % of the Cu atoms would be located at the surface. If an ideal alkanethiolate monolayer on Cu is considered, less than 1 at. % sulfur in the total sample would correspond to the formation of a monolayer. The expected Cu/S ratios for the CuNWs from elemental analysis should be on the order of ~ 99, under the assumption of a monodisperse sample of nanowires with the dimensions specified above. The low Cu/S ratios of the samples indicated the formation of RS-Cu complexes on the surface of CuNWs. (2) In the case of monolayers, an increase in weight loss percent should be proportional to the molar mass of the different thiols; however, a larger than anticipated adsorption of 1-butanethiol was obtained relative to the adsorption of 1-octanethiol and 1-octadecanethiol. This can only be explained if multilayers have formed, which in the case of C_4H_9SH have led to more adsorption of the thiol and greater crystallinity, as evidenced by the higher melting points, versus the melting points of the multilayers obtained with $C_8H_{17}SH$ and $C_{18}H_{37}SH$. (3) Surface modification of AgNWs using $C_8H_{17}SH$ demonstrated significantly less adsorption of thiol compared to CuNWs. The difference in thiol adsorption between CuNWs and AgNWs is attributed to the surface oxidation of the CuNWs after liberation from PAO templates. The presence of oxides on copper promoted the formation of a multilayer, while in the case of oxide-free AgNWs the formation of a monolayer was more likely.

The formation of multilayers of alkanethiols has been reported for Cu and Au surfaces in previous studies.[5-7] The presence of multilayers is related to the presence of oxides at the metal surface. For instance, Kim et al. found evidence of the formation of multilayers on gold surfaces from STM analysis and quartz crystal microbalance measurements. Up to 4 monolayers of n-$C_{18}H_{37}SH$ formed on gold when the sample was exposed to the thiol solution for 3-7 days.[6] Woodward et al. found islands of 20-200 nm in diameter located on the RS/Au monolayer surface according to AFM observations.[7] The height of the islands on the surface of Au substrates corresponded to the height of approximately two monolayers of the thiols. The formation of these multilayers was attributed to oxidation of the Au surface. In addition, they rationalize the structure of the multilayer as composed of a bilayer of Au/alkanethiol complexes.[7]

One of the reasons for using alkanethiols to modify the surface of CuNWs is the ability of alkanethiols to act as reducing agents and remove oxides from copper surfaces.[10] After liberation in NaOH(aq) solutions, the presence of oxides and chemisorption of methanol on copper nanowire surfaces was evident from XPS analysis. Oxide formation on the CuNWs was expected to result from the etching of the PAO templates in aqueous solutions of NaOH(aq) and from performing the liberation in air. Using alkanethiolates, however, helped to remove copper oxides to a small degree. The signal corresponding to Cu(II) species in XP spectra disappeared after the treatment with $C_8H_{17}SH$ and $C_{18}H_{37}SH$, but non-negligible amounts of oxygen were still present. XPS characterization of functionalized CuNWs indicates that the alkanethiolate multilayer formed on a surficial layer composed of Cu(0), Cu(I) and O.

In previous studies related to the alkanethiolate adsorption on oxidized copper surfaces, the formation of dialkyl disulfides have been reported. For instance, the addition of alkanethiols to colloidal solutions of Cu nanoparticles led to the formation of dialkyl disulfides $(RS)_2$. Crystals of $(C_{16}H_{33}S)_2$ and $(C_{18}H_{37}S)_2$ were identified.[8] It is considered that the reduction of copper oxides by alkanethiols occurred through the following reactions:[5,8,9,12]

On elemental copper:

$$RSH + Cu(0) \rightarrow RSCu_{(surf)} + 1/2\ H_2$$

On copper oxides:

$$2RSH + 2CuO \rightarrow (RS)_2 + Cu_2O + H_2O$$

$$2RSH + Cu_2O \rightarrow 2RSCu_{(surf)} + H_2O$$

In this work, dialkyl disulfides $(RS)_2$ could have resulted from the surface functionalization of copper nanowires, given the presence of copper oxides at the surface. However, these compounds can be removed using solvents such as toluene, benzene, hexanes, chloroform, and methylene chloride. Indeed, XPS and ^{13}C NMR analyses of functionalized copper nanowires showed the presence of RS-Cu thiolate bonds, and no evidence of unbound thiol or disulfides, indicating that the rinsing steps in methylene chloride were effective in removing the dialkyl disulfide that could have precipitated at the surface of the nanowires.

Given that XPS and ^{13}C NMR analyses provided (1) direct evidence of the thiolate bond (RS-Cu) and (2) absence of impurities of unbound thiols and disulfides in the alkanethiol-functionalized CuNWs, it can be inferred that S atoms in the multilayer must be associated to species containing S-Cu bonds. Thus, a multilayer composed of RS-Cu complexes must be considered. The possibility of formation of surficial complexes of Cu and Au on oxidized surfaces treated with alkanethiols have been reported before.[5,7] The elucidation of such a complex multilayer on CuNWs is definitely a difficult task, but the evidence obtained in this work points to the possibility of having complexes of metal species in the multilayer similar to those considered by Woodward et. al. on oxidized gold surfaces.[7] Figure 3.14 shows a schematic representation of possible self-assembled structures on CuNWs after their surface modification with alkanethiols. A self-assembled monolayer of alkanethiol forms on a layer of Cu and Cu_2O nanowire surface (Fig. 3.14a). The multilayer may comprise layered self-assembled copper alkanethiolate complexes as indicated in Figure 3.14b. In these structures, sulfur atoms from the alkanethiols are bound to copper atoms arranged in a plane as has been reported previously.[24-27] One may speculate that the formation of the multilayer in the CuNW surface would require the diffusion of copper (I) species from the surface to form the multilayer complex, a process that might be driven by the reduction of CuO by the alkanethiols. C_4H_9SH might have facilitated the diffusion of copper (I) species from the nanowire surface, given the small size of the molecule compared to $C_{18}H_{37}SH$, leading to a higher molar adsorption of C_4H_9SH relative to longer alkanethiols.

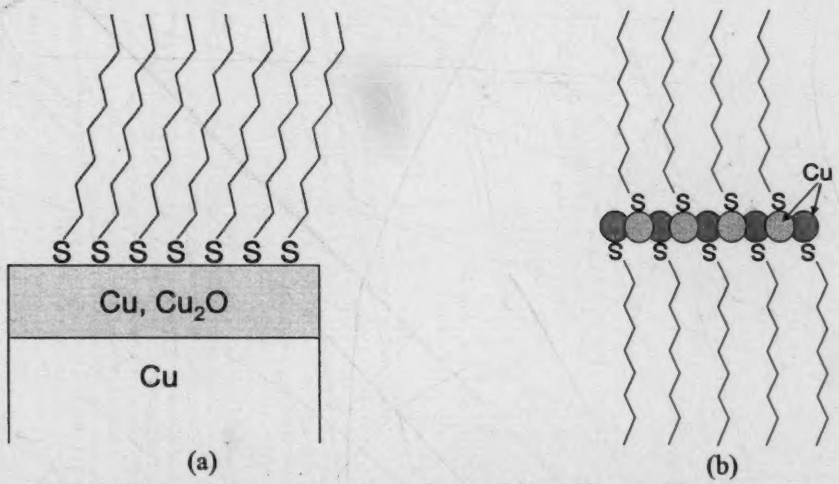

Figure 3.14. Schematic representation of possible self-assembled structures formed on CuNWs after surface modification with alkanethiols. (a) monolayer on the nanowire surface and (b) self-assembled alkanethiolate copper complexes that may be present in the multilayer.[24-27]

3.5 Conclusions

Copper nanowires produced by AC electrodeposition and liberation from PAO templates were surface functionalized with alkanethiols to decrease the strong agglomeration forces that take place between copper surfaces when methanol is removed after the liberation process. Consequently, surface modification enhances the CuNW dispersion into polymer matrixes, as will be shown further in Chapters 4 and 5. Although studies about the self-assembly of alkanethiols on Cu surfaces have been reported previously,[5,9-12,32] the mechanism and structure of self-assembled structures at oxidized-Cu surfaces have not been completely elucidated. However, it is known that the presence of oxides at the metal surface promotes the formation of multilayers.[5,7] Characterization of functionalized copper nanowires by XPS, XRD, NMR, TGA and elemental analysis indicated the presence of alkanethiolates (RS-Cu) and significant adsorption of alkanethiols. The data is consistent with the presence of self-assembled RS-Cu complexes at the surface of the CuNWs. The presence of the multilayer is expected to affect the dispersion and the electrical percolation of the nanowires in polymer nanocomposites.

3.6 References

1. Du, F. M.; Fischer, J. E.; Winey, K. I., *J. Polym. Sci., Part B: Polym. Phys.* **2003,** 41, (24), 3333-3338.
2. Mitchell, C. A.; Bahr, J. L.; Arepalli, S.; Tour, J. M.; Krishnamoorti, R., *Macromolecules* **2002,** 35, (23), 8825-8830.
3. Gelves, G. A.; Murakami, Z. T. M.; Krantz, M. J.; Haber, J. A., *J. Mater. Chem.* **2006,** 16, (30), 3075-3083.
4. Sexton, B. A., *Surf. Sci.* **1979,** 88, (2-3), 299-318.
5. Keller, H.; Simak, P.; Schrepp, W.; Dembowski, J., *Thin Solid Films* **1994,** 244, (1-2), 799-805.
6. Kim, Y. T.; McCarley, R. L.; Bard, A. J., *Langmuir* **1993,** 9, (8), 1941-1944.
7. Woodward, J. T.; Walker, M. L.; Meuse, C. W.; Vanderah, D. J.; Poirier, G. E.; Plant, A. L., *Langmuir* **2000,** 16, (12), 5347-5353.
8. Chen, T. Y.; Chen, S. F.; Sheu, H. S.; Yeh, C. S., *J. Phys. Chem. B* **2002,** 106, (38), 9717-9722.
9. Sung, M. M.; Sung, K.; Kim, C. G.; Lee, S. S.; Kim, Y., *J. Phys. Chem. B* **2000,** 104, (10), 2273-2277.

10. Laibinis, P. E.; Whitesides, G. M.; Allara, D. L.; Tao, Y. T.; Parikh, A. N.; Nuzzo, R. G., *J. Am. Chem. Soc.* **1991,** 113, (19), 7152-7167.

11. Laibinis, P. E.; Whitesides, G. M., *J. Am. Chem. Soc.* **1992,** 114, (23), 9022-9028.

12. Ron, H.; Cohen, H.; Matlis, S.; Rappaport, M.; Rubinstein, I., *J. Phys. Chem. B* **1998,** 102, (49), 9861-9869.

13. Rosencwa, A.; Wertheim, G. K.; Guggenhe, H., *Phys. Rev. Lett.* **1971,** 27, (8), 479-&.

14. Larson, P. E., *J. Electron Spectrosc. Relat. Phenom.* **1974,** 4, (3), 213-218.

15. McIntyre, N. S.; Cook, M. G., *Anal. Chem.* **1975,** 47, (13), 2208-2213.

16. Bukhtiyarov, V. I.; Kaichev, V. V.; Prosvirin, I. P., *Top. Catal.* **2005,** 32, (1-2), 3-15.

17. Prosvirin, I. P.; Tikhomirov, E. P.; Sorokin, A. M.; Kaichev, V. V.; Bukhtiyarov, V. I., *Kinet. Catal.* **2003,** 44, (5), 662-668.

18. Laiho, T.; Leiro, J. A.; Heinonen, M. H.; Mattila, S. S.; Lukkari, J., *J. Electron Spectrosc. Relat. Phenom.* **2005,** 142, (2), 105-112.

19. Castner, D. G.; Hinds, K.; Grainger, D. W., *Langmuir* **1996,** 12, (21), 5083-5086.

20. Rieley, H.; Kendall, G. K.; Zemicael, F. W.; Smith, T. L.; Yang, S. H., *Langmuir* **1998,** 14, (18), 5147-5153.

21. Ang, T. P.; Wee, T. S. A.; Chin, W. S., *J. Phys. Chem. B* **2004,** 108, (30), 11001-11010.

22. Sandhyarani, N.; Antony, M. P.; Selvam, G. P.; Pradeep, T., *J. Chem. Phys.* **2000,** 113, (21), 9794-9803.

23. Sandhyarani, N.; Resmi, M. R.; Unnikrishnan, R.; Vidyasagar, K.; Ma, S. G.; Antony, M. P.; Selvam, G. P.; Visalakshi, V.; Chandrakumar, N.; Pandian, K.; Tao, Y. T.; Pradeep, T., *Chem. Mater.* **2000,** 12, (1), 104-113.

24. Dance, I. G.; Fisher, K. J.; Banda, R. M. H.; Scudder, M. L., *Inorg. Chem.* **1991,** 30, (2), 183-187.

25. Espinet, P.; Lequerica, M. C.; Alvarez, J. M. M., *Chem. Eur. J* **1999,** 5, (7), 1982-1986.

26. Bensebaa, F.; Ellis, T. H.; Kruus, E.; Voicu, R.; Zhou, Y., *Langmuir* **1998,** 14, (22), 6579-6587.

27. Sandhyarani, N.; Pradeep, T., *J. Mater. Chem.* **2001,** 11, (4), 1294-1299.

28. Dance, I. G., *Polyhedron* **1986,** 5, (5), 1037-1104.

29. Badia, A.; Gao, W.; Singh, S.; Demers, L.; Cuccia, L.; Reven, L., *Langmuir* **1996,** 12, (5), 1262-1269.

30. Badia, A.; Cuccia, L.; Demers, L.; Morin, F.; Lennox, R. B., *J. Am. Chem. Soc.* **1997,** 119, (11), 2682-2692.

31. Gelves, G. A.; Lin B.; Sundararaj, U.; Haber, J. A., *Adv. Funct. Mater.* **2006,** 16, 2423-2430.

32. Jennings, G. K.; Laibinis, P. E., *Colloids Surf., A* **1996,** 116, (1-2), 105-114.

Chapter 4

Cu and Ag nanowire/Polystyrene nanocomposites produced by solution processing

4.1 Introduction

Polystyrene (PS) was selected as the polymer matrix with which to prepare polymer nanocomposites, because it is one the most widely studied and used commodity polymers. Thus, the effects of the copper and silver nanowires on the properties of these nanocomposites could be easily identified. A few works related to the preparation of nanowire/PS nanocomposites can be found in the literature. These studies have been published recently and are briefly mentioned as follows: Co nanowires (12-24 nm in diameter and 1 μm in length) were electrodeposited in films of di-block copolymers of PS and poly(methylmethacrylate),[1,2] for the study of the magnetic properties of Co nanowire arrays; Pd nanowires (250 nm in diameter) were electrodeposited on Highly Oriented Pyrolytic Graphite (HPOG) and then transferred by a shadow masking technique into PS films for the preparation of a PS nanocomposite with hydrogen sensing properties;[3] Ag nanorod (30 nm)/PS nanocomposite was prepared by a so called reverse-micelle-gas antisolvent-ultrasound method, which resulted in composite nanorods of controllable length (200 nm to microns in length).[4] Very recently, and in a similar approach to that developed in this work, Ag nanowires (300 nm, 10 μm) fabricated in porous alumina templates have been incorporated in polymer films of an immiscible blend 30/70 of polystyrene/poly(vinyl pyrrolidone).[5] Nonetheless, to the best of our knowledge, the electrical and rheological percolation of metal nanowire/polymer nanocomposites using melt mixing or solution process have not been studied.

PS nanocomposites containing SWNT and MWNT have received more attention. Some specific applications of CNT/PS nanocomposites that have been reported are: field emission,[6] EMI shielding foams,[7] and microwave absorbing materials.[8] Carbon nanotube/PS nanocomposites have been prepared by solution mixing,[7,9-16] melt mixing,[17,18] and in situ polymerization.[19-21] For instance, very low electrical percolation thresholds of 0.05 to 0.3 wt. % for SWNT/PS and 0.014 wt % for MWNT/PS have been reported.[21]. Other efforts of producing PS nanocomposites with interesting electrical or inductive properties have been demonstrated using carbon nanotubes doped with B or filled with Fe, respectively.[22,23] However, the rheological properties of PS nanocomposites have been scarcely studied, and a complete analysis of the relation between dispersion, electrical, and rheological properties of SWNT/PS or MWNT/PS composites still remains to be elucidated

Copper and silver nanowires produced by the PAO template-directed synthesis were used to prepare metal nanowire/PS nanocomposites by solution processing. The effect of the concentration and chemical modification with alkanethiols of copper and silver nanowires on the dispersion, and electrical and viscoelastic properties of polymer nanocomposites were studied. Electrical and rheological characterization of the nanocomposites was essential for an understanding of the relationship between the microstructure and the properties of the nanocomposites.

4.2 Experimental

4.2.1 Preparation of polystyrene nanocomposites by solution processing

Cu or Ag nanowire/polystyrene nanocomposites were produced by dispersing the nanowires (unfunctionalized or chemically functionalized) in a 1.2 wt.-% solution of polystyrene resin (Styron 666D, Dow Chemical, M.I = 7.5, M_w = 200,000 g/mol, and T_g = 100 °C) in CH_2Cl_2 using an ultrasonic bath (35 W average power, 38.5-40.5 kHz). The bulk densities of copper (8.96 g/cm^3) and PS (1.04 g/cm^3) were used to calculate the amounts of CuNWs and polymer to be used in each experiment. A sonication time of 30 minutes was utilized applying ultrasound for 5 min with a 5 min rest period between sonications. The suspension was cast in an evaporation dish, the solvent evaporated and the resultant nanocomposite dried in a vacuum oven at 50 °C for 24 h to obtain ~120 μm thick films. The polymer composite films were cut into small pieces (~ 4 mm^2) and then hot pressed at 200 °C and 1.5 metric tons for 5 min in a 0.8 mm thick, 25.4 mm diameter stainless steel mold, separated by aluminum foil from top and bottom stainless steel plates.

4.2.2 SEM and TEM of nanocomposites

For SEM analysis of nanocomposites, hot molded samples were immersed in liquid nitrogen for 5 minutes and freeze fractured. Samples were chromium coated to enable surface electrical conductivity and facilitate imaging of the nanocomposites. SEM images were collected using a JEOL 6301F Field Emission Scanning Electron Microscope. Backscattered electron images were collected using an accelerating voltage of 20 kV. For TEM analysis of nanocomposites, hot molded samples were embedded in epoxy resin and then ultramicrotomed to give sections ~70 nm thick using an Ultracut diamond knife at room temperature. TEM images were collected using a Philips Morgagni 268 microscope at an acceleration voltage of 70 kV.

4.2.3 Measurement of electrical resistivity of nanocomposites

The electrical resistivity of polymer nanocomposites was measured by two different techniques using two different setups as follows. At the beginning of this study, the instrumentation available for resistivity measurements consisted of an ETS Model 804B resistivity probe and a 617 Keithley Electrometer. This setup was capable of measuring resistances up to 2×10^{11} Ohms using a constant current method. The volume resistance of the samples was measured between the disk electrode of the probe acting as the top electrode and a polished copper plate acting as the bottom electrode (Figure 4.1a). The measured volume resistance, R_v, was converted to volume resistivity, ρ_v, using equation (4.1)

$$\rho_v=(A/t)R_v \tag{4.1}$$

where, A is the effective area of the measuring electrode (0.85 cm^2), and t is the average thickness of the specimen. The measurements were performed under atmospheric conditions on samples pre-conditioned at 0% humidity for 24 h. Conductive rubber sheet (Zoflex® CD75, volume resistivity = 0.06 Ω·cm) was utilized to improve the electrical contact of the specimens to the copper plate electrode.

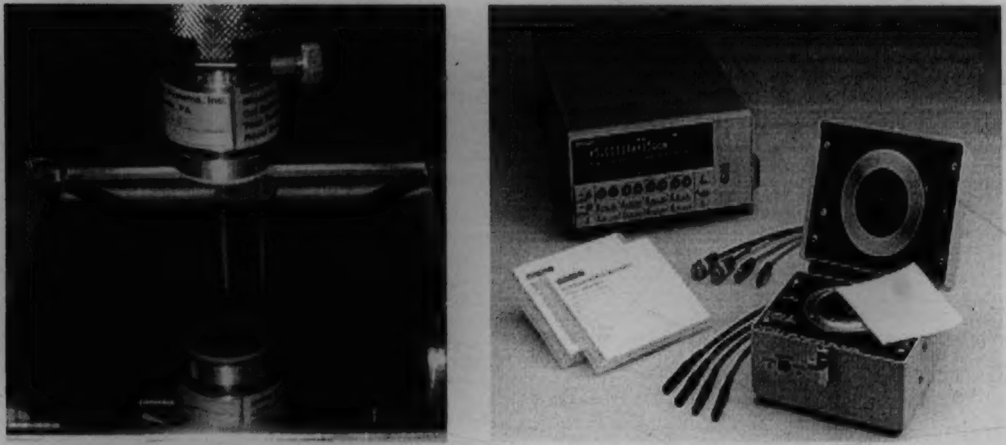
(a) (b)

Figure 4.1. Photographs of the two different probes used for measurement of volume electrical resistivity of polymer nanocomposites. (a) Electrical resistivity probe ETS-804B used along with a Keithley Electrometer 617; the reflected image on the copper plate shows the inner disk and the ring of the probe, (b) 6517A Keithley electrometer and 8009 Keithley resistivity test fixture.

In order to make electrical resistivity measurements in the range between 10^3 and 10^{16} Ω for the characterization of polymers and their composites, a more specialized measurement setup was acquired. This setup consisted of a 6517A Keithley electrometer, 8009 Keithley resistivity test fixture, and Keithley 6524 high resistance measurement software (Figure 4.1b). Table 4.1 shows the specifications of the 8009 resistivity probe. Alternating voltages from 10 to -10 V or 100 to -100 V were used for conductive or resistive samples, respectively. The alternating voltage reduces the effect of inherent background currents, improving the accuracy of the measurement. The measured volume resistance, R_v, was converted to volume resistivity, ρ_v, using equation (4.1), where A, the effective area of the specimen was equal to 4.99 cm^2. The electrical resistivity was measured using 100 V for samples with $R > 10^6$ Ω and 10 V for samples with $R < 10^6$ Ω according to ESD STM11.12-2000. Parafilm® layers with a 25.4 mm hole in the centre for the sample to fit in were utilized to avoid contact between the top and bottom electrodes of the fixture. The measurements were performed under atmospheric conditions on samples pre-conditioned at 0 % humidity for 24 h. Three to six replicate samples were prepared and measured at each concentration of nanowires.

Table 4.1. Specifications of the Model 8009 Keithley resistivity test fixture.

Parameter	Specification
Volume resistivity range	$10^3 - 10^{18}$ Ω·cm
Surface resistivity range	$10^3 - 10^{17}$ Ω
Center electrode	50.8 mm O.D. ± 0.05 mm conductive rubber pad
Top electrode	85.7 mm O.D. ± 0.05 mm, 54 mm diameter conductive rubber pad
Ring electrode	57.2 mm I.D. ± 0.05 mm
Electrode material	Type #303 stainless steel
Pad resistivity	10 Ω/sq max.

4.2.4 Rheological characterization

Dynamic rheological characterization was performed on hot molded samples 25.4 mm in diameter and 0.8 mm thick using a Rheometrics Inc. RMS800 Rheometer with a 25 mm parallel plate fixture at 200 °C under nitrogen atmosphere. Frequency sweeps were performed at low strains (0.09 - 10%), where the materials show linear viscoelastic behavior.

4.3 Results

4.3.1 Dispersion and electrical percolation of metal nanowires in PS nanocomposites

Cu and Ag nanowires produced by template-directed synthesis in PAO templates were used to prepare PS nanocomposites using a solution processing method. The dispersion of the nanowires into the polymer matrix and the effect of the concentration of metal (Cu, Ag) nanowires on the electrical resistivity of the composites were studied.

4.3.1.1 Dispersion and electrical resistivity of CuNW/PS nanocomposites - Initial experiments

Initial experiments preparing nanocomposites were developed using copper nanowires produced using PAO templates that consisted of pores ~ 25 nm in diameter and ~ 16 μm deep. These experiments were carried out before the scale-up of the synthesis of nanowires was accomplished.

CuNW/PS nanocomposites were produced by dispersing different amounts of copper nanowires into a solution of polystyrene in CH_2Cl_2. Figure 4.2 shows scanning electron microscopy images of freeze-fractured portions of a nanocomposite prepared with 4 vol. % CuNWs. The nanowires are observed as bright spots or domains in backscattered SEM images, as indicated in Figure 4.2. A fraction of the CuNWs do not disperse in the solution, and apparently segregate during the slow drying process to form a higher-concentration nanowire layer at the bottom of the film (polymer cast). Considering this, fast evaporation of the solvent was tested using reduced pressures. However, SEM characterization of the samples prepared using fast evaporation showed that drying the cast film quickly decreased the degree of segregation only marginally. This indicates that the unfunctionalized CuNWs form relatively large agglomerates during the filtration process, which do not re-disperse upon application of ultrasound and settle quickly. Upon cutting up and hot pressing this segregated film to produce the resistivity test samples, the high concentration layer becomes buckled and re-oriented, as seen in the low magnification image (Figure 4.2a). There is, however, still a considerable fraction of Cu nanowires well-dispersed in the polymer-rich portion of the composite (Figure 4.2b).

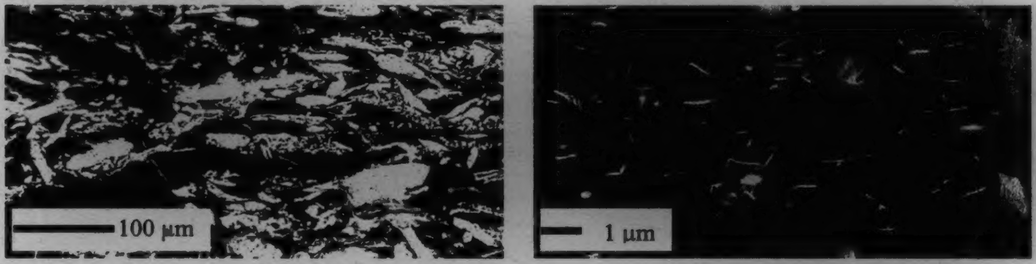

(a) (b)

Figure 4.2. Backscattered SEM images for a freeze-fractured sample of a CuNW/PS nanocomposite containing 4 vol. % CuNWs: (a) low magnification image of a cross section showing agglomerates of unfunctionalized CuNWs and (b) high magnification image of a cross section showing the presence of dispersed nanowires in the polymer between the agglomerates.

The results of electrical resistivity measurements on nanocomposites containing different concentrations of Cu nanowires are shown in Table 4.2. The volume electrical resistivity (ρ) of the composites showed percolation behavior above concentrations of 2.0 vol. % Cu nanowires. A dramatic decrease in ρ of approximately 7 orders of magnitude occurred between concentrations of 2.0 and 4.0 vol. % Cu. This is explained by the formation of an interconnected conductive network of the nanowires in the polymer matrix. The standard deviation of the 2.0 vol. % composite (approximately three orders of magnitude) indicates that this concentration is close to the percolation threshold of the nanowires in the polymer matrix, where small changes in the microstructure might result in significant variations on the resistivity. In contrast, the small standard deviation of the electrical resistivity at higher concentrations of nanowires indicates consistent values corresponding to electrically conductive composites. However, a complete percolation curve was not obtained from these experiments, because measurements of electrical resistivity values of nanocomposites prepared with concentrations lower than 2.0 vol. % of nanowires was not possible with the available test system (ETS Model 804B resistivity probe and 617 Keithley Electrometer).

Table 4.2. Average volume electrical resistivity and standard deviations calculated for Cu nanowire/PS nanocomposites with different concentrations of Cu nanowires (prepared in 16 μm thick PAO templates using the smaller-scale process, average length = 1.78 ± 1.37 μm).

Cu Conc. (Vol. %)	ρ ($\Omega\cdot$cm)	Log (ρ, $\Omega\cdot$cm)	No. of Specimens	Standard Deviation
2.0	3.57×10^9	9.55	4	0.99
4.0	6.04×10^1	1.78	3	0.28
6.0	1.50×10^4	4.17	3	0.35
10.0	4.92×10^1	1.69	1	-

Polymer composites were also prepared using commercial copper powder utilizing a procedure similar to that used to prepare the CuNW/polymer nanocomposites. Table 4.3 shows the electrical resistivity obtained from composites containing micron-sized copper particles (< 1.5 μm particle size). In this case, the resistivity values did not indicate the occurrence of electrical percolation even up to concentrations of 10 vol. % copper, as expected. The percolation threshold for randomly dispersed spherical particles is ~ 16 vol. %;[24,25] hence, the observed behavior of the blends prepared using commercial spherical particles is expected, and intended only as a control to illustrate that small size and high aspect-ratio nanowires are required to achieve percolation at low volume fractions of metal.

Table 4.3. Average volume electrical resistivity and standard deviations calculated for spherical micron-sized Cu particle/PS nanocomposites at different concentrations of copper.

Cu Conc. (Vol. %)	ρ ($\Omega\cdot$cm)	Log (ρ, $\Omega\cdot$cm)	No. of Specimens	Standard deviation
4.0	2.35×10^{11}	11.37	3	0.23
6.0	3.54×10^{10}	10.55	3	0.37
8.0	3.80×10^{9}	9.58	3	0.22
10.0	2.35×10^{9}	9.37	3	0.19

Considering that irreversible agglomeration of CuNWs was observed after the liberation from the PAO templates, chemical modification of the surface of the CuNWs was carried out using 1-octadecanethiol ($C_{18}H_{37}SH$). The long chain of the alkanethiol was expected to coat the nanowires through covalent bonding of the sulfur atoms of the thiol to the Cu atoms at the surface of CuNW, i.e. the formation of copper-alkanethiolates. In addition, van der Waals forces between the functionalized CuNWs will be overcome in hydrophobic solvents, facilitating their mixing in the polymer solution. Enhanced dispersion of the nanowires in the polymer matrix was also expected, due to a decrease in the interfacial tension between polymer chains and the modified surface of the nanoparticles. For experimental consistency, CuNWs prepared using PAO templates 16 μm thick were utilized. The methodology for the chemical modification of the nanowires and their characterization were described in Chapter 3. The effect of the surface modification of CuNWs with $C_{18}H_{37}SH$ on the dispersion and electrical properties of polystyrene nanocomposites was then studied.

Figure 4.3 shows backscattered electron SEM images of freeze-fractured samples of nanocomposites containing 4.0 vol. % $C_{18}H_{37}SH$-CuNWs. Scanning electron microscopy of freeze-fractured portions of the nanocomposites indicates distinct differences between nanocomposites containing unfunctionalized (Fig. 4.2) and $C_{18}H_{37}SH$ functionalized nanowires (Fig. 4.3). It is evident that the functionalized nanowires re-disperse much better than the unfunctionalized nanowires (Fig 4.2), which become much more tightly agglomerated during the filtration step. Surface modification of CuNWs with $C_{18}H_{37}SH$ reduced the effect of irreversible agglomeration of the nanowires and facilitated their suspension in the polymer solution. The enhanced dispersion of the nanowires should increase the probability for the formation of an electrically interconnected network of nanowires given that a greater number of nanowires are dispersed throughout the matrix.

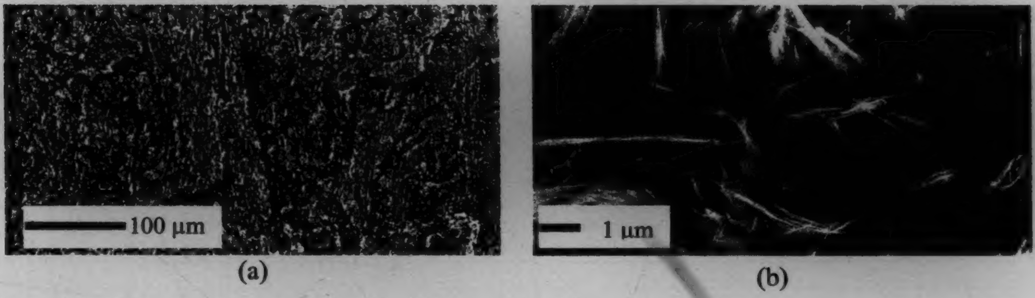

(a) (b)

Figure 4.3. Backscattered SEM images for a freeze-fractured sample of $C_{18}H_{37}S$-CuNW/PS nanocomposite containing 4 vol. % CuNWs: (a) low magnification image showing absence of CuNW agglomerates and (b) high magnification image of a cross section showing good dispersion of functionalized nanowires.

The average volume electrical resistivities and standard deviations for the polymer nanocomposites containing different concentrations of $C_{18}H_{37}S$-CuNWs are presented in Table 4.4 Electrical percolation of $C_{18}H_{37}S$-CuNWs in the polystyrene matrix did not occur, as can be inferred from the invariant resistivity of the sample up to concentrations of 10 volume percent. The relatively thick alkyl thiol coating improves dispersion, but also acts as an electrically insulating layer on each nanowire. Nonetheless, these results led to the conclusion that achieving a percolated network at low volume fraction of conductive filler requires a balance between good dispersion of the nanoparticles in the polymer and the formation of good electrical contacts between the conductive particles.

Table 4.4. Average volume electrical resistivity and standard deviations calculated for $C_{18}H_{37}S$-CuNW/PS nanocomposites for different concentrations of copper.

Cu Conc. (Vol. %)	ρ ($\Omega\cdot$cm)	Log (ρ, $\Omega\cdot$cm)	No. of Specimens	Standard deviation
1	1.01×10^{11}	11.02	3	0.03
2	7.76×10^{10}	10.89	3	0.14
4	1.70×10^{11}	11.23	3	0.09
5	1.12×10^{11}	11.05	1	-
10	4.90×10^{11}	11.69	1	-

4.3.1.2 Electrical percolation of CuNWs and AgNWs in PS

Given the promising results obtained with nanocomposites containing unfunctionalized CuNWs described earlier, as well as the importance of determining the entire electrical percolation curve for the PS nanocomposites prepared by solution process, two objectives were pursued. First, the synthesis of CuNWs was scaled-up to the multigram scale, necessary for the preparation of replicate samples at multiple concentrations. An increase in the yield of CuNWs by increasing the thickness of the PAO templates was also implemented during the scale-up (Chapter 2). Second, a new electrical resistivity measurement instrument capable of measuring high resistivity values corresponding to the pristine polymer was acquired. The results of a systematic evaluation of electrical percolation of metal nanowires are presented below.

In this section, the results of dispersion and electrical percolation of Cu and Ag nanowires synthesized in and liberated from ~ 35 μm thick PAO templates are described. Given silver's greater resistance to oxidation and its lower electrical resistivity (1.6×10^{-6} $\Omega\cdot$cm) than copper (1.7×10^{-6} $\Omega\cdot$cm), silver nanowires were anticipated to yield more conductive nanocomposites beyond the percolation threshold. The electrical percolation curves for PS nanocomposites containing either Cu or Ag nanowires were evaluated utilizing instrumentation designed for the measurement of volume electrical resistivities in the range 10^{3}-10^{18} $\Omega\cdot$cm.

Secondary and backscattered SEM images of PS nanocomposites containing concentrations of CuNWs from 0.25 to 4.0 vol. % are shown in Figures 4.4 and 4.5. Bright domains in the backscattered electron SEM images correspond to the CuNWs. Low magnification SEM images (Fig. 4.4) show the distribution of the nanowires throughout the thickness of hot-molded specimens; small agglomerates are observed at low concentration of CuNWs, and the number and size of agglomerates increases as the copper concentration increases. As discussed in the previous section, layers of agglomerates result from segregation of nanowires during the preparation of the nanocomposites by solution processing. Large CuNW agglomerates are preferentially located at the bottom of the nanocomposite film obtained after evaporation of the solvent. High magnification SEM images (Fig. 4.5) of the regions located between the agglomerates show an increase in the density of individual nanowires dispersed in the sample with increasing CuNW concentration.

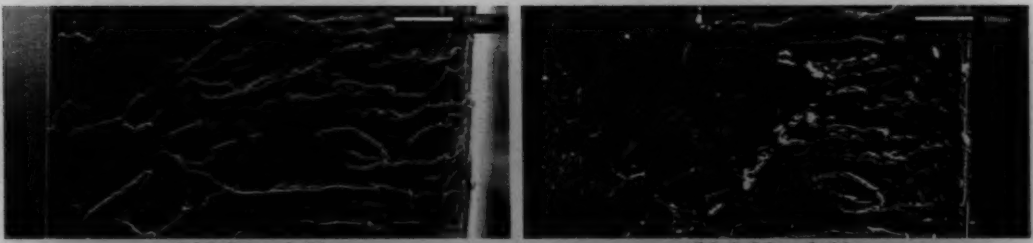

(a)0.25 vol. % (b) 0.25 vol. %

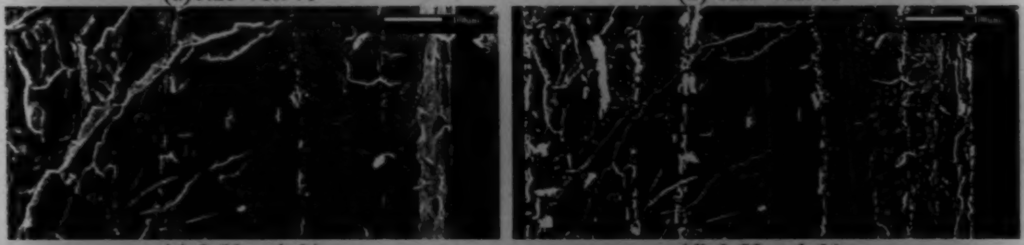

(c) 0.50 vol. % (d) 0.50 vol. %

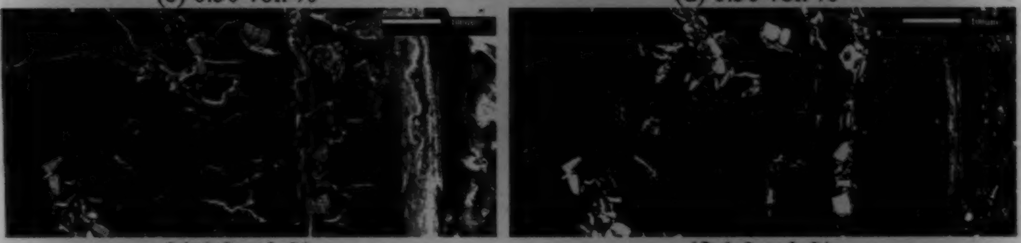

(e) 1.0 vol. % (f) 1.0 vol. %

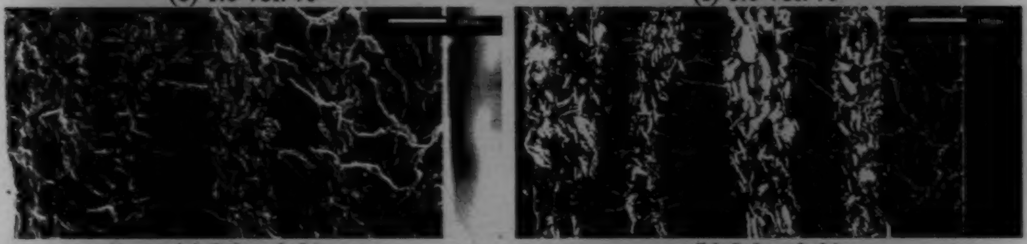

(g) 2.0 vol. % (h) 2.0 vol. %

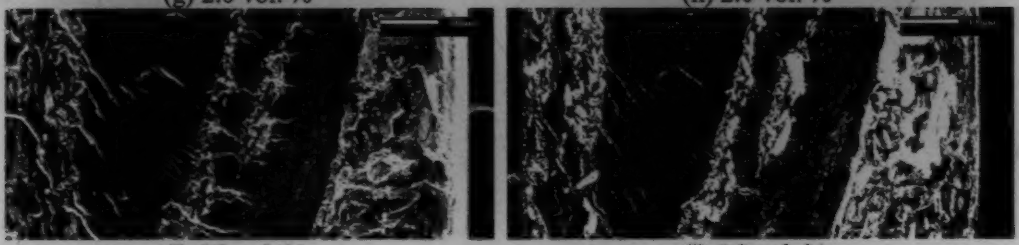

(i) 4.0 vol. % (j) 4.0 vol. %

Figure 4.4. Low magnification secondary (left) and backscattered (right) SEM images of freeze-fractured samples of solution-processed CuNW/PS nanocomposites containing different concentrations of CuNWs. The distribution of CuNWs is shown across the thickness of the samples.

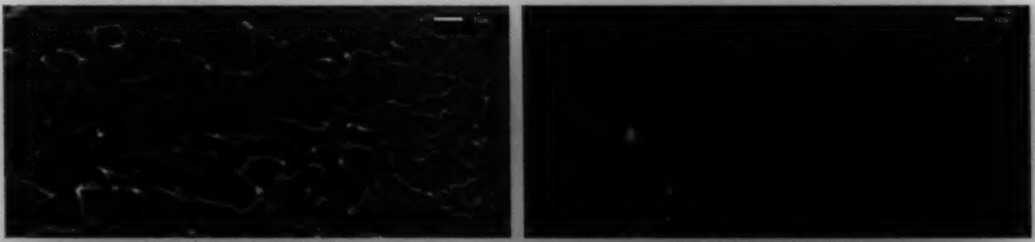

(a) 0.25 vol. % Cu (b) 0.25 vol. % Cu

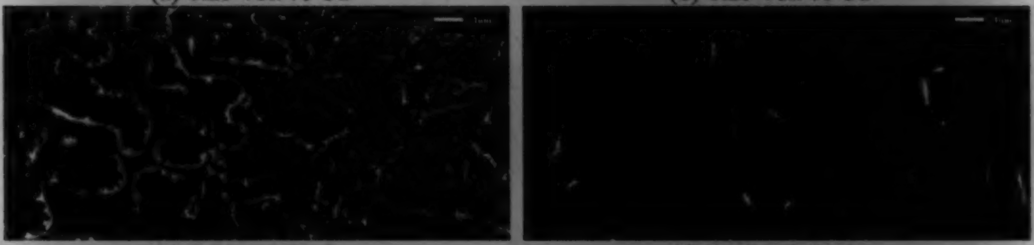

(c) 0.50 vol. % Cu (d) 0.50 vol. % Cu

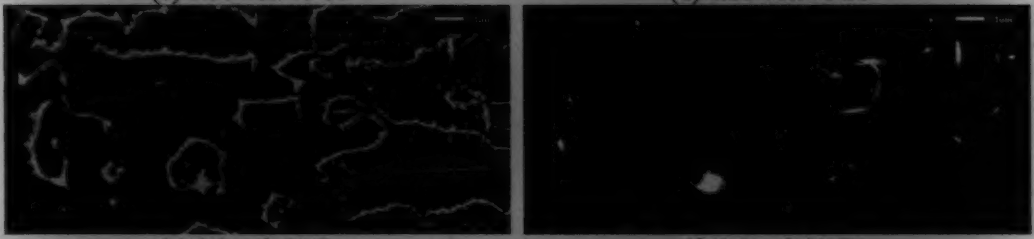

(e) 1.0 vol. % Cu (f) 1.0 vol. % Cu

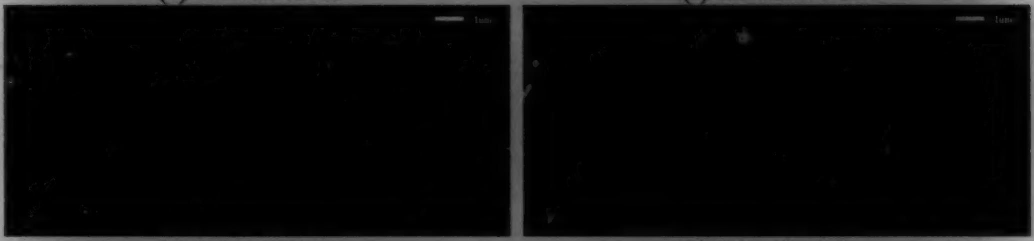

(g) 2.0 vol. % Cu (h) 2.0 vol. % Cu

(i) 4.0 vol. % Cu (j) 4.0 vol. % Cu

Figure 4.5. High magnification secondary (left) and backscattered (right) SEM images of freeze-fractured samples of solution-processed CuNW/PS nanocomposites containing different concentrations of CuNWs. The dispersion of individual nanowires increases with Cu concentration. Surface features on secondary images (left) are due to polymer fracture.

Figure 4.6 shows TEM images of a nanocomposite containing 1 vol. % copper. The nanowires are randomly oriented throughout the polymer matrix. Well-dispersed and agglomerated nanowires are observed. In addition, zones with higher concentrations of CuNWs are observed, corroborating the results from SEM analysis of the samples. High magnification TEM images showed nanowires ~ 1-2 μm in length, as well as small fragments only ~ 50 nm in length, which might be the result of degradation during processing of the nanocomposites.

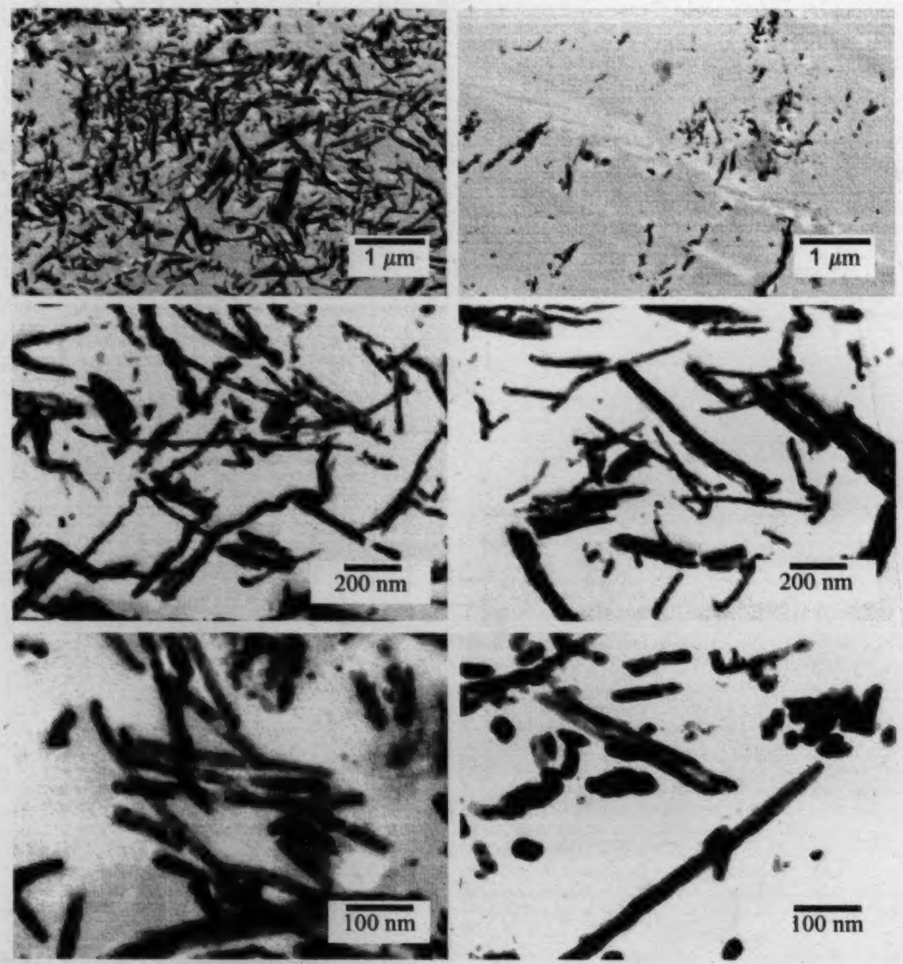

Figure 4.6. TEM images of CuNW/PS nanocomposite containing 1.0 vol. % CuNWs.

Similarly, SEM and TEM characterization was applied to PS nanocomposites containing AgNWs. Figures 4.7 and 4.8 show secondary and backscattered SEM images at low and high magnification of AgNW/PS nanocomposites. Low magnification SEM images show segregation of AgNWs in PS similar to that observed in CuNW/PS nanocomposites. Layers of higher concentration of silver nanowires were observed in conjunction with well-dispersed nanowires. TEM images of AgNW/PS nanocomposites (Figure 4.9) indicate the presence of well-dispersed nanowires along with agglomerated nanowires. Low magnification TEM images show AgNW bundles and well-dispersed nanowires, up to ~ 1 micron in length. High magnification images show small fragments of nanowires only ~ 100 nm in length, suggesting degradation of the AgNWs during the preparation of the nanocomposites.

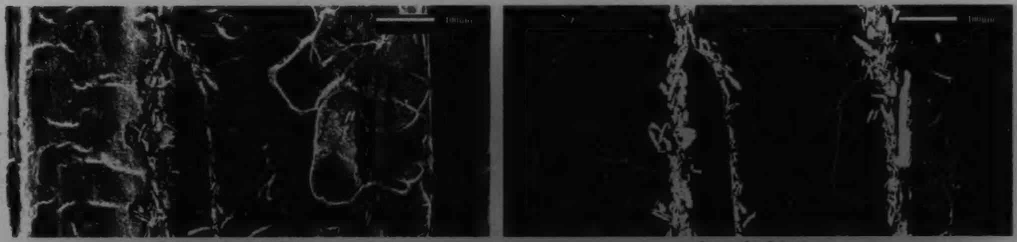

1.0 vol. % Ag 1.0 vol. % Ag

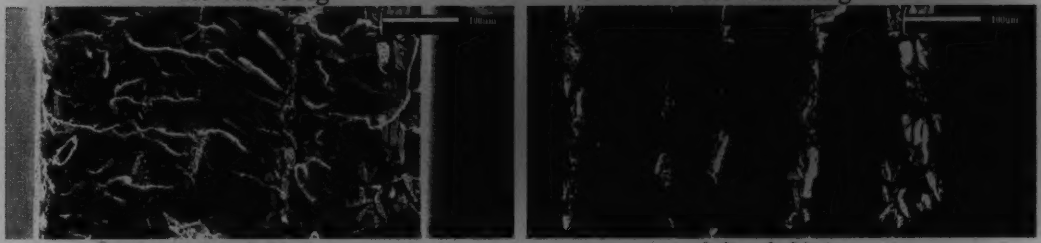

2.0 vol. % Ag 2.0 vol. % Ag

Figure 4.7. Low magnification secondary and backscattered SEM images of freeze-fractured samples of solution-processed AgNW/PS nanocomposites containing different concentrations of AgNWs. The distribution of the nanowires is shown across the thickness of the samples.

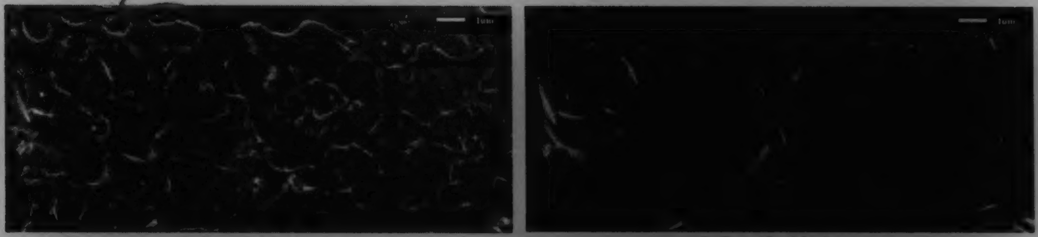

1.0 vol. % Ag 1.0 vol. % Ag

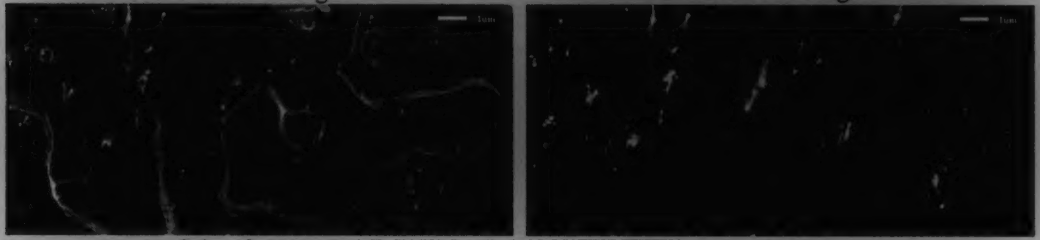

2.0 vol. % Ag 2.0 vol. % Ag

Figure 4.8. High magnification secondary and backscattered SEM images of freeze-fractured samples of solution-processed AgNW/PS nanocomposites containing different concentrations of AgNWs. Surface features on secondary images (left) are due to polymer fracture.

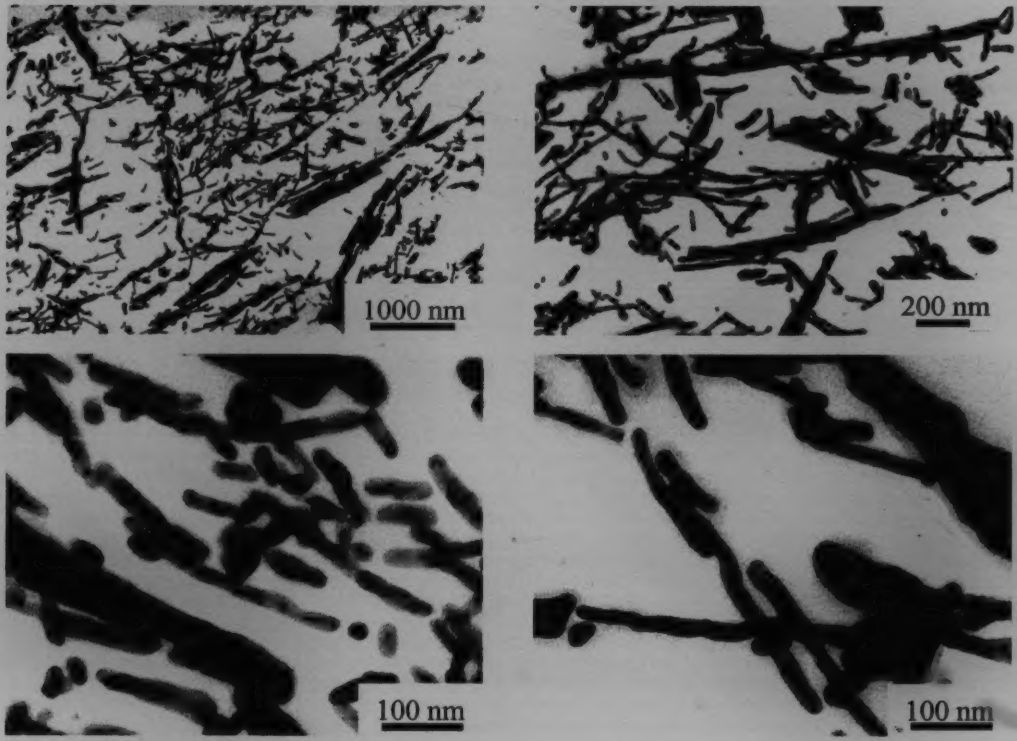

Figure 4.9. TEM images of AgNW/PS nanocomposite containing 1.0 vol. % AgNWs.

The volume electrical resistivity (ρ) for hot molded specimens of PS nanocomposites containing different concentrations of CuNWs and AgNWs are shown in Figure 4.10. The average ρ values and their standard deviations calculated from measurements of three to six samples at each concentration are specified in Tables 4.5 and 4.6. The ρ for pure PS is in the order of 10^{16} Ω·cm. A change of less than one order of magnitude in ρ is observed for the nanocomposites containing 0.25 vol. % of Cu and Ag nanowires. More significant changes in ρ of ~ 4 and ~ 9 orders of magnitude versus pure PS were observed for 0.50 vol. % CuNWs and 0.75 vol. % AgNWs, respectively. This indicates that at these concentrations, electrically conductive networks have formed. Above 1.0 vol. % of nanowires, the resistivity of the PS nanocomposites decreases gradually, as shown in Figure 4.10, so that ρ decreases by ~ 10 and ~ 11 orders of magnitude versus the pristine polymer for 4.0 vol. % Cu and Ag nanowires, respectively.

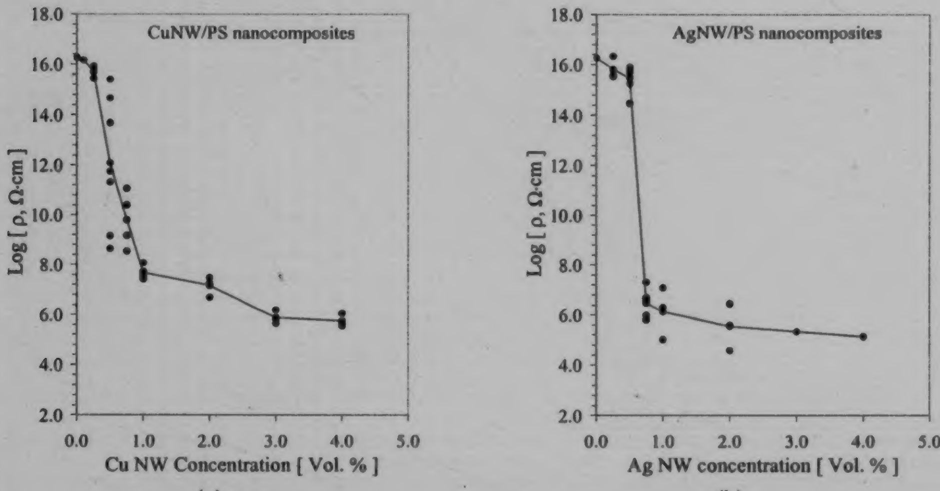

(a) (b)

Figure 4.10. Volume electrical resistivity of PS nanocomposites for different concentrations of Cu and Ag nanowires. (a) CuNW/PS and (b) AgNW/PS. Lines connect the average ρ_v.

Table 4.5. Average volume electrical resistivity and standard deviations calculated for Cu nanowire/polystyrene nanocomposites with different concentrations of Cu.

Cu Conc. (Vol. %)	ρ ($\Omega\cdot$cm)	Log (ρ, $\Omega\cdot$cm)	No. of Specimens	Standard Deviation
0.00	1.86×10^{16}	16.27	1	-
0.10	1.48×10^{16}	16.17	1	-
0.25	2.75×10^{15}	15.69	3	0.24
0.50	1.23×10^{12}	12.09	7	2.63
0.75	6.17×10^{9}	9.79	4	1.15
1.00	4.79×10^{7}	7.68	4	0.29
2.00	1.45×10^{7}	7.16	4	0.34
3.00	7.76×10^{5}	5.89	3	0.28
4.00	5.62×10^{5}	5.75	3	0.27

Table 4.6. Average volume electrical resistivity and standard deviations calculated for Ag nanowire/polystyrene nanocomposites with different concentrations of Ag

Ag Conc. (Vol. %)	ρ ($\Omega\cdot$cm)	Log (ρ, $\Omega\cdot$cm)	No. of Specimens	Standard Deviation
0.00	1.86×10^{16}	16.27	1	-
0.25	6.46×10^{15}	15.81	3	0.45
0.50	2.95×10^{15}	15.47	6	0.54
0.75	3.02×10^{6}	6.48	5	0.60
1.00	1.38×10^{6}	6.14	3	1.05
2.00	3.55×10^{5}	5.55	4	0.77
3.00	2.14×10^{5}	5.33	1	-
4.00	1.35×10^{5}	5.13	1	-

The average electrical resistivities of the nanocomposites were converted to values of conductivity, σ ($\sigma = 1/\rho$), and then used to calculate the percolation threshold by using the power law for the conductivity of the composite:[24]

$$\sigma \propto (V - Vc)^{t} \qquad (4.2)$$

where, σ is the DC conductivity of the composite, V is the volume percent content of the particles, Vc is the percolation threshold of the particles in the composite, and t is the critical exponent. The best fitting of the conductivity values versus the nanowire concentration to a linear equation was obtained for Vc_{CuNW} = 0.46 vol. % and Vc_{AgNW} = 0.51 vol. % as indicated in Figures 4.11 and 4.12, respectively. A higher percolation threshold for silver than for copper nanowires may be related to the different aspect ratio distributions of the two types of particles.

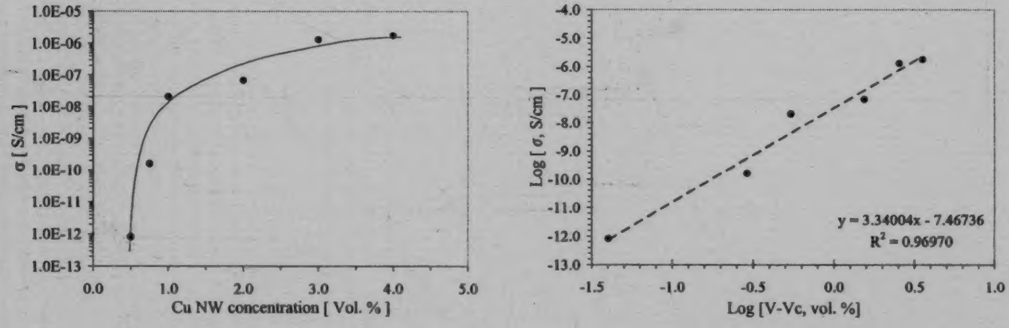

(a) (b)

Figure 4.11. (a) Electrical conductivity of CuNW/PS nanocomposites above the electrical percolation threshold of copper nanowires, and (b) log-log plot of the electrical conductivity as a function of ($V - Vc$), where, Vc is the percolation threshold = 0.46 vol. %. Critical exponent t = 3.34. Line in (a) is a guide to the eye and line in (b) corresponds to the linear least-square fit of the data.

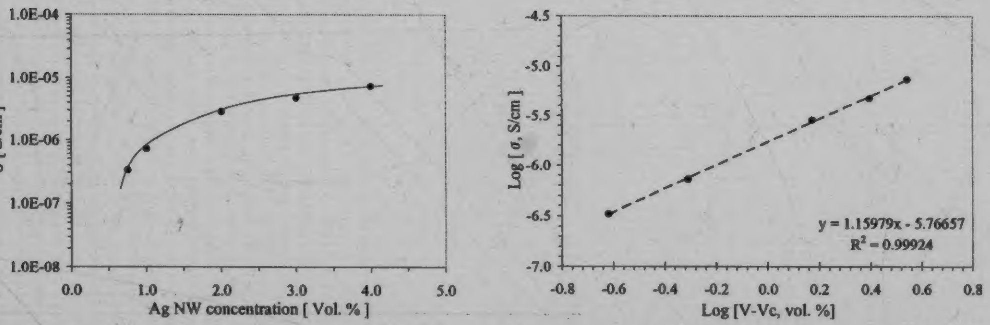

Figure 4.12. (a) Electrical conductivity of Ag NW/PS nanocomposites above the electrical percolation threshold of silver nanowires, and (b) log-log plot of the electrical conductivity as a function of $(V - Vc)$, where, Vc is the percolation threshold = 0.51 vol. %. Critical exponent $t = 1.16$. Line in (a) is a guide to the eye and line in (b) corresponds to the linear least-square fit of the data.

According to percolation theory, the universal value of the critical exponent "t" in the relationship between conductivity and volume fraction of a 3D network is ~ 1.6,[24] for the random distribution of the conductive particles in the nonconductive matrix. The critical exponents calculated were 3.34 and 1.16 for CuNWs and AgNWs, respectively. Thus, the critical exponents deviate from the $t \sim 1.6$ predicted by percolation theory. The difference in the critical exponents for CuNWs and AgNWs versus percolation theory may be attributed to a non-random distribution of the nanoparticles in the composites, which consists of agglomerated and well-dispersed individual NWs, as demonstrated by SEM and TEM characterization. Calculations of critical exponents in studies of polymer nanocomposites containing carbon nanotubes and other fillers have resulted in values different from those predicted by theory.[26] A discussion of some of the reasons why the critical exponent does not obey the percolation theory has been presented by Balberg et al.[27-29] One of the reasons for such behavior is the mechanism of electronic conductivity by electron tunneling.

Despite the slightly higher conductivity of Ag versus Cu, and the evidence of no surface oxidation on AgNWs, the electrical percolation of AgNWs occurred at a higher volume fraction than that of Cu nanowires (Fig. 4.10). The difference is primarily attributed to the lower aspect ratios of the Ag nanowires (up to 200) in comparison to copper nanowires (up to 400) as shown in Chapter 2, although differences in surface chemistry and distribution may also be contributing factors.

At concentrations above the percolation threshold, the resistivity of the nanocomposite depends primarily upon the conductivity of the nanofiller; therefore, it is expected that silver nanowires will produce more conductive nanocomposites than copper, given the higher conductivity of Ag versus Cu, and the fact that some surface oxidation exists on the Cu nanowires, but not on the Ag nanowires. Indeed, the resistivity of the nanocomposites after percolation indicate a plateau between 1×10^6 - 1×10^5 $\Omega\cdot$cm for compositions from 1 to 4 vol. % AgNWs, and $1\times10^7 - 1\times10^5$ $\Omega\cdot$cm for compositions from 1 to 4 vol % CuNWs. It is worth mentioning that, as predicted at the beginning of this work, percolated metal nanowire/PS nanocomposites presented ρ values within the range specified for materials with electrostatic dissipation properties as recommended by the Electrostatic Discharge Association (1×10^4 - 1×10^{11} $\Omega\cdot$cm; www.esda.org).[30]

4.3.2 The effect of surface functionalization on dispersion and electrical percolation

4.3.2.1 Dispersion of $C_8H_{17}S$-CuNWs

Considering the results from initial experiments of nanocomposites prepared with different concentrations of $C_{18}H_{37}S$-CuNWs, described in section 4.3.1.1, experiments using shorter alkyl thiols, such as $C_8H_{17}SH$, were carried out to demonstrate the feasibility of achieving electrical percolation of chemically modified nanowires in a polymer matrix. Short chain alkylthiol could promote enhanced dispersion of the nanoparticles without significantly affecting the electrical properties of the composites produced. In this section, the characterization of dispersion and electrical properties of polystyrene nanocomposites containing $C_8H_{17}S$-CuNWs will be described.

Copper nanowires used in these experiments were synthesized in 35 μm thick PAO templates. As was discussed in chapter 3, the degree of thiol adsorption in copper nanowires is related to the concentration of the thiol in solution during the surface functionalization process. Using low concentration solutions results in relatively low coverage of the nanowires. Thus, it was important to determine the effect of functionalizing copper nanowires using different 1-octanethiol concentrations on the dispersion and electrical properties of polystyrene nanocomposites. The results obtained from these experiments are presented below.

Table 4.7 shows the volume electrical resistivities of 1.0 vol. % $C_8H_{17}S$-CuNW/PS nanocomposites prepared using CuNWs modified in solutions of different concentrations of $C_8H_{17}SH$ (0.1, 1.0, 2.5, and 5.0 mM).

Table 4.7. Volume electrical resistivity of 1.0 vol. % CuNW/polystyrene nanocomposites containing unfunctionalized copper nanowires and copper nanowires chemically functionalized in different concentrations of 1-octanethiol (mM = 0.1, 1.0, 2.5 and 5.0)

CuNW/PS Nanocomposites	Cu Conc. (Vol. %)	ρ ($\Omega \cdot$cm)	Log (ρ, $\Omega \cdot$cm)
CuNW/PS	1.0	4.79×10^7	7.68
0.1mM-$C_8H_{17}S$-CuNW/PS	1.0	5.25×10^7	7.72
1.0mM-$C_8H_{17}S$-CuNW/PS	1.0	5.75×10^{11}	11.76
2.5mM-$C_8H_{17}S$-CuNW/PS	1.0	4.37×10^{11}	11.64
5.0mM-$C_8H_{17}S$-CuNW/PS	1.0	3.55×10^{11}	11.55

The average electrical resistivity of 1.0 vol. % CuNW/PS nanocomposites prepared using unfunctionalized nanowires is shown for comparison. A concentration of 1.0 vol. % was selected based on the percolation curve of CuNW/PS nanocomposites described in section 4.3.1.2 that indicates the formation of percolated composites above 0.5 vol. %. The resistivity of the 0.1mM-$C_8H_{17}S$-CuNW/PS is similar to that of the composite prepared with unfunctionalized nanowires (CuNW/PS), which indicated that the electron flow through a conductive network of conductive particles is likely when relatively poorly covered CuNWs were utilized. With higher coverages of $C_8H_{17}SH$ on the nanowires, obtained with more concentrated solutions of thiol (1.0 mM), the resistivity of the nanocomposites increases by approximately four orders of magnitude versus the composite containing unfunctionalized nanowires; a further increase in the electrical resistivity of the nanocomposites was not observed when using nanowires functionalized in more concentrated solutions (2.5 and 5.0 mM) of thiol. These results suggest that a critical surface coverage of CuNWs has been obtained when modified in $\geq$1.0 mM $C_8H_{17}SH$ solutions. This agrees well with the elemental and TGA analyses of $C_8H_{17}S$-CuNWs that showed a plateau in the adsorption of thiol above concentrations of 2.5 mM.

Figures 4.13 and 4.14 show backscattered electron SEM images of freeze-fractured samples of nanocomposites containing 1.0 vol. % $C_8H_{17}S$-CuNWs. Interestingly, low magnification images (Fig. 4.13) show fewer and smaller agglomerates of copper nanowires, as the concentration of thiol used for the chemical modification of nanowires increases from 0.1 to 5.0 mM. Correspondingly, high magnification images (Fig. 4.14) taken from the zones located between the agglomerates show a gradual increase in the density of the nanowires, i.e. enhanced dispersion, as the thiol concentration used for the chemical modification increases. Agglomerates of nanowires observed in Figure 4.13 for nanocomposites prepared with 0.1 mM-$C_8H_{17}S$-CuNW are similar to those observed in samples prepared with unfunctionalized CuNWs (Fig 4.4). The presence of agglomerates, as well as the electrical resistivity of the nanocomposites, suggest that irreversible agglomeration of nanowires and electrical interconnection is possible, due to incomplete coverage of the nanowires by the thiol. When more concentrated solutions of thiol are used, the coverage of the nanowires by the thiol increases, increasing the dispersion and the electrical resistivity of the nanocomposites.

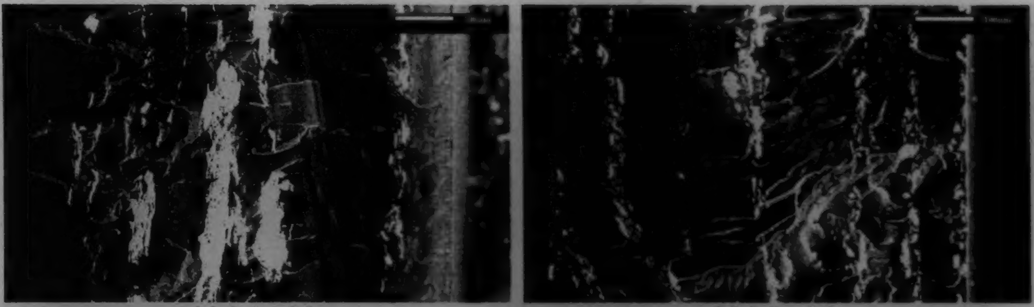

(a) 0.1 mM (b) 1.0 mM

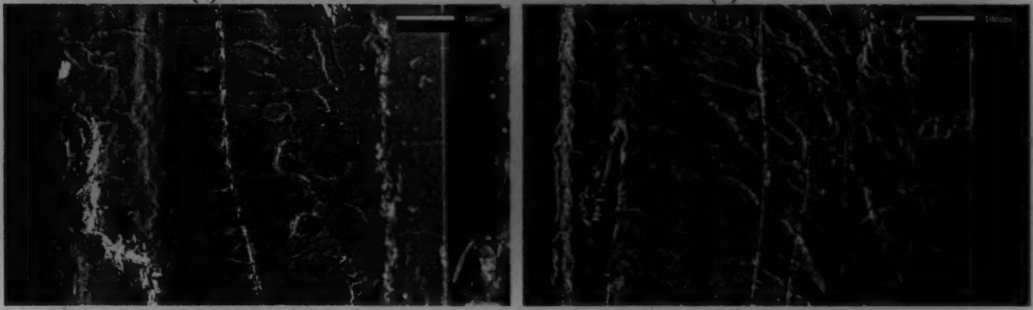

(c) 2.5 mM (d) 5.0 mM

Figure 4.13. Low magnification backscattered SEM images of solution processed PS nanocomposites containing $C_8H_{17}S$-CuNWs functionalized with different concentrations of $C_8H_{17}SH$: (a) 0.1 mM, (b) 1.0 mM, (c) 2.5 mM, and (d) 5.0 mM. Bright domains indicate agglomerated copper nanowires.

For the dispersion of $C_8H_{17}S$-CuNWs, SEM images at high and low magnification (Fig 4.13 and 4.14) indicate a significant enhancement in the dispersion of Cu nanowires that were surface functionalized in 5.0 mM $C_8H_{17}SH$ solutions. These experiments corroborated the conclusions obtained from elemental and thermogravimetric analysis described in Chapter 3, which indicated that CuNWs were efficiently covered by the thiol when concentrations of 5.0 mM $C_8H_{17}SH$ were used. Therefore, solutions of 5.0 mM $C_8H_{17}SH$ were selected to prepare functionalized copper nanowires and study the effect of the surface functionalization on the electrical percolation of CuNWs in the PS nanocomposite, as described below.

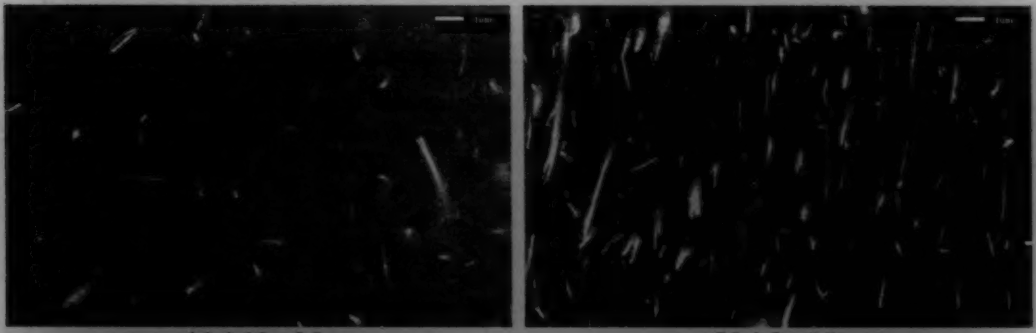

(a) 0.10 mM (b) 1.0 mM

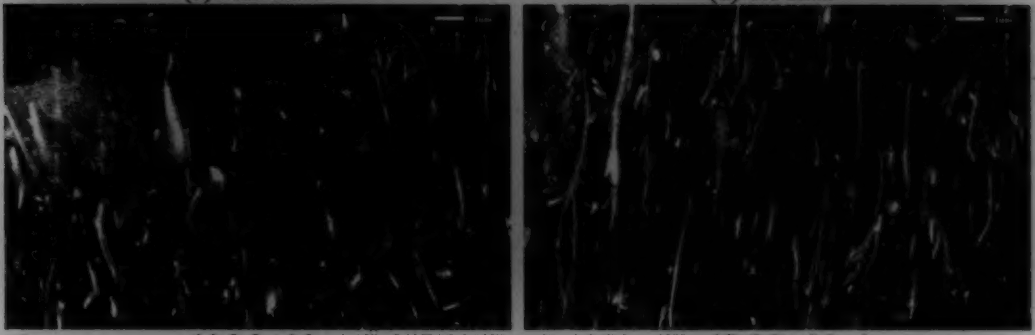

(c) 2.5 mM (d) 5.0 mM

Figure 4.14. High magnification backscattered SEM images of solution processed PS nanocomposites containing $C_8H_{17}S$-CuNWs functionalized with different concentrations of $C_8H_{17}SH$: (a) 0.1 mM, (b) 1.0 mM, (c) 2.5 mM, and (d) 5.0 mM. Bright domains indicate individual copper nanowires.

4.3.2.2 Electrical percolation of $C_8H_{17}S$-CuNWs

Figure 4.15 shows the volume electrical resistivities for hot molded PS nanocomposites prepared using different concentrations of $C_8H_{17}SH$-CuNWs. The resistivity of nanocomposites containing unfunctionalized CuNWs is also reproduced in Figure 4.15 in order to facilitate the comparison. Table 4.8 shows the average resistivity at each composition and their respective standard deviations. A concentration of 0.10 vol. % $C_8H_{17}S$-CuNWs does not produce a significant change in the resistivity versus the pristine polymer. An increase of the concentration to 0.25

vol. % produces a change in the resistivity of ~ 2 orders of magnitude, which is a more significant change than that observed in nanocomposites prepared using unfunctionalized CuNWs. At 1.0 and 2.0 vol. %, a more significant change in the resistivity of ~ 5 orders of magnitude occurred, indicating that a network containing $C_8H_{17}S$-CuNWs has formed. At 4.0 vol. % $C_8H_{17}S$-CuNWs, a further decrease in the resistivity for a total of ~ 9 orders of magnitude decrease was observed, which indicates a consolidated electrically conductive network.

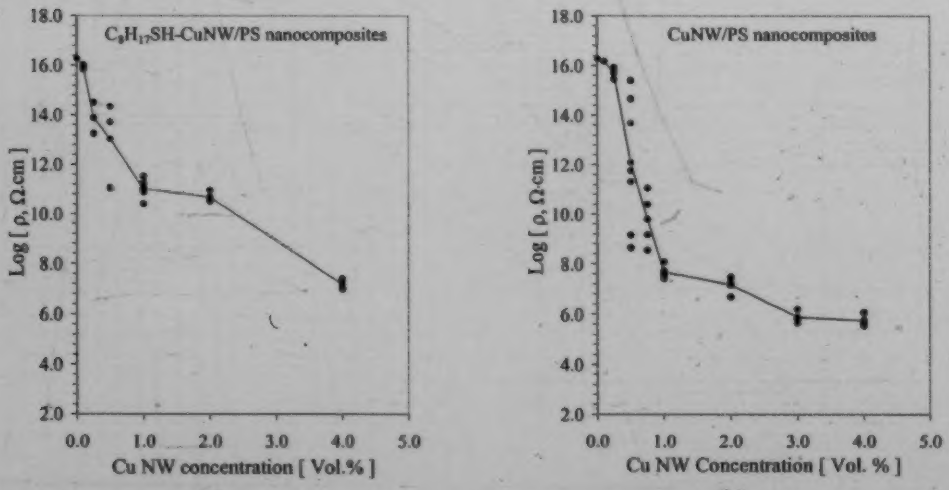

(a) (b)

Figure 4.15. Volume electrical resistivity of polystyrene nanocomposites for different concentrations of (a) copper nanowires surface functionalized with $C_8H_{17}SH$ (b) unfunctionalized copper nanowires. Lines connect the average ρ_v at each concentration.

The analysis of the percolation threshold by fitting the data to the power law equation did not result in an acceptable linear fit (correlation coefficient > 0.95). However, to elucidate the electrical percolation threshold, one may analyze the differences in the electrical resistivities of the composites with nanowire concentration. Thus, the electrical resistivity of the 0.25 vol. % nanocomposite is approximately 2 orders of magnitude lower than pure PS and 0.1 vol. % nanocomposite. In addition, a difference of more than one order of magnitude between the electrical resistivity values of nanocomposites with a concentration of 0.25 vol. % of $C_8H_{17}S$-CuNWs and 0.25 vol. % CuNWs indicates that the formation of electrically conductive networks of $C_8H_{17}S$-CuNWs start at lower concentrations than for unfunctionalized CuNWs. Indeed, this indicates that enhanced dispersion of the nanowires increases the probability of the formation of an interconnected nanowire network. One must consider that the alkanethiolate coating on CuNWs increases the electrical resistivity of the nanocomposite, so that the effect of the enhancement is diminished, preventing a more significant decrease in electrical resistivity at 0.25 vol. % $C_8H_{17}S$-CuNWs.

Table 4.8. Average volume electrical resistivity and standard deviations calculated for $C_8H_{17}S$-CuNW/polystyrene nanocomposites at different concentrations of Cu.

Cu Conc. (Vol. %)	ρ ($\Omega\cdot$cm)	Log (ρ, $\Omega\cdot$cm)	No. of specimens	Standard Deviation
0.00	1.86×10^{16}	16.27	-	-
0.10	7.76×10^{15}	15.89	2	0.09
0.25	7.59×10^{13}	13.88	3	0.89
0.50	1.07×10^{13}	13.03	3	1.75
1.00	1.05×10^{11}	11.02	4	0.48
2.00	4.68×10^{10}	10.67	3	0.25
4.00	1.51×10^{7}	7.18	3	0.22

One may also notice a small difference between the electrical resistivity of $C_8H_{17}S$-CuNW/PS nanocomposites after percolation and that of composites prepared with unfunctionalized CuNWs. The resistivities of $C_8H_{17}S$-CuNW/PS nanocomposites are one to three orders of magnitude higher than those for CuNW/PS nanocomposites at concentrations $\geq$ 1.0 vol. %. Considering that electrically conductive nanowire networks have been established at these concentrations, this difference is attributed to the alkanethiolate coating on the surface of the nanowires that enhances the dispersion of the nanowires in the polymer matrix and reduces the electrical percolation threshold, but also acts as a barrier for the electron flow between the conductive nanowires.

4.3.2.3 Fragmentation of $C_8H_{17}S$-AgNWs

As described in Chapter 3, AgNWs surface functionalized with $C_8H_{17}SH$ do not contain as much chemisorbed thiol as the CuNWs. As discussed previously, this may be related to the formation of a monolayer of an alkanethiolate coating on the oxide-free surface of silver nanowires produced by the PAO template-directed synthesis. In an effort to demonstrate that electrical properties of metal nanowire/PS composites could be enhanced by the surface treatment of nanowires with a thiol monolayer, $C_8H_{17}S$-AgNW/PS nanocomposites were prepared by solution-processing similarly to the $C_8H_{17}S$-CuNW/PS nanocomposites.

Considering the percolation curve obtained for silver nanowires, a concentration of 1.0 vol. % Ag was selected for the preparation of $C_8H_{17}S$-AgNW/PS nanocomposites, which is above the percolation threshold indicated by AgNW/PS nanocomposites. Good conductivity of the samples was expected, given the high conductivity of silver, the enhancement of nanowire dispersion by the alkyl chain of the thiol and the formation of a thinner thiol coating on silver nanowires. However, the volume electrical resistivity registered for the hot-molded specimens was on the order of 10^{15} Ω·cm (Table 4.9), which was close to the resistivity of the pristine polymer.

Table 4.9. Volume electrical resistivity of $C_8H_{17}S$-AgNW/PS nanocomposites containing 1.0 vol. % Ag and prepared by different methods.

Preparation Method	Ag Conc. (Vol. %)	ρ (Ω·cm)	Log (ρ, Ω·cm)
Solution casting-hot molding*	1.0	3.70×10^{15}	15.57
Solution casting-hot molding*	1.0	5.09×10^{15}	15.71
Solution casting-melt mixing-hot molding	1.0	1.14×10^{16}	16.06

* replicate samples

Although the results of the electrical resistivity of the composite were intriguing, the characterization of the morphology of the $C_8H_{17}S$-AgNW/PS nanocomposites clearly showed fragmentation (break-up) of the functionalized silver nanowires into nanospheres. Backscattered SEM images of the $C_8H_{17}S$-AgNW/PS are presented in Figure 4.16. Nanospheres of up to 100 nm in diameter are formed from break-up of individual nanowires uniformly dispersed throughout the sample. This observation provided a plausible explanation for the high resistivity of the samples, given that the percolation threshold predicted by theory for spheres is considerably higher than for high aspect-ratio particles (16 vol. % vs < 1 vol. %).[24,25] Therefore, the fragmentation of the $C_8H_{17}S$-AgNWs had a negative impact on the electrical properties of the composites.

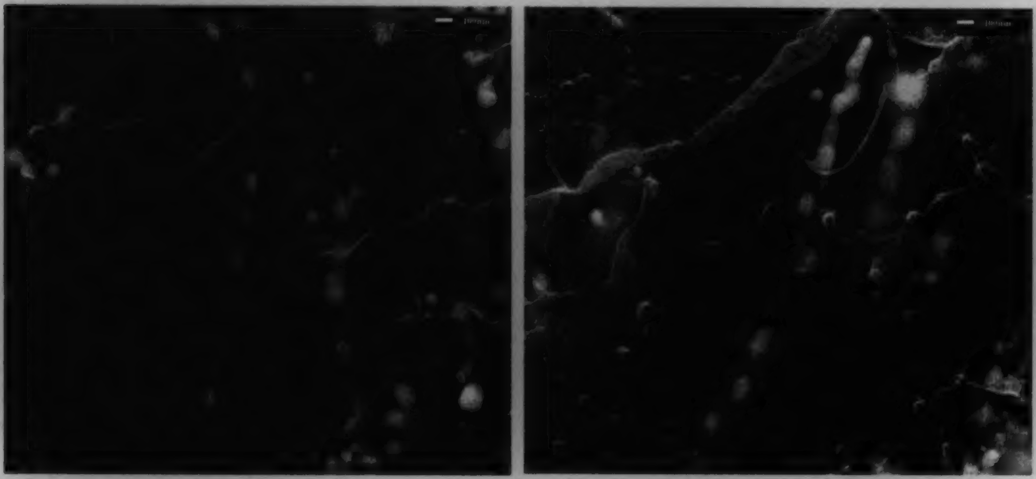

Figure 4.16. SEM images of $C_8H_{17}S$-AgNW/PS nanocomposites prepared by solution casting-hot molding show the break up of silver nanowires into nanospheres.

To determine the step at which AgNW break-up occurred, the morphology of silver nanowires dispersed in PS after different stages of the preparation of the nanocomposites by solution mixing and hot molding was observed by SEM analysis. The break-up of functionalized silver nanowires was not observed in cast films prepared by solution processing (after solution casting and solvent evaporation), in which steps of ultrasound and annealing at 50 °C for 24 hours were used. Individual $C_8H_{17}S$-AgNWs are clearly observed in backscattered images of cast-films, as shown in Figure 4.17a. This indicates that the break-up occurred during the second step of the preparation method, hot molding, which consists of molding a specimen under pressure (1.5 metric tons) and temperature (200 °C) to obtain wafer test specimens.

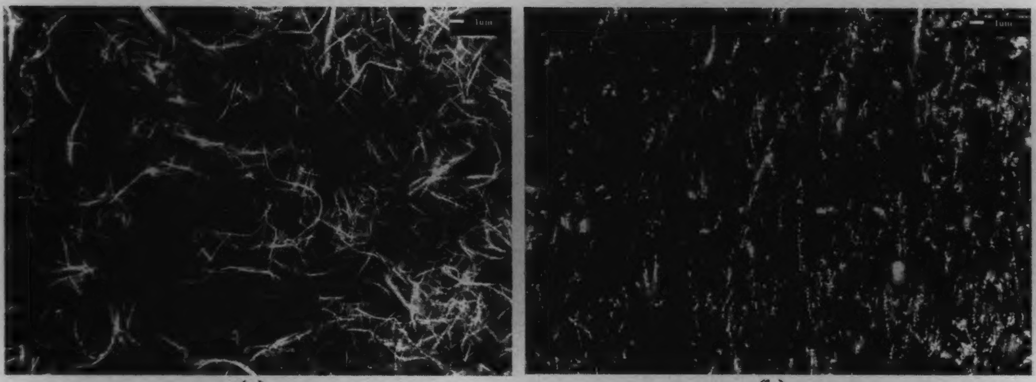

(a) (b)

Figure 4.17. Backscattered SEM images of $C_8H_{17}S$-AgNW/PS nanocomposites. (a) PS nanocomposite film obtained after solution casting and solvent evaporation, showing no fragmentation of $C_8H_{17}S$-AgNWs and (b) PS Nanocomposite after hot molding showing the break-up of $C_8H_{17}S$-AgNWs after hot molding.

Similarly, the morphology of a nanocomposite prepared by an additional step of melt mixing (before hot molding) was followed by backscattered electron SEM. Characterization of the samples indicated significant break-up of the functionalized nanowires after melt mixing (Figure 4.18); a process that consists in applying shear stress to polymer melts to enable mixing. Figure 4.19 shows secondary and backscattered electron SEM images of the $C_8H_{17}S$-AgNW/PS composites after solution casting, melt mixing and hot molding processing steps. Acute fragmentation of the $C_8H_{17}S$-AgNWs was clearly observed. PS nanocomposites containing fragmented AgNWs showed poor electrical conductivity at concentrations of 1.0 vol. %, as shown in Table 4.9.

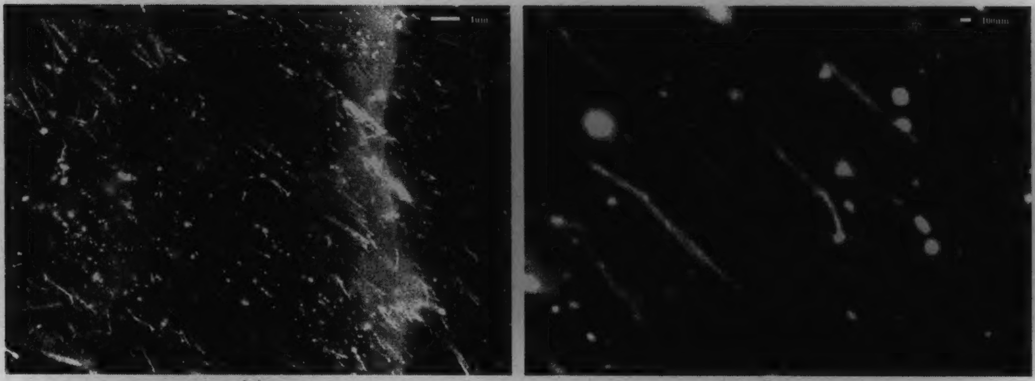

(a) (b)

Figure 4.18. Backscattered SEM images of freeze-fractured samples of $C_8H_{17}S$-AgNW/PS nanocomposites prepared by solution casting-melt mixing showing silver nanowires and silver nanospheres formed from fragmentation of $C_8H_{17}S$-AgNWs.

4.3.3 Rheological percolation of metal nanowire/PS nanocomposites

In the case of filled polymers, the rheological response is dependent on the distribution and dispersion of the nanoparticles in the polymer matrix. It has become a popular technique for the characterization of polymer nanocomposites, such as those composed of inorganic particles dispersed in a polymer matrix, in order to elucidate changes in the microstructure of the composite that are related directly to the phenomena of electrical and rheological percolation.[26,31-33]

In this section, the results of the effect of the concentration, surface functionalization and dispersion of metal nanowires on the rheological behavior of the PS nanocomposites will be presented.

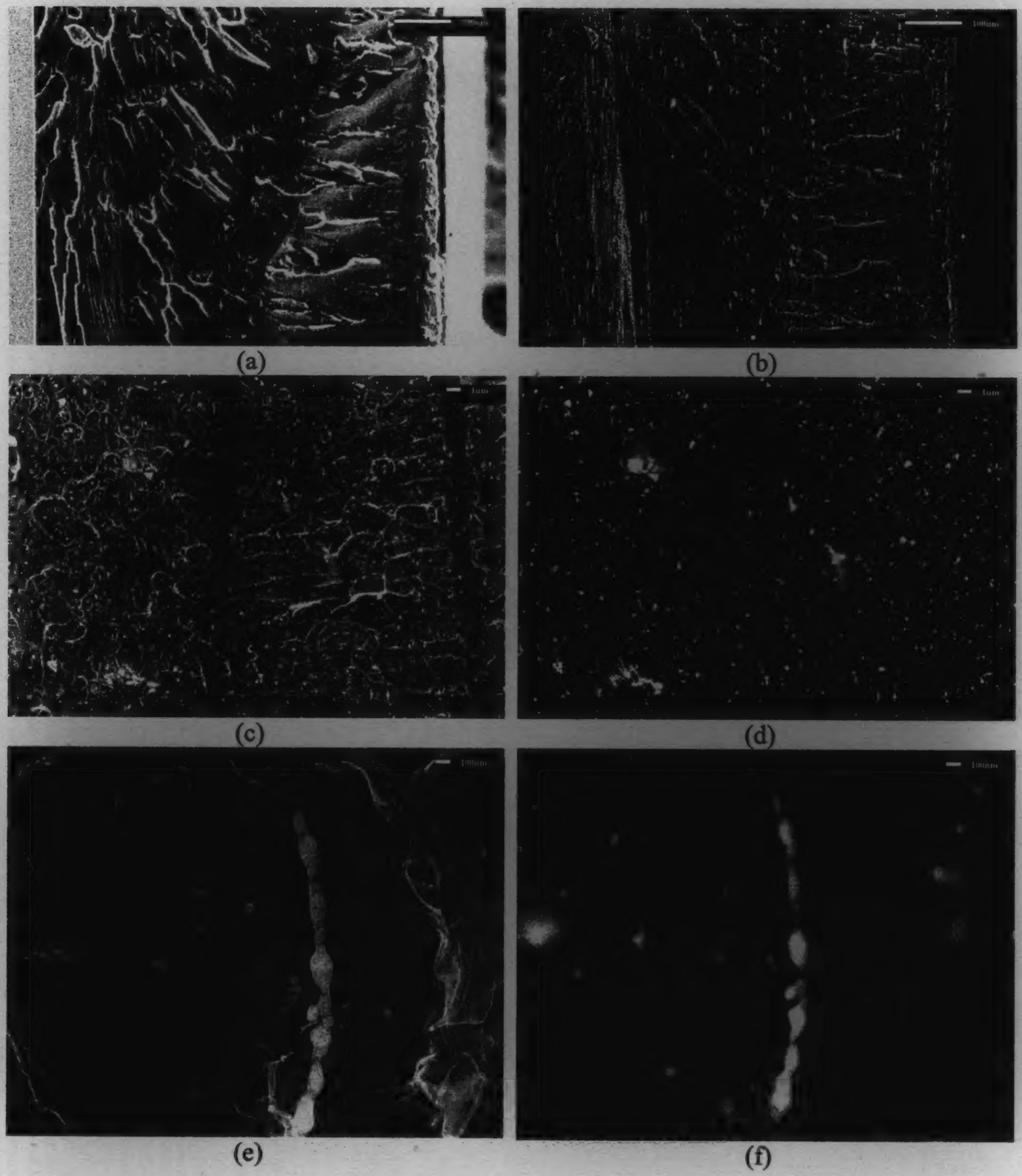

Figure 4.19. Several magnification SEM images of a freeze-fractured sample of $C_8H_{17}S$-AgNW/PS nanocomposite (1.0 vol. % Ag) prepared by solution casting-melt mixing-hot molding showing dispersion and significant break-up of silver nanowires. (a, c, e) Secondary electron SEM images, (b, d, f) Backscattered electron SEM images.

4.3.3.1 Viscoelastic properties of CuNW/PS nanocomposites

The results of viscoelastic characterization of pure PS and PS nanocomposites prepared with different concentrations of unfunctionalized copper nanowires by solution processing are indicated in Figure 4.20. It is evident that the presence of the nanowires significantly affects the behavior of the polystyrene matrix, especially at low frequencies.

The complex viscosity ($|\eta^*|$) versus frequency, shown in Figure 4.20a, indicates the complex viscosity increases with increasing concentration of unfunctionalized CuNWs. A Newtonian plateau in $|\eta^*|$ at low frequencies (0.1 - 1.0 rad/s) is observed for pure PS and PS containing 0.25 and 0.50 vol. % Cu. At 1.0 vol. % and above, a different frequency response of $|\eta^*|$ is observed, specifically at low frequencies, i.e. the plateau is no longer observed. At concentrations of 2.0, 3.0, and 4.0 vol. %, $|\eta^*|$ has a power law dependence on the frequency, and a significant increase in $|\eta^*|$ at low frequencies is indicative of yield stress. Figure 4.20b shows the dependence of $|\eta^*|$ as a function of CuNW concentration. An approximately linear dependence of Log $|\eta^*|$ versus CuNW concentration was observed at high frequencies (10 and 100 rad/s), while it was non-linear at low frequencies (0.1 and 1.0 rad/s). A small increase in $|\eta^*|$ of ~ 8 times was observed at 100 rad/s for 4.0 vol. % versus the pristine polymer, while a more significant increase of ~100 times was observed at low frequency (0.1 rad/s).

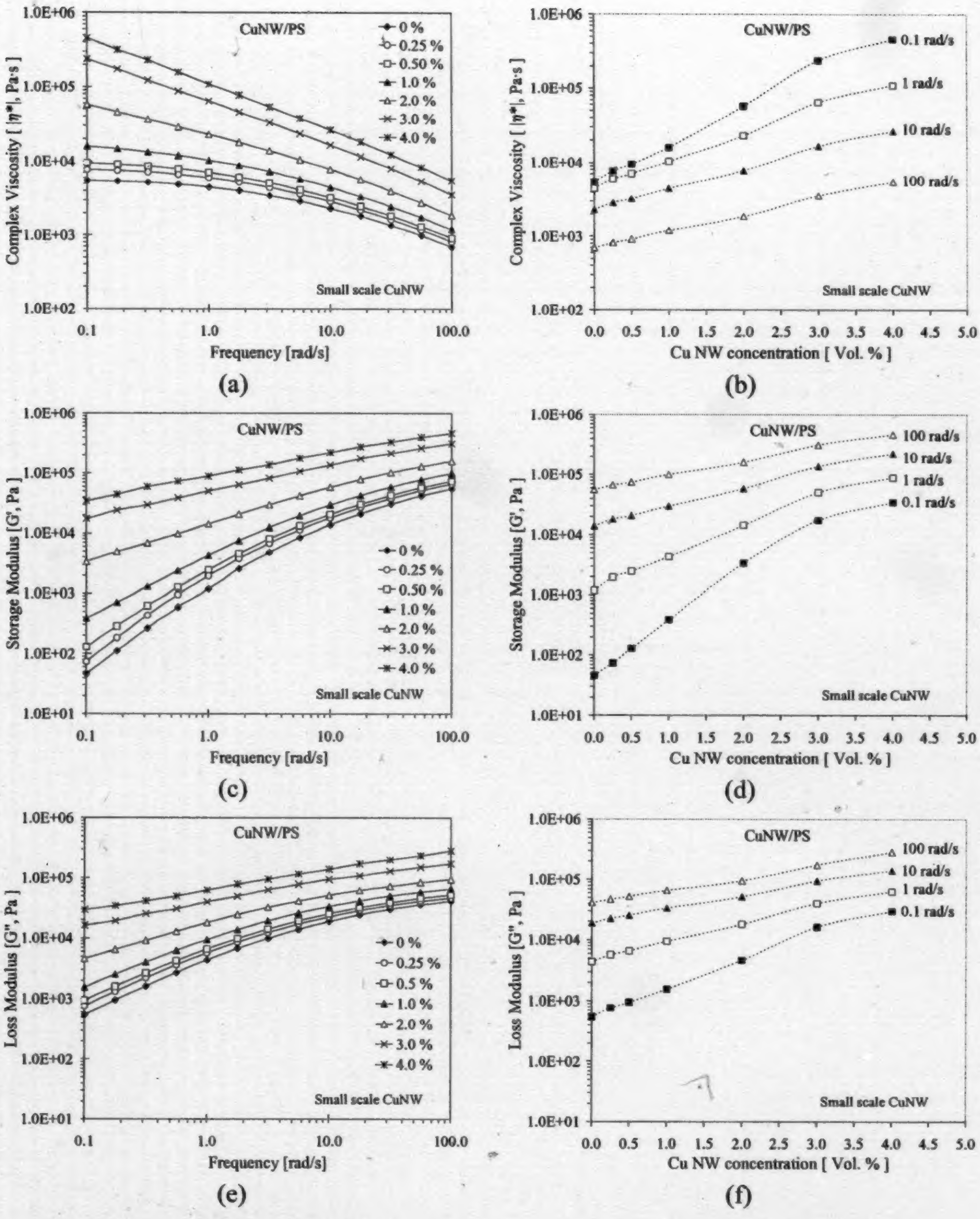

Figure 4.20. Rheological characterization of solution-processed CuNW/PS nanocomposites at 200 °C. Complex viscosity (|*η**|), storage modulus (*G'*), and loss modulus (*G"*) as a function of: (a,c,e) frequency and (b,d,f) concentration of CuNWs, at several frequencies. Lines are guides to the eye.

The response at low frequency and the loss of the Newtonian plateau in $|\eta^*|$ with larger vol. % CuNWs indicate changes in the microstructure of the composite with increasing concentration. At low frequencies, the polymer chains can relax after the applied stress. As the nanowire concentration increases, the relaxation of the polymer chains at low frequencies gradually changes and at a certain concentration (rheological percolation threshold), a transition from a liquid-like to a solid-like viscoelastic behavior occurs. As mentioned in the introduction (Chapter 1), the solid-like behavior is due to the formation of a polymer-nanofiller network.[26,31,33]

The frequency response of $|\eta^*|$ at high frequencies provides information about the response of the composite at conditions typically used in industrial processing of polymers, such as melt mixing. The small variation in $|\eta^*|$ of approximately 8 times from pure PS to 4.0 vol. % at 100 rad/s indicates that the viscosity of the nanocomposites is not greatly increased by the introduction of low concentrations of CuNWs. This enables us to predict that although slightly higher viscosities are expected, similar processing conditions could be used for the nanocomposite and pure PS, which is advantageous for mass production of metal nanowire/PS nanocomposites. A small variation in $|\eta^*|$ at high frequencies is one of the benefits of using nanofillers, such as those used in this work.

The change in the frequency response of the storage modulus (G') at low frequencies is generally used to identify significant changes in the microstructure of the filled polymer and to elucidate the rheological percolation threshold. Figures

4.20c and 4.20e show the storage modulus (*G'*) and loss modulus (*G"*) versus frequency of polystyrene nanocomposites prepared using different concentrations of unfunctionalized CuNWs. *G'* and *G"* are less dependent on frequency as the CuNW concentration increases, indicating the formation of a polymer-nanowire network within the range of concentrations used. Figures 4.20d and 4.20f show *G'* and *G"* versus CuNW concentration at different frequencies; at high frequency (100 rad/s), a weak dependence of *G'* on the nanowire concentration is observed, indicating that the CuNWs do not significantly alter the dynamics of the PS chains. At low frequencies, a dependence on the nanowire concentration is clearly observed, indicating that the long-range dynamics of the PS chains is significantly affected by the CuNWs.

In order to elucidate the rheological percolation threshold of these nanocomposites, several plots of rheological data were used. Figure 4.21 shows the storage modulus versus loss modulus at particular frequencies for nanocomposites containing unfunctionalized CuNWs. In this plot, a shift and a change in the slope of *G'* versus *G"* is indicative of a significant change in the microstructure of the filled polymer.[26] The data has been divided into two plots corresponding to low concentrations (0.5 – 1.0 vol. %, Fig. 4.21a) and high concentrations (2.0 – 4.0 vol. %, Fig. 4.21b) in order to show clearly the changes in the *G'* vs *G"* curve. A significant shift of the *G'* vs *G"* curve of nanocomposites versus that of pure PS can be observed between concentrations of 0.5 - 1.0 vol. % CuNWs. Beyond 2.0 vol. %, the *G'* vs *G"* curve shows more significant changes versus that of pristine polymer (Fig. 4.21b).

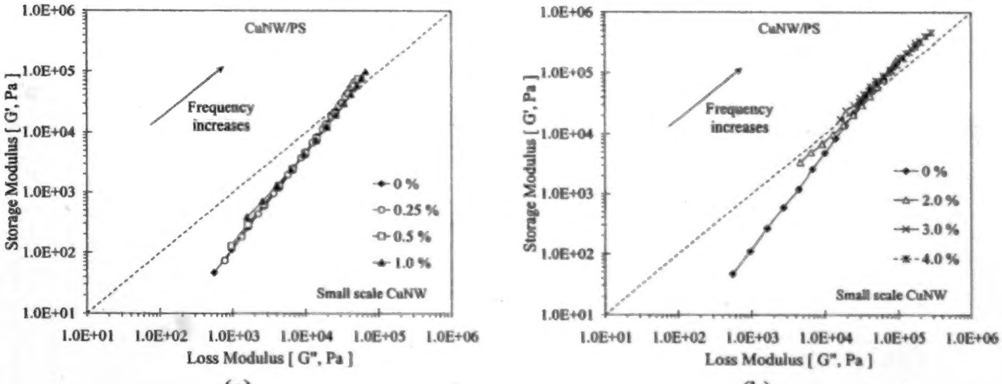

(a) (b)

Figure 4.21. Storage modulus (G') as a function of the loss modulus (G'') of solution-processed CuNW/PS nanocomposites. (a) Low concentrations of CuNWs (0.25-1.0 vol. %) and (b) high concentrations of CuNWs (2.0-4.0 vol. %). The change in G' vs G'' curve between 0.5 and 1.0 vol. % indicates the formation of a polymer-nanowire network. Lines are guides to the eye.

Figure 4.22 shows the phase angle (δ) as a function of the absolute value of the complex modulus $|G^*|$ (van Gurp-Palmen plot) for CuNW/PS nanocomposites. The phase angle for pure PS approaches 90° at low values of the complex modulus, indicating viscous flow behavior. A change from this behavior results from changes in the microstructure of the filled polymer. In the case of CuNW/PS composites, a significant change can be observed from 0.5 to 1.0 vol. %. Figure 4.23 shows a plot of the ratios $G'_{NW/PS} \ / \ G'_{PS}$ as a function of the CuNW concentration in a linear scale from 0 to 2.0 vol. % CuNWs. The figure indicates how $G'_{NW/PS}$ varies with respect to that of pure PS and is used here to show clearly the changes in G' as a result of CuNW concentrations close to the percolation threshold. For instance, Wu et al,[34] found that 3-dimensional networks of particles begin to form when G' of the composite is 7 times that of the pure polymer, regardless of the system. For CuNW/PS composites, the $G'_{CuNW/PS} / G'_{PS}$ showed an increase from ~3 to ~ 10 from 0.5 to 1.0 vol. %. This increase indicates the concentration at which the formation of a polymer-nanowire network and the rheological percolation threshold occurs.

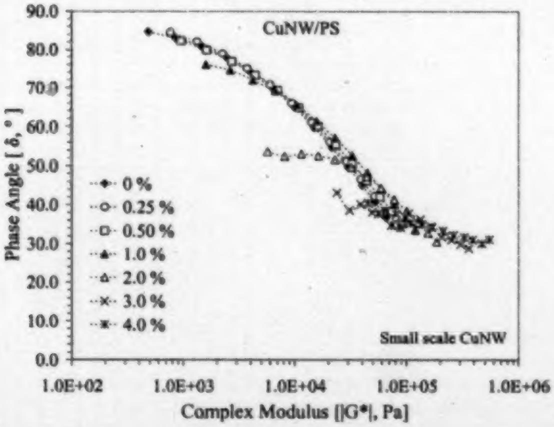

Figure 4.22. Phase angle (δ) as a function of the absolute value of the complex modulus (van Gurp-Palmen Plot) of solution-processed CuNW/PS nanocomposites. Lines are guides to the eye.

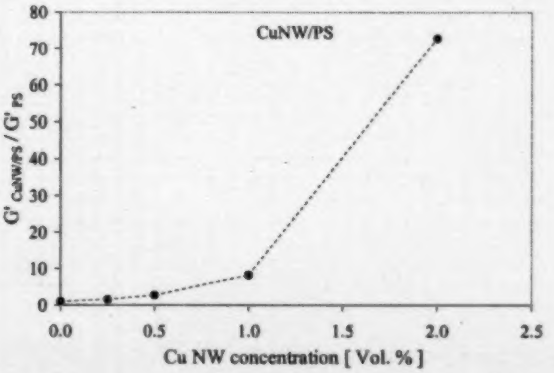

Figure 4.23. Storage modulus (G') of CuNW/PS nanocomposites over G' of pure PS at 0.1 rad/s as a function of the CuNW concentration up to 2.0 vol. %. The change in $G'_{CuNW/PS}/G'_{PS}$ observed for concentrations of 0.5 - 1.0 vol. % Cu indicates formation of a polymer-nanowire network. Line is guide to the eye.

In conclusion, the rheological percolation of CuNW/PS composites occurs between 0.5 and 1.0 vol. %. This concentration range agrees well with the electrical percolation threshold of these nanocomposites (0.46 vol. %, section 4.3.1.2) and indicates that the rheological and electrical percolation of unfunctionalized copper nanowires occur almost simultaneously.

4.3.3.2 Viscoelastic properties of $C_8H_{17}S$-CuNW/PS nanocomposites

As shown in section 4.3.2, the surface functionalization of CuNWs using $C_8H_{17}SH$ altered the dispersion and electrical percolation threshold of the nanocomposites. In this section, the effect of chemical modification of copper nanowires on the rheological behavior of the nanocomposites will be discussed. The results of viscoelastic characterization of pure PS and PS nanocomposites prepared with different concentrations of $C_8H_{17}S$-CuNWs by solution processing are presented in Figure 4.24.

Figure 4.24a shows the complex viscosity ($|\eta^*|$) of the PS nanocomposites with different concentrations of $C_8H_{17}S$-CuNWs. An increase in $|\eta^*|$ with the concentration of $C_8H_{17}S$-CuNWs is observed, similar to the nanocomposites containing unfunctionalized CuNWs described in section 4.3.3.1. However, a smaller increase in $|\eta^*|$ due to $C_8H_{17}S$-CuNWs than that due to unfunctionalized CuNWs was obtained, specifically for concentrations of 0.5, 1.0 and 2.0 vol. %. The Newtonian plateau of $|\eta^*|$ at low frequencies (0.1 - 1.0 rad/s), a sign of liquid-like behavior, is not

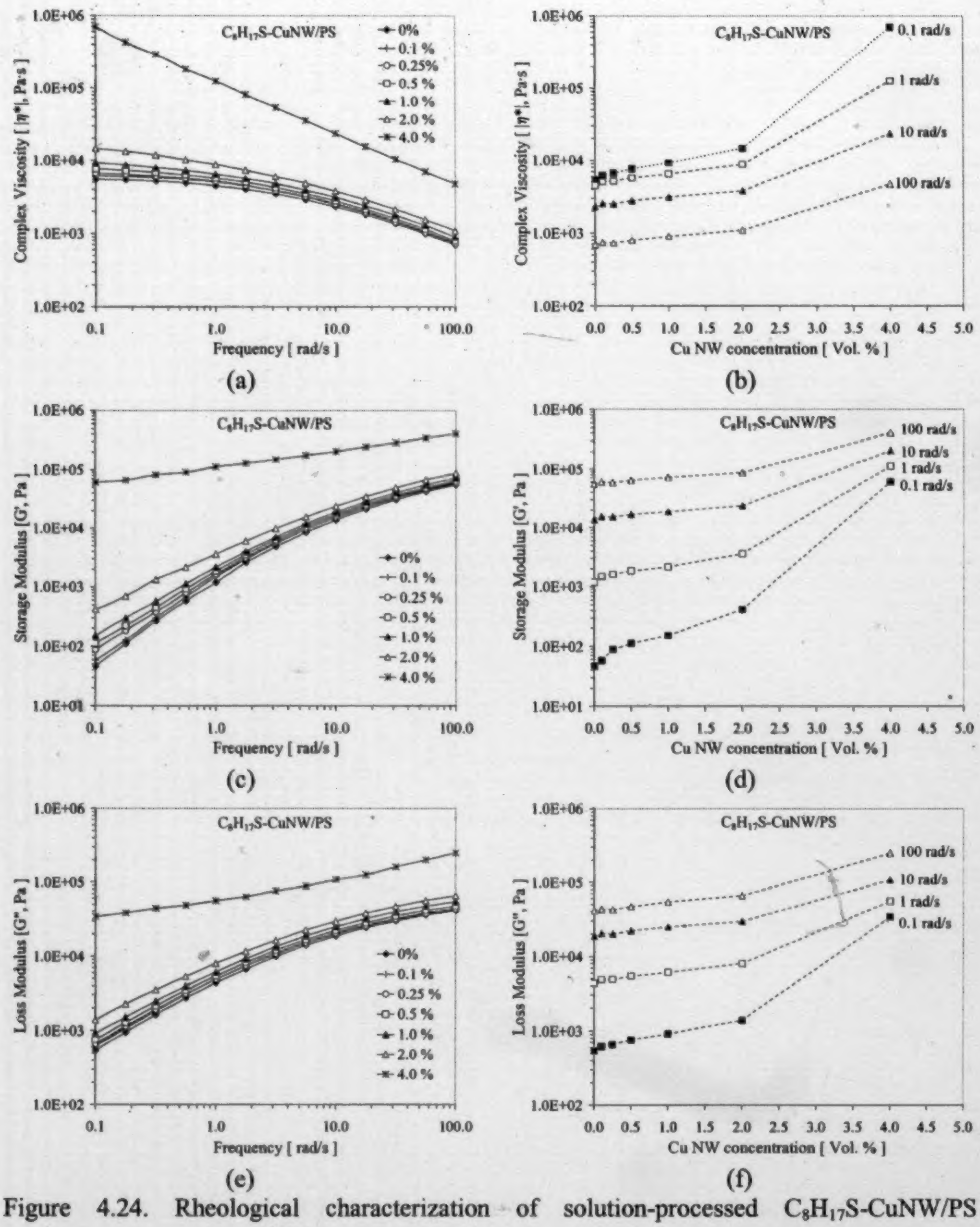

Figure 4.24. Rheological characterization of solution-processed $C_8H_{17}S$-CuNW/PS nanocomposites at 200 °C. Complex viscosity ($|\eta^*|$), storage modulus (G'), and loss modulus (G'') as a function of: (a,c,e) frequency and (b,d,f) concentration of $C_8H_{17}S$-CuNWs, at several frequencies. Lines are guides to the eye.

observed at 4.0 vol. % $C_8H_{17}S$-CuNWs, instead a power law dependence of $|\eta^*|$ was obtained, indicating the formation of the polymer-nanowire network.

Figure 4.24b shows the viscosity dependence on the concentration of $C_8H_{17}S$-CuNWs. At high frequencies (10 and 100 rad/s), there is almost no dependence of $|\eta^*|$ with respect to the concentration of functionalized copper nanowires from 0.25 to 2.0 vol. %. For instance, at high frequency (100 rad/s), $|\eta^*|$ of 2.0 vol. % $C_8H_{17}S$-CuNW/PS is only two times that of pure PS, which is a negligible increase for 2.0 vol. % of filler. The frequency dependence of $|\eta^*|$ at high frequency (100 rad/s) is actually smaller than that observed for unfunctionalized CuNWs, which is a favorable outcome of the chemical modification of the nanowires. It is worth mentioning that nanocomposites at 2.0 vol. % are above the electrical percolation (section 4.3.2.2). Thus, surface functionalized nanowires produce useful electrical properties, with lower viscosities of the nanocomposites, and therefore will require less demanding processing conditions than those for CuNW/PS composites.

The results in Figures 4.24a and 4.24b indicate that the viscosity of pure PS is barely increased by the introduction of functionalized nanowires up to concentrations of 2.0 vol. %. The viscosity of $C_8H_{17}S$-CuNW/PS was lower than for CuNW/PS at concentrations around the formation of a polymer-nanowire network. The similarity of the viscosity at 4.0 vol. % for PS nanocomposites containing unfunctionalized and functionalized nanowires indicates that at concentrations significantly higher than the percolation threshold, the frequency response of $|\eta^*|$ is primarily dependent on a polymer-CuNW network rather than on a polymer-polymer network.

The frequency responses of *G'* and *G"* for the $C_8H_{17}S$-CuNW/PS nanocomposites are shown in Figures 4.24c and 4.24e. *G'* and *G"* increase with the concentration of $C_8H_{17}S$-CuNWs. At low nanowire content, *G'* shows similar frequency response to that of pure PS. At 4.0 vol. %, *G'* shows little dependence on the frequency, resulting from the restriction of polymer-chain movement due to the polymer-CuNW network. Figure 4.24d shows *G'* for different concentrations of $C_8H_{17}SH$-CuNWs. At high frequency (100 rad/s), a small dependence on nanowire concentration is observed. At low frequency (0.1 rad/s), a small change in *G'* can be observed between 0.1 and 0.5 vol. % resulting from the effect of well-dispersed nanowires and restriction of the polymer chain relaxation. Above 1.0 vol. %, significant changes occur. An increase in *G'* of three orders of magnitude (~1300 times) versus pristine PS is observed for a concentration of 4.0 vol. %.

Different plots of rheological data were used to elucidate the rheological percolation threshold for PS nanocomposites containing chemically modified nanowires, as described earlier for CuNW/PS nanocomposites. Figure 4.25 presents the storage modulus versus loss modulus at particular frequencies for nanocomposites containing $C_8H_{17}S$-CuNWs. A significant shift of the *G'* vs *G"* curve of nanocomposites versus that of pure PS can be observed between concentrations 1.0 - 2.0 vol. % $C_8H_{17}S$-CuNWs.

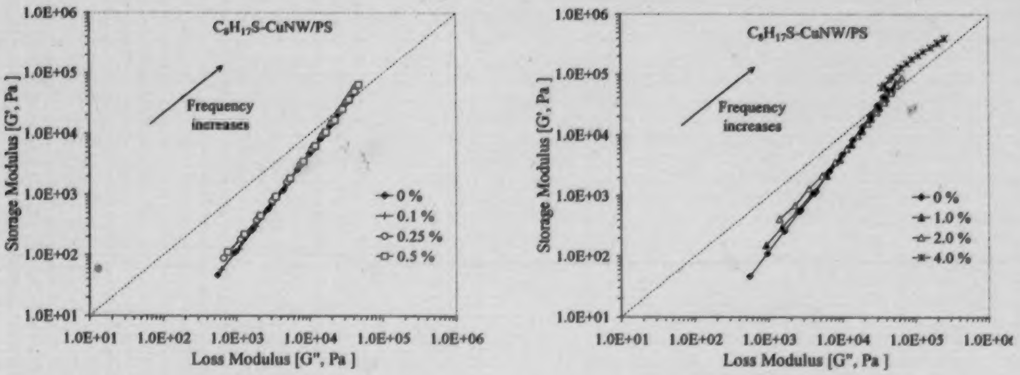

(a) (b)

Figure 4.25. Storage modulus (*G'*) as a function of the loss modulus (*G''*) of solution-processed $C_8H_{17}S$-CuNW/PS nanocomposites. (a) Low concentrations of $C_8H_{17}S$-CuNWs (0.1 - 0.5 vol. %) and (b) high concentrations of $C_8H_{17}S$-CuNWs (1.0 - 4.0 vol. %). Lines are guides to the eye.

Figure 4.26 shows plots of the phase angle (δ) as a function of the absolute value of the complex modulus |G*| (van Gurp-Palmen plot) for nanocomposites containing $C_8H_{17}S$-CuNWs. A change in the microstructure of the nanocomposites between 1.0 and 2.0 vol. % can be inferred from the deviation of δ from the viscous flow behavior of pure PS in which δ approaches 90°. Similarly, Figure 4.27 shows a plot of the ratios $G'_{NW/PS}$ / G'_{PS} as a function of the CuNW concentration on a linear scale from 0 to 2.0 vol. % $C_8H_{17}S$-CuNWs. The data previously shown for CuNW/PS have been included in Figure 4.27 for comparison purposes. For $C_8H_{17}S$-CuNW/PS composites, the ratio $G'_{C_8H_{17}S-CuNW/PS}$ / G'_{PS} shows a change from ~ 3 to ~ 9 at concentrations between 1.0 and 2.0 vol. %, indicating the percolation threshold. According to these plots, the formation of a polymer-nanowire network occurred at concentrations between 1.0 and 2.0 vol. % $C_8H_{17}S$-CuNWs.

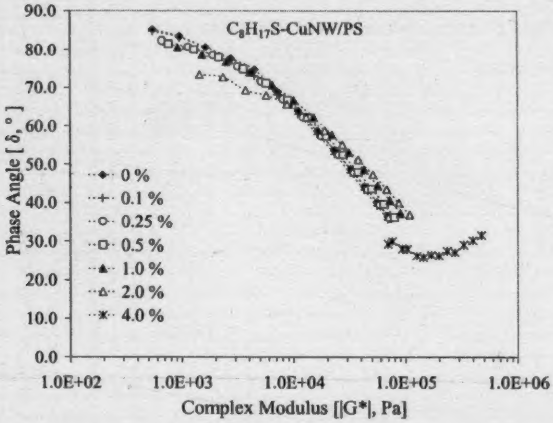

Figure 4.26. Phase angle as a function of the absolute value of the complex modulus (van Gurp-Palmen Plot) of solution-processed $C_8H_{17}S$-CuNW/PS nanocomposites. Lines are guides to the eye.

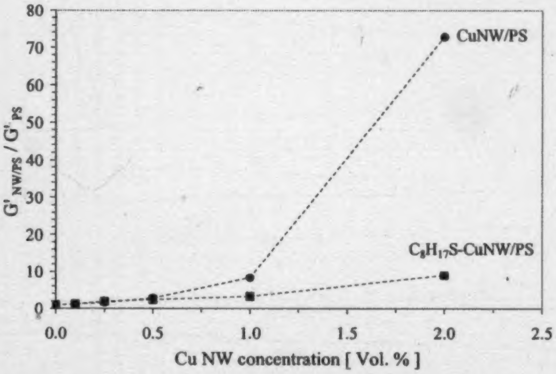

Figure 4.27. Storage modulus (G') of $C_8H_{17}S$-CuNW/PS nanocomposites over G' of pure PS at 0.1 rad/s as a function of the $C_8H_{17}S$-CuNW concentration up to 2.0 vol. %. The change in $G'_{C8H17\text{-}SCuNW/PS}/G'_{PS}$ observed for concentrations of 1.0 – 2.0 vol. % Cu indicates formation of a polymer-nanowire network. The data of CuNW/PS is included for comparison purposes. Lines are guides to the eye.

Higher values of *G'* in filled-polymers at low frequencies may be expected when the filler is well dispersed compared to polymers containing filler forming agglomerates.[31] By contrast, it is known that a decrease in $|\eta^*|$ and *G'* in filled polymers results from the presence of surface functionalities on the fillers.[35] In this work, $|\eta^*|$ and *G'* values were experimentally lower for nanocomposites containing 0.1 - 2.0 vol. % well-dispersed copper nanowires ($C_8H_{17}S$-CuNWs) than for those containing the same concentrations of a mixture of dispersed and agglomerated nanowires (unfunctionalized CuNWs). Thus, the effect of the surface functionality of the CuNWs on the storage modulus might have been significantly larger than that of enhanced dispersion on $|\eta^*|$ and *G'*. This combination of effects results in lower values of viscoelastic properties for $C_8H_{17}S$-CuNW/PS versus CuNW/PS composites at concentrations close to the percolation threshold, in which the viscoelastic properties depend on both a combination of polymer-polymer and polymer-nanowire networks.

In summary, the viscoelastic properties of the $C_8H_{17}S$-CuNW/PS nanocomposites showed rheological percolation over a different range of nanowire concentrations than did the electrical percolation (Section 4.3.2.2). Changes in the microstructure of the filled polymer inferred from the frequency response of $|\eta^*|$, *G'*, and *G"*, as well as, the *G'* vs *G"* curve, and van Gurp-Palmen plots have confirmed that the rheological percolation threshold of $C_8H_{17}S$-CuNWs at 200 °C occurred between 1.0 and 2.0 vol. %. The rheological percolation threshold of functionalized nanowires was higher than the electrical percolation threshold (~ 0.25 vol. %).

4.3.3.3 Viscoelastic properties of AgNW/PS nanocomposites

The results of viscoelastic characterization of PS nanocomposites containing silver nanowires are presented in Figure 4.28. The complex viscosity ($|\eta^*|$) of AgNW/PS increases with the content of Ag nanowires, as shown in Figure 4.28a. A change in the Newtonian plateau at low frequency is observed between 1.0 and 2.0 vol. % AgNWs. This indicates the approximate rheological percolation threshold at which the polymer-AgNW network modifies the mobility of the polymer chains in the nanocomposite. The viscosity showed power law dependence for concentrations from 2.0 to 4.0 vol. %. Figure 4.28b shows the viscosity response to the concentration of AgNW at different frequencies. A gradual increase in viscosity at low concentrations is observed at all frequencies. At low frequency (0.1 rad/s), an increase in $|\eta^*|$ of ~ 30 times versus pure PS was obtained at 4.0 vol. %, which is lower than that obtained for 4.0 vol. % CuNW/PS (~ 100 times versus pure PS).

Figures 4.28c to 4.28f show *G'* and *G"* as a function of frequency and concentration of AgNWs. Both *G'* and *G"* increase with increasing concentration of nanofiller. The change in the frequency response of *G'* is evident between 1.0 and 2.0 vol. % AgNWs. The difference in *G'* frequency response of AgNW/PS versus CuNW/PS nanocomposites at similar concentration of nanofiller may indicate that AgNWs disperse less efficiently than CuNWs in PS.

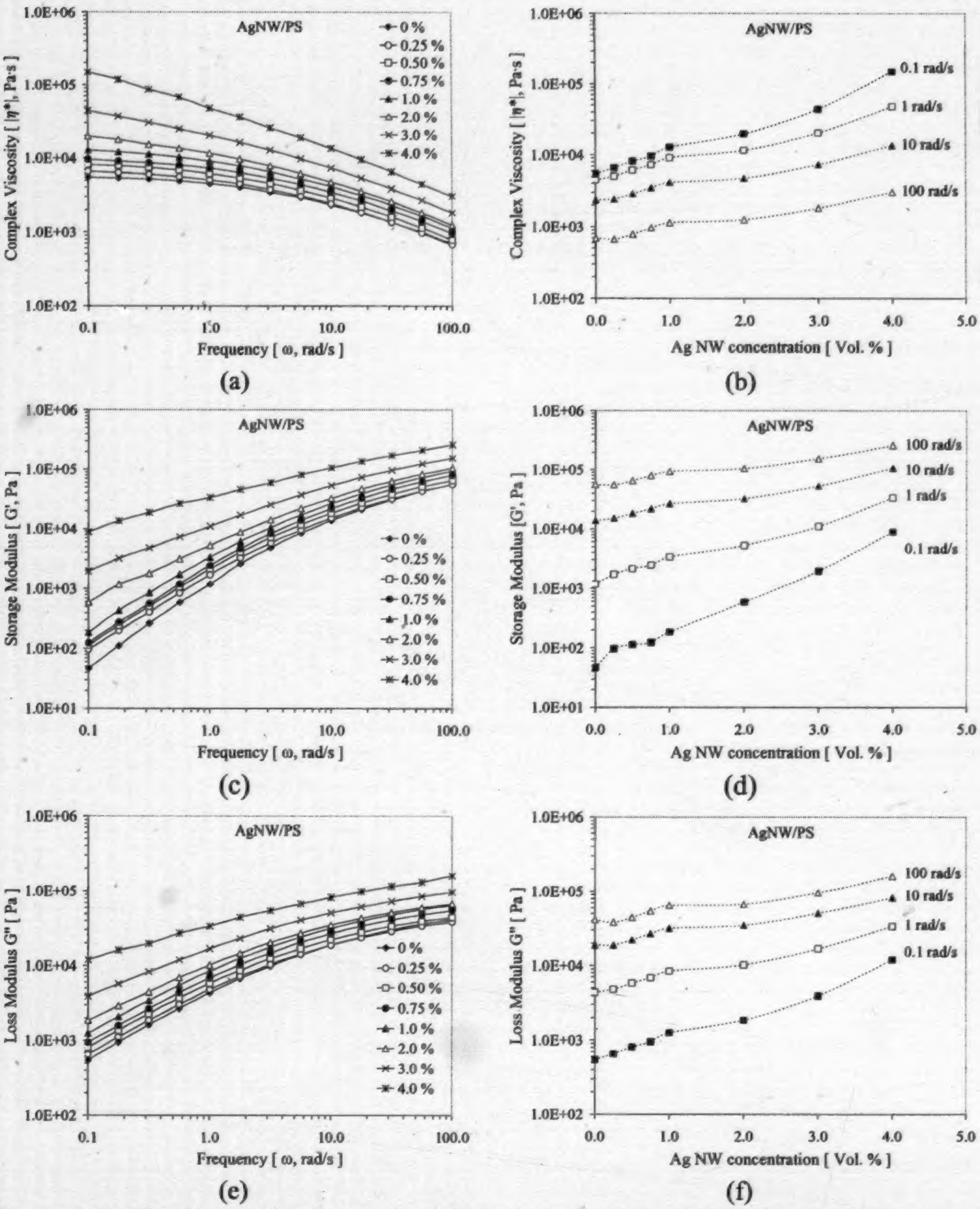

Figure 4.28. Rheological characterization of solution-processed AgNW/PS nanocomposites at 200 °C. Complex viscosity (|η^*|), storage modulus (G'), and loss modulus (G'') as a function of: (a,c,e) frequency and (b,d,f) concentration of AgNW, at several frequencies. Lines are guides to the eye.

The phase angle (δ) as a function of the absolute value of the complex modulus |G*| (van Gurp-Palmen plot) for AgNW/PS nanocomposites is shown in Figure 4.29. As described earlier, δ approaches 90° for pure PS indicating viscous flow behavior. A significant change in the shape of δ occurs between 1.0 and 2.0 vol. %. The *G'* vs *G"* plot (Figure 4.30) also indicates a shift of the *G'* vs *G"* curve from the PS between 1.0 and 2.0 vol. %.

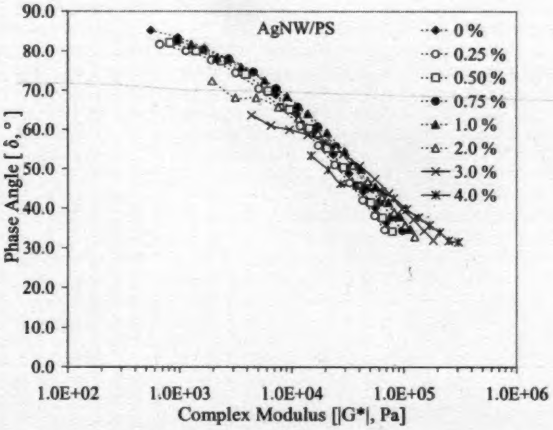

Figure 4.29. Phase angle as a function of the absolute value of the complex modulus (van Gurp-Palmen Plot) of solution-processed AgNW/PS nanocomposites. Lines are guides to the eye.

Figure 4.31 shows the ratio of *G'* of AgNW/PS nanocomposites to that of pure PS. A significant change in *G'* of the polymer composite occurs between 1.0 and 2.0 vol. % of AgNWs. At 4.0 vol. %, an increase of ~ 100 times was obtained (not shown in Fig. 4.31), indicating that a polymer-AgNW network was established.

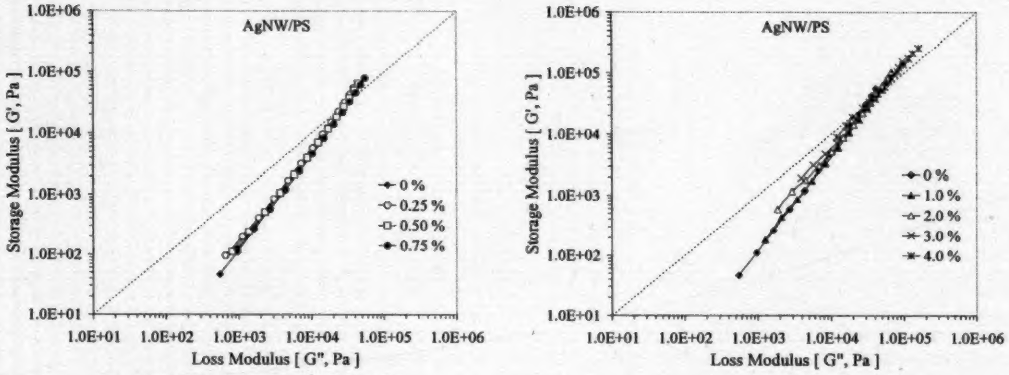

(a) (b)

Figure 4.30. Storage modulus (*G'*) as a function of the loss modulus (*G"*) of solution-processed AgNW/PS nanocomposites. (a) Low concentrations of AgNWs (0.25-0.75 vol. %) and (b) high concentrations of AgNWs (1.0-4.0 vol. %). The change in *G'* vs *G"* curve between 1.0 and 2.0 vol. % indicates the formation of a polymer-nanowire network. Lines are guides to the eye.

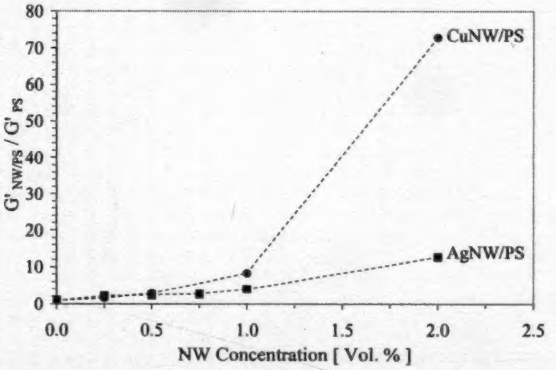

Figure 4.31. Storage modulus (*G'*) of AgNW/PS nanocomposites over *G'* of pure PS at 0.1 rad/s as a function of the AgNW concentration up to 2.0 vol. %. The change in $G'_{AgNW/PS}/G'_{PS}$ observed for concentrations of 1.0 – 2.0 vol. % AgNW indicates the formation of a polymer-nanowire network. The data of CuNW/PS is included for comparison purposes. Lines are guides to the eye.

In conclusion, changes in the viscoelastic properties of the AgNW/PS nanocomposite indicate the formation of a polymer-AgNW network at concentrations between 1.0 and 2.0 vol. %. In this case, the higher rheological percolation threshold versus CuNWs is mainly attributed to the fact that there was less dispersion of AgNWs in PS, as it can be inferred from a comparison of the data for *G'* at low frequencies versus CuNW/PS nanocomposites. Low dispersion of the AgNWs in PS causes the rheological percolation threshold of AgNWs to occur at higher concentrations than the electrical percolation threshold. Although AgNWs and CuNWs have different length distributions, the effect of this difference on the rheological behavior of the nanocomposites may not be as important as the difference in dispersion.

4.4 Discussion

Table 4.10 summarizes the electrical and rheological percolation thresholds obtained for solution-processed metal nanowire/PS nanocomposites related to the different types of nanowires, their average aspect ratios and the extent of dispersion. The extent of dispersion of the nanocomposites was inferred from both SEM characterization and rheological characterization of the different nanocomposites as described above.

Table 4.10. Electrical and rheological percolation thresholds for metal nanowire/PS nanocomposites.

Polymer nanocomposite	Average length (μm)[a]	Average aspect ratio (l/d)[b]	Extent of dispersion[c]	Electrical percolation threshold (Vol. %)	Rheological percolation threshold (Vol. %)
CuNW/PS	1.78 ± 1.37	71 ± 55	Fair	0.46	0.5 - 1.0
$C_8H_{17}S$-CuNW/PS	1.78 ± 1.37	71 ± 55	Good	0.25	1.0 - 2.0
AgNW/PS	1.37 ± 0.76	55 ± 30	Low	0.51	1.0 - 2.0

[a] before mixing with PS, [b] d = 25 nm, [c] According to SEM and rheological characterization

Results in Table 4.10 indicate that the electrical percolation threshold for CuNW/PS is lower than for AgNW/PS nanocomposites. This has been attributed to differences between the aspect ratio distribution of the nanoparticles, as well as to the different extent of dispersion. The surface functionalization of CuNWs increased the dispersion of the nanowires, decreasing the electrical percolation threshold relative to unfunctionalized CuNWs. The formation of electrically conductive networks of nanowires occurred at concentrations below the rheological percolation threshold. This is contrary to what is expected for well dispersed and randomly distributed nanocomposites.[26,31,33,36] However, NW/PS nanocomposites prepared using unfunctionalized Cu and Ag nanowires in this study are the result of the dispersion of individual nanowires and nanowire agglomerates in the polymer matrix. Therefore, the relation of the electrical and rheological percolation thresholds with the nanowire concentration is different. Figure 4.32 illustrates nanowire/polymer nanocomposites containing individual and agglomerate nanowires. The electrical conductivity is dictated by the connectivity between the nanowires in the polymer-nanowire and nanowire-nanowire networks (Figure 4.32a). This connectivity may occur at low concentrations, as a result of the dispersed individual nanowires interconnecting agglomerates in the nanocomposite. At similar concentrations, the polymer-polymer networks dominate the rheological behavior, given that the mechanical behavior of the polymer chains located between the agglomerates is not significantly affected by the presence of individual nanowires. At higher concentration, rheological percolation occurs due to the significant effect of a larger content of individual nanowires on the mechanical response of the polymer chains. Therefore, the rheological percolation requires a higher concentration of individual and agglomerate nanowires than does the electrical percolation.

PS nanocomposites prepared with surface functionalized CuNWs resulted in a different behavior of the polymer-polymer and polymer-nanowire networks compared to the networks formed when unfunctionalized nanowires are used. The rheological percolation threshold at 200 °C of the CuNW/PS nanocomposites shifts to higher concentration when the nanowires are chemically functionalized. The different behavior of the polymer-polymer and polymer-nanowire networks formed in $C_8H_{17}S$-CuNW/PS nanocomposites is attributed to the effects of the surface chemistry of the nanowires and the enhanced interaction between nanowire and polymer chains that might enable lubricating effects, resulting in a decrease in the viscoelastic properties of the nanocomposites, especially at concentrations below or close to the percolation threshold. The lubricating effect resulting from using copper nanowires functionalized with thiols will be further discussed in Chapter 5.

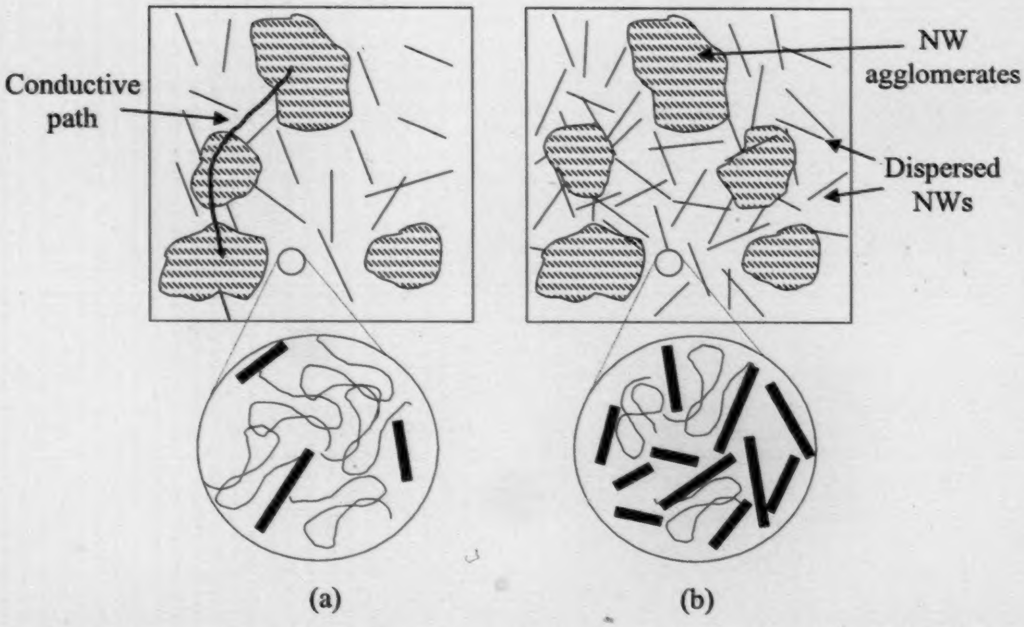

Figure 4.32. Schematic representation of the microstructure of metal nanowire/polymer nanocomposites containing individual and agglomerate nanowires. (a) At the electrical percolation threshold, electrically conductive networks of nanowires are established, but polymer chains between agglomerates dominate the rheological behavior. (b) At the rheological percolation threshold, the mechanical behavior of the polymer chains is restricted by the nanowires.

In studies related to dynamic and electrical characterization of filled polymers, the electrical percolation threshold generally follows the rheological percolation threshold.[31] In this respect, one should not forget the dependence of the flow characteristics of the polymer-polymer and polymer-nanowire networks with temperature. For instance, electrical resistivity measurements are usually carried out at room temperature, whereas the rheological characterization is carried out at temperatures above Tg of the polymer. Thus, a plausible correlation of the rheological and electrical percolation may depend on the response of the viscoelastic behavior of the composite with temperature. For instance, the rheological percolation of MWNT/PC composites demonstrated an increase from 0.5 to 5 wt. % in the rheological percolation threshold with an increase of temperature from 170 to 280 °C.[26] Thus, the rheological percolation threshold does not necessarily have to be lower than the electrical percolation threshold. In this work, a constant temperature of 200 °C was used for the viscoelastic characterization of the samples, which enabled us to compare the effects of different nanowires on the viscoelastic behavior of the polymer-nanowire network. Further studies could be performed to determine the influence of temperature on the rheological percolation threshold of the nanocomposites.

The electrical percolation thresholds for Ag and Cu nanowires reported here are comparable to the thresholds reported for polymer nanocomposites containing fullerene carbon nanotubes.[21,26,31,33,37] Theoretical studies and simulations have reported percolation thresholds of 1.0 and 0.05 vol.% for well distributed particles with aspect ratios of 100 and 1000, respectively.[24,38] Although the metal nanowire/polymer nanocomposites reported in this study are not ideally dispersed nanocomposites, the percolation curves obtained experimentally indicate that low percolation thresholds are attainable in polymer nanocomposites having individual dispersion as well as segregated nanowires. Variations in the electrical percolation threshold are expected from different processing conditions that produce different degrees of dispersion and alignment of the high aspect ratio nanofillers, as demonstrated by Du et al.[36]

Electrical percolation and enhanced dispersion of surface functionalized CuNWs in solution-processed PS nanocomposites was obtained using $C_8H_{17}SH$ chemisorption on the nanowires. In spite of the presence of multilayers of RS-Cu complexes on the functionalized CuNWs, the results of electrical characterization of the nanocomposites suggest that the CuNWs are not entirely passivated to electron flow and lower electrical percolation thresholds are attained due to an increased in the probability of electrical contact between particles brought by enhanced dispersion. Because surface modification with $C_8H_{17}SH$ enhances the dispersion of the nanowires into the polymer matrix, and the electrical properties are different from nanocomposites prepared with unfunctionalized CuNWs, surface modification with $C_8H_{17}SH$ is promising for the control of irreversible agglomeration after liberation from PAO templates; moreover, enhanced dispersion of nanowires in PS nanocomposites prepared by melt mixing may also be expected. The electrical properties of nanocomposites with concentrations $\geq$ 1.0 vol. % of surface functionalized CuNWs are appropriate for applications as electrostatically dissipative materials (10^4-10^{11} $\Omega\cdot$cm, www.esda.org), similar to CuNW/PS and AgNW/PS nanocomposites.

The break-up of the functionalized silver nanowires may be related to the instability of the high aspect-ratio nanowires at elevated temperatures (in this case

200 °C). For instance, Rayleigh instability of individual copper nanowires (30-50 nm diameter) on a SiO_2 surface was reported at temperatures above 400 °C.[39] Nichols and Mullins developed the approach of Rayleigh instability to solids.[40] In their model, a solid cylinder is unstable to sinusoidal perturbations of the type $r = r_o + \delta \sin (2\pi/\lambda) z$, where r is the initial radius of the cylinder, δ is the amplitude, λ is the wavelength of the perturbation, and z is the coordinate along the cylinder axis. When the perturbation has $\lambda > 2\pi r_o$, the cylinder is unstable, undulations are developed and increase with time until the cylinder breaks up into spheres. This model was developed assuming isolated solid cylinders with isotropic surface energy. In the particular case of changes in morphology due primarily to surface diffusion, the model predicts that the spheres reach a separation dictated by the wavelength of maximum growth, $\lambda_M = 2\pi\sqrt{2}\, r_o$. It is worth mentioning that this theoretical model has been applied previously in studies of morphological changes of Cu and Au nanowires, and correlations between experimental and calculated sphere diameters and sphere separation distances have been obtained, which supports the Rayleigh instability of the nanowires.[39,41] In the current work, break up of AgNWs could have been the result of a combined effect of surface functionalization, polymer matrix, shear stress and/or pressure during the melt mixing and hot molding process of their nanocomposites, which can be far from the ideal conditions of the model developed by Nichols and Mullins. However, the model may be useful in the development of future studies devoted to provide an insight to the fragmentation of nanowires in polymer nanocomposites. The break up of high aspect-ratio metal nanowires may

have serious implications in the preparation of polymer nanocomposites requiring low electrical percolation thresholds.

4.5 Conclusions

Metal nanowire/polymer nanocomposites were prepared by solution mixing of Cu or Ag nanowires and PS. Low electrical percolation thresholds of 0.46 vol. % Cu and 0.51 vol. % Ag in a PS matrix were attained by the high aspect-ratio nanofillers. Changes of 10 and 11 orders of magnitude in the electrical resistivity of the nanocomposites versus pure polymer were obtained with CuNWs and AgNWs, respectively. Lower aspect-ratios and less surface oxidation of silver compared to copper nanowires has influenced the sharpness of the percolation threshold and the level of conductivity of the percolated composites. TEM and SEM characterization of the nanocomposites indicated individual and agglomerated nanowires that cooperatively resulted in low electrical percolation thresholds.

Surface functionalization of copper nanowires with alkanethiols prevented the irreversible aggregation of the nanowires, and improved the dispersion in a PS matrix. The effect of increased dispersion on the electrical resistivity of the nanocomposites was reduced by the presence of RS-Cu complexes at the surface of functionalized nanowires. $C_{18}H_{37}S$-CuNW showed significant of passivation, resulting in PS nanocomposites with low electrical conductivity. By contrast, $C_8H_{17}SH$-CuNW/PS showed the formation of electrically conductive networks at lower concentrations than when unfunctionalized CuNWs were used.

Surface functionalization of silver nanowires with $C_8H_{17}SH$ resulted in fragmentation (break-up) of nanowires into spheres after applying shear stress and/or pressure at temperatures above the Tg of the polymer. Although the phenomenon of fragmentation of silver nanowires in PS deserves further study to elucidate a fundamental understanding of the instability of the nanowires, this phenomena will have negative implications on melt mixing of polymer nanocomposites that require low electrical percolation thresholds via the presence of high aspect ratio nanoparticles.

The effect of CuNWs and AgNWs on the rheological behavior of PS nanocomposites was significant. The formation of polymer-nanowire networks was evident from changes of viscoelastic properties of the nanocomposites, such as the complex viscosity and storage modulus at low frequencies. These changes were utilized to determine differences in the dispersion of the nanowires, as well as to elucidate changes in the composite microstructure and determine the rheological percolation threshold of the nanocomposites.

For relatively well-dispersed nanowire/polymer nanocomposites (i.e. CuNW/PS or $C_8H_{17}S$-CuNW/PS), the evolution of the microstructure, and electrical and rheological properties with the concentration of nanowires is as follows:

- At low concentration, well dispersed nanowires lead to the formation of a few polymer-nanowire networks and the nanocomposite may show a small decrease in the resistivity. Enhanced dispersion will lead to formation of polymer-nanowire networks at lower concentration. The rheological behavior is dominated by polymer-polymer networks.

- At intermediate concentrations, in the vicinity of the rheological percolation threshold, the formation of more polymer-nanowire and nanowire-nanowire networks contributes to increased electrical conductivity. The rheological behavior is controlled by both polymer-polymer and polymer-nanowire networks.
- At high concentration, beyond the rheological percolation threshold, consolidated electrically conductive polymer-nanowire and nanowire-nanowire networks are established that control the electrical and rheological behavior of the composite.

The electrical properties of metal nanowire/PS nanocomposites resemble those reported in the literature for nanocomposites prepared using single- (SWNT) and multi-walled (MWNT) carbon nanotubes, indicating that the use of metal nanowires may be an alternative to carbon nanotubes for the preparation of polymer nanocomposites in applications such as electrostatic dissipation.

4.6 References

1. Yalcin, O.; Yildiz, F.; Ozdemir, M.; Aktas, B.; Koseoglu, Y.; Bal, M.; Tuominen, M. T., *J. Magn. Magn. Mater.* **2004,** 272-76, 1684-1685.

2. Thurn-Albrecht, T.; Schotter, J.; Kastle, C. A.; Emley, N.; Shibauchi, T.; Krusin-Elbaum, L.; Guarini, K.; Black, C. T.; Tuominen, M. T.; Russell, T. P., *Science* **2000,** 290, (5499), 2126-2129.

3. Atashbar, M. Z.; Banerji, D.; Singamaneni, S.; Bliznyuk, V., *Mol. Cryst. Liq. Cryst.* **2005,** 427, 217-224.

4. Zhang, J. L.; Liu, Z. M.; Han, B. X.; Jiang, T.; Wu, W. Z.; Chen, J.; Li, Z. H.; Liu, D. X., *J. Phys. Chem. B* **2004,** 108, (7), 2200-2204.

5. Wu, K. H.; Lu, S. Y., *Macromol. Rap. Comm.* **2006,** 27, (6), 424-429.

6. Poa, C. H.; Silva, S. R. P.; Watts, P. C. P.; Hsu, W. K.; Kroto, H. W.; Walton, D. R. M., *Appl. Phys. Lett.* **2002,** 80, (17), 3189-3191.

7. Yang, Y. L.; Gupta, M. C., *Nano Lett.* **2005,** 5, (11), 2131-2134.

8. Saib, A.; Bednarz, L.; Daussin, R.; Bailly, C.; Lou, X.; Thomassin, J. M.; Pagnoulle, C.; Detrembleur, C.; Jerome, R.; Huynen, I., *IEEE Trans. Microw. Theor. Techn.* **2006,** 54, (6), 2745-2754.

9. Blake, R.; Coleman, J. N.; Byrne, M. T.; McCarthy, J. E.; Perova, T. S.; Blau, W. J.; Fonseca, A.; Nagy, J. B.; Gun'ko, Y. K., *J. Mater. Chem.* **2006,** 16, 4206-4213.

10. Chang, T. E.; Kisliuk, A.; Rhodes, S. M.; Brittain, W. J.; Sokolov, A. P., *Polymer* **2006,** 47, (22), 7740-7746.

11. Hill, D. E.; Lin, Y.; Rao, A. M.; Allard, L. F.; Sun, Y. P., *Macromolecules* **2002,** 35, (25), 9466-9471.

12. Lin, T. S.; Cheng, L. Y.; Hsiao, C. C.; Yang, A. C. M., *Mater. Chem. Phys.* **2005,** 94, (2-3), 438-443.

13. Mitchell, C. A.; Bahr, J. L.; Arepalli, S.; Tour, J. M.; Krishnamoorti, R., *Macromolecules* **2002,** 35, (23), 8825-8830.

14. Ramasubramaniam, R.; Chen, J.; Liu, H. Y., *Appl. Phys. Lett.* **2003,** 83, (14), 2928-2930.

15. Regev, O.; ElKati, P. N. B.; Loos, J.; Koning, C. E., *Adv. Mater.* **2004,** 16, (3), 248-250.

16. Safadi, B.; Andrews, R.; Grulke, E. A., *J. Appl. Pol. Sci.* **2002,** 84, (14), 2660-2669.

17. Bellayer, S.; Gilman, J. W.; Eidelman, N.; Bourbigot, S.; Flambard, X.; Fox, D. M.; De Long, H. C.; Trulove, P. C., *Adv. Funct. Mater.* **2005,** 15, (6), 910-916.

18. Choi, Y. J.; Hwang, S. H.; Hong, Y. S.; Kim, J. Y.; Ok, C. Y.; Huh, W.; Lee, S. W., *Polym. Bull.* **2005,** 53, (5-6), 393-400.

19. Viswanathan, G.; Chakrapani, N.; Yang, H. C.; Wei, B. Q.; Chung, H. S.; Cho, K. W.; Ryu, C. Y.; Ajayan, P. M., *J. Am. Chem. Soc.* **2003,** 125, (31), 9258-9259.

20. Zhang, B.; Fu, R. W.; Zhang, M. Q.; Dong, X. M.; Lan, P. L.; Qiu, J. S., *Sens. Actuators, B* **2005,** 109, (2), 323-328.

21. Curran, S. A.; Zhang, D. H.; Wondmagegn, W. T.; Ellis, A. V.; Cech, J.; Roth, S.; Carroll, D. L., *J. Mater. Res.* **2006,** 21, (4), 1071-1077.

22. Watts, P. C. P.; Hsu, W. K.; Chen, G. Z.; Fray, D. J.; Kroto, H. W.; Walton, D. R. M., *J. Mater. Chem.* **2001,** 11, (10), 2482-2488.

23. Watts, P. C. P.; Hsu, W. K.; Randall, D. P.; Kotzeva, V.; Chen, G. Z., *Chem. Mater.* **2002,** 14, (11), 4505-4508.

24. Kirkpatrick, S., *Rev. Mod. Phys.* **1973,** 45, (4), 574-588.

25. Lux, F., *J. Mater. Sci.* **1993,** 28, (2), 285-301.

26. Pötschke, P.; Abdel-Goad, M.; Alig, I.; Dudkin, S.; Lellinger, D., *Polymer* **2004,** 45, (26), 8863-8870.

27. Balberg, I., *Phys. Rev. Lett.* **1987,** 59, (12), 1305-1308.

28. Balberg, I., *Philos. Mag. B.* **1987,** 56, (6), 991-1003.

29. Balberg, I.; Binenbaum, N.; Wagner, N., *Phys. Rev. Lett.* **1984,** 52, (17), 1465-1468.

30. Electrostatic Discharge Association Home Page. http://www.esda.org (August 2005),

31. Du, F. M.; Scogna, R. C.; Zhou, W.; Brand, S.; Fischer, J. E.; Winey, K. I., *Macromolecules* **2004,** 37, (24), 9048-9055.

32. Potschke, P.; Bhattacharyya, A. R.; Janke, A., *Eur. Polym. J.* **2004,** 40, (1), 137-148.

33. Pötschke, P.; Fornes, T. D.; Paul, D. R., *Polymer* **2002,** 43, (11), 3247-3255.

34. Wu, G.; Asai, S.; Sumita, M.; Hattori, T.; Higuchi, R.; Washiyama, J., *Colloid Polym. Sci.* **2000,** 278, (3), 220-228.

35. Shenoy, A. V., *Rheology of filled polymer systems*. Kluwer Academy Publishers: Dordrecht, 1999.

36. Du, F. M.; Fischer, J. E.; Winey, K. I., *Phys. Rev. B* **2005,** 72, (12), 121404, 1-4.

37. Du, F. M.; Fischer, J. E.; Winey, K. I., *J. Polym. Sci., Part B: Polym. Phys.* **2003,** 41, (24), 3333-3338.

38. Garboczi, E. J.; Snyder, K. A.; Douglas, J. F.; Thorpe, M. F., *Phys. Rev. E* **1995,** 52, (1), 819-828.

39. Toimil-Molares, M. E.; Balogh, A. G.; Cornelius, T. W.; Neumann, R.; Trautmann, C., *Appl. Phys. Lett.* **2004,** 85, (22), 5337-5339.

40. Nichols, F. A.; Mullins, W. W., *Trans. Met. Soc. AIME* **1965,** 233, (10), 1840-1848.

41. Karim, S.; Toimil-Molares, M. E.; Balogh, A. G.; Ensinger, W.; Cornelius, T. W.; Khan, E. U.; Neumann, R., *Nanotechnology* **2006,** 17, (24), 5954-5959.

Chapter 5

Copper nanowire/Polystyrene nanocomposites prepared by melt mixing: Surface functionalization, dispersion, and electrical-rheological percolation

5.1 Introduction

In Chapter 4, the preparation, dispersion, and electrical-rheological percolation of metal nanowire (Cu, Ag)/polymer nanocomposites prepared by solution processing were presented. Electrical percolation thresholds of bare nanowires of 0.46 vol. % Cu and 0.51 vol. % Ag were obtained.[1,2] Solution processing of polymer nanocomposites has been the method of choice in many studies of carbon nanotube-based nanocomposites.[3-10] The use of ultrasound and/or in-situ polymerization in the presence of nanofillers has resulted in good dispersion of the nanoparticles and low electrical percolation thresholds. However, the preparation of polymer nanocomposites by melt mixing is desirable, given conventional processes in the polymer industry, such as extrusion and injection molding, which do not require solvents.[11] Solvent handling can be a significant problem when producing large quantities.

The use of inorganic nanofillers in the preparation of polymer composites introduced the necessity of mediating a good interaction between the polymer chains and nanoparticle surfaces, in order to reduce the strong agglomeration forces between the particles and to promote homogeneous distribution in the polymer matrix. This is of particular importance for processing of polymer nanocomposites by melt mixing. For instance, the agglomeration of carbon nanotubes is considered to be a serious impediment to harnessing their potential in nanocomposites and substantial effort has been directed towards enhancing their dispersion via surface modification and/or different methods of composite preparation.[7,12] For instance, surface modification of nanotubes enabled the formation of a percolated network with a low content of nanotubes.[7] In the particular case of metal nanowires, the self assembly of organic molecules at the surface creates a new interface between the conductive particles, and this affects the electrical properties of the nanocomposites (see Chapter 4). Furthermore, little is known about the extent to which the electrical properties of the polymer nanocomposites will be affected by the surface chemistry of metal nanowires.

Gram amounts of materials are required to perform experimental studies of the melt mixing process for the preparation of polymer nanocomposites. This motivated the scale-up of the synthesis of copper nanowires described in Chapter 2. In addition, Sundararaj and collaborators[13] developed a miniature minimixer known as the APAM, for the preparation of small amounts of polymer nanocomposites using mixing conditions (shear stress and flow patterns) similar to those used in industrial equipment for polymer processing. In this chapter, the dispersion, electrical, and rheological characterization of polymer nanocomposites prepared by melt mixing of unfunctionalized and functionalized copper nanowires into polystyrene melt in an

APAM are studied and compared to the properties of nanocomposites prepared by solution processing. Alkanethiols were used to chemically modify the copper nanowires, reduce nanowire agglomeration, and enhance their dispersion in the polymer matrix. The effect of the surface chemistry on the electrical and rheological properties of the nanocomposites was studied. For instance, a decrease in the complex viscosity of the nanocomposites containing low amounts of surface functionalized copper nanowires has been observed; a phenomenon rarely observed for polymers containing fillers.

5.2 Experimental

5.2.1 Synthesis and chemical modification of CuNWs

Copper nanowires were produced using template-directed synthesis in porous aluminum oxide templates fabricated by the two-step anodization of aluminum (Al) electrodes (10 cm × 25 cm) in H_2SO_4. Details of the synthesis and liberation of Cu nanowires have been described in Chapter 2. CuNWs used in the preparation of PS nanocomposites by melt mixing were prepared using the larger-scale system that produces CuNWs ~ 25 nm in diameter and 1.29 ± 0.83 μm in length.[14,15] In the final step of the synthesis, the nanowires were dispersed in methanol (CH_3OH). Measured volumes of 1-butanethiol (C_4H_9SH), and 1-octanethiol ($C_8H_{17}SH$) (Sigma-Aldrich, used as received) were added to methanolic suspensions of the nanowires containing ~ 1.6 mg Cu / ml CH_3OH. The mixtures of CuNW suspensions and alkanethiols were sonicated for 5 minutes and then stirred with a magnetic stir bar for 1 hour, filtered, rinsed vigorously with CH_2Cl_2, dried under vacuum for 24 hours and finally transferred into a nitrogen-filled glove box.

5.2.2 Preparation of polymer nanocomposites by melt mixing

Polystyrene (PS, Styron 666D) was provided by Dow Chemical Co, M.I. = 7.5, M_w = 200,000 g/mol, and Tg = 100 °C. The bulk densities of copper and PS are 8.96 g/cm^3 and 1.04 g/cm^3, respectively. The amount of copper nanowires used for the preparation of the nanocomposites was calculated using the bulk density of copper, and in the case of functionalized CuNWs, also considering the percent weight loss measured during thermogravimetric analysis. Samples of CuNWs were mixed with pellets of PS in a preheated (200 °C) mixing cup of the APAM[13] in a glove box under nitrogen (N_2). The mixing conditions were: 100 rpm, 200 °C, 10 minutes and rotation in the counter-clockwise direction. Table 5.1 shows the specifications of the APAM and a photograph is presented in Figure 5.1.

Table 5.1. Specifications of the Alberta Polymer Asymmetric Minimixer (APAM)[13]

Rotation Speeds (rpm)	Maximum shear rate (1/s)	Average shear rate (1/s)	Approximate mixing mass (g)	Mixing time (min)
25	68	8.3	2	1-20
50	136	16.6		
100	272	33.2		
200	544	66.4		

Nanocomposite specimens for electrical and rheological characterization were prepared by hot molding in a stainless steel mold with an empty cavity 25.4 mm in diameter and 0.8 mm thick using a Carver No.2086 hot press at 200°C and 1.5 metric tons of pressure for 5 min. Aluminum foil was used to separate the stainless steel plates from the nanocomposites specimens.

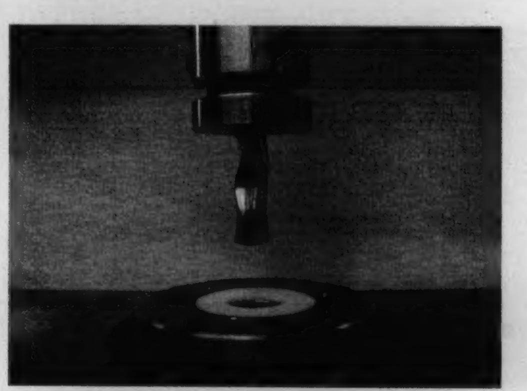

Figure 5.1. Photograph of the Alberta Polymer Asymmetric Minimixer (APAM).[13]

5.2.3 Morphology characterization

The morphologies of freeze-fractured surfaces of the composites were analyzed using a JEOL 6301F field emission scanning electron microscope (SEM). The samples were sputter-coated with chromium before imaging in the SEM. Backscattered electron images were collected using a 20 kV accelerating voltage.

5.2.4 Rheological characterization

Dynamic rheological characterization was performed on hot molded samples 25.4 mm in diameter and 0.8 mm thick using a Rheometrics Inc. RMS800 Rheometer with a 25 mm parallel plate fixture at 200 °C under nitrogen atmosphere. Frequency sweeps were performed at low strains (0.09 - 10%), where the materials show linear viscoelastic behavior.

5.2.5 Electrical resistivity measurements

Hot molded samples 25.4 mm in diameter and 0.8 mm thick were used for bulk electrical resistivity measurements utilizing a 6517A Keithley electrometer, 8009 Keithley resistivity test fixture, and Keithley 6524 high resistance measurement software. The electrical resistivity was measured using 100 V or 10 V, depending on the resistivity range of the samples, according to ESD STM11.12-2000. Specifically, the electrical resistivities were measured as follows: for samples prepared with CuNWs, 100 V for 0, 0.5 and 1.0 vol. %, 10 V for 2.0 to 4.0 vol. %; for samples with BT-CuNWs, OT-CuNWs, 100 V for 0.5 to 2.0 vol. %, and 10 V for 3.0 and 4.0 vol. %.

5.2.6 Glass transition temperature by Differential Scanning Calorimetry

The glass transition of pristine polymer and polymer nanocomposites was measured using a Perkin Elmer Pyris 1 Differential Scanning Calorimeter. Samples were heated up to 250 °C using a heating rate of 10 °C/min, cooled down to room temperature and then heated again to 250 °C using a heating rate of 10 °C/min. Tg was measured from the second heating cycle.

5.3 Results

5.3.1 Dispersion of as-liberated and surface functionalized copper nanowires in PS prepared by melt mixing

The morphology of polystyrene nanocomposites containing unfunctionalized copper nanowires or functionalized copper nanowires with $C_8H_{17}SH$ and C_4H_9SH was studied by SEM with backscattered electron detection, which, as shown in Chapter 4, enhances the contrast between the organic polymer phase and the metallic nanofiller. Figure 5.2 shows SEM images taken from freeze fractures of hot-molded specimens. Bright domains in the backscattered image show the nanowires dispersed in the polymer matrix. Low magnification images (Fig. 5.2 a, c, and e) show agglomerates of less than 100 μm that correspond to nanowires incompletely dispersed and distributed across the thickness of the freeze-fractured samples. Small agglomerates are observed in SEM images of PS containing functionalized CuNWs (Fig. 5.2 c, e). In addition, the density of the agglomerates (number of agglomerates per scanned area) in the nanocomposites seems to be lower when alkylthiol functionalized nanowires are utilized. Individual nanowires are clearly observed from high magnification images, which shows that the density of individual nanowires is significantly higher in the nanocomposites containing alkylthiol functionalized CuNWs (Fig. 5.2 d, f) than in those with unfunctionalized CuNWs (Fig. 5.2 b). Hence, morphology characterization of the nanocomposites by SEM with backscattered electron detection strongly indicates that enhanced dispersion of nanofiller in the polystyrene matrix was obtained as a result of chemical modification of CuNWs.

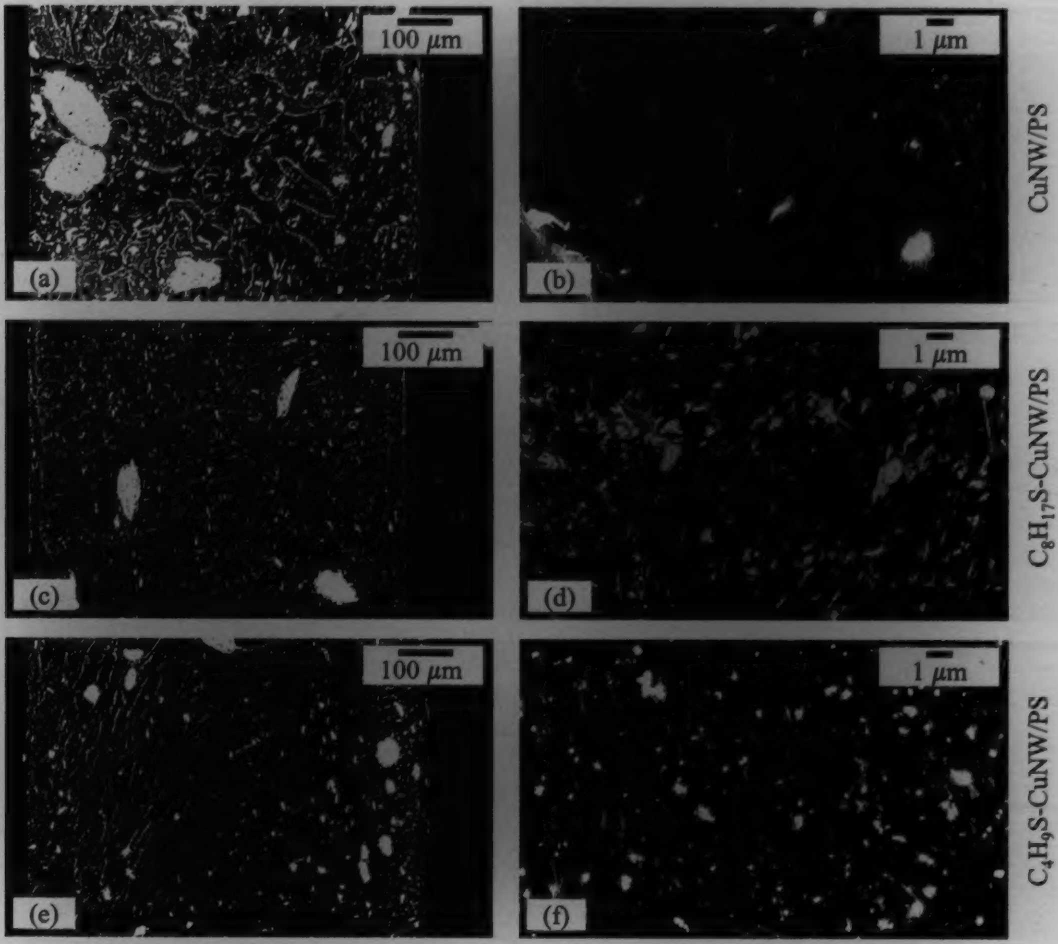

Figure 5.2. Backscattered electron SEM images of polystyrene nanocomposites containing 4 vol. % CuNW. Bright domains correspond to copper nanowires dispersed in the polymer matrix. PS nanocomposites containing (a,b) unfunctionalized nanowires, (c,d) $C_8H_{17}S$-CuNW, and (e,f) C_4H_9S-CuNW. The images show the enhancement of dispersion of copper nanowires using surface modification with $C_8H_{17}SH$ and C_4H_9SH.

5.3.2 Rheological behavior of melt-mixed CuNW/PS nanocomposites

Pellets of pure PS were treated in the APAM at 200 °C using mixing conditions similar to those used for preparation of nanocomposites in this study. The results of viscoelastic characterization of pure PS and PS nanocomposites prepared with unfunctionalized copper nanowires at several concentrations are presented in Figure 5.3. The complex viscosity ($|\eta^*|$), storage modulus (G') and loss modulus (G'') increase gradually with increasing nanowire content. However, the variation in the frequency response of the viscoelastic properties is not as great as was previously described in Chapter 4 for PS nanocomposites prepared by solution processing, or as great as in other studies of polymer nanocomposites containing carbon nanotubes.[7,16,17] It is known that the rheological behavior of a filled composite is similar to that of the pure polymer when the nanofiller is not well dispersed.[16] At low frequency (0.1 rad/s), for the 4 vol. % CuNW/PS nanocomposite, $|\eta^*|$ is only double that of PS (Fig. 5.3 b), and G' is approximately 4 times that of PS (Fig. 5.3 d). The frequency response of $|\eta^*|$ and G' for CuNW/PS nanocomposites is similar to that of pure PS.

At low frequencies, polystyrene exhibits terminal behavior of the storage modulus (G') and loss modulus (G''). The introduction of nanofiller should alter the terminal behavior, enabling the formation of an interconnected structure that may be detected from changes in the slope of the frequency response of G'. It is well known that a structure of interconnected, high aspect-ratio particles in a polymer composite can be inferred from the plateau of G' and G'' versus frequency at low frequencies.[16-19] The low frequency range corresponds to the time frame in which the polymer chains have enough time to disentangle and relax.[20] For example, for this PS, the characteristic relaxation time is approximately 1s.

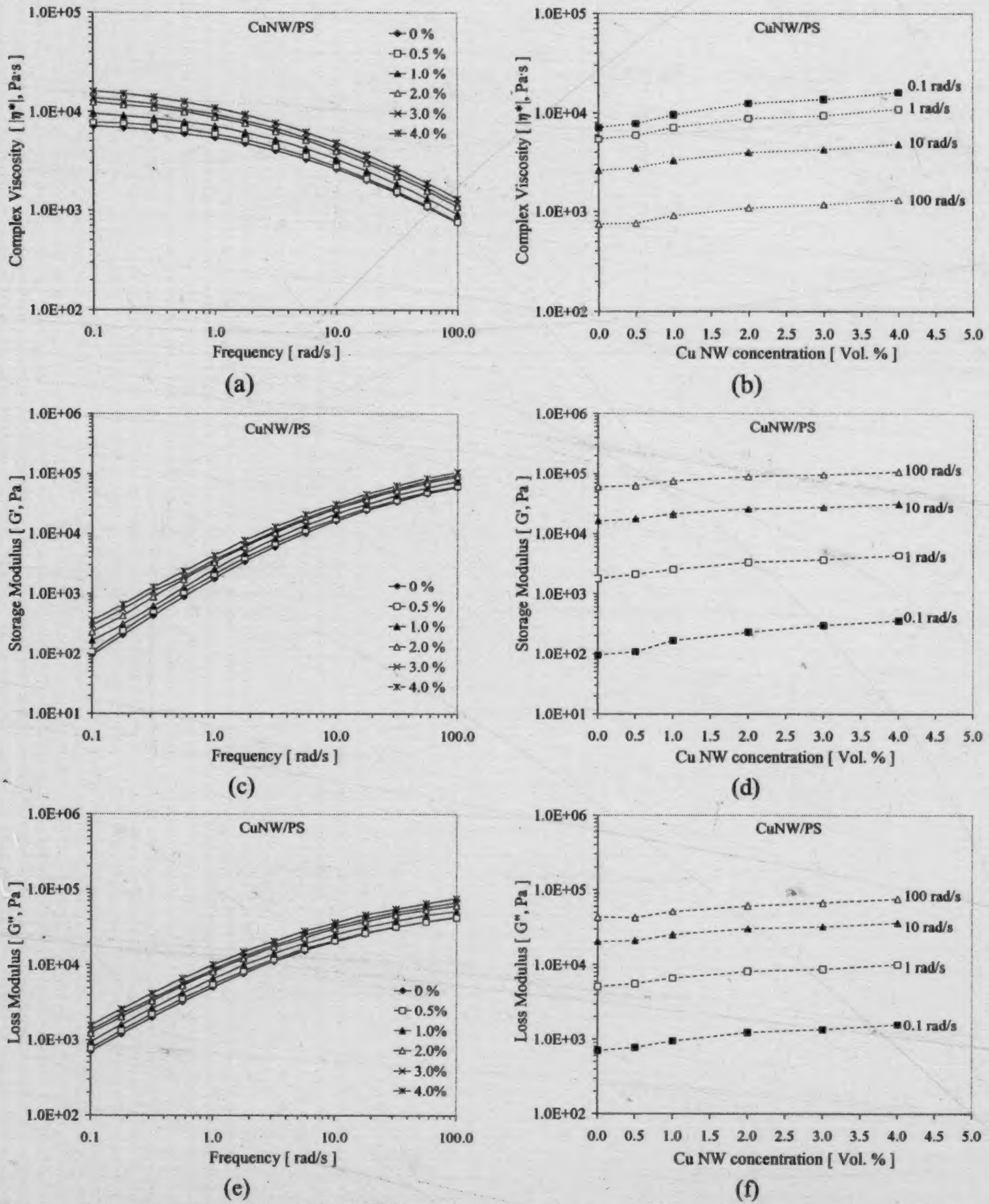

Figure 5.3. Complex viscosity ($|\eta^*|$), storage modulus (G') and loss modulus (G'') of CuNW/polystyrene nanocomposites prepared by melt mixing in an APAM as a function of (a,c,e) frequency and (b,d,f) concentration of unfunctionalized Cu nanowires. Lines are guides to the eye.

Table 5.2 shows the slopes of Log G' and Log G'' versus Log ω of CuNW/PS nanocomposites in the range of frequency between 0.1 and 1.0 rad/s, as a function of concentration of unfunctionalized CuNWs. The slopes do not change significantly with CuNW concentration, indicating that the CuNWs have a negligible effect on the terminal behavior of PS. The lack of significant change in the viscoelastic properties with increasing concentration of unfunctionalized nanowires is related to poor dispersion of the nanowires into PS. As described previously, limited dispersion of unfunctionalized copper nanowires was observed by SEM.

Table 5.2. Slopes of Log G' and Log G'' versus Log ω at frequencies between 0.1 and 1.0 rad/s for CuNW/PS nanocomposites prepared by melt mixing.

Cu Conc. (Vol. %)	$\frac{dLogG'}{dLog\omega}$	$\frac{dLogG''}{dLog\omega}$
0	1.27	0.86
0.5	1.29	0.86
1.0	1.19	0.85
2.0	1.17	0.83
3.0	1.09	0.81
4.0	1.09	0.81

Figure 5.4 shows the viscoelastic properties of pure polystyrene and nanocomposites containing several concentrations of $C_8H_{17}S$-CuNWs. Interestingly, an unusual decrease in the complex viscosity of the nanocomposites at low concentrations of $C_8H_{17}S$-CuNWs can be observed relative to the pure polymer (Fig. 5.4 a, b). The viscosity of nanocomposites containing 0.5 and 1.0 vol. % showed a similar frequency response to that of PS, indicating a plateau at low frequencies, but

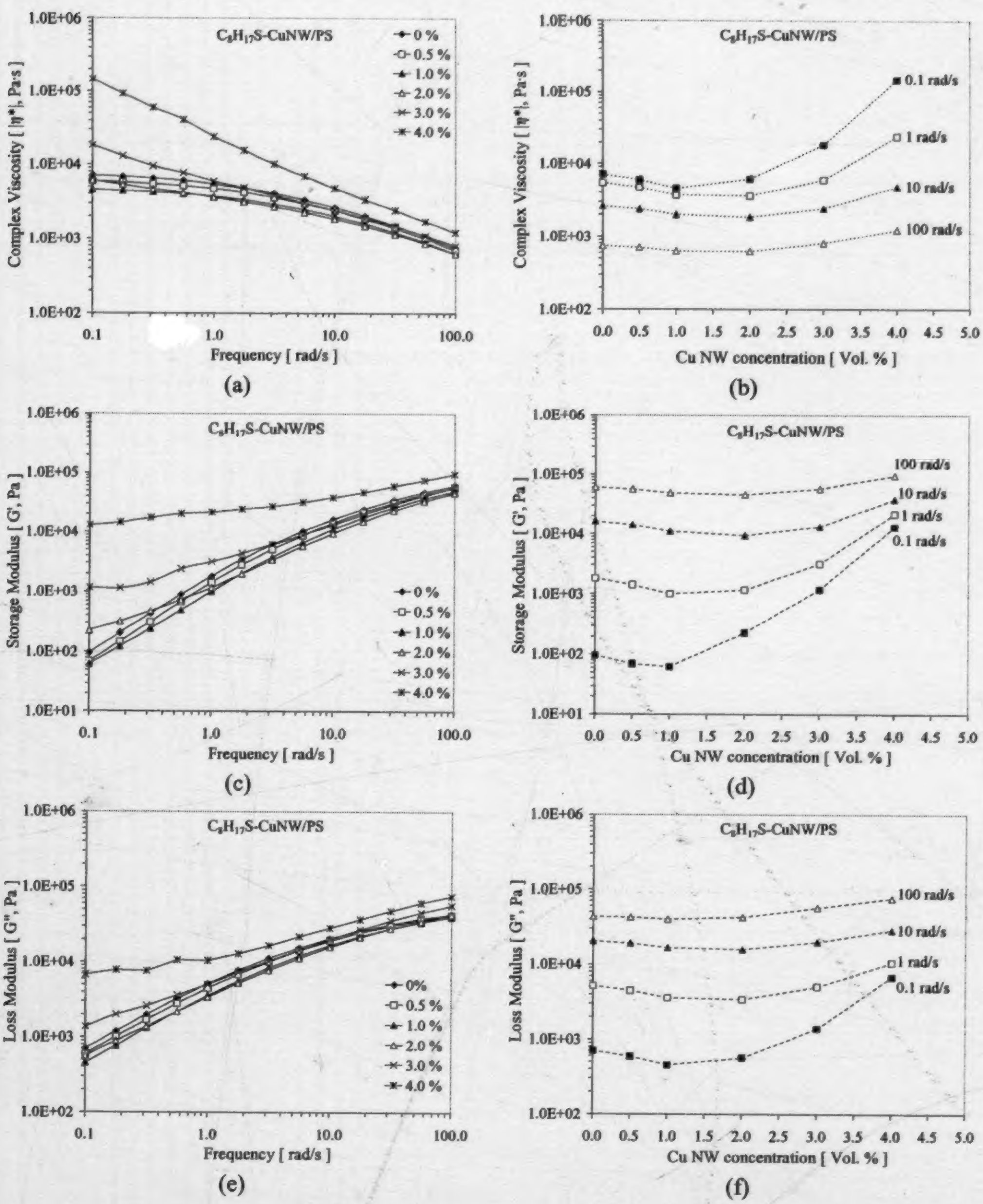

Figure 5.4. Complex viscosity ($|\eta^*|$), storage modulus (G') and loss modulus of C$_8$H$_{17}$S-CuNW/polystyrene nanocomposites prepared by melt mixing in an APAM as a function of (a, c, e) frequency and (b, d, f) concentration of copper nanowires. Lines are guides to the eye.

with lower viscosity than pure PS (Fig. 5.4a). At 2.0 vol. % the viscosity of the composite showed a power law dependence on frequency; i.e. the plateau at low frequency is not observed. At 2.0 vol. % CuNWs, the complex viscosity also remains lower than that of pure PS, but higher than that of 1.0 vol. %. At concentrations of 3.0 and 4.0 vol. %, the viscosity increases significantly with respect to that of pure PS and low concentration composites; moreover, a power law frequency dependence of the viscosity is observed over the complete range of frequencies studied. The largest increase in the viscosity (~ 20 times) with respect to pure PS is observed at 4.0 vol. % CuNWs. Figure 5.4b, which presents the variation of complex viscosity of the composites at different frequencies, shows that at low frequency (0.1 rad/s), a minimum viscosity is observed for 1.0 vol. % and a significant increase in the viscosity occurs above 2.0 vol. %. At higher frequencies, the initial decrease in the viscosity with concentration of $C_8H_{17}S$-CuNWs is in the following order: PS > 0.5 % > 1.0 % > 2.0 %. At high frequency (100 rad/s) the viscosity does not vary significantly with $C_8H_{17}S$-CuNW concentration.

Figure 5.4c shows the storage modulus *G'* as a function of frequency of polystyrene nanocomposites with different concentrations of $C_8H_{17}S$-CuNWs. The frequency response of *G'* of composites prepared with 0.5 and 1.0 % of nanowires is similar to that of pure PS; however, *G'* at these concentrations is lower than that of PS for the range of frequencies studied. At 2.0 vol. %, the frequency response varies compared to pure PS; *G'* is lower than that of pure PS, 0.5 and 1.0 vol. % at high frequencies, whereas, at low frequencies, the slope of *G'* versus frequency is smaller and *G'* becomes higher for 2.0 vol. % than that of pure PS, 0.5 and 1.0 vol. %. That is, there is a shoulder at low frequencies which indicates the formation of a polymer-nanowire network. At 3.0 vol. %, *G'* shows higher values than that of 2 vol. % for all frequencies and a plateau at low frequency is clearly observed. Finally, at 4.0 vol. %, *G'* becomes higher than pure PS for all frequencies with a weak dependence on frequency. *G'* increases ~ 2 orders of magnitude from pure PS to 4 vol. % composite at the lowest frequency studied (0.1 rad/s). Figure 5.4d shows *G'* at different frequencies, as a function of the copper concentration in the composites. At low frequency (0.1 rad/s), *G'* decreases from pure PS to 0.5 and 1.0 vol. %, and then a significant increase is observed for 2 vol. % and above. At high frequency (100 rad/s), *G'* becomes almost independent on the $C_8H_{17}S$-CuNW content. Significant changes were also observed for *G"*.

Table 5.3 shows the slopes of Log *G'* and Log *G"* versus Log ω of CuNW/PS nanocomposites in the range of frequency between 0.1 and 1.0 rad/s, as a function of concentration of $C_8H_{17}S$-CuNWs. The change in the slope of *G'* versus frequency at 2.0 vol. % copper is an indication that a combined polymer-nanowire network has been established (Table 5.3). The changes in the slope of *G'* versus frequency, as well as viscosity variations versus concentration, suggest that rheological percolation of $C_8H_{17}S$-CuNWs occurs between 1.0 and 2.0 vol. %.

Table 5.3. Slopes of Log *G'* and Log *G"* versus Log *ω* at frequencies between 0.1 and 1.0 rad/s for $C_8H_{17}S$-CuNW/PS nanocomposites prepared by melt mixing.

Cu Conc. (Vol. %)	$\frac{dLogG'}{dLog\omega}$	$\frac{dLogG''}{dLog\omega}$
0	1.27	0.86
0.5	1.31	0.88
1.0	1.21	0.90
2.0	0.71	0.78
3.0	0.47	0.55
4.0	0.23	0.20

Figure 5.5 shows the viscoelastic properties of pure PS and PS nanocomposites containing different concentrations of C_4H_9S-CuNWs. The frequency response of the viscosity of these samples showed some differences from that of nanocomposites containing $C_8H_{17}S$-CuNWs, as follows. The decrease in viscosity at low concentrations of C_4H_9S-CuNWs (0.5 and 1.0 vol. %) is greater than for $C_8H_{17}S$-CuNW composites. This might be the result of differences in the viscosity of long and short chain alkyl thiols, as will be discussed later. A distinct change in the response of the complex viscosity versus frequency can be observed at a concentration of 1.0 vol. %, i.e. the plateau at low frequency is not observed (Fig. 5.5a). In the case of $C_8H_{17}S$-CuNW composites, this change was observed at 2.0 vol. %. Moreover, the complex viscosity of a 4 vol. % nanocomposite is linearly dependent on frequency and it is ~ 200 times higher than that of pure PS and 20 times higher than obtained for $C_8H_{17}S$-CuNWs at low frequency, which suggests that enhanced dispersion of C_4H_9S-CuNWs was obtained.

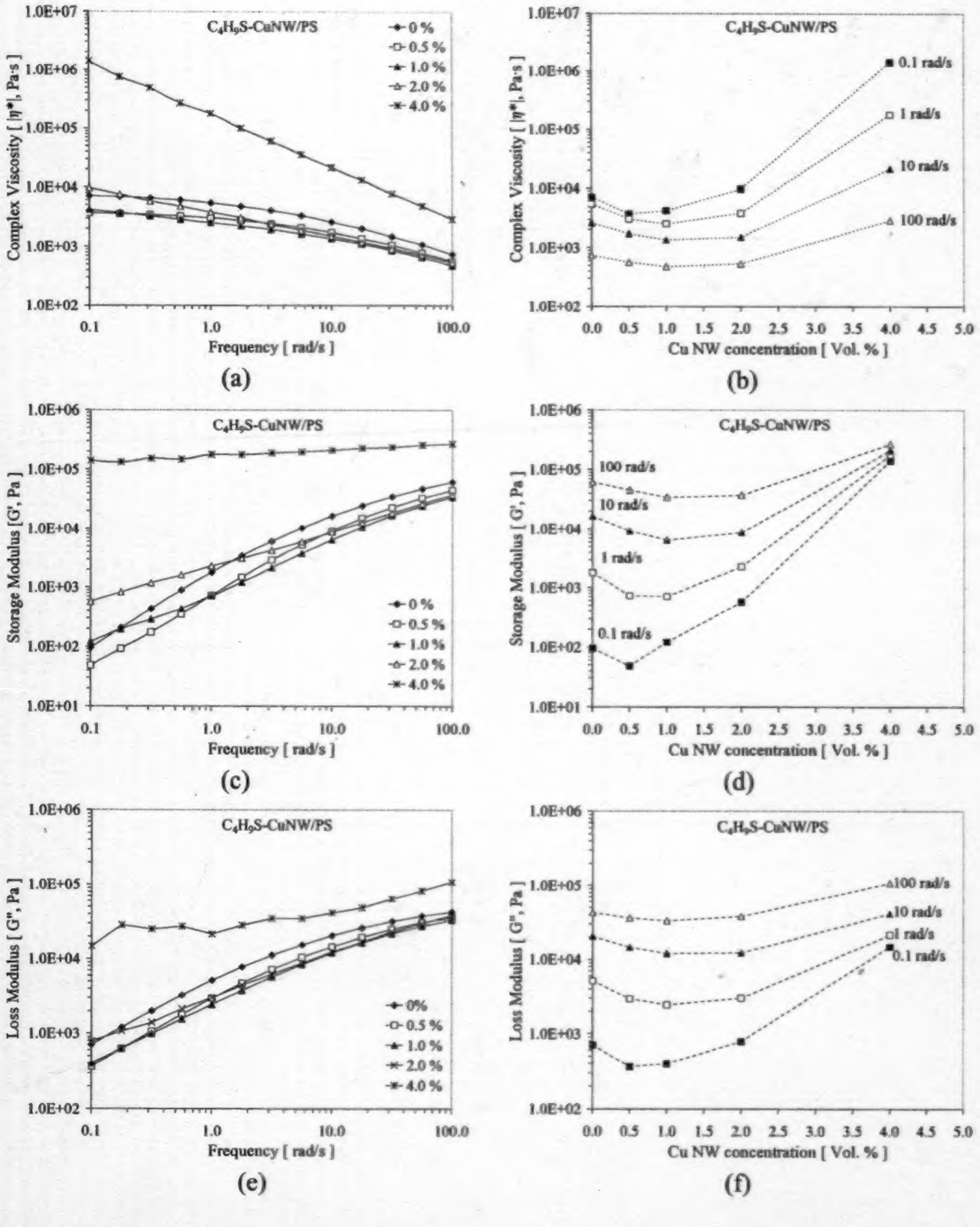

(a) (b)

(c) (d)

(e) (f)

Figure 5.5. Complex viscosity (|η*|), storage modulus (*G'*) and loss modulus of C$_4$H$_9$S-CuNW/polystyrene nanocomposites prepared by melt mixing in an APAM as a function of (a, c, e) frequency and (b, d, f) concentration of copper nanowires. Lines are guides to the eye.

Figure 5.5c shows *G'* as a function of frequency of PS nanocomposites with different concentrations of C_4H_9S-CuNWs. The frequency response for *G'* of the 0.5 vol. % composite indicates a similar dependence as that of pure PS, except that the 0.5 vol. % composite has lower *G'* values. The 1.0 vol. % composite has lower modulus than PS at high frequency and a plateau of *G'* versus frequency at low frequencies. The 2.0 vol. % C_4H_9S-CuNW composite has lower *G'* values than pure PS at high frequency, but there is a more significant change in slope at low frequencies than for the 1 vol. % composite. At 4 vol. %, the *G'* slope is almost zero, showing practically no dependence on frequency in the range studied. Figure 5.5d shows clearly the initial decrease in *G'* at low concentration of C_4H_9S-CuNWs for different frequencies with relative to the *G'* value for pure PS. For instance, at low frequency (0.1 rad/s), *G'* decreases for 0.5 vol. % but increases at higher concentrations, showing a significant change of ~ 3 orders of magnitude (~ 1500 times) at 4.0 vol. % relative to pure PS. At high frequency, *G'* is slightly lower for concentrations of 0.5, 1.0 and 2.0 vol. %, and shows only a modest increase of ~ 4 times at 4.0 vol. %.

Table 5.4 shows the slopes of Log *G'* and Log *G"* versus Log ω of PS nanocomposites in the range of frequency between 0.1 and 1.0 rad/s, as a function of concentration of C_4H_9S-CuNWs. The change in the slope of *G'* at 1.0 vol. % indicates the formation of a polymer-nanowire network. Considering the change in the slope of *G'* versus frequency (Table 5.4, Fig. 5.5c) as well as the variation in the response of the viscosity versus concentration described above, the rheological percolation threshold of C_4H_9S-CuNWs occurs between 0.5 and 1.0 vol. %. The evidence of enhanced dispersion of C_4H_9S-CuNWs seen by rheological characterization explains the lower rheological percolation threshold versus that for $C_8H_{17}S$-CuNWs.

Table 5.4. Slopes of Log *G'* and Log *G"* versus Log ω at frequencies between 0.1 and 1.0 rad/s for C_4H_9S-CuNW/PS nanocomposites prepared by melt mixing.

Cu Conc. (Vol. %)	$\frac{dLogG'}{dLog\omega}$	$\frac{dLogG''}{dLog\omega}$
0	1.27	0.86
0.5	1.17	0.91
1.0	0.75	0.79
2.0	0.60	0.59
4.0	0.10	0.12

Figure 5.6 shows a comparison of plots of *G'* vs *G"* and phase angle versus complex modulus for PS nanocomposites containing unfunctionalized CuNWs, $C_8H_{17}S$-CuNWs and C_4H_9S-CuNWs. In the *G'* vs *G"* plots (Fig. 5.6 a, c, e), a shift in the position of the data points and a change in the slope is used to identify significant changes in the microstructure of the polymer composite that are related to rheological percolation.[17] No visible changes are observed in *G'* vs *G"* of CuNW/PS nanocomposites, as a consequence of the limited dispersion of unfunctionalized nanowires. For $C_8H_{17}S$-CuNW/PS a significant change in the slope is observed between 1.0 and 2.0 vol. %, and for C_4H_9S-CuNW/PS, the change is observed between 0.5 and 1.0 vol. %. The phase angle versus complex modulus plots (Fig. 5.6

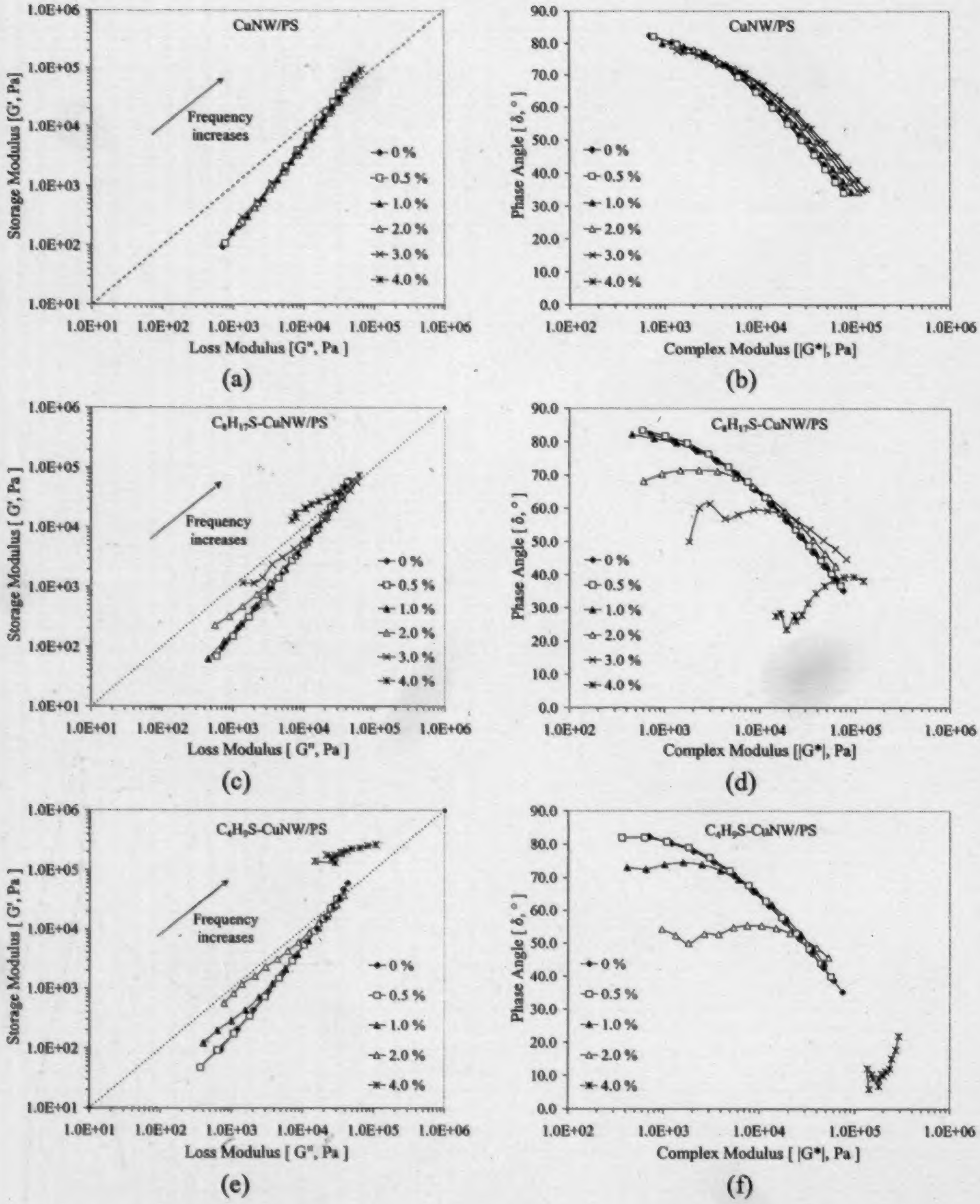

(a) (b)

(c) (d)

(e) (f)

Figure 5.6. Storage modulus (*G'*) versus loss modulus (*G''*) and phase angle versus complex modulus for PS nanocomposites prepared by melt mixing in an APAM (a, b) using unfunctionalized CuNW, (c, d) $C_8H_{17}S$-CuNW, and (e, f) C_4H_9S-CuNW. Lines are guides to the eye.

b, d, f) indicate that CuNW/PS nanocomposites do not deviate from the behavior of pure PS, while changes are observed for $C_8H_{17}S$-CuNW/PS and C_4H_9S-CuNW/PS nanocomposites at concentrations 1.0 - 2.0 vol. % and 0.5 - 1.0 vol. %, respectively. These plots corroborate a negligible effect of unfunctionalized CuNWs on the viscoelastic properties of PS nanocomposites prepared by melt mixing, and confirm the rheological percolation thresholds of chemically functionalized copper nanowires.

5.3.3 Electrical resistivity of melt-mixed CuNW/PS nanocomposites

Electrical resistivity measurements of nanocomposites prepared using different concentrations of unfunctionalized CuNWs, C_4H_9S-CuNWs and $C_8H_{17}S$-CuNWs are shown in Figure 5.7. A sharp decrease in the volume resistivity of 9 orders of magnitude (from 10^{16} to 10^7 $\Omega\cdot$cm) is observed for 2.0 vol. % of unfunctionalized copper nanowires relative to PS. This change in the electrical resistivity of the composite is due to the formation of an electrically percolated network of copper nanowires. Above 2.0 vol. % CuNWs, the volume electrical resistivity remains relatively constant. Interestingly, for nanocomposites prepared using C_4H_9S-CuNWs and $C_8H_{17}S$-CuNWs, a gradual decrease rather than a sharp decrease in the electrical resistivity is observed at concentrations ≥1.0 vol. %. A final plateau for the electrical resistivity was not observed within the range of concentrations of alkanethiol functionalized CuNWs studied. Variations of 5 and 3 orders of magnitude in the electrical resistivity were observed for pure PS versus PS nanocomposites containing 4 vol. % of C_4H_9S-CuNWs and $C_8H_{17}S$-CuNWs, respectively.

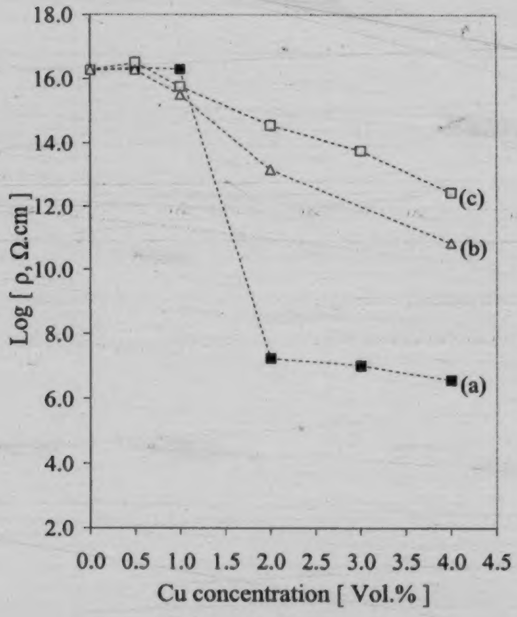

Figure 5.7. Volume electrical resistivity of polystyrene nanocomposites prepared by melt mixing using different concentrations of (a) unfunctionalized copper nanowires and copper nanowires functionalized with (b) C_4H_9SH, and (c) $C_8H_{17}SH$. Lines are guides to the eye.

5.4 Discussion

The reasons why alkanethiols were used for surface modification of CuNWs were discussed in Chapter 3. It is worth mentioning that 1-octadecanethiol ($C_{18}H_{37}SH$) seemed to provide more protection against surface oxidation of nanowires than $C_8H_{17}SH$ and C_4H_9SH. However, considering the passivation effect that the long chain alkanethiol, $C_{18}H_{37}SH$, might have on the nanowires, and the electrical properties of nanocomposites prepared containing $C_{18}H_{37}S$-CuNWs,[2] in this work, shorter alkanethiols ($C_8H_{17}SH$ and C_4H_9SH) were used to study the effect of surficial thiolates on the dispersion, electrical and rheological properties of polystyrene nanocomposites prepared by melt mixing.

5.4.1 Effect of surface functionalization of CuNWs on dispersion

Backscattered electron SEM images of the nanocomposites with thiol functionalized nanowires showed a higher density of copper nanowires dispersed in the polymer matrix (Fig. 5.2d, and f) when compared to SEM images of composites containing unfunctionalized nanowires (Fig. 5.2b). Enhanced dispersion of surface functionalized CuNWs was also evident from the rheological characterization of their composites, which showed significant variations in the storage modulus after a percolated network formed (Figs. 5.4 and 5.5). Indeed, at low frequencies, higher values of G' relative to PS, and slopes of G' versus frequency approaching zero are both indicators of an increased dispersion of copper nanowires; provided that other factors affecting rheology such as filler orientation, polymer molecular weight, size and aspect-ratio of the filler are constant, as they are in this case.

5.4.2 Effect of surface functionalization of CuNWs on rheology of melt-mixed CuNW/PS nanocomposites

In terms of rheological characterization, several results of this study need to be addressed. The similar frequency dependence of the complex viscosity and storage modulus of pure polystyrene and of composites containing unfunctionalized CuNWs indicates that melt mixing in the APAM was poor. Indeed, melt mixing provided less dispersion than solution processing using ultrasound did (Chapter 4).[2,15] Thus, a significant impact on the rheological properties was not observed in this study when unfunctionalized copper nanowires were used. In the case of alkanethiol functionalized copper nanowires, significant variations in the viscoelastic properties were observed, because the nanowires were well dispersed throughout the polymer matrix by melt mixing in the APAM.

The observed decrease in the complex viscosity and the storage modulus at low concentrations of NWs, combined with well-dispersed nanowires is intriguing. A few studies have reported a reduction in viscosity for polymer composites containing nanofillers. The phenomenon has been attributed either to preferential adsorption of long polymer chains on SWNTs, as in the case of SWNT-filled Ultra High Molecular Weight (UHMW) PE,[21] or to changes of free volume and entanglement confinement, as in the case of linear PS filled with PS nanoparticles.[22,23] Other studies related to polymers filled with inorganic materials such as clay, calcium silicate, and calcium carbonate have reported a decrease in the viscosity due to the plasticizing effect of coupling agents used for the compatibilization of the inorganic/organic interface.[24-26] The effect of the alkanethiol functionalization of the copper nanowires on the decrease in the complex viscosity of the nanocomposites is explained below.

Considering the temperatures for thermal desorption obtained from thermogravimetric analysis of alkanethiol functionalized copper nanowires presented in Chapter 3, as well as the temperature of processing of the nanocomposites (200 °C), copper thiolates at the surface of the CuNWs may thermally desorb during the melt mixing process. The thermal stability of thiol monolayers on copper surfaces has been studied previously.[27] Of the C-S-$Cu_{(surf)}$ bonds in the alkanethiol covalently bonded to the copper surface, the C-S bond is thermodynamically less stable than the Cu-S bond; hence, the thiolate will most probably thermally decompose by a scission of the C-S bond rather than the Cu-S bond. Additionally, rheological characterization of $C_8H_{17}S$-CuNW/PS nanocomposites prepared by solution processing at room temperature (Chapter 4) did not show decrease in the complex viscosity at low concentrations of copper nanowires versus pure PS. Therefore, during melt mixing of PS and alkanethiol functionalized nanowires, alkyl chains are likely released into the polymer matrix from the copper alkanethiolates formed at the surface of the CuNWs. The hydrocarbons released from the CuNW surface into the PS matrix introduce a plasticizing effect leading to a decrease in the complex viscosity of the nanocomposites.

The decrease in T_g (Table 5.5) of PS nanocomposites containing functionalized nanowires versus that of either pristine PS or PS containing unfunctionalized CuNWs is consistent with the plasticizing effect proposed above. The greater decrease in viscosity of nanocomposites containing low concentrations of C_4H_9S-CuNWs versus $C_8H_{17}S$-CuNWs (Figs. 5.4 and 5.5) may be explained by considering the lower viscosity of short versus long chain alkyl compounds, and their effect on the final viscosity of the nanocomposites.

Table 5.5. T_g of pure PS, PS processed by melt mixing, and PS nanocomposites containing 1 vol. % Cu of unfunctionalized and functionalized nanowires.

Nanocomposite	T_g (°C)
Pristine PS666D	98.7
PS666D processed by melt mixing	97.8
CuNW/PS	97.1
$C_8H_{17}S$-CuNW/PS	93.7
C_4H_9S-CuNW/PS	93.4

Nanosized particles approaching the dimensions of the radius of gyration of the polymers might lead to changes in free volume and entanglements. For instance, an increase of free space was reported in studies of the free volume distribution of polyethylene-carbon black (CB) composites: from 146.8 $Å^3$ for the pristine polymer to 204.5 $Å^3$ for a composite with 29 parts of CB particles (~ 33 nm particle size) per hundred of resin.[28] Moreover, studies of molecular transport and selectivity of nanocomposite membranes based on glassy polymers such as poly(4-methyl-2-pentyne) demonstrated an increase in free volume of the composite caused by enhanced dispersion of silica nanoparticles.[29] This increase in free volume has been attributed to the presence of well-dispersed non-porous particles (~ 13 nm in diameter) with comparable dimensions to those of the polymer chains. It is believed that the copper nanowires ~ 25 nm in diameter used in this study did not have a significant effect on the free volume and/or chain entanglement, given that a decrease in the viscosity of nanocomposites prepared by solution processing was not observed.

The rheological response of CuNW/PS composites at different frequencies are the result of the polymer-nanowire networks formed in the composite, similar to those considered for carbon nanotubes;[17] at concentrations below rheological percolation, the entangled polymer-polymer network is dominant, whereas at concentrations above percolation, a combined entangled network and polymer-nanowire network dominate the rheological response. This is unlike electrical percolation where the nanowire-nanowire network is the dominant factor dictating the electrical resistivity response. The results of viscoelastic properties of composites containing functionalized nanowires showed that before percolation, the viscosity and G' responses are similar to that of pure PS, indicating that the chain entanglement prevails; this behavior is observed up to 0.5 vol. % in the case of C_4H_9S-CuNWs and up to 1.0 vol. % in the case of $C_8H_{17}S$-CuNWs. Beyond these concentrations, a combined effect of networks was observed, because variations in the slope of G' and viscosity at low frequencies are evident, particularly at low frequencies. At 4.0 vol. %, the rheological response of the nanocomposites seemed to be dominated by the polymer-nanowire network at all frequencies.

5.4.3 Effect of surface functionalization of CuNWs on electrical percolation of melt-mixed CuNW/PS nanocomposites

A significant variation in the electrical conductivity (which is the inverse to the electrical resistivity) of nanocomposites above concentrations of only 1.0 vol. % indicates the formation of an electrically conductive network of unfunctionalized CuNWs (Fig. 5.7a). This electrical percolation threshold of melt-mixed nanocomposites compares well with lower concentrations of 0.46 vol. % at which electrical conductivity was obtained in solution-processed composites containing unfunctionalized CuNWs.[1] This is attributed to the limited dispersion of CuNWs resulting from the melt mixing process, as well as to the lower aspect-ratio of the CuNWs prepared by the larger-scale process with respect to CuNWs prepared by the smaller-scale system that was used in the preparation of PS nanocomposites by solution processing described in Chapter 4 (1.29 ± 0.83 μm from the larger scale process versus 1.78 ± 1.37 μm from smaller scale process).[1,15]

One of the challenges faced in the development of inorganic nanoparticle/polymer composites is the strong agglomeration of the nanosized filler. Although CuNWs produced by the PAO template-directed synthesis[14] showed a strong tendency to irreversibly agglomerate, results of this work demonstrate that a combination of well-dispersed CuNWs and agglomerated CuNWs leads to electrically conductive composites at low concentrations either by solution processing or melt mixing. However, the presence of metal nanowire agglomerates could prevent the formation of an electrically conductive network at lower concentrations. In this study, surface modification of CuNWs with alkanethiols resulted in significant dispersion in melt mixed nanocomposites; however, the electrical conductivity of nanocomposites prepared with surface modified CuNWs showed only a gradual increase with increasing content of C_4H_9S-CuNWs and $C_8H_{17}S$-CuNWs. For 4 vol. % nanocomposites, increases of approximately 5 and 3 orders of magnitude were observed relative to the pristine polymer and more conductive composites were obtained with short chain alkanethiol functionalized nanowires (C_4H_9S-CuNWs).

The electrical conductivity in filled polymer composites is dominated by electron tunneling or hopping and the particles do not necessarily have to be in direct physical contact with each other in order to permit electron conductivity throughout the composite. Instead, a conductive pathway progressively forms as the gap between conductive particles is reduced with increasing filler concentration. For instance, in carbon-black-polymer composites, it has been shown that the electrical conductivity of the composites is determined by tunneling mechanism through percolating networks of conductive particles.[30-33] It has also been shown that for composites containing loadings of carbon black aggregates above the percolation threshold, a polymer layer of ~ 20 Å may still remain between the aggregates, which suggest a contribution of electron tunneling to the electrical conductivity of the composites at high filler concentrations.[30]

In the case of PS nanocomposites prepared in this study, the alkyl chain lengths of C_4H_9SH and $C_8H_{17}SH$ from the S atom to the end methyl group are 6.0 Å and 11.1 Å respectively. A monomolecular layer of these alkyl thiols on CuNWs might enable the electron transfer in the nanocomposites through electron tunneling or hopping. Furthermore, given the inverse proportionality between charge transfer and the molecular gap between conductive particles, the electronic conductivity should be higher for nanocomposites prepared with C_4H_9S-CuNWs than for $C_8H_{17}S$-

CuNWs. Studies of molecular junctions showed the possibility of tunneling electrons through self assembled thiol monolayers (SAMs) located between conductors.[34] In polymer nanocomposites containing thiol functionalized CuNWs, not only SAMs, but also a polymer phase may be located between the metal particles, so an increased number of energy barriers for electron transfer, and diminished electron conductivity, may be expected.

The lower conductivity of the composites prepared with alkanethiol functionalized CuNWs relative to that of unfunctionalized CuNW composites might also be related to the fact that the self assembly of more than one monolayer on the copper surface can occur,[35-38] due to the presence of some surface oxidation of liberated nanowires.[14] The elucidation of the mechanism of copper alkanethiolate formation on Cu surfaces remains challenging,[39] and further studies of the surface modification of CuNWs may help to elucidate the effect of surface oxidation on thiol adsorption and the electrical percolation threshold of composites prepared using functionalized CuNWs by this route.

5.4.4 Rheological and electrical percolation of melt-mixed CuNW/PS nanocomposites

The rheological percolation threshold of unfunctionalized CuNWs could not be identified, because the low dispersion of the nanowires by melt mixing produced an insignificant change in the viscoelastic properties of the composites relative to the pure polymer. It is known that in well-dispersed composites, the rheological percolation threshold is lower than the electrical percolation threshold, given that the distance between conductive particles necessary to reach rheological percolation is greater than that required for electrical percolation.[16,17] Therefore, the electrical percolation of unfunctionalized CuNWs in PS nanocomposites prepared by melt mixing occurred through a conductive network formed by the combination of individual and agglomerated nanowires. Thus, individually dispersed nanowires favor electrical contact at low concentrations throughout the composite, while the agglomerated nanowires permit the entangled polymer-polymer network to dominate the rheological behavior.

For nanocomposites containing functionalized copper nanowires, the rheological percolation thresholds were between 1.0-2.0 vol. % for $C_8H_{17}S$-CuNW/PS, and 0.5 - 1.0 vol. % for C_4H_9S-CuNW/PS. The difference in the thresholds was attributed to better dispersion of C_4H_9S-CuNWs, and therefore their ability to disrupt the mobility of the polymer chains at lower concentrations. Although, the electrical resistivity of the nanocomposites did not show an abrupt change, a gradual decrease of the resistivity occurred at concentrations $\geq$1.0 vol. %.

A comparison of the electrical and rheological properties obtained for PS nanocomposites prepared by melt mixing and solution processing (Chapter 4) indicate that dispersion of the nanowires in a polymer solution resulted in electrical and rheological percolation at lower concentrations than obtained by melt mixing. This is attributed to enhanced dispersion of the nanowires (as-liberated and chemically modified) in PS obtained by solution processing.

5.5 Conclusions

Melt mixing in a miniature polymer melt mixer, the APAM, was performed to prepare copper nanowire/polystyrene nanocomposites. Unfunctionalized copper nanowires presented limited dispersion. The electrical and rheological behavior of the nanocomposites containing bare copper nanowires results from a combined effect of agglomerated and individually dispersed nanowires. This leads to electrical conductivity at relatively low nanowire concentration (2.0 vol. %), as well as rheological behavior mainly dominated by polymer-polymer networks at concentrations both below and above the electrical percolation threshold.

Chemisorption of alkanethiols on CuNW surfaces led to significant enhancement of nanowire dispersion in PS nanocomposites prepared by melt mixing. Changes in rheological and electrical behavior of the nanocomposites prepared with functionalized Cu nanowires occurred within the concentration range of 0.5 to 2.0 vol. % Cu. Significant changes in the rheological behavior of nanocomposites containing functionalized copper nanowires indicated the formation of polymer-nanowire networks with a solid-like behavior. By contrast, the electrical resistivity of the nanocomposites with functionalized CuNWs did not show abrupt changes, but rather an almost linear dependence for copper concentrations ≥1.0 vol. % Cu, which suggests that functionalized copper nanowires formed polymer-nanowire and nanowire-nanowire networks with reduced electrical conductivity due to the chemisorption of alkanethiols. The dependence of the electrical resistivity on concentration may offer the possibility of controlling the final resistivity of nanocomposites by using different surface chemistries on the nanofillers.

5.6 References

1. Gelves, G. A.; Lin B.; Sundararaj, U.; Haber, J. A., *Adv. Funct. Mater.* **2006,** 16, 2423-2430.
2. Gelves, G. A.; Sundararaj, U.; Haber, J. A., *Macromol. Rap. Comm.* **2005,** 26, (21), 1677-1681.
3. Blake, R.; Coleman, J. N.; Byrne, M. T.; McCarthy, J. E.; Perova, T. S.; Blau, W. J.; Fonseca, A.; Nagy, J. B.; Gun'ko, Y. K., *J. Mater. Chem.* **2006,** 16, 4206-4213.
4. Chang, T. E.; Kisliuk, A.; Rhodes, S. M.; Brittain, W. J.; Sokolov, A. P., *Polymer* **2006,** 47, (22), 7740-7746.
5. Hill, D. E.; Lin, Y.; Rao, A. M.; Allard, L. F.; Sun, Y. P., *Macromolecules* **2002,** 35, (25), 9466-9471.
6. Lin, T. S.; Cheng, L. Y.; Hsiao, C. C.; Yang, A. C. M., *Mater. Chem. Phys.* **2005,** 94, (2-3), 438-443.
7. Mitchell, C. A.; Bahr, J. L.; Arepalli, S.; Tour, J. M.; Krishnamoorti, R., *Macromolecules* **2002,** 35, (23), 8825-8830.
8. Ramasubramaniam, R.; Chen, J.; Liu, H. Y., *Appl. Phys. Lett.* **2003,** 83, (14), 2928-2930.

9. Safadi, B.; Andrews, R.; Grulke, E. A., *J. Appl. Pol. Sci.* **2002,** 84, (14), 2660-2669.

10. Yang, Y. L.; Gupta, M. C., *Nano Lett.* **2005,** 5, (11), 2131-2134.

11. Breuer, O.; Sundararaj, U., *Polym. Compos.* **2004,** 25, (6), 630-645.

12. Du, F. M.; Fischer, J. E.; Winey, K. I., *J. Polym. Sci., Part B: Polym. Phys.* **2003,** 41, (24), 3333-3338.

13. Breuer, O.; Sundararaj, U.; Toogood, R. W., *Polym. Eng. Sci.* **2004,** 44, (5), 868-879.

14. Gelves, G. A.; Murakami, Z. T. M.; Krantz, M. J.; Haber, J. A., *J. Mater. Chem.* **2006,** 16, (30), 3075-3083.

15. Lin, B.; Gelves, G. A.; Haber, J. A.; Sundararaj, U., *Ind. Eng. Chem. Accepted* **2006**.

16. Du, F. M.; Scogna, R. C.; Zhou, W.; Brand, S.; Fischer, J. E.; Winey, K. I., *Macromolecules* **2004,** 37, (24), 9048-9055.

17. Pötschke, P.; Abdel-Goad, M.; Alig, I.; Dudkin, S.; Lellinger, D., *Polymer* **2004,** 45, (26), 8863-8870.

18. Pötschke, P.; Fornes, T. D.; Paul, D. R., *Polymer* **2002,** 43, (11), 3247-3255.

19. Lin, B.; Sundararaj, U.; Pötschke, P., *Macromol. Mater. Eng.* **2006,** 291, (3), 227-238.

20. Shenoy, A. V., *Rheology of filled polymer systems*. Kluwer Academy Publishers: Dordrecht, 1999.

21. Zhang, Q. H.; Lippits, D. R.; Rastogi, S., *Macromolecules* **2006,** 39, (2), 658-666.

22. Tuteja, A.; Mackay, M. E.; Hawker, C. J.; Van Horn, B., *Macromolecules* **2005,** 38, (19), 8000-8011.

23. Mackay, M. E.; Dao, T. T.; Tuteja, A.; Ho, D. L.; Van Horn, B.; Kim, H. C.; Hawker, C. J., *Nat. Mater.* **2003,** 2, (11), 762-766.

24. Han, C. D.; Sandford, C.; Yoo, H. J., *Polym. Eng. Sci.* **1978,** 18, (11), 849-854.

25. Monte, S. J.; Sugerman, G., *Polym.-Plast. Technol. Eng.* **1979,** 13, (2), 115-135.

26. Maiti, S. N.; Singh, G.; Ibrahim, M. N., *J. Appl. Polym. Sci.* **2003,** 87, (9), 1511-1518.

27. Lai, Y. H.; Yeh, C. T.; Cheng, S. H.; Liao, P.; Hung, W. H., *J. Phys. Chem. B* **2002,** 106, (21), 5438-5446.

28. Patnaik, A.; Zhu, Z.; Yang, G.; Sun, Y., *Phys. Status Solidi A* **1998,** 169, (1), 115-125.

29. Merkel, T. C.; Freeman, B. D.; Spontak, R. J.; He, Z.; Pinnau, I.; Meakin, P.; Hill, A. J., *Science* **2002,** 296, (5567), 519-522.

30. Sichel, E. K., *Carbon-black polymer composites*. Marcel Dekker: New York, 1982.

31. Sichel, E. K.; Gittleman, J. I.; Sheng, P., *Phys. Rev. B* **1978,** 18, (10), 5712-5716.

32. Sheng, P.; Sichel, E. K.; Gittleman, J. I., *Phys. Rev. Lett.* **1978,** 40, (18), 1197-1200.

33. Balberg, I., *Phys. Rev. Lett.* **1987,** 59, (12), 1305-1308.

34. McCreery, R. L., *Chem. Mater.* **2004,** 16, (23), 4477-4496.

35. Keller, H.; Simak, P.; Schrepp, W.; Dembowski, J., *Thin Solid Films* **1994,** 244, (1-2), 799-805.

36. Kim, Y. T.; McCarley, R. L.; Bard, A. J., *Langmuir* **1993,** 9, (8), 1941-1944.

37. Ron, H.; Cohen, H.; Matlis, S.; Rappaport, M.; Rubinstein, I., *J. Phys. Chem. B* **1998,** 102, (49), 9861-9869.

38. Woodward, J. T.; Walker, M. L.; Meuse, C. W.; Vanderah, D. J.; Poirier, G. E.; Plant, A. L., *Langmuir* **2000,** 16, (12), 5347-5353.

39. Love, J. C.; Estroff, L. A.; Kriebel, J. K.; Nuzzo, R. G.; Whitesides, G. M., *Chem. Rev.* **2005,** 105, (4), 1103-1169.

Chapter 6

Concluding remarks and future Work

6.1 General conclusions

In this thesis, the synthesis of metal nanowires in gram quantities using PAO templates, and the study of the dispersion, electrical and rheological properties of metal nanowire/polymer nanocomposites produced by solution or melt-mixing were described.

The strategy for the synthesis of metal nanowires utilized in this work was the AC electrodeposition into porous aluminum oxide templates (PAO). To the best of our knowledge, little has been reported about actual yields of nanostructures produced by hard-template synthesis, as well as the effect of liberation procedures (template dissolution) on the surface chemistry and morphology of the nanostructures. Although high aspect ratio nanowires ($l/d > 1000$) can be attained using synthesis in hard-templates, feasible aspect ratios of liberated-nanowires have not been reported in the literature.[1-6] The current work is a contribution to these aspects, which are experimentally and fundamentally necessary for large-scale synthesis of metal nanowires or other nanostructures in PAO templates.

AC electrodeposition through the barrier layer of PAO templates is advantageous relative to DC electrodeposition, when the large-scale synthesis of metal nanowires or nanostructures is considered. AC electrodeposition does not require multiple steps of electrode preparation, as DC electrodeposition does. Therefore, template-directed synthesis is simplified because processes such as evaporation of back-metal contacts, opening of the pore bottoms, dissolution of the barrier layer, attaching of electrodes to holders, and the manipulation of thin and brittle membranes required to enable DC electrodeposition, are not necessary. In addition, high purity Al plates can be reused through many cycles for the preparation of PAO templates and AC electrodeposition, facilitating more efficient use of Al electrodes. However, AC electrodeposition of nanomaterials into PAO templates through the barrier layer at the bottom of the pores is challenging, given the interplay of the variables involved during the growth of the templates and electrodeposition of the nanostructures.

The synthesis of nanowires developed in this thesis consisted of the following steps: (1) electrochemical or chemical polishing of Al, (2) two-step anodization in H_2SO_4(aq) (3) AC electrodeposition, (4) dissolution of PAO template and liberation of nanowires using NaOH(aq), (5) dispersion using ultrasound, and (6) solid-liquid separation. A smaller-scale system was first implemented using high purity 5 cm × 11 cm Al plates (450 cm^2 of Al per batch). This process yielded 1.68 mg/cm^2 (756 ± 58.5 mg/batch) of CuNWs 25 nm in diameter with average lengths of 1.78 ± 1.37 μm. Subsequently, a larger-scale system was implemented using 10 cm × 25 cm Al plates; this system used 4,400 cm^2 of high purity Al plates and yielded 0.786 mg/cm^2 (3,459 270 mg/batch) of CuNWs 25 nm in diameter with average lengths of 1.29 ± 0.83 μm. Similarly, once adequate conditions for AC electrodeposition were obtained, the synthesis of AgNWs using the smaller-scale system yielded 0.90 mg/cm^2 (405 ± 33.0 mg/batch) of AgNWs 25 nm in diameter with average length of 1.37 ± 0.76 μm. This process enabled us to produce sufficient quantities of high aspect ratio metal nanowires required for preparation and studies of metal nanowire/polymer nanocomposites.

Liberation of Cu and Ag nanowires from PAO templates using acidic or basic solutions resulted in nanostructures with different surface chemistry and morphology. For instance, although the use of acidic conditions resulted in less surface oxidation in CuNWs, significant changes in the morphology of the nanowires were observed. Indeed, the morphology of acid-liberated nanowires did not resemble the shape and diameter of the pores in PAO templates. Therefore, strong basic conditions were recommended for the liberation of Cu and Ag nanowires. Cu nanowires with small degree of oxidation, and oxide-free Ag nanowires were characterized by XRD, XPS, SEM, TEM, and TGA.

Compared to metal nanowires prepared by solution methods (soft-template methods and variations),[7-9] which require the use of surfactants or chemisorbed substances for preferential growth of nanostructures in one dimension, Cu and Ag nanowires produced by synthesis in PAO templates presented cleaner surfaces that may be more adaptable for surface functionalization. In addition, template-directed synthesis in PAO provides capability to produce different kinds of nanostructures with different aspect ratios by tuning of the pore dimensions (4 - 400 nm in diameter and tens of micrometers in depth) and conditions of AC electrodeposition. By contrast, a smaller range of materials and aspect ratios are attainable by solution methods up to date.[7-9]

High-aspect ratio metal nanowires were shown to be an alternative to carbon nanotubes for the modification of the electrical properties of polymer nanocomposites with low amounts of nanofiller. The presence of the nanofiller affected the mechanical behavior of the polymer chains. Electrical and rheological percolations were investigated in this work. In the case of filled-polymers, percolation refers to the change in a specific property (e.g. electrical resistivity, storage modulus) of the composite at a certain concentration of the filler. The electrical and rheological properties of (CuNW or AgNW)/polymer nanocomposites prepared by solution processing or melt-mixing were studied in an effort to elucidate the changes in the microstructure and macroscopic properties of the nanocomposite with increasing nanowire concentration. Hence, significant changes in electrical resistivity of the nanocomposite are attributed to the formation of electrically-conductive polymer-nanowire and nanowire-nanowire networks, and changes in the viscoelastic properties are attributed to the dynamic transition of the composite from liquid-like to solid-like behavior of the polymer-nanowire network. The mechanical behavior of the nanocomposites is important to determine the response of the material to conditions that polymeric materials experience in real life.[10,11]

Polymer nanocomposites prepared by the solution method showed low electrical percolation thresholds of 0.46 vol. % Cu and 0.51 vol. % Ag, for CuNW/PS and AgNW/PS nanocomposites, respectively.[12] Changes of 10 and 11 orders of magnitude in the electrical resistivity of the nanocomposites relative to pure PS were obtained for CuNWs and AgNWs, respectively.[12] The analysis of the morphology, electrical resistivity and viscoelastic characteristics of the nanocomposites led us to conclude that the phenomena of electrical and rheological percolation in these nanocomposites are attributed to the concomitant interaction of individual nanowires and agglomerated nanowires. Thus, at concentrations close to the percolation threshold, well-dispersed nanowires enabled the formation of electrically conductive networks by interaction with agglomerated nanowires dispersed throughout the matrix. In addition, polymer-polymer networks located between the agglomerate nanowires dominate the mechanical behavior of the nanocomposite; hence, rheological percolation (solid-like behavior) was not observed. At concentrations above the electrical percolation threshold, a polymer-nanowire network was consolidated throughout the matrix resulting in rheological percolation. In the case of well-dispersed nanofillers, it is known that the rheological percolation threshold occurs at lower concentration than the electrical percolation threshold, given that the distance between the filler particles required for restriction of mobility of polymer chains in the nanocomposite is higher than that required for electrical percolation.[13-20] However, for metal NW/PS nanocomposites prepared in the current work, the presence of individual and agglomerate nanowires produced electrical percolation at lower concentrations than that required for rheological percolation. This interpretation was extended to melt-mixed CuNW/PS nanocomposites as described below.

CuNW/PS nanocomposites prepared by the melt-mixing method showed electrical percolation at a higher concentration of CuNWs than those obtained with solution-processed nanocomposites. It is inferred, from rheological characterization of the composites, that dispersion of CuNWs by melt-mixing was significantly less than that obtained by the solution method. Thus, the same concentration of nanofiller, melt-mixed nanocomposites contain a lower fraction of well-dispersed individual nanowires than solution-processed composites and higher volume fractions of copper are required to enable electrical conductivity in the polymer nanocomposite. Interestingly, in melt-mixed CuNW/PS nanocomposites, polymer-polymer networks dominate the rheological behavior at concentrations above the electrical percolation threshold, which gives further evidence that significantly lower dispersion of CuNWs is obtained with the melt-mixing process. Electrical conductivity is desirable while maintaining the processibility of the polymer. In this regard, it is worth mentioning that obtaining useful electrical properties without the need of complete dispersion of the nanowires indeed might be advantageous; however, the electrical percolation threshold might be significantly higher than those attainable by well-dispersed nanowires.

Although low electrical percolation thresholds of CuNWs and AgNWs were attained by the presence of well-dispersed and agglomerated nanowires, lower electrical percolations thresholds are desirable. It is expected that optimum dispersion of the nanoparticles would result in lower electrical percolation thresholds. To overcome the agglomeration between nanowires, surface modification of the particles with alkanethiols of different alkyl chain length was investigated. To the best of our knowledge, the effect of the surface chemistry of metal nanowires on the electrical and rheological percolation phenomena in nanocomposites has not been reported in the literature. The enhanced dispersion of CuNWs surface functionalized with alkanethiols was evident from SEM and rheological characterization of their nanocomposites. Indeed, lower electrical percolation thresholds were obtained with surface functionalized CuNWs than with unfunctionalized CuNWs, but the presence of alkanethiolate multilayers on the functionalized CuNW surfaces resulted in polymer nanocomposites with higher electrical resistivities than those obtained with unfunctionalized nanowires.

6.2 Future work

6.2.1 Synthesis of nanowires in PAO templates

The synthesis of nanowires by AC electrodeposition in PAO templates is a feasible route for the synthesis of other metal nanostructures in gram amounts, facilitating the path for research and development of new materials that require high volumes of high quality nanomaterials. Nonetheless, more studies are necessary to understand the electrical behavior of the barrier layer and of the Al/PAO/nanostructure junctions formed during the electrochemical reactions in the pores, in order to enable the synthesis of other metals, alloys and/or compound nanostructures with different diameters (i.e. aspect ratios), as well as to further increase the efficiency of pore filling in PAO templates.

The presence of a small amount of oxide on the CuNW surface is unavoidable, given the conditions required for PAO template dissolution. The elimination of oxidation from CuNWs is critical for the formation of self-assembled alkanethiol monolayers; therefore, developing methods to decrease surface oxidation before functionalization of the nanoparticles will be required. In this aspect, using reducing agents for surface treatment of the CuNWs is recommended, prior to the surface modification with alkanethiols to prevent the formation of alkanethiolate multilayers. For instance, hydrazine, which decomposes into N_2 and H_2O, could be one possibility to use in order to prevent further oxidation of CuNWs.[7] By contrast, AgNWs liberated from PAO templates do not require additional treatment before surface functionalization.

6.2.2 Dispersion of metal nanowires in polymer nanocomposites

Surface functionalized AgNWs showed lower adsorption of the thiol compared to CuNWs, as discussed in Chapter 3. The fragmentation of surface functionalized silver nanowires highlighted the instability of high aspect-ratio nanoparticles to specific conditions of surface chemistry, applied stress, and temperature. Rayleigh instability of the nanowires might be the reason for this phenomenon.[21,22] In this regard, the study of fragmentation of metal nanowires of different aspect ratios may provide insight into the dynamics of fragmentation. Larger diameters and short lengths (lower aspect ratios) should result in nanowires with enhanced stability when exposed to conditions of high temperature and stress, such as those required for polymer processing. PAO template-directed synthesis provides an excellent route to the synthesis of gram quantities of AgNWs with different diameters and aspect ratios, and will facilitate the realization of such studies. Once the stability of the alkanethiol functionalized AgNWs under the conditions of polymer processing is established, lowering of the electrical percolation threshold in the nanocomposites might be expected as result of improved dispersion. It is worth noting that studies should be developed in order to optimize the dispersion for obtaining lower electrical percolation thresholds in these nanocomposites. Other strategies to improve the dispersion of metal nanowires are described below.

In the case of CuNWs, the formation of self-assembled alkanethiol monolayers might be difficult to attain, given that surficial oxidation of CuNWs during liberation from PAO templates needs to be efficiently prevented. Thus, for the use of copper nanowires as electrically conductive nanofillers, other strategies to enhance dispersion of metal nanowires may be further investigated. In this study, polymer nanocomposites were prepared by solution mixing and melt mixing. Another approach for the preparation of nanocomposites is in-situ polymerization. For instance, studies with carbon nanotube-based/polystyrene nanocomposites have shown that emulsion polymerization of styrene may result in enhanced dispersion of the nanoparticles and low electrical percolation thresholds.[23] Stabilization of suspensions of metal nanowires in the polymerization media will be required for effective coating of the nanowires with the polymer.[23] Similar procedures may be developed for preparation of metal nanowire/polymer nanocomposites. A polymer-coating of the metal nanowires may be obtained by impregnation in polymer solutions containing low concentrations, which will enable increased dispersion of metal nanowires by solution or melt-mixing. A driving force is still needed to facilitate efficient coating of the nanowires by the polymer, and the use of co-polymers that enable covalent bonding to the metal surface might be recommended.[24] In addition, chemical reactions between metal nanowire surfaces and polymers might lead to improvement of mechanical properties of the nanocomposites.[17]

6.2.3 Electrical percolation threshold

In order to reduce the electrical percolation threshold of metal nanowire/polymer nanocomposites several approaches can be pursued. (1) *High aspect ratios*: well-dispersed high aspect ratio nanofillers result in lower electrical percolation thresholds. As shown in this work, the aspect ratio of nanowires prepared in PAO templates decreases as a result of the liberation process. Given that the mechanical resistance of the nanowires to breaking into short segments might be higher for thicker nanowires, one may suggest the effect of pore diameter in PAO templates on the length distribution (aspect ratio distribution) of liberated nanowires be studied. Hence, the feasibility of lowering the electrical percolation thresholds of metal nanowire/polymer nanocomposites by increasing the aspect ratio will be evaluated. It is worth considering other recently developed methods for synthesizing of nanowires by solution methods. These may provide other routes for the preparation of polymer nanocomposites with high-aspect ratio metal nanowires.[7-9] (2) *Alignment*: Du et al.[14] showed that aligned SWNTs in PMMA nanocomposites using extrusion can result in an increase of the percolation threshold. In addition, they found that intermediate alignment of SWNTs may result in higher conductivities than isotropic dispersions of SWNTs. Similar studies with metal nanowires may contribute to the understanding of the effects of isotropic, anisotropic, and intermediate alignment in the properties of nanocomposites. For instance, metal nanowire heterostructures containing magnetic segments might facilitate alignment using magnetic fields. (3) *Dispersion*: optimum dispersion of the nanofiller is required to facilitate control of alignment and distribution. Alternatives for future work previously described in section 6.2.2 should be considered. (4) *Double percolation:* the preferential dispersion of the nanowires in one phase of an immiscible polymer blend enables electrical conductivity at reduced volume fractions of the nanofiller.[25] For instance, Pötschke et al. reported the reduction of the electrical percolation threshold of MWNT from 1.0 to 0.41 wt. % using co-continuous blends of PC/PE.[25] The concomitant interaction of these factors might lead to the preparation of metal nanowire/polymer nanocomposites with lower electrical percolation thresholds than those obtained in the current work.

6.3 References

1. AlMawlawi, D.; Liu, C. Z.; Moskovits, M., *J. Mater. Res.* **1994,** 9, (4), 1014-1018.
2. Preston, C.; Moskovits, M., *J. Phys. Chem.* **1993,** 97, 8495-8503.
3. Davydov, D. N.; Sattari, P. A.; AlMawlawi, D.; Osika, A.; Haslett, T. L.; Moskovits, M., *J. Appl. Phys.* **1999,** 86, (7), 3983-3987.
4. Sun, M.; Zangari, G.; Metzger, R. M., *IEEE Trans. Magn.* **2000,** 36, (5), 3005-3008.
5. Sun, M.; Zangari, G.; Shamsuzzoha, M.; Metzger, R. M., *Appl. Phys. Lett.* **2001,** 78, (19), 2964-2966.
6. Nielsch, K.; Muller, F.; Li, A.-P.; Gosele, U., *Adv. Mater.* **2000,** 12, (8), 582-586.
7. Chang, Y.; Lye, M. L.; Zeng, H. C., *Langmuir* **2005,** 21, (9), 3746-3748.
8. Sun, Y. G.; Xia, Y. N., *Adv. Mater.* **2002,** 14, (11), 833-837.
9. Murphy, C. J.; Gole, A. M.; Hunyadi, S. E.; Orendorff, C. J., *Inorg. Chem.* **2006,** 45, (19), 7544-7554.
10. Breuer, O.; Sundararaj, U., *Polym. Compos.* **2004,** 25, (6), 630-645.
11. Shenoy, A. V., *Rheology of filled polymer systems*. Kluwer Academy Publishers: Dordrecht, 1999.
12. Gelves, G. A.; Lin B.; Sundararaj, U.; Haber, J. A., *Adv. Funct. Mater.* **2006,** 16, 2423-2430.
13. Haggenmueller, R.; Gommans, H. H.; Rinzler, A. G.; Fischer, J. E.; Winey, K. I., *Chem. Phys. Lett.* **2000,** 330, (3-4), 219-225.

14. Du, F. M.; Fischer, J. E.; Winey, K. I., *Phys. Rev. B* **2005,** 72, (12), 121404, 1-4.

15. Du, F. M.; Scogna, R. C.; Zhou, W.; Brand, S.; Fischer, J. E.; Winey, K. I., *Macromolecules* **2004,** 37, (24), 9048-9055.

16. Du, F. M.; Fischer, J. E.; Winey, K. I., *J. Polym. Sci., Part B: Polym. Phys.* **2003,** 41, (24), 3333-3338.

17. Moniruzzaman, M.; Winey, K. I., *Macromolecules* **2006,** 39, (16), 5194-5205.

18. Haggenmueller, R.; Zhou, W.; Fischer, J. E.; Winey, K. I., **2003,** 3, (1-2), 105-110.

19. Pötschke, P.; Fornes, T. D.; Paul, D. R., *Polymer* **2002,** 43, (11), 3247-3255.

20. Pötschke, P.; Abdel-Goad, M.; Alig, I.; Dudkin, S.; Lellinger, D., *Polymer* **2004,** 45, (26), 8863-8870.

21. Toimil-Molares, M. E.; Balogh, A. G.; Cornelius, T. W.; Neumann, R.; Trautmann, C., *Appl. Phys. Lett.* **2004,** 85, (22), 5337-5339.

22. Bid, A.; Bora, A.; Raychaudhuri, A. K., *Phys. Rev. B* **2005,** 72, 113415, 1-3.

23. Wang, Z.; Lu, M.; Li, H. L.; Guo, X. Y., **2006,** 100, (1), 77-81.

24. Hill, D. E.; Lin, Y.; Rao, A. M.; Allard, L. F.; Sun, Y. P., *Macromolecules* **2002,** 35, (25), 9466-9471.

25. Pötschke, P.; Bhattacharyya, A. R.; Janke, A., *Carbon* **2004,** 42, (5-6), 965-969.

Appendix A

Surface functionalization of CuNWs using benzenethiol and characterization of C_6H_5S-CuNW/PS nanocomposites

A.1 Introduction

Benzenethiol was utilized for surface functionalization of CuNWs. Given the similarity of its structure to that of PS, benzenethiol-functionalized CuNWs would be expected to improve the dispersion and electrical properties of the composites. However, surface functionalization of CuNWs with benzenethiol yielded poor results for both dispersion and electrical properties as described below.

A.2 Surface functionalization of CuNWs using benzenethiol

Samples of CuNWs in methanol suspensions were treated with concentrations of 5.0 mM benzenethiol (C_6H_5SH, Aldrich, 97 %) using a similar procedure to that described in the experimental section in Chapter 3. Thermogravimetric analysis of C_6H_5S-CuNWs heated to 550 °C showed a desorption temperature of 303 °C and weight loss percent of 21.3 %. Table A1 shows the results of elemental analysis for a typical sample of C_6H_5S-CuNWs. These results demonstrated much more significant chemisorption of benzenethiol than alkanethiols on CuNW surfaces (Chapter 3). Unlike alkanethiol functionalized CuNWs, when C_6H_5S-CuNWs were treated with ultrasound in CH_2Cl_2 solutions, dispersion of the nanowires was not observed (i.e. the nanowires remained at the bottom of the flask), which indicated that strong agglomeration forces were acting to prevent the nanowires dispersion.

Table A1. Elemental analysis of copper nanowires functionalized with C_6H_5SH.

RS-CuNW	S	C	H	C+S+H	C/S	H/C	Cu/S
	(%)	(%)	(%)	(%)			
C_6H_5S-CuNW	7.12	15.53	1.12	23.77	5.8	0.9	5.40

A.3 C_6H_5S-CuNW/PS nanocomposites - dispersion and electrical resistivity

C_6H_5S-CuNWs were utilized for the preparation of polystyrene nanocomposites by melt-mixing process in the APAM using similar conditions to those used for preparation of nanocomposites using alkanethiol-functionalized nanowires (Chapter 5). Figure A1 shows the results of rheological characterization of the C_6H_5S-CuNW/PS nanocomposites. The dispersion of the C_6H_5S-CuNWs into PS was poor as shown in Figure A1, which shows a significant amount of large agglomerates of up to 150 μm in size. The number of agglomerates observed was higher than for nanocomposites prepared using unfunctionalized CuNWs (Chapter 5).

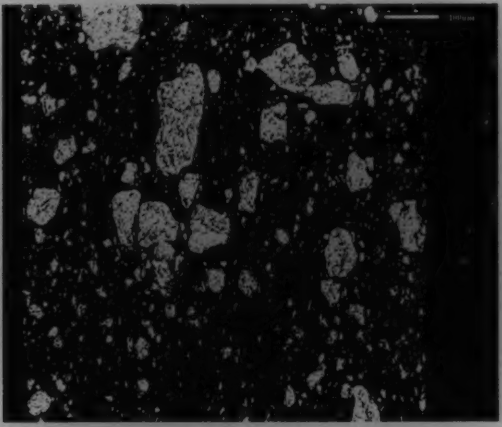

Figure A1. Backscattered SEM image of melt-mixed C_6H_5S-CuNW/PS nanocomposites containing 4.0 vol. % Cu. The image showed poor dispersion of C_6H_5S-CuNW in a PS matrix.

Table A1 shows the volume electrical resistivities obtained for C_6H_5S-CuNW/PS nanocomposites with different concentrations of nanowires. The electrical resistivity remained unchanged up to concentrations of 2.0 vol. %. At 4.0 vol. %, a change of almost 3 orders of magnitude in the electrical resistivity is observed.

Table A2. Average volume electrical resistivity and standard deviation calculated for C_6H_5S-CuNW/PS nanocomposites at different concentrations of copper.

Cu Conc. (Vol. %)	ρ[a] ($\Omega\cdot$cm)	Log (ρ, $\Omega\cdot$cm)
0.0	1.86×10^{16}	16.27
0.5	2.04×10^{16}	16.31
1.0	8.91×10^{15}	15.95
2.0	4.17×10^{15}	15.62
4.0	1.38×10^{13}	13.14

[a] measured using 100 V.

A.4 Conclusion

The dispersion of CuNWs surface functionalized using benzenethiol was poor. The nanowires do not disperse by the action of ultrasound or applied stress during melt mixing. The electrical resistivity of the nanocomposites indicates the formation of conductive networks at concentrations of 4.0 vol. % Cu. The limited dispersion of C_6H_5S-CuNWs in the polymer indicates that strong agglomeration forces occur likely due to the formation of multilayers of RS-Cu complexes (Chapter 3).